

University of Groningen

Spin Transport and Proximity-Induced Magnetism in Graphene-Based van der Waals Structures

Leutenantsmeyer, Johannes Christian

IMPORTANT NOTE: You are advised to consult the publisher's version (publisher's PDF) if you wish to cite from it. Please check the document version below.

Document Version

Publisher's PDF, also known as Version of record

Publication date:

2018

[Link to publication in University of Groningen/UMCG research database](#)

Citation for published version (APA):

Leutenantsmeyer, J. C. (2018). *Spin Transport and Proximity-Induced Magnetism in Graphene-Based van der Waals Structures*. Rijksuniversiteit Groningen.

Copyright

Other than for strictly personal use, it is not permitted to download or to forward/distribute the text or part of it without the consent of the author(s) and/or copyright holder(s), unless the work is under an open content license (like Creative Commons).

The publication may also be distributed here under the terms of Article 25fa of the Dutch Copyright Act, indicated by the "Taverne" license. More information can be found on the University of Groningen website: <https://www.rug.nl/library/open-access/self-archiving-pure/taverne-amendment>.

Take-down policy

If you believe that this document breaches copyright please contact us providing details, and we will remove access to the work immediately and investigate your claim.

Downloaded from the University of Groningen/UMCG research database (Pure): <http://www.rug.nl/research/portal>. For technical reasons the number of authors shown on this cover page is limited to 10 maximum.

Spin Transport and Proximity-Induced Magnetism in Graphene-Based van der Waals Structures

Johannes Christian Leutenantsmeyer



University of Groningen
**Zernike Institute
for Advanced Materials**

Spinograph
Spintronics in Graphene



The work described in this thesis was performed in the research group Physics of Nanodevices at the Zernike Institute for Advanced Materials at the University of Groningen, The Netherlands.

Cover: Illustration of the different device geometries studied in this thesis. The gray hexagons represent graphene with sketches of typical data in red. Front side: Comparison between spin precession in graphene on hBN (green) and graphene in proximity to a magnet (yellow) as studied in Chapter 4 and Chapter 5. The spin transport in the bottom device is anisotropic in pristine bilayer graphene encapsulated in hBN (Chapter 7). Back side: Illustration of bias-dependent spin injection through a trilayer hBN tunnel barrier as discussed in Chapter 6

Zernike Institute PhD thesis series 2018-35
ISSN: 1570-1530
ISBN: 978-94-034-1273-3
ISBN: 978-94-034-1272-6 (electronic version)

Printed by: Gildeprint, Enschede



rijksuniversiteit
 groningen

Spin Transport and Proximity-Induced Magnetism in Graphene-Based van der Waals Structures

Proefschrift

ter verkrijging van de graad van doctor aan de
Rijksuniversiteit Groningen
op gezag van de
rector magnificus prof. dr. E. Sterken
en volgens besluit van het College voor Promoties.

De openbare verdediging zal plaatsvinden op

vrijdag 21 december 2018 om 14:30 uur

door

Johannes Christian Leutenantsmeyer

geboren op 19 juni 1989
te Nordhorn, Duitsland

Promotor

Prof. dr. ir. B.J. van Wees

Copromotor

Dr. I.J. Vera-Marun

Beoordelingscommissie

Prof. dr. B. Noheda Pinuaga

Prof. dr. S.O. Valenzuela

Prof. dr. J. Fernández-Rossier

Contents

1	Introduction	1
1.1	Evolution of Microelectronics to Nanoelectronics	1
1.2	Spintronics: Exploiting the Spin Degree of Freedom	3
1.3	Two-Dimensional Materials for Spintronics	3
1.4	Outline	4
1.5	Supplementary Literature	5
	References	6
2	Two-Dimensional Materials: From Graphene to Transition Metal Dichalco-	
	genides	7
2.1	Graphene: Two-Dimensional Graphite	7
2.2	Electronic Properties of Graphene	8
2.3	Graphene Spintronics	13
2.4	Spin Injection into Graphene	14
2.5	Non-Local Spin Valve	16
2.6	Hanle Spin Precession	18
2.7	Spin Relaxation, Spin-Orbit and Spin-Valley Coupling in Graphene . .	20
2.8	Integrated van der Waals Heterostructures	22
2.9	Ferromagnetic Proximity Effect	24
	References	26
3	Fabrication and Measurement Techniques	33
3.1	Exfoliation and Characterization of Graphene and hBN	33
3.2	Fabrication of van der Waals Heterostructures	34
3.3	Electron Beam Lithography	35
3.4	Deposition of Metallic Contacts	36
3.5	Measurement Techniques	36
	References	37

4 Proximity-Induced Room-Temperature Ferromagnetism in Graphene Probed with Spin Currents	39
4.1 Introduction	39
4.2 Sample Fabrication and Characterization	40
4.3 Analysis and Discussion	42
4.4 Conclusion	45
4.5 Methods	46
4.6 Supplementary Information	46
4.6.1 Characterization of the YIG Films	46
4.6.2 Charge and Spin Transport Properties of the Graphene Flake	47
4.6.3 Discussion of the Full Spin Precession Data Sets	48
4.6.4 Absence of Potential YIG Stray Fields	50
4.6.5 Comparison to a Reference Sample	52
4.6.6 Comparison to Spin Modulation in Metal/YIG Systems	52
4.6.7 Full Set of Spin Transport Modulation Data	53
4.6.8 Spin Transport Modulation at Room Temperature	54
4.6.9 Modeling	54
4.6.10 Absence of a Parallel Magnon Transport Channel	56
References	57
5 Efficient Bias-Dependent Spin Injection into Graphene on YIG through Bilayer hBN Tunnel Barriers	59
5.1 Introduction	59
5.2 Sample Preparation and Contact Characterization	60
5.3 Bias-Dependent Spin Injection through Bilayer hBN Tunnel Barriers into Single and Bilayer Graphene on YIG	62
5.4 Bias-Dependent Spin Precession Measurements and Estimation of the Proximity-Induced Exchange Field in Bilayer hBN/Graphene on YIG	65
5.5 Bias-Dependent Spin Precession in Bilayer hBN/Bilayer Graphene on YIG	68
5.6 Conclusion	70
5.7 Supplementary Information	70
5.7.1 Full Set of the hBN Tunnel Barrier Characterization	70
5.7.2 Estimation of the Spin Relaxation Length in Sample B	71
5.7.3 Origin of the Background in the Hanle Curves in Sample B	73
References	74
6 Efficient Spin Injection into Graphene through Trilayer hBN Tunnel Barriers	77
6.1 Introduction	77
6.2 Sample Preparation and Contact Characterization	78

6.3	Spin Transport and Precession Measurements	80
6.4	Bias-Dependence of the Spin Injection Efficiency	81
6.5	Calculation of the DC Spin Polarization	83
6.6	Isotropy of the Spin Injection Mechanism	84
6.7	Two-Terminal DC Spin Transport Measurements up to Room Temperature	85
6.8	Summary	86
6.9	Supplementary Information	87
6.9.1	Fabrication Details	87
6.9.2	Determination of the Contact Spin Polarizations	87
6.9.3	Full Set of Spin Transport Parameters	89
6.9.4	Extraction of the Magnetization Angle	89
6.9.5	Quantum Capacitance Correction to DC Bias-Induced Gating	90
	References	91
7	Observation of Spin-Valley-Coupling-Induced Large Spin-Lifetime Anisotropy in Bilayer Graphene	95
7.1	Introduction	95
7.2	Results and Discussion	96
7.3	Conclusion	103
7.4	Supplementary Information	103
7.4.1	Fabrication Details	103
7.4.2	Charge and Spin Transport Characterization	105
7.4.3	Estimation of the Electric Field	106
7.4.4	Spin-Lifetime Anisotropy at Zero DC Bias	107
7.4.5	Measurements over Different Injector-Detector Spacings	108
7.4.6	Low Temperature Anisotropy Measurements	108
7.4.7	Carrier Concentration-Dependence of the In-Plane Spin-Lifetime	109
7.4.8	Spin Precession Measurements with In-Plane Magnetic Fields	110
7.4.9	Carrier Density-Dependence of the Magnetoresistance	111
7.4.10	Modeling of the Spin-Lifetime Anisotropy	111
7.4.11	Effect of the Contact Resistance on the Anisotropy	113
7.4.12	Measurement of the Contact Resistances	115
7.4.13	Measurements on a Second BLG Device	115
	References	116
8	Outlook	119
8.1	Spin Transport Measurements on Graphene on YIG	119
8.2	Anomalous Hall Effect in Graphene on YIG	120
8.3	Spin Injection and Detection into Graphene Using Two-Dimensional Ferromagnets	122

8.4 Spin to Charge Conversion in Graphene and TMDs	123
8.5 Related Spin Lifetime Anisotropy Experiments	125
References	126
Summary	127
Samenvatting	131
A Detailed Fabrication Techniques and Recipes	135
A.1 Fabrication of One-Dimensional Contacts	135
A.2 Liquid Gating of Graphene on YIG	135
A.3 YIG Cleaning Recipe	136
A.4 Transfer of CVD Graphene from Copper Foil	137
A.5 Electron Beam Lithography on YIG	137
A.6 Standard Electron Beam Lithography Recipe	137
A.7 High Resolution Electron Beam Lithography	138
A.8 Negative Electron Beam Lithography with HSQ	138
Acknowledgements	139
Publications	141
Curriculum Vitae	143

Abstract

The rapid development of the last decades in the semiconductor industry has led to the dawn of the information age. While the requirements to the information technology hardware increase rapidly with increasing applications like the internet of things, the current development approach of down scaling is predicted to reach its fundamental limit during the next decade. Further progress will require the implementation of novel concepts that are currently in the research stage. A promising route for this purpose is the exploitation of the spin degree of freedom, known under the term spintronics. This research field has been growing rapidly over the last thirty years and already demonstrated the potential to trigger new developments in the semiconductor industry.

This chapter discusses the potential of two-dimensional materials for the field of spintronics. Graphene and its related materials are atomically thin and provide a wide range of unique properties that are attractive for applications. The combination of these materials to create customized devices has the potential to be the ideal platform for the next generation devices which combine high performance with low energy consumption and maintain progress to meet the future requirements of the information age.

1.1 Evolution of Microelectronics to Nanoelectronics

During the 20th century, several key inventions led to the development of microelectronic devices and triggered the beginning of the information age. In particular, the invention of the transistor and the integrated circuits (ICs) in the 1950s and 1960s as well as their tremendous development over the following decades has dramatically increased the range of application for microelectronics. As a consequence, computers have gained popularity and spread into nearly all aspects of daily life.

Due to the use of relays and vacuum tubes, the early computer systems were expensive, bulky and slow. The paradigm change came with the invention of the solid state transistor in 1947 and the development of the metal-oxide-semiconductor field-effect transistor (MOSFET). The fabrication of MOSFETs by lithography in a planar process on silicon wafers was the key component to the integration of large numbers of components onto a single chip. The ICs on a processor are the core element of modern computers and are essential for their processing speed.

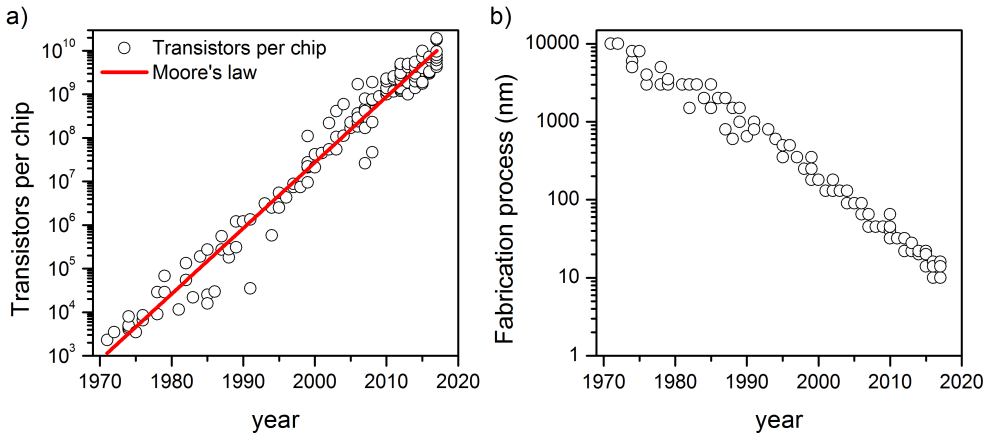


Figure 1.1: Development of integrated circuits from 1970 to 2018. a) Increase of transistors per chip. The red line describes “Moore’s law”, the doubling of the transistor density every two years. b) The scale of the smallest elements on a chip characterizes the fabrication process which started in 1970 with $10\ \mu\text{m}$ and is currently passing the $10\ \text{nm}$ mark. Data taken from [1].

Until today, most advancements of the computer industry were realized by increasing the amount of transistors on the processor chip. Figure 1.1a shows the evolution of the transistor density of commercial processor units between 1970 and 2018. While the Intel 4004 from 1971 had just over 2 000 transistors, single chips can nowadays house several billion transistors. This trend is described by the so-called “Moore’s law”, published in 1965 by the Intel founder Gordon Moore [2]. It describes his observation that the transistor density of ICs doubled annually between 1957 and 1965. This correlation was later adjusted to a doubling every two years and holds until today [3]. Nowadays, the miniaturization and the increase of the transistor density has been realized by the improvement of lithography systems. The advancement in the semiconductor fabrication process is shown in Figure 1.1b. It is characterized by the size of the smallest elements on the IC. The first commercially fabricated processors had elements as small as $10\ \mu\text{m}$, while their size has reduced nowadays by three orders of magnitude. As of 2018, most ICs are manufactured in the $10\ \text{nm}$ process, microelectronics has become nanoelectronics. Further development plans involve the introduction of extreme ultraviolet lithography, which is planned to further reduce the scale to $7\ \text{nm}$ by 2019 and to $5\ \text{nm}$ until 2021 [4].

Despite the continuous achievements and development efforts in the semiconductor industry, it is clear that this progress cannot continue forever. The miniaturization approach is about to reach a fundamental limit. As the feature sizes decreases to the atomic scale, quantum effects and dissipation of excess heat becomes a bot-

tleneck for further development [3, 5]. As a consequence, novel concepts “beyond Moore” are required to maintain advancement in the semiconductor industry and meet to the increasing requirements of the information age.

1.2 Spintronics: Exploiting the Spin Degree of Freedom

A promising platform for the next generation information technology is “spin electronics” (or “spintronics”). This term describes the exploitation of the electron spin for electronics where spin currents are used as information carrier instead of charge currents. The use of the spin degree of freedom for data storage or logic devices has the potential for faster devices with higher density and lower power consumption than conventional devices.

The spin is the quantum mechanical analog of the classical angular momentum and is quantized for electrons either up- or downwards with respect to the quantization axis. A spin polarized current has an excess of one spin species which usually relaxes back to an unpolarized spin current while loosing the spin information.

The “spin transistor” is a concept proposed in 1990 by Datta and Das [6] in which spin currents are used for logic applications analogous to conventional transistors. The output of conventional transistors is determined by its resistivity, where “on” and “off” correspond to the high and low resistive state of the semiconducting channel. In the spin transistor “on” and “off” states are determined by the spin polarization, “up” or “down”. The realization of such a spin-based transistor requires the tackling of several experimental challenges and a true spin transistor needs still to be demonstrated. Two major challenges for the realization of a spin transistor are the efficient control of spins and the short spin-lifetime in most materials at room temperature.

1.3 Two-Dimensional Materials for Spintronics

In most metals that are compatible with the processes in the semiconductor industry the distance that spin currents can travel before they relax back to an unpolarized state is limited to a few tens of nanometers at room temperature. Graphene, a single atomic layer of graphite, promises to carry spin information over hundreds of micrometers [7], making it an appealing material for spintronics. Spin transport in graphene over several tens of micrometers has already been demonstrated experimentally [8, 9], underlining its potential. The long distance spin transport originates from the weak spin-orbit interaction that spins experience in graphene. However, this comes at the cost of a relatively inefficient control of spins in graphene.

Transition metal dichalcogenides (TMDs) are layered materials in which a transition metal atom (e.g. Mo or W) is sandwiched between two chalcogen atoms (e.g. S,

Se or Te). Monolayers of TMDs are bound in a bulk crystal by van der Waals forces, analogous to graphite. In contrast to graphene, TMDs are semiconductors with a strong spin-orbit coupling. The concept of integrated van der Waals structures combines different layered materials to heterostructures. Proximity effects between the individual layers can give rise to novel and customizable device properties [10].

Several theoretical and experimental studies have investigated how the proximity of graphene to a different material can induce new properties into graphene. Heterostructures of graphene and TMDs are of particular interest since the strong spin-orbit coupling in TMDs can increase the weak intrinsic spin-orbit strength in graphene from 12 μeV to above 10 meV [11, 12]. Furthermore, graphene/TMD heterostructures show a gate-controlled spin absorption from graphene into the TMD. This can be used as a spin switch, a step towards the realization of a spin transistor [13, 14]. TMDs, in which the inversion symmetry is broken show a coupling between the spin and valley degree of freedom. This coupling can be imprinted into graphene by proximity interaction [15, 16]. Several studies have explored the possibility to induce magnetism into graphene and create a two-dimensional ferromagnet. Graphene on the ferromagnetic insulator YIG has a proximity-induced exchange field that can be controlled with the YIG magnetization and affects a spin current in the device [17, 18].

In conclusion, the combination of different layered materials to integrated van der Waals structures promises a wide range of application in fundamental and applied studies. Spin transport in these devices provides new routes to transport and control spins in nanoscaled devices.

1.4 Outline

This thesis is focused on the introduction of magnetism into graphene by the proximity to a ferrimagnet and the spin transport in graphene fully encapsulated by hexagonal boron nitride (hBN) and is divided into the following chapters:

Chapter 2 introduces the class of two-dimensional materials. The basic electronic properties of graphene are presented, and the mechanisms of spin injection, detection and transport are discussed. Next, the concept of integrated van der Waals heterostructures is introduced. The effect of spin-orbit coupling on spin transport and relaxation in graphene is described and different approaches to induce magnetism into graphene are reviewed.

Chapter 3 discusses the experimental techniques used to fabricate and characterize graphene-based van der Waals heterostructures. Additional techniques and detailed fabrication recipes are presented in Appendix A.

Chapter 4 reports the first experimental study of magnetic graphene by using spin transport. A magnetic exchange field is induced into graphene on YIG. The strength of the exchange field is quantified in two independent experiments consistently in the order of 0.2 T, a value below the expected magnitude from *ab initio* calculations. Moreover, the exchange-field-induced spin precession is used to modulate spin currents in graphene efficiently, making the graphene/YIG heterostructure an interesting system to explore novel ways to control spin currents in graphene.

Chapter 5 employs a tunnel barrier of a bilayer flake of the two-dimensional material hBN for the efficient spin injection into graphene on YIG. Bilayer hBN tunnel barriers show a characteristic dependence of the spin injection efficiency on an applied DC bias current. This chapter demonstrates the applicability of this technique to the graphene/YIG system. Large spin accumulations are injected with differential spin polarization values of up to -60% , which is comparable to fully hBN encapsulated devices. The proximity-induced exchange field is estimated in one sample to be 85 mT. This is in agreement with the relatively low magnitude from Chapter 4.

Chapter 6 presents experimental results on spin injection into bilayer graphene using a trilayer hBN tunnel barrier which allows the characterization of spin transport in a fully hBN encapsulated system. The performance of bilayer hBN and trilayer hBN is comparable and the experimental observations allow to exclude several proposed origins of the DC bias-dependence.

Chapter 7 reports the first measurement of a spin-valley-coupling-induced spin-lifetime anisotropy in pristine bilayer graphene. The lifetime for spins pointing out-of-plane is found to be at the charge neutrality point up to eight times greater than for in-plane spins. The observation is explained with the intrinsic, valley-dependent spin-orbit splitting of $\sim \pm 12 \mu\text{eV}$ which results in a valley-dependent spin splitting once the inversion symmetry is broken.

Chapter 8 reviews projects that were performed during the last four years, but are not discussed in this thesis. However, the preliminary results of these experiments motivate further investigation.

1.5 Supplementary Literature

The following articles provide a good overview of the field of spintronics in graphene and 2D materials and are endorsed as a basic introduction:

- Spin transport in graphene/transitionmetal dichalcogenide heterostructure. J.H. Garcia, M. Vila, A.W. Cummings, and S. Roche. *Chemical Society Reviews* **47**(9), 3359–3379, 2018.

- Graphene spintronics: the European Flagship perspective. S. Roche, et al., *2D Materials* **2**(3), 030202, 2015.
- Graphene Spintronics, W. Han, R.K. Kawakami, M. Gmitra, and J. Fabian, *Nature Nanotechnology* **9**(10), 794-807, 2014.

References

- [1] K. Rupp. Microprocessor Trend Data. github.com/karlrupp/microprocessor-trend-data, 2018.
- [2] G.E. Moore. Cramming more components onto integrated circuits. *Electronics*, **38**(8), 144, 1965.
- [3] T.N. Theis and H.-S.P. Wong. The End of Moore's Law: A New Beginning for Information Technology. *Computing in Science & Engineering*, **19**(2), 41, 2016.
- [4] R. Courtland. Moore's law's next step: 10 nanometers. *IEEE Spectrum*, **54**(1), 52, 2017.
- [5] I.L. Markov. Limits on fundamental limits to computation. *Nature*, **512**(7513), 147, 2014.
- [6] S. Datta and B. Das. Electronic analog of the electro-optic modulator. *Applied Physics Letters*, **56**(7), 665, 1990.
- [7] D. Huertas-Hernando, F. Guinea, and A. Brataas. Spin-orbit-mediated spin relaxation in graphene. *Physical Review Letters*, **103**(14), 146801, 2009.
- [8] M. Drögeler, C. Franzen, F. Volmer, T. Pohlmann, L. Banszerus, M. Wolter, K. Watanabe, T. Taniguchi, C. Stampfer, and B. Beschoten. Spin Lifetimes Exceeding 12 ns in Graphene Nonlocal Spin Valve Devices. *Nano Letters*, **16**(6), 3533, 2016.
- [9] J. Ingla-Aynés, R.J. Meijerink, and B.J. van Wees. Eighty-Eight Percent Directional Guiding of Spin Currents with 90 μm Relaxation Length in Bilayer Graphene Using Carrier Drift. *Nano Letters*, **16**(8), 4825, 2016.
- [10] A.K. Geim and I.V. Grigorieva. Van der Waals heterostructures. *Nature*, **499**(7459), 419, 2013.
- [11] Z. Wang, D.K. Ki, J.Y. Khoo, D. Mauro, H. Berger, L.S. Levitov, and A.F. Morpurgo. Origin and magnitude of 'designer' spin-orbit interaction in graphene on semiconducting transition metal dichalcogenides. *Physical Review X*, **6**(4), 041020, 2016.
- [12] T. Wakamura, F. Reale, P. Palczynski, S. Guéron, C. Mattevi, and H. Bouchiat. Strong Anisotropic spin-orbit Interaction Induced in Graphene by Monolayer WS_2 . *Physical Review Letters*, **120**(10), 106802, 2018.
- [13] W. Yan, O. Txoperena, R. Llopis, H. Dery, L.E. Hueso, and F. Casanova. A two-dimensional spin field-effect switch. *Nature Communications*, **7**, 13372, 2016.
- [14] A. Dankert and S.P. Dash. Electrical gate control of spin current in van der Waals heterostructures at room temperature. *Nature Communications*, **8**, 16093, 2017.
- [15] L.A. Benítez, J.F. Sierra, W. Savero Torres, A. Arrighi, F. Bonell, M.V. Costache, and S.O. Valenzuela. Strongly anisotropic spin relaxation in graphene/transition metal dichalcogenide heterostructures at room temperature. *Nature Physics*, **14**(3), 303, 2018.
- [16] T.S. Ghiasi, J. Ingla-Aynés, A.A. Kaverzin, and B.J. van Wees. Large Proximity-Induced Spin Lifetime Anisotropy in Transition-Metal Dichalcogenide/Graphene Heterostructures. *Nano Letters*, **17**(12), 7528–7532, 2017.
- [17] J.C. Leutenantsmeyer, A.A. Kaverzin, M. Wojtaszek, and B.J. van Wees. Proximity induced room-temperature ferromagnetism in graphene probed with spin currents. *2D Materials*, **4**(1), 014001, 2017.
- [18] S. Singh, J. Katoch, T. Zhu, K.-Y. Meng, T. Liu, J.T. Brangham, F. Yang, M.E. Flatté, and R.K. Kawakami. Strong Modulation of Spin Currents in Bilayer Graphene by Static and Fluctuating Proximity Exchange Fields. *Physical Review Letters*, **118**(18), 187201, 2017.

Chapter 2

Two-Dimensional Materials: From Graphene to Transition Metal Dichalcogenides

Abstract

This chapter introduces the class of layered two dimensional materials. First, the electronic properties of graphene and the basic concepts of charge and spin transport are introduced. The concepts of spin relaxation, spin-orbit and spin-valley coupling are discussed. Next, the concept of integrated van der Waals heterostructures to create customized and atomically thin devices is presented. Lastly, the ferromagnetic proximity effect to induce magnetism into graphene is discussed.

2.1 Graphene: Two-Dimensional Graphite

When a bulk crystal of graphite is sliced down to single atomic thickness, the remaining material is known as graphene. A monolayer of graphene (Figure 2.1b) consists of sp^2 hybridized carbon atoms which are arranged in the form of a hexagonal honeycomb lattice with a spacing of 142 pm between the atoms. Single and bilayer graphene are the most prominent representatives of the class of two-dimensional materials and have a wide range of applications [1], ranging from life sciences [2] to aeronautics [3]. This thesis is focused on the charge and spin transport, where graphene and its related materials have the potential to become the ideal platform for the next generation spintronic devices [4–6].

Graphite and thin layers of it have already been studied theoretically and experimentally for several decades. After theoretical calculations of the graphene band structure in the late 1940s [7], lamellae of few atoms thickness were investigated in the 1960s by transmission electron microscopy [8]. The authors analyzed thin graphite flakes and concluded different flake thicknesses depending on the contrast ratio. Isolated graphene was believed to be not stable, and the research focused for the next decades on nanotubes, thin multilayers and fullerenes [9].

The range of carbon-based nano materials extends over different dimensions. The three dimensional form shown in Figure 2.1d is known as diamond and is one of the hardest materials known. The zero dimensional fullerenes (or buckyballs, Figure 2.1e) are spherical structures of carbon atoms whose existence was first postu-

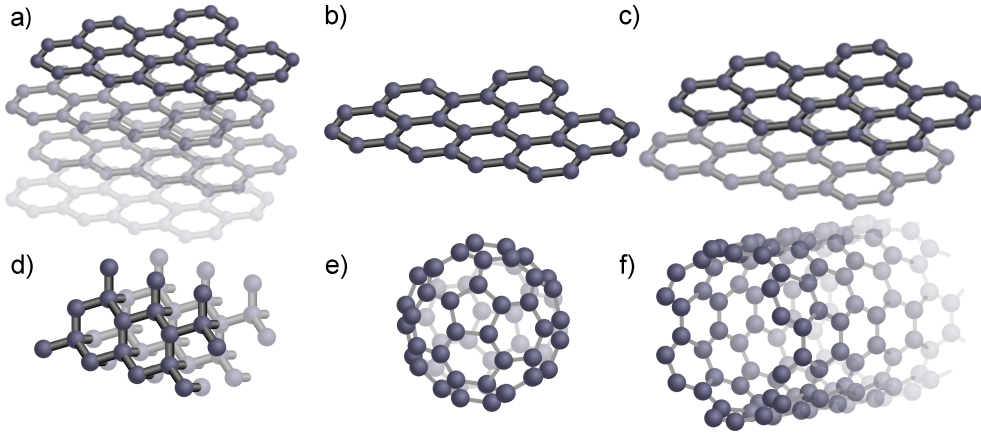


Figure 2.1: The different allotropes of carbon nanostructures: a) graphite (also known as multilayer graphene), b) (single layer) graphene, c) AB-stacked bilayer graphene, d) diamond e) C60-fullerene and f) carbon nanotube.

lated in the 1970s and experimentally found and studied in the 1980s [10]. A bigger impact on fundamental research was caused by the one dimensional carbon nanotubes (CNTs, Figure 2.1f). After their discovery in the 1970s, CNTs quickly attracted interest for the next decades. Their outstanding mechanical and electrical properties such as a Young's modulus of several hundred GPa and tensile strength of several tens of GPa are unprecedented in nature [11]. The conductivity of heat and electricity of CNTs is several orders of magnitude larger than the ones compared to copper. By controlling the growth of CNTs, their properties can be tuned from conducting to semiconducting, making the material suitable for nanoscaled transistors and appealing to succeed silicon in the semiconductor industry. Reference [12] comprehensively reviews the research on carbon-based nano materials. Several break-through discoveries were reported on carbon-based nano-materials prior to the first exfoliation of graphene using the scotch-tape method [13]. This simple method to create large flakes of atomically thin graphene triggered an intense research interest on graphene and related two-dimensional materials. Today, graphene is on the verge to enter the market and several commercial products employ graphene and its derivatives to improve the product properties [1, 14].

2.2 Electronic Properties of Graphene

The characteristic electronic properties of graphene originate from the hybridization of the carbon atoms. Isolated carbon has the atomic configuration $1s^2 2s^2, 2p^4$. In

a bound state, the 2s orbital can hybridize with the 2p orbitals into an sp-hybrid-orbital. When all p orbitals hybridize, four sp³ states result and form σ bonds in a tetrahedral structure with the neighboring atoms. In this configuration, the valence electrons are strongly bound, and consequently diamond is a strong electrical insulator with a band gap of 5 eV.

In graphene the 2s orbital hybridizes with two 2p orbitals (p_x and p_y). As a consequence, strong σ bonds are formed in the plane with an angle of 120° between the atoms (Figure 2.2a). In bulk graphite, the p_z orbitals bond weakly via electrostatic van der Waals forces to the adjacent layer. The weak inter-layer bonding results in an easier separation of individual layers than a breaking of the in-plane bonds. Consequently, large areas of graphene can be easily peeled apart using the scotch tape method. The p_z orbitals of graphene hybridize to a π band, which is the origin of the electronic properties of graphene. Early works on the calculation of the graphene band structure employed the tight binding approach with second nearest neighbor hopping [7, 15, 16].

The honeycomb lattice of graphene can be described with the two sublattices A and B with the primitive vectors \mathbf{a} and \mathbf{b} of the Bravais lattice:

$$\mathbf{a} = \frac{a}{2} \begin{pmatrix} 3 \\ \sqrt{3} \end{pmatrix}, \quad \mathbf{b} = \frac{a}{2} \begin{pmatrix} 3 \\ -\sqrt{3} \end{pmatrix}, \quad (2.1)$$

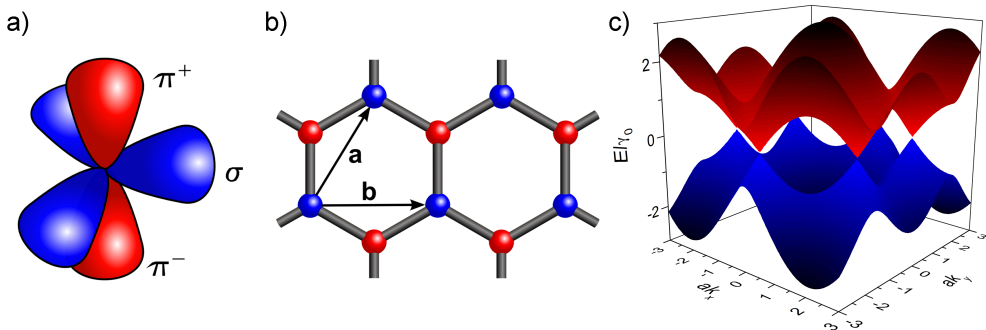


Figure 2.2: a) The electronic configuration of the carbon atom orbitals in the sp² hybridization. Within the plane, three hybridized sp orbitals form σ -bonds to the neighboring carbon atoms, the unbound p_z orbitals hybridizes with the neighboring p_z orbitals to the delocalized π band. b) Both graphene sublattices (red and blue) and the base vectors \mathbf{a} and \mathbf{b} are sketched. c) The electronic band structure is calculated using the tight-binding approach.

where $a = 142$ pm denotes the atomic distance of the carbon-carbon bond. The corresponding reciprocal lattice vectors \mathbf{a}_R and \mathbf{b}_R are:

$$\mathbf{a}_R = \frac{2\pi}{3a} \begin{pmatrix} 1 \\ \sqrt{3} \end{pmatrix}, \quad \mathbf{b}_R = \frac{2\pi}{3a} \begin{pmatrix} 1 \\ -\sqrt{3} \end{pmatrix}. \quad (2.2)$$

The first Brillouin zone of the reciprocal lattice has also a hexagonal symmetry. The conduction and valence band touch in the six corners and can be divided into two pairs that represent the K and K' valleys:

$$\mathbf{K} = \frac{2\pi}{3a} \begin{pmatrix} 1 \\ \sqrt{3} \end{pmatrix}, \quad \mathbf{K}' = \frac{2\pi}{3a} \begin{pmatrix} 1 \\ -\sqrt{3} \end{pmatrix}. \quad (2.3)$$

Using the tight binding approach the dispersion relation of the lowest conduction (+) and highest valence (-) bands can be calculated:

$$E_{\pm}(k_x, k_y) = \pm\gamma_0 \sqrt{1 + 4 \cos\left(\frac{\sqrt{3}k_x a}{2}\right) \cos\left(\frac{k_y a}{2}\right) + 4 \cos^2\left(\frac{k_y a}{2}\right)}, \quad (2.4)$$

where $\gamma_0 \sim 3.2$ eV [17] is the hopping energy between the first neighbor π orbitals. The characteristic features of the band structure are the absence of a gap and the touching of the electron and hole bands in the Dirac point (also called charge neutrality point, CNP) at K and K' = 0. At this point, the density of states and carrier concentration is theoretically zero and no electronic states can be occupied by either electrons or holes. However, fluctuations e.g. arising from finite temperatures give rise to a finite density of states at the CNP. The dispersion relation between energy and momentum $\mathbf{q} = \mathbf{k} - \mathbf{K}^{(\prime)}$ is close to the Dirac point linear and can be approximated with [18]:

$$E_{\pm}(\mathbf{q}) \approx \pm \hbar v_F \mathbf{q}, \quad (2.5)$$

where \hbar describes the reduced Planck constant and $v_F = 10^6$ m/s [18, 19] the Fermi velocity in graphene. The band structure is often reduced to the linear parts around the Dirac point (as shown in Figure 2.3b).

Bilayer graphene has different electronic properties than single layer graphene and exists in two configurations: in the AA stacking the carbon atoms of both layers lay exactly on top of each other. This configuration does not exist in nature but can be artificially grown [20]. The AB (or Bernal) stacking occurs in natural graphite where one of the carbon atom of the second layer is located over the center of hexagon of the other layer (Figure 2.1c). For the calculation of the band structure, the electron hopping between the carbon atoms on the dimer sites has to be taken into account ($\gamma_1 \sim 0.4$ eV). The resulting dispersion relation is quadratic and reads [18]:

$$E_{\pm}(\mathbf{q}) = \hbar^2 v_F^2 \mathbf{q}^2 / \gamma_1. \quad (2.6)$$

An interesting feature of bilayer graphene is the opening of a band gap of up to 200 meV under an applied perpendicular electric field [21–23]. Furthermore, the combination of two single layer graphene flakes to a bilayer flake has shown exotic properties such as superconductivity when the individual crystal planes of both layers are twisted by 1.1° [24, 25].

In a graphene field effect transistor (Figure 2.3a), a gate electrode is separated from the graphene channel through an insulating gate oxide layer. The carriers in

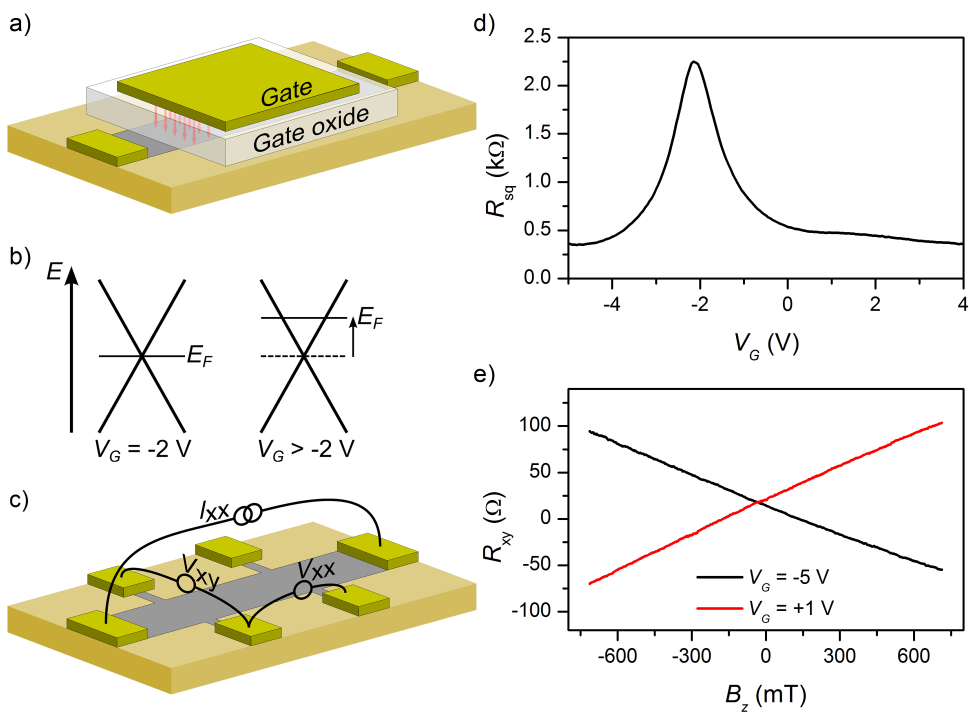


Figure 2.3: a) Schematic of a graphene field effect transistor, where an electric field is applied with a top gate. b) Sketch of the single layer graphene band structure, where an electric field applied via through a gate (V_G) shifts the Fermi energy E_F . When passing the charge neutrality point with a carrier concentration of $n \sim 0$, the carriers change from holes to electrons. c) Illustration of a graphene Hall bar device. The contact configuration for the measurement of the longitudinal $R_{xx} = V_{xx}/I_{xx}$ and transverse $R_{xy} = V_{xy}/I_{xx}$ is indicated. d) Experimental modulation of the graphene square resistance R_{sq} with an applied gate voltage V_G . The neutrality point is represented as a peak in the resistance (here at $V_G = -2$ V) and can indicate the doping level of the graphene. e) The slope of the transverse Hall resistance (R_{xy}) can be used to determine the carrier concentration n . The sign of the slope changes depending on the type of carriers.

graphene can be controlled by applying an electric field which shifts the Fermi energy level along the density of states (Figure 2.3b). When the Fermi level crosses the Dirac point, the carriers in the graphene flake change from holes to electrons. Theoretically, pristine graphene has the Fermi energy lying in the Dirac point. However, the presence of dopants arising from fabrication processes or the atmosphere shift the Fermi level away from the neutrality point. The data shown in Figure 2.3d has the CNP at $V_G = -2$ V.

To determine the CNP experimentally, the square resistance R_{sq} of the device is measured at different V_G (Figure 2.3d). The electric field shifts the Fermi energy E_F in the graphene channel and at the CNP the minimum of occupied states results in a peak in the square resistance R_{sq} . Widely used substrates for graphene consist of doped silicon with an oxidized surface. The advantage of the doped silicon substrate is that a gate voltage V_G can be applied to this layer and an electric field is applied to the graphene flake through the silicon oxide. In contrast to other gating techniques, the known parameters of the gate oxide allow the calculation of the carrier concentration n via:

$$n = \epsilon_0 \epsilon (V_G - V_{\text{CNP}}) / (e \cdot t_G), \quad (2.7)$$

where $\epsilon_0 = 8.8 \times 10^{-12}$ F/m is the vacuum permittivity, $\epsilon = 3.9$ the dielectric permittivity of SiO_2 , t_G the SiO_2 thickness, V_{CNP} the V_G at the CNP, and e the electron charge.

A different approach to determine n uses the Hall effect. The change of the slope of the transverse Hall resistance $R_{\text{xy}}(B_z)$ allows the direct calculation of n . For an accurate measurement, a graphene flake is patterned into a Hall bar geometry (Figure 2.3c). Carriers in a perpendicular magnetic field (B_z) experience the Lorentz force $F_L = -ev_x B_z$. As a consequence, charge carrier in the current direction x are deflected perpendicularly (y -direction) to the carrier velocity v_x . The transverse voltage V_y between two opposing contacts with the spacing w is determined by:

$$V_y = B_z v_x w = j_x B_z w / ne = R_H j_x B_z w, \quad (2.8)$$

$$R_{\text{xy}} = V_y / (j_x \cdot w) = R_H B_z, \quad (2.9)$$

where $j_x = nev_x$ is the current density along the channel. The Hall coefficient is defined as $R_H = 1/ne$ and allows the calculation of the carrier concentration. The carrier mobility μ can be calculated from n and R_{sq} via:

$$\mu = \frac{1}{neR_{\text{sq}}}. \quad (2.10)$$

Typical mobilities in graphene on silicon oxide substrates are of the order several $1\,000 \text{ cm}^2/\text{Vs}$, hexagonal boron nitride (hBN) encapsulated graphene can exceed $100\,000 \text{ cm}^2/\text{Vs}$.

2.3 Graphene Spintronics

Apart from their charge, all electrons have a magnetic moment called spin. In a quantized picture, the spin points along the quantization axis, which is defined by a present magnetic field. A spin points either upwards (“spin up”) or downwards (“spin down”). A conventional charge current (Figure 2.4a) has an equal amount of spin up and spin down and therefore no spin polarization. A spin polarized current has an excess of one spin species moving along with the electrons. In a pure spin current (Figure 2.4b) electrons carrying the spin move into opposite directions according to their spin species. The appealing feature of pure spin currents is that no net movement of electrons is required, and effects like Joule heating can be suppressed. Heating effects play an important role along with the miniaturization of electronic components and have become a bottleneck for the development of smaller and faster transistors [27, 28].

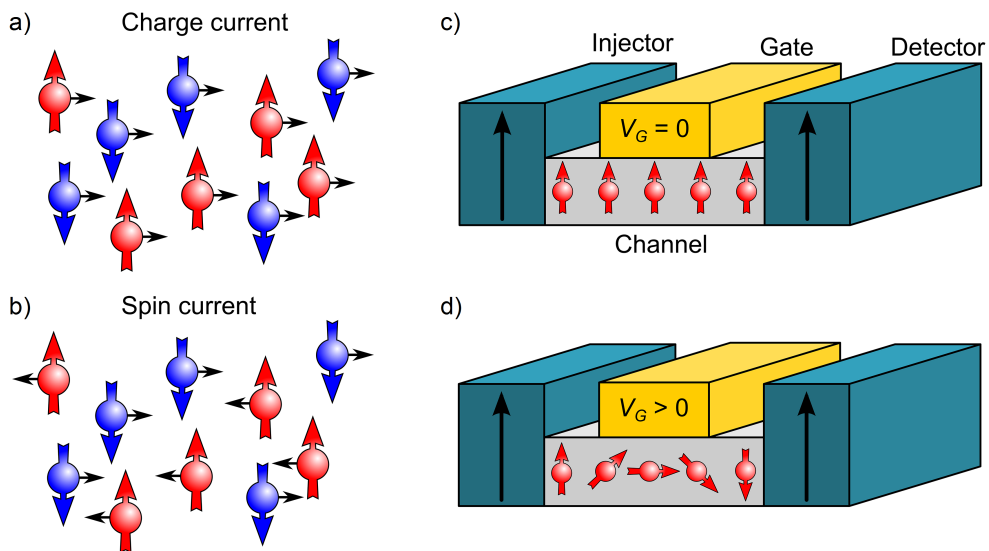


Figure 2.4: a) In a charge current without polarization equal amounts of electrons have a spin up and down. All electrons and spins move into one direction. b) In a pure spin current, electrons with spin up move into a different direction than electrons with spin down. As a consequence, no net charge current is moving and only spins are transported. c) Schematic of a spin transistor as proposed by Datta and Das [26]. Spins are injected into a two-dimensional channel and detected using conventional ferromagnetic electrodes. The spin transistor is in its “on” state. d) Using a gate electrode, the transported spins are controlled during the transport through the channel to alter the output signal.

A strategy to address this issue effectively is the use of spin currents instead of charge currents for electronics, known under the keyword spintronics. The analog of the conventional (charge) transistor is the spin transistor, a concept proposed by Datta and Das in 1990 [26]. It involves the injection and detection of spins through a ferromagnetic material into a non-magnetic and ballistic channel [29–32]. The states of the transistor are modulated via an applied gate voltage which controls the spins during transport. In the sketched on state in Figure 2.4c, the spins are transported unaffected through the channel and the detector would sense a high signal. In the off state in Figure 2.4d, down spins reach the detector, which is sensitive to up spins and senses a negative signal. The realization of a true spin transistor relies crucially on three experimental challenges:

Efficient spin injection and detection: Ideally the electrodes would inject and detect only one spin species into the channel. While some materials have shown a large spin polarization, the electrical injection of a fully spin polarized charge current into a nonmagnetic material still needs to be demonstrated.

Efficient spin transport: The material of the spin channel needs to conduct spins efficiently over the relevant length scale. The initial proposal from Datta and Das employed a two-dimensional electron gas at the interface of indium-aluminum-arsenide and indium-gallium-arsenide. However, the realized lifetime of spin currents at room temperature in this material is limited and the corresponding length scale is far below 1 μm . Therefore, a more promising channel material is graphene, which has demonstrated a spin diffusion length of several tens of μm [33, 34]. Theoretically, spins can travel several hundred μm in graphene [35]. However, the spin transistor concept requires a ballistic, one dimensional spin transport channel, where all spins move uniformly in one direction. In contrast, today's long distance spin transport relies on diffusive spin transport.

Efficient control of spins: Graphene provides a long spin relaxation length due to its low intrinsic spin-orbit coupling. However, the low interaction of spins in graphene becomes problematic since it lowers the efficiency of controlling spins. The spin transistor requires the rotation of spins through gate-tunable spin-orbit interaction, which is not efficient in graphene. Other concepts to control spins in graphene involve the proximity of graphene to YIG [36, 37] to induce additional spin precession, the absorption and dephasing of spins in a transition metal dichalcogenide [38, 39], and the relaxation via proximity coupling [40, 41].

2.4 Spin Injection into Graphene

The process of spin injection from a ferromagnet into graphene is schematically shown in Figure 2.5. A ferromagnetic electrode (cobalt) with a tunnel barrier is deposited on top of a graphene flake and a current is driven through the ferromagnet

into graphene. The band structure of a ferromagnet (Figure 2.5b) is characterized by the exchange splitting between the majority band, parallel to the magnetization of the ferromagnet, and the minority band. As a consequence, more majority than minority spins are present at the Fermi energy E_F in the ferromagnet. The current driven into a non-magnetic material carries the asymmetry of spins and, as a result, the spin imbalance of the ferromagnet is injected into the non-magnetic material. Contacts for spin injection employ a tunnel barrier to enhance the spin injection efficiency. When magnetic and non-magnetic material are in direct contact, the spin injection efficiency is less than 0.1% due to the conductivity mismatch [42]. The (spin) resistance of cobalt is significantly lower than of graphene, which can exceed in high quality graphene several $k\Omega$. As a consequence of the lower spin resistance of the ferromagnet, the injected spins diffuse back into the ferromagnet and reduce the spin accumulation in the non-magnetic material.

The introduction of a tunnel barrier circumvents this issue [43]. Materials like Al_2O_3 , TiO_2 and MgO are commonly used and have shown an effective spin polarization of up to 30% [44]. Using a tunnel barrier of two layers of hBN Gurram et al. [45] showed that the differential spin injection and detection efficiencies can be

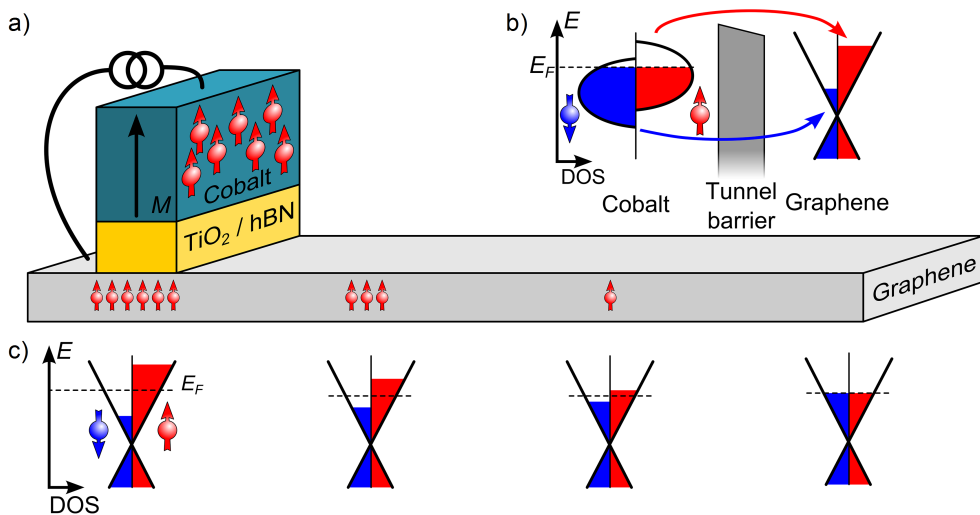


Figure 2.5: a) Schematic process of spin injection from a magnetic (here: cobalt) into a non-magnetic material like graphene. Note that the magnetization of cobalt lies in general in the film plane and is sketched as out-of-plane for illustration purposes. A tunnel barrier (TiO_2 or hBN) is employed to prevent the back flow of injected spins from graphene into the ferromagnet. b) Schematic process of spin polarized tunneling from the band structure of a ferromagnet through a tunnel barrier into graphene. c) The injected spin accumulation diffuses in the channel and decays with distance from the injector until the all spins are dephased.

increased to values as high as 100% by applying a DC bias current additionally to an AC measurement current.

Once injected into graphene, the spin accumulation diffuses in the material (Figure 2.5c). The spin accumulation dephases over the spin relaxation time τ_s . Since the transport process of spin is diffusive, the relaxation length λ can be correlated with τ_s and the spin diffusion constant D_s via $\lambda = \sqrt{D_s \tau_s}$. While theory predicts a spin relaxation length above 100 μm [35, 46], experimentally only a few tens of μm [33, 34] have been demonstrated. Despite of several theoretical and experimental works investigating the limitations of spin transport in graphene, the underlying mechanism is still under debate. As a consequence of the limited transport length, the spin signals are relatively small, often less than 1 Ω . Compared to the ohmic background of these devices, which often exceed the spin signal by several orders of magnitude, the measurement of small spin signals on large background signals is challenging. Additionally, magnetoresistive effects can mimic spin signals, making the clear identification of a spin signal in a two-terminal geometry complicated.

2.5 Non-Local Spin Valve

A method to reliably measure spin signals down to the $\text{m}\Omega$ range employs the separation of charge and spin transport in a “non-local” geometry, sketched in Figure 2.6a [47]. An AC current is driven from the injector to an outer reference electrode. The injected spin accumulation diffuses in both directions along the channel. The spin accumulation is sensed as a non-local voltage V_{NL} between the detector and the second reference electrode. The signal is determined by:

$$V_{\text{NL}} = P_{\text{det}} \mu_s / e, \quad (2.11)$$

where P_{det} is the spin polarization of the detector electrode and μ_s the spin chemical potential underneath the detector for up and down spin. The non-local resistance R_{NL} is then defined as:

$$R_{\text{NL}} = V_{\text{NL}} / I_{\text{AC}}. \quad (2.12)$$

Figure 2.6b shows the distance-dependence of the spin chemical potential μ for spin up (red) and down (blue).¹ In parallel magnetization alignment the detector senses the signal $V_{\text{NL}}(\text{P})$, determined by the difference of μ at the detector and at the reference electrode. When the detector magnetization is reversed, $V_{\text{NL}}(\text{AP})$ becomes negative. The sketch assumes non-magnetic reference electrodes, that are not sensitive to a spin accumulation. To simplify the fabrication procedures, the reference

¹Note that the linear effect of the electric field caused by the potential drop of the AC current at the channel on the average chemical potential is neglected here.

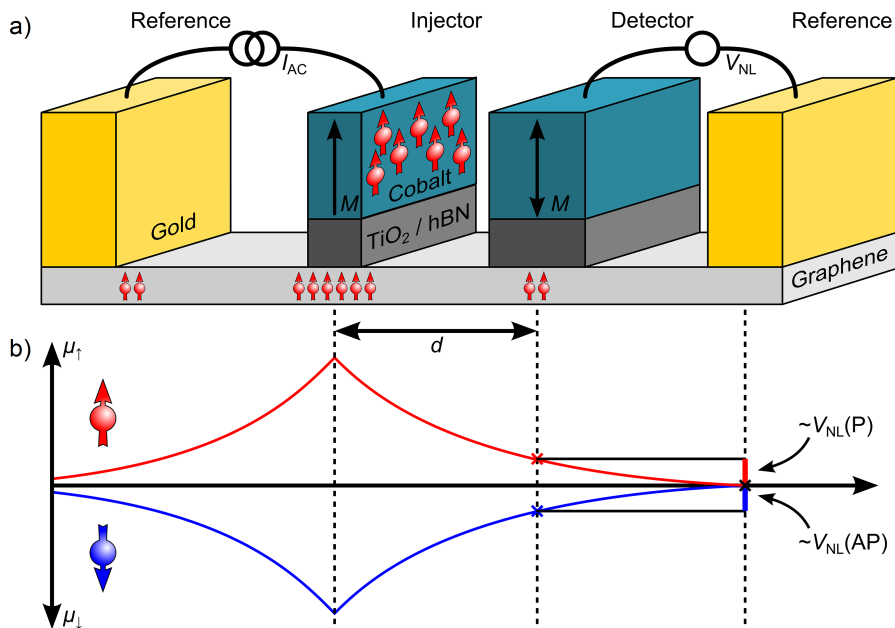


Figure 2.6: a) Schematic of a non-local measurement. The inner electrodes (injector and detector) are ferromagnetic and inject/detect a spin accumulation in the graphene flake. b) The chemical potential of the spin accumulation in the non-local measurement geometry decays with increasing distance to the detector and determines the non-local voltage.

electrodes are often also magnetic and consequently sensitive to a spin accumulation. If the distance between the electrodes and reference is short, the reference contacts can also contribute to the non-local signal which results in additional switches.

To measure the spin transport, a magnetic field is applied parallel or antiparallel to the electrode magnetization and switches the magnetization of the injector and detector independently. Typical data is shown in Figure 2.7a. The non-local resistance in parallel alignment R_{NL} is 82Ω . When the magnetization alignment is switched to antiparallel, the sign of R_{NL} switches to -82Ω . The spin signal can be determined from this measurement by calculating $\Delta R_{NL} = R_{NL}(P) - R_{NL}(AP) = 164 \Omega$. To estimate the spin relaxation length of the device, we measure the distance-dependence of ΔR_{NL} which is defined as:

$$\Delta R_{NL} = \pm P_{in} P_{det} \lambda \frac{R_{sq}}{w} \exp(-d/\lambda), \quad (2.13)$$

where P_{in} is the spin polarization of the injector and w the width of the flake. The \pm accounts for both parallel and antiparallel configurations. Note that a background of R_{NL} can arise due to ohmic and thermoelectric contributions, which are not spin-

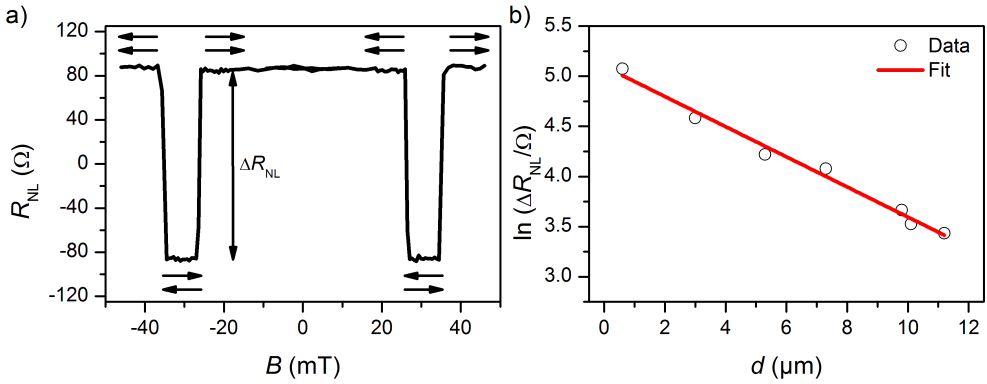


Figure 2.7: a) R_{NL} for the different magnetization configurations of the injector and detector electrodes (“spin valve” measurement). b) The distance-dependent measurement of the spin valves allows the extraction of the materials spin relaxation length, here $(6.7 \pm 0.5) \mu\text{m}$.

dependent and therefore neglected here [48, 49]. The slope of the logarithmic plot of ΔR_{NL} in Figure 2.7b is proportional to $-1/\lambda = (-0.15 \pm 0.01) \mu\text{m}^{-1}$. The spin relaxation length for this particular device is $(6.7 \pm 0.5) \mu\text{m}$.

2.6 Hanle Spin Precession

To obtain a deeper insight into the spin transport in diffusive systems, spin precession experiments allow to determine the spin diffusion constant D_s , relaxation time τ_s and relaxation length λ [50]. When spins are exposed to a perpendicular magnetic field, the spins start to precess around the magnetic field axis [51]. This effect is called Hanle spin precession and allows an accurate characterization of spin transport parameters. The process is schematically shown in Figure 2.4a. Spins are injected into the graphene channel along the y -direction and rotate around B_z in the x - y -plane. Spin precession measurements with the magnetic field applied in-plane and out-of-plane are shown in Figure 2.8b and 2.8c. The data is measured in parallel (black) and antiparallel alignment (red) of the injector and detector electrodes, leading to a positive or negative R_{NL} at $B_z = 0$ and $B_x = 0$.

The measurement of the spin precession with a magnetic field applied along the x -axis is shown in Figure 2.8c. Similarly to the spin precession under B_z , the application of B_x causes spins to precess perpendicular to the magnetic field axis, here in the y - z -plane. ΔR_{NL} in both measurements shows a similar magnitude and width, indicating comparable spin transport parameters. B_x is measured in Figure 2.8b only up to 40 mT since larger magnetic fields cause the magnetization to switch towards B_x .

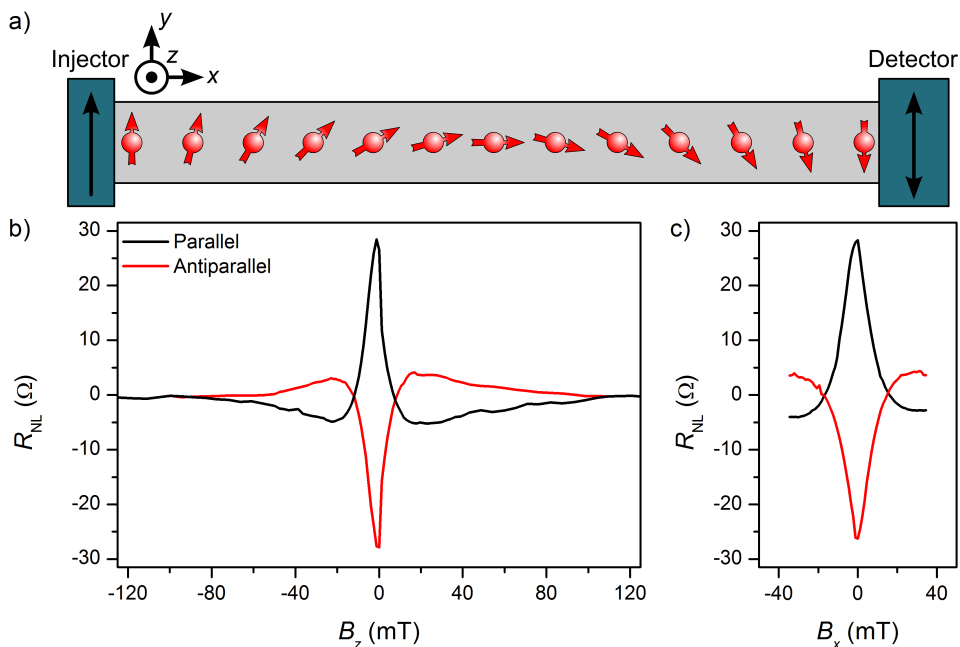


Figure 2.8: a) Schematic spin precession in a simplified geometry with a magnetic field applied out-of-plane (B_z). Spins along the y -axis are injected and rotate around B_z during transport. The detector is only sensitive to the spins along its magnetization axis, and senses in the sketched configuration a negative signal. Note that the dephasing of spins is not illustrated. b) Spin precession measurement of R_{NL} under B_z and c) B_x . The injector-detector spacing is $d = 7.3 \mu\text{m}$.

To extract the spin transport parameters from the precession curves, the data is fit to the solution of the three dimensional Bloch spin diffusion equation:

$$0 = D_s \nabla \begin{bmatrix} \mu_x \\ \mu_y \\ \mu_z \end{bmatrix} - \frac{1}{\tau_s} \begin{bmatrix} \mu_x \\ \mu_y \\ \mu_z \end{bmatrix} + \frac{g\mu_B}{\hbar} \begin{bmatrix} B_x \\ B_y \\ B_z \end{bmatrix} \times \begin{bmatrix} \mu_x \\ \mu_y \\ \mu_z \end{bmatrix}, \quad (2.14)$$

where $g = 2$ denotes the gyromagnetic factor and μ_B the Bohr magneton.

The first term of the Bloch equation accounts for the diffusion of spins along the gradient of the spin chemical potential. The second term describes spin relaxation and the third term the spin precession in a magnetic field B . In the case where only B_z is applied to the spins, the non-local resistance is given by [52]:

$$R_{NL}(d, B_z) = \pm \frac{R_{sq}}{w} P_{in} P_{det} D_s \Re \left(\frac{1}{2\sqrt{D_s}} \frac{\exp(-d)\sqrt{\lambda^{-2} - i\omega/D_s}}{\sqrt{\tau_s^{-1} - i\omega}} \right), \quad (2.15)$$

where $\omega = \frac{g\mu_B}{\hbar} B_z$ denotes the Larmor frequency. The fitting of the data in Figure 2.8b with Equation 2.15 yields $D_s = (310 \pm 10) \text{ cm}^2/\text{s}$ and $\tau_s = (1.35 \pm 0.06) \text{ ns}$. The corresponding spin relaxation length is $\lambda = \sqrt{D_s \tau_s} = (6.5 \pm 0.5) \mu\text{m}$, which is in good agreement with the value obtained from the distance-dependent spin valve measurements in Figure 2.7b.

Spin transport in graphene can be strongly anisotropic, the spin-lifetimes of in-plane (τ_{\parallel}) and out-of-plane (τ_{\perp}) can differ. A simple approach to study the spin-lifetime anisotropy ($\tau_{\perp}/\tau_{\parallel}$) rotates the injector and detector electrodes out-of-plane with a large magnetic field ($B_z \sim 1.6 \text{ T}$). Using this approach Tombros et al. [53] concluded, that spin relaxation in single layer graphene is anisotropic by measuring a 20% reduction of R_{NL} for perpendicular spins. However, the application of large magnetic fields comes along with magnetoresistive effects of the graphene channel, making the separation of anisotropy and magnetoresistance complicated.

An elegant approach to avoid magnetoresistive effects uses oblique spin precession [54–57]. The magnetic field B_{β} is applied in an angle β between sample plane and perpendicular axis. The injected in-plane spins precess around B_{β} and for $\beta = 90^\circ$, the spins precess only in-plane. At oblique angles, the in-plane magnetic field component of B_{β} causes the spins to precess partially from in-plane to out-of-plane. Figure 2.8b shows that at $B_z \sim 100 \text{ mT}$ the in-plane spins have fully dephased, and the comparison between $R_{\text{NL}}(B = 0)$ with $R_{\text{NL}}(B \sim 0.1 \text{ T})$ at different angles β , $R_{\text{NL}\beta}$, allows the separation of the in-plane and out-of-plane spin precession [55, 56]. The anisotropy $\tau_{\perp}/\tau_{\parallel}$ can be calculated from the angle-dependence of $R_{\text{NL}\beta}/R_{\text{NL}0}$ and the fitting with [54, 56]:

$$\frac{R_{\text{NL}\beta}}{R_{\text{NL}0}} = \sqrt{\frac{\tau_{\beta}}{\tau_{\parallel}}} \exp \left[\frac{-d}{\lambda_{\parallel}} \left(\sqrt{\frac{\tau_{\parallel}}{\tau_{\beta}}} - 1 \right) \right] \cos^2(\beta), \quad (2.16)$$

$$\frac{\tau_{\beta}}{\tau_{\parallel}} = \left(\cos^2(\beta) + \frac{\tau_{\parallel}}{\tau_{\perp}} \sin^2(\beta) \right)^{-1}. \quad (2.17)$$

Since this measurement requires relatively small magnetic fields ($\sim 0.1 \text{ T}$), compared to the rotation of the electrode magnetization (1.5 T – 2 T), this method avoids strong magnetoresistive contributions. Experimental results using this technique have found $\tau_{\perp}/\tau_{\parallel}$ to be between 0.8 and 1 in pristine monolayer graphene [54, 57], whereas bilayer graphene can have an anisotropy of up to 8 [58].

2.7 Spin Relaxation, Spin-Orbit and Spin-Valley Coupling in Graphene

The spin relaxation time in solid state systems is typically determined by the strength of the spin-orbit interaction λ_I . λ_I couples the spin degree of freedom to the momen-

tum of the electrons and links momentum scattering with spin relaxation. The magnitude of the spin-orbit coupling is proportional to the fourth power of the atomic number, leading to a strong effect in heavy elements (such as GaAs). Since the spin-orbit interaction can also limit spin transport, light elements (like carbon) are appealing for spintronics as they promise long spin-lifetimes. *Ab initio* calculations predict the strength of the intrinsic spin-orbit coupling λ_I in graphene to be 12 μeV [35]. Theory suggests long spin relaxation times of the order of μs and lengths of $\sim 100 \mu\text{m}$ [35, 46]. The first experimental studies of spin transport in graphene found $\tau_s \sim 100 \text{ ps}$ and λ below 2 μm [59]. Despite of the improvement of spin transport parameters to $\tau_s = 12 \text{ ns}$ and $\lambda \sim 30 \mu\text{m}$ by employing hBN [33], the discrepancy between theory and experiment suggest that, besides of the intrinsic spin-orbit coupling, additional spin relaxation sources must play a relevant role.

In semiconductors and metals, spin relaxation is usually described using the Elliot-Yafet and Dyakonov-Perel scattering mechanisms [5, 60, 61]. In the case of Elliot-Yafet mechanism, the spin flip occurs during scattering, and τ_s is proportional to the momentum relaxation time $\tau_p = 2D_c/v_F^2$, where D_c denotes the charge diffusion coefficient. For graphene this relation becomes $\tau_s \sim (E_F/\lambda_I)^2 \tau_p$ [62]. In case of the Dyakonov-Perel mechanism, spins precess between scattering events around the spin-orbit fields. In this case faster scattering implies lower precession angles and τ_p becomes inversely proportional to τ_s , $\tau_s \sim (\hbar/\lambda_I)^2 \tau_p^{-1}$ [63]. A recent theoretical work suggests that resonant scattering by magnetic impurities [64], which can arise during device fabrication, can reduce the spin-lifetimes to the 100 ps range. In the presence of random spin-orbit fields, the coupling between spin and pseudospin of the graphene sublattices was reported to also lower the spin-lifetimes to the experimentally realized range [65, 66]. However, experimental results have not yet led to a conclusion which mechanism is responsible for limiting the spin relaxation in graphene.

Despite of the potential for long distance spin transport arising from weak spin-orbit interaction, it is desirable to control the spin-orbit strength in graphene to realize spin manipulation. Several theoretical and experimental works have calculated the effect of adatoms, which convert the graphene sp^2 hybridized orbitals into sp^3 bonds and increase the λ_I from 12 μeV to the meV scale [67, 68]. Experimental works have claimed to enhance λ_I up to 2.5 meV [69] and 20 meV [70] using adatoms.

A different approach to increase λ_I combines graphene with a TMD [71, 72]. TMDs provide a spin-orbit coupling in the meV range [5], which can be imprinted into graphene by proximity effects and was measured in charge transport experiments [72–75]. Spin transport experiments in TMD/graphene devices have shown spin-lifetimes of a few ps and a strong spin-lifetime anisotropy [40, 41] where the lifetime of spins differs for spins pointing out-of-plane (τ_\perp) and in-plane (τ_\parallel). This effect originates in graphene/TMD from the valley-dependence of the spin precession. The in-plane spin-orbit coupling has a Rashba-type spin texture whereas the

out-of-plane component is determined by the valley-Zeeman coupling strength λ_{VZ} [63, 76]. λ_{VZ} has opposing signs in the K and K' valleys due to time reversal symmetry. As a consequence, τ_{iv} becomes relevant for spin relaxation and the spin-lifetime anisotropy becomes:

$$\frac{\tau_{\perp}}{\tau_{\parallel}} = \left(\frac{\lambda_{VZ}}{\lambda_R} \right)^2 \frac{\tau_{iv}}{\tau_p} + \frac{1}{2}, \quad (2.18)$$

where λ_R denotes the Rashba spin-orbit coupling strength and τ_{iv} the intervalley scattering time. Experimentally, spin-lifetime anisotropies of $\tau_{\perp}/\tau_{\parallel} \sim 10$ have been reported in monolayer graphene in proximity with MoS_2 , WS_2 [40] and MoSe_2 [41]. However, the spin-lifetimes in those devices were below 100 ps.

The electronic structure of bilayer graphene has an intrinsic λ_I of 12 μeV [77]. The spin-orbit fields point at the K and K' point out-of-plane and induce, when the inversion symmetry is broken, a spin splitting of similar magnitude. However, the sign of the spin splitting differs in the K and K' valley and is therefore valley-dependent. As a consequence, the spin transport in bilayer graphene is similarly to graphene/TMD devices anisotropic with $\tau_{\perp}/\tau_{\parallel} \sim 8$ but provides spin-lifetimes above 1 ns [58].

2.8 Integrated van der Waals Heterostructures

Despite of the already wide range of applications for pristine graphene, its potential gets greatly enhanced when graphene is combined with other layered, two-dimensional materials. In this context, the two-dimensional insulator hBN has attracted a lot of attention for its use for graphene spintronics. The first experimental studies of spin transport in graphene were limited by the cleanliness of graphene, mechanical exfoliation using a scotch tape leaves often glue residues behind. But also the finite roughness of the commonly used SiO_2 substrates can induce corrugations into the graphene, which, like charge traps, limit the performance of the device [78]. Attempts to increase the spin transport length and mobility included the suspension of graphene, which has enhanced the spin transport parameters substantially [79]. However, most improvement was realized with the encapsulation of graphene in hBN.

Boron nitride is a crystalline compound with applications ranging from the use as lubricant to cosmetics. For the study of two-dimensional materials, the hexagonal form is of special interest as it is a layered material isomorph to graphene with boron and nitrogen atoms on the sublattices. Similarly to graphene, hBN single layers have a strong in-plane bond and a weaker, van der Waals bond with adjacent layers. As an insulating material with an indirect band gap of 6 eV [80], it can be combined with graphene to form heterostructures where hBN can protect graphene from environmental influences. Furthermore, the atomic flatness of hBN promotes smooth

graphene flakes and avoids corrugations. But also the hydrophobicity of hBN reduces organic residues or water in the device. As a consequence, the longest spin relaxation lengths were measured in encapsulated graphene [33, 34].

Given the positive effect of hBN on the spin transport in graphene and the ability of exfoliating hBN down to monolayers, it is desirable to create devices where the graphene is fully encapsulated in hBN. The electrical connection is realized through a thin hBN layer, which acts as a tunnel barrier. Several groups have investigated and characterized hBN as a tunnel barrier [45, 81–84]. Thin flakes of hBN have proven to be a suitable tunnel barrier for spin injection promoting homogeneous spin transport. An additional feature is the dependence of the spin injection and detection efficiency on an applied DC bias to the hBN barrier [45].

Besides atomically thin materials like graphene and hBN, the family of two-dimensional materials can be extended to layered materials, such as transition metal dichalcogenides. TMDs have the structure MX_2 where M denotes a transition metal (e.g. Mo or W) and X a chalcogenide atom (e.g. S, Se or Te). Thin flakes of TMDs can be exfoliated using the scotch tape technique. Widely studied materials are molybdenum disulfide (MoS_2) [85] and tungsten disulfide (WS_2) [72]. Both materials exhibit semiconducting behavior and monolayers of both materials have been used to create transistors with a larger on/off ratios than pristine graphene.

The concept of integrated van der Waals heterostructures picks up the idea of combining two-dimensional materials with different individual properties to devices with customized properties, only a few atoms thin [86]. The fabrication of such heterostructures requires the controlled alignment of two-dimensional materials, which can be realized with various pickup and transfer techniques [87–89]. Recent experimental works on van der Waals heterostructures have shown that proximity effects between graphene and adjacent TMDs can alter the properties of the graphene flake. These studies included the enhanced spin-orbit coupling strength [73, 74] and the transfer of spin-valley coupling from TMDs into graphene [40, 41].

A highly desired building block for integrated van der Waals structures is a two-dimensional ferromagnet. In this context, theoretical and experimental studies have investigated the introduction of magnetism into graphene by adatoms or proximity coupling [36, 90–97]. Recently, magnetism was discovered in intercalated TMDs such as $\text{Fe}_{0.25}\text{TaS}_2$ [98], $\text{Mn}_{0.25}\text{TaS}_2$ [99] and layered materials as $\text{Cr}_2\text{Ge}_2\text{Te}_6$ [100] and CrI_3 [101]. Spin transport measurements in a magnetic tunnel junction of the two-dimensional materials $\text{Fe}_3\text{GeTe}_2/\text{hBN}/\text{Fe}_3\text{GeTe}_2$ have shown a tunneling spin polarization of 66% and demonstrated the potential of spintronics in integrated van der Waals heterostructures [102]. The device shown in Figure 2.9f consists of a few-layer graphene flake, encapsulated in hBN. A flake of the magnetic TMD $\text{Mn}_{0.25}\text{TaS}_2$ is implemented to investigate spin injection from magnetic TMDs into graphene. Preliminary data, obtained in a device with $\text{Fe}_{0.25}\text{TaS}_2$ is discussed in Section 8.3.

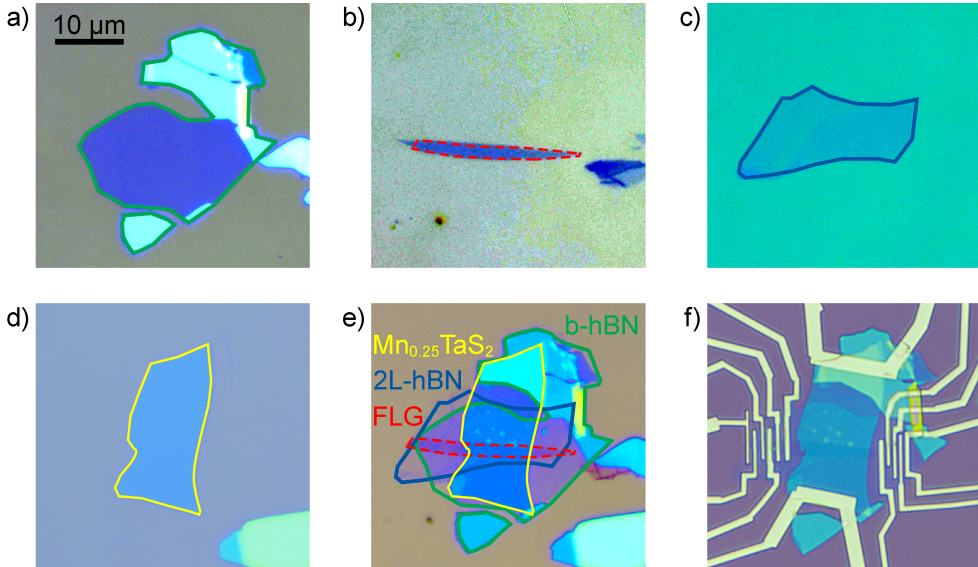


Figure 2.9: The optical images of the building blocks of a van der Waals heterostructure: a) few-layer hBN, used as substrate, b) few-layer graphene, c) bilayer hBN, used as tunnel barrier, d) $\text{Mn}_{0.25}\text{TaS}_2$ flake, a magnetic TMD, e) combination of the flakes to final device stack, f) the contacted device.

2.9 Ferromagnetic Proximity Effect

The introduction of magnetism into graphene attracts interest for fundamental and applied studies. Magnetism is usually based on d or f shell electrons, which would not be present in carbon-based magnets. Experiments on proton beam irradiated graphite have shown a ferro- and ferrimagnetic behavior of graphite after exposure [103]. This concept was transferred to graphene by first principle calculations by Yazyev and Helm [104], suggesting the possibility to induce magnetism into graphene by defects. The calculations predict magnetic moments between $1.12 \mu_B$ – $1.53 \mu_B$ per vacancy. The effect can also be generated by chemisorbed hydrogen adatoms with a resulting magnetic moment of $1 \mu_B$ per hydrogen adatom. Experimentally, magnetism in hydrogenated graphene was reported by SQUID measurements [105] and magnetic force microscopy [90]. McCreary et al. [91] have studied the spin transport in hydrogenated graphene spin valves. The controlled hydrogenation of graphene introduced an additional feature to the spin valve measurement, which the authors identify as spin relaxation due to paramagnetic moments. While those studies indicate the presence magnetism in graphene, the hydrogenation of graphene affects and sacrifices the good transport qualities of graphene. McCreary

et al. reported a reduction of the spin signal from 8.8Ω to 1.4Ω after 8 s of hydrogenation and a decrease of the carrier mobility from $6100 \text{ cm}^2/\text{Vs}$ to $500 \text{ cm}^2/\text{Vs}$. The approach followed in this thesis induces magnetism through a less invasive technique, the magnetic proximity effect.

Proximity effects induce new properties into an adjacent material through a short range interaction at the interface. The first experimental demonstration of a magnetic proximity effect was reported by Tedrow et al. [106]. Superconducting aluminum films in proximity to the ferromagnetic insulator (FMI) EuO were found to have a spin-dependent Zeeman splitting, which originates from the exchange interaction between the electrons in the aluminum film and the magnetic moments of the Eu atoms.

Graphene in proximity to a ferromagnet exhibits a splitting of the graphene energy bands as sketched in Figure 2.10b. In pristine graphene spin up and spin down bands lay on top of each other (Figure 2.10a). The exchange interaction induced into magnetic graphene splits the spin up and spin down bands by $\Delta E_{\text{exch}} = g\mu_B B_{\text{exch}}$, analogous to a Zeeman splitting $\Delta E_{\text{Zeeman}} = g\mu_B B$ in a magnetic field B . Therefore, the induced exchange interaction can be seen as a quasi-magnetic field B_{exch} . Consequently, the exchange field can be used to control spins in graphene.

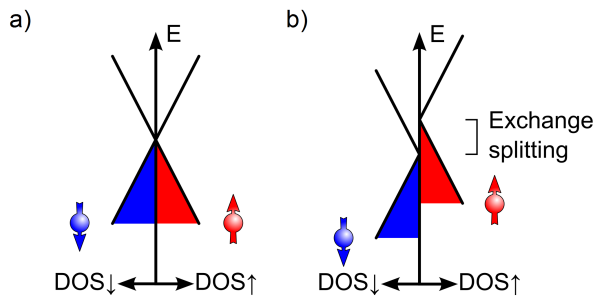


Figure 2.10: a) The band structure of pristine graphene does not exhibit a spin splitting of spin up and spin down band. b) In magnetic graphene both spin bands are split by ΔE_{exch} .

Ab initio calculations by Yang et al. [107] showed that the proximity of graphene to the FMI EuO results in a spin polarization of the graphene π orbitals of up to 24%. The exchange splitting of the bands at the Dirac point was reported to be close to 30 meV, which corresponds to an exchange field of several hundred Tesla. While EuO was shown to grow on graphene [92], the FMI used in this thesis is Yttrium-Iron-Garnet ($\text{Y}_3\text{Fe}_5\text{O}_{12}$, YIG). YIG is a synthetic garnet which exhibits ferrimagnetism up to 550 K. The ferrimagnetism arises from the iron atoms that occupy octahedral and tetrahedral sites in the garnet and compensate each other incompletely. As a consequence a net magnetic moment remains. *Ab initio* calculations of graphene

on YIG predict a proximity-induced exchange splitting in graphene of the order of 40 meV [108].

The use of YIG substrates has several experimental advantages over other FMI. The high Curie temperature of 550 K allows experiments to be conducted at or even above room temperature whereas the FMI EuO and EuS have Curie temperatures below 100 K. Furthermore, these materials are oxidizing in ambient condition, whereas YIG is stable in air, making it suitable for direct exfoliation and conventional graphene transfer techniques. YIG has an in-plane magnetization anisotropy with a coercive field of less than 0.1 mT. As a consequence, the magnetization can be rotated in the sample plane with small magnetic fields. The out-of-plane saturation field of 0.2 T is relatively small and accessible in the laboratory environment. A drawback of the use of YIG substrates is that the essential surface is exposed to the ambient atmosphere during graphene transfer, which can affect the proximity interaction negatively.

Several experimental studies have investigated graphene/YIG heterostructures. A non-linear contribution in the Hall voltage of a graphene device was explained with the anomalous Hall effect which is a typical feature of magnetic materials [93]. After the antisymmetrization of R_{xy} , a remaining component was observed, that saturated between 200 mT and 300 mT, which roughly corresponds to the (bulk) perpendicular saturation field of the YIG substrate. The authors argued that the only conceivable origin of this non-linear contribution is the anomalous Hall effect. Further experiments investigated the spin to charge conversion in graphene on YIG [94] and the Zeeman-spin-Hall effect [95] in graphene/EuS which all indicated the presence of a proximity-induced exchange field in graphene/FMI heterostructures. However, these experiments allow only an indirect characterization of B_{exch} . A direct measurement by using spin currents reported B_{exch} to be of the order of 0.2 T [36], several orders of magnitude below the theoretical calculations of idealized systems. However, further experimental studies reported also a B_{exch} below 1 T [37, 96, 97, 109].

References

- [1] A.C. Ferrari et al. Science and technology roadmap for graphene, related two-dimensional crystals, and hybrid systems. *Nanoscale*, 7(11), 4598, 2015.
- [2] K. Kostarelos and K.S. Novoselov. Graphene devices for life. *Nature Nanotechnology*, 9(10), 744, 2014.
- [3] E.J. Siochi. Graphene in the sky and beyond. *Nature Nanotechnology*, 9(10), 745, 2014.
- [4] G. Fiori, F. Bonaccorso, G. Iannaccone, T. Palacios, D. Neumaier, A. Seabaugh, S.K. Banerjee, and L. Colombo. Electronics based on two-dimensional materials. *Nature Nanotechnology*, 9(10), 768, 2014.
- [5] W. Han, R.K. Kawakami, M. Gmitra, and J. Fabian. Graphene spintronics. *Nature Nanotechnology*, 9(10), 794, 2014.

- [6] S. Roche, J. Åkerman, B. Beschoten, J.-C. Charlier, M. Chshiev, S.P. Dash, B. Dlubak, J. Fabian, A. Fert, M.H.D. Guimarães, F. Guinea, I. Grigorieva, C. Schönemberger, P. Seneor, C. Stampfer, S.O. Valenzuela, X. Waintal, and B.J. van Wees. Graphene spintronics: the European Flagship perspective. *2D Materials*, **2**(3), 030202, 2015.
- [7] P.R. Wallace. The band theory of graphite. *Physical Review*, **71**(9), 622, 1947.
- [8] H.P. Boehm, A. Clauss, G.O. Fischer, and U. Hofmann. Dünnsche Kohlenstoff-Folien. *Zeitschrift für Naturforschung*, **17**, 150, 1962.
- [9] A.K. Geim and K.S. Novoselov. The rise of graphene. *Nature Materials*, **6**(3), 183, 2007.
- [10] H.W. Kroto, J.R. Heath, S.C. O'Brien, R.F. Curl, and R.E. Smalley. C₆₀: Buckminsterfullerene. *Nature*, **318**(6042), 162, 1985.
- [11] M.-F. Yu, O. Lourie, M.J. Dyer, K. Moloni, T.F. Kelly, and R.S. Ruoff. Strength and Breaking Mechanism of Multiwall Carbon Nanotubes Under Tensile Load. *Science*, **287**, 637, 2000.
- [12] O.A. Shenderova, V.V. Zhirnov, and D.W. Brenner. Carbon Nanostructures. *Critical Reviews in Solid State and Materials Sciences*, **27**(3-4), 227, 2002.
- [13] K.S. Novoselov, A.K. Geim, S.V. Morozov, D. Jiang, Y. Zhang, S.V. Dubonos, I.V. Grigorieva, and A.A. Firsov. Electric field effect in atomically thin carbon films. *Science*, **306**(5696), 666, 2004.
- [14] A. Zurutuza and C. Marinelli. Challenges and opportunities in graphene commercialization. *Nature Nanotechnology*, **9**(10), 730, 2014.
- [15] J.W. McClure. Band Structure of Graphite and de Haas-van Alphen Effect. *Physical Review*, **108**(3), 612, 1957.
- [16] J.C. Slonczewski and P.R. Weiss. Band structure of graphite. *Physical Review*, **109**(2), 272, 1958.
- [17] J.-C. Charlier, J.-P. Michenaud, X. Gonze, and J.-P. Vigneron. Tight-binding model for the electronic properties of simple hexagonal graphite. *Physical Review B*, **44**(24), 13237, 1991.
- [18] A.H. Castro Neto, F. Guinea, N.M.R. Peres, K.S. Novoselov, and A.K. Geim. The electronic properties of graphene. *Reviews of Modern Physics*, **81**(1), 109, 2009.
- [19] S. Das Sarma, S. Adam, E.H. Hwang, and E. Rossi. Electronic transport in two-dimensional graphene. *Reviews of Modern Physics*, **83**(2), 407, 2011.
- [20] K. Yan, H. Peng, Y. Zhou, H. Li, and Z. Liu. Formation of bilayer bernal graphene: Layer-by-layer epitaxy via chemical vapor deposition. *Nano Letters*, **11**(3), 1106, 2011.
- [21] E.V. Castro, K.S. Novoselov, S.V. Morozov, N.M.R. Peres, J.M.B. Lopes dos Santos, J. Nilsson, F. Guinea, A.K. Geim, and A.H. Castro Neto. Biased bilayer graphene: Semiconductor with a gap tunable by the electric field effect. *Physical Review Letters*, **99**(21), 216802, 2007.
- [22] J.B. Oostinga, H.B. Heersche, X. Liu, A.F. Morpurgo, and L.M.K. Vandersypen. Gate-induced insulating state in bilayer graphene devices. *Nature Materials*, **7**(2), 151, 2008.
- [23] Y. Zhang, T.-T. Tang, C. Girit, Z. Hao, M.C. Martin, A. Zettl, M.F. Crommie, Y. Ron Shen, and F. Wang. Direct observation of a widely tunable bandgap in bilayer graphene. *Nature*, **459**(7248), 820, 2009.
- [24] Y. Cao, V. Fatemi, S. Fang, K. Watanabe, T. Taniguchi, E. Kaxiras, and P. Jarillo-Herrero. Unconventional superconductivity in magic-angle graphene superlattices. *Nature*, **556**(7699), 43, 2018.
- [25] Y. Cao, V. Fatemi, A. Demir, S. Fang, S.L. Tomarken, J.Y. Luo, J.D. Sanchez-Yamagishi, K. Watanabe, T. Taniguchi, E. Kaxiras, R.C. Ashoori, and P. Jarillo-Herrero. Correlated insulator behaviour at half-filling in magic-angle graphene superlattices. *Nature*, **556**(7699), 80, 2018.
- [26] S. Datta and B. Das. Electronic analog of the electro-optic modulator. *Applied Physics Letters*, **56**(7), 665, 1990.
- [27] I.L. Markov. Limits on fundamental limits to computation. *Nature*, **512**(7513), 147, 2014.
- [28] T.N. Theis and H.-S.P. Wong. The End of Moore's Law: A New Beginning for Information Technology. *Computing in Science & Engineering*, **19**(2), 41, 2016.
- [29] J. Wunderlich, B.-G. Park, A.C. Irvine, L.P. Zarbo, E. Rozkotova, P. Nemeč, V. Novak, J. Sinova, and T. Jungwirth. Spin Hall Effect Transistor. *Science*, **330**(6012), 1801, 2010.

- [30] H.C. Koo, J.H. Kwon, J. Eom, J. Chang, S.H. Han, and M. Johnson. Control of Spin Precession in a Spin-Injected Field Effect Transistor. *Science*, **325**(5947), 1515, 2009.
- [31] C. Betthausen, T. Dollinger, H. Saarikoski, V. Kolkovsky, G. Karczewski, T. Wojtowicz, K. Richter, and D. Weiss. Spin-transistor action via tunable landau-zener transitions. *Science*, **337**(6092), 324, 2012.
- [32] P. Chuang, S.-C. Ho, L.W. Smith, F. Sfigakis, M. Pepper, C.-H. Chen, J.-C. Fan, J.P. Griffiths, I. Farrer, H.E. Beere, G.A.C. Jones, D.A. Ritchie, and T.-M. Chen. All-electric all-semiconductor spin field-effect transistors. *Nature Nanotechnology*, **10**(1), 35, 2015.
- [33] M. Drögeler, C. Franzen, F. Volmer, T. Pohlmann, L. Banszerus, M. Wolter, K. Watanabe, T. Taniguchi, C. Stampfer, and B. Beschoten. Spin Lifetimes Exceeding 12 ns in Graphene Non-local Spin Valve Devices. *Nano Letters*, **16**(6), 3533, 2016.
- [34] J. Ingla-Aynés, M.H.D. Guimarães, R.J. Meijerink, P.J. Zomer, and B.J. van Wees. 24- μm Spin Relaxation Length in Boron Nitride Encapsulated Bilayer Graphene. *Physical Review B*, **92**(20), 201410, 2015.
- [35] D. Huertas-Hernando, F. Guinea, and A. Brataas. Spin-orbit coupling in curved graphene, fullerenes, nanotubes, and nanotube caps. *Physical Review B*, **74**(15), 155426, 2006.
- [36] J.C. Leutenantsmeyer, A.A. Kaverzin, M. Wojtaszek, and B.J. van Wees. Proximity induced room-temperature ferromagnetism in graphene probed with spin currents. *2D Materials*, **4**(1), 014001, 2017.
- [37] S. Singh, J. Katoch, T. Zhu, K.-Y. Meng, T. Liu, J.T. Brangham, F. Yang, M.E. Flatté, and R.K. Kawakami. Strong Modulation of Spin Currents in Bilayer Graphene by Static and Fluctuating Proximity Exchange Fields. *Physical Review Letters*, **118**(18), 187201, 2017.
- [38] W. Yan, O. Txoperena, R. Llopis, H. Dery, L.E. Hueso, and F. Casanova. A two-dimensional spin field-effect switch. *Nature Communications*, **7**, 13372, 2016.
- [39] A. Dankert and S.P. Dash. Electrical gate control of spin current in van der Waals heterostructures at room temperature. *Nature Communications*, **8**, 16093, 2017.
- [40] L.A. Benítez, J.F. Sierra, W. Savero Torres, A. Arrighi, F. Bonell, M.V. Costache, and S.O. Valenzuela. Strongly anisotropic spin relaxation in graphene/transition metal dichalcogenide heterostructures at room temperature. *Nature Physics*, **14**(3), 303, 2018.
- [41] T.S. Ghiasi, J. Ingla-Aynés, A.A. Kaverzin, and B.J. van Wees. Large Proximity-Induced Spin Lifetime Anisotropy in Transition-Metal Dichalcogenide/Graphene Heterostructures. *Nano Letters*, **17**(12), 7528, 2017.
- [42] G. Schmidt, D. Ferrand, L.W. Molenkamp, A.T. Filip, and B.J. van Wees. Fundamental obstacle for electrical spin injection from a ferromagnetic metal into a diffusive semiconductor. *Physical Review B*, **62**(8), R4790, 2000.
- [43] E.I. Rashba. Theory of electrical spin injection: Tunnel contacts as a solution of the conductivity mismatch problem. *Physical Review B*, **62**(24), R16267, 2000.
- [44] W. Han, K. Pi, K.M. McCreary, Y. Li, J.J.I. Wong, A.G. Swartz, and R.K. Kawakami. Tunneling spin injection into single layer graphene. *Physical Review Letters*, **105**(16), 167202, 2010.
- [45] M. Gurram, S. Omar, and B.J. van Wees. Bias induced up to 100% spin-injection and detection polarizations in ferromagnet/bilayer-hBN/graphene/hBN heterostructures. *Nature Communications*, **8**(1), 248, 2017.
- [46] D. Huertas-Hernando, F. Guinea, and A. Brataas. Spin-orbit-mediated spin relaxation in graphene. *Physical Review Letters*, **103**(14), 146801, 2009.
- [47] F.J. Jedema, A.T. Filip, and B.J. van Wees. Electrical spin injection and accumulation at room temperature in an all-metal mesoscopic spin valve. *Nature*, **410**(6826), 345, 2001.
- [48] F.L. Bakker, A. Slachter, J.P. Adam, and B.J. van Wees. Interplay of peltier and seebeck effects in nanoscale nonlocal spin valves. *Physical Review Letters*, **105**(13), 136601, 2010.

- [49] F. Volmer, M. Drögeler, T. Pohlmann, G. Güntherodt, C. Stampfer, and B. Beschoten. Contact-induced charge contributions to non-local spin transport measurements in Co/MgO/graphene devices. *2D Materials*, **2**(2), 024001, 2015.
- [50] F.J. Jedema, H.B. Heersche, A.T. Filip, J.J.A. Baselmans, and B.J. van Wees. Electrical detection of spin precession in a metallic mesoscopic spin valve. *Nature*, **416**(6882), 713, 2002.
- [51] W. Hanle. Über magnetische Beeinflussung der Polarisation der Resonanzfluoreszenz. *Zeitschrift für Physik*, **30**(1), 93, 1924.
- [52] M.H.D. Guimarães. Spin and Charge Transport in Graphene Devices in the Classical and Quantum Regimes. PhD thesis, University of Groningen, 2015.
- [53] N. Tombros, S. Tanabe, A. Veligura, C. Jozsa, M. Popinciuc, H.T. Jonkman, and B.J. van Wees. Anisotropic spin relaxation in graphene. *Physical Review Letters*, **101**(4), 046601, 2008.
- [54] B. Raes, J.E. Scheerder, M.V. Costache, F. Bonell, J.F. Sierra, J. Cuppens, J. van de Vondel, and S.O. Valenzuela. Determination of the spin-lifetime anisotropy in graphene using oblique spin precession. *Nature Communications*, **7**, 11444, 2016.
- [55] B. Raes, A.W. Cummings, F. Bonell, M.V. Costache, J.F. Sierra, S. Roche, and S.O. Valenzuela. Spin precession in anisotropic media. *Physical Review B*, **95**(8), 085403, 2017.
- [56] T. Zhu and R.K. Kawakami. Modeling the oblique spin precession in lateral spin valves for accurate determination of the spin-lifetime anisotropy: Effect of finite contact resistance and channel length. *Physical Review B*, **97**(14), 144413, 2018.
- [57] S. Ringer, S. Hartl, M. Rosenauer, T. Völkl, M. Kadur, F. Hopperditzel, D. Weiss, and J. Eroms. Measuring anisotropic spin relaxation in graphene. *Physical Review B*, **97**(20), 205439, 2018.
- [58] J.C. Leutenantsmeyer, J. Ingla-Aynés, J. Fabian, and B.J. van Wees. Observation of Spin-Valley-Coupling-Induced Large Spin-Lifetime Anisotropy in Bilayer Graphene. *Physical Review Letters* **121**(12), 127702, 2018.
- [59] N. Tombros, C. Jozsa, M. Popinciuc, H.T. Jonkman, and B.J. van Wees. Electronic spin transport and spin precession in single graphene layers at room temperature. *Nature*, **448**(7153), 571, 2007.
- [60] R.J. Elliott. Theory of the effect of spin-orbit coupling on magnetic resonance in some semiconductors. *Physical Review*, **96**(2), 266, 1954.
- [61] Y. Yafet. g Factors and Spin-Lattice Relaxation of Conduction Electrons. *Solid State Physics - Advances in Research and Applications*, **14**(C), 1–98, 1963.
- [62] H. Ochoa, A.H. Castro Neto, and F. Guinea. Elliot-Yafet Mechanism in Graphene. *Physical Review Letters*, **108**(20), 206808, 2012.
- [63] J.H. Garcia, M. Vila, A.W. Cummings, and S. Roche. Spin transport in graphene/transition metal dichalcogenide heterostructures. *Chemical Society Reviews*, **47**(9), 3359, 2018.
- [64] D. Kochan, M. Gmitra, and J. Fabian. Spin relaxation mechanism in graphene: Resonant scattering by magnetic impurities. *Physical Review Letters*, **112**, 116602, 2014.
- [65] D. Van Tuan, F. Ortman, D. Soriano, S.O. Valenzuela, and S. Roche. Pseudospin-driven spin relaxation mechanism in graphene. *Nature Physics*, **10**(11), 857, 2014.
- [66] D. Van Tuan, F. Ortman, A.W. Cummings, D. Soriano, and S. Roche. Spin dynamics and relaxation in graphene dictated by electron-hole puddles. *Scientific Reports*, **6**, 21046, 2016.
- [67] A.H. Castro Neto and F. Guinea. Impurity-induced spin-orbit coupling in graphene. *Physical Review Letters*, **103**(2), 026804, 2009.
- [68] M. Gmitra, D. Kochan, and J. Fabian. Spin-Orbit Coupling in Hydrogenated Graphene. *Physical Review Letters*, **110**(24), 246602, 2013.
- [69] J. Balakrishnan, G. Kok Wai Koon, M. Jaiswal, A.H. Castro Neto, and B. Özyilmaz. Colossal enhancement of spin-orbit coupling in weakly hydrogenated graphene. *Nature Physics*, **9**(5), 284, 2013.
- [70] J. Balakrishnan, G.K.W. Koon, A. Avsar, Y. Ho, J.H. Lee, M. Jaiswal, S.-J. Baeck, J.-H. Ahn, A. Ferreira, M.A. Cazalilla, A.H.C. Neto, and B. Özyilmaz. Giant spin Hall effect in graphene grown by

chemical vapour deposition. *Nature Communications*, **5**, 4748, 2014.

- [71] M. Gmitra and J. Fabian. Graphene on transition-metal dichalcogenides: A platform for proximity spin-orbit physics and optospintronics. *Physical Review B*, **92**(15), 155403, 2015.
- [72] Z. Wang, D.-K. Ki, H. Chen, H. Berger, A.H. MacDonald, and A.F. Morpurgo. Strong interface-induced spin-orbit interaction in graphene on WS₂. *Nature Communications*, **6**, 8339, 2015.
- [73] Z. Wang, D.K. Ki, J.Y. Khoo, D. Mauro, H. Berger, L.S. Levitov, and A.F. Morpurgo. Origin and magnitude of ‘designer’ spin-orbit interaction in graphene on semiconducting transition metal dichalcogenides. *Physical Review X*, **6**(4), 041020, 2016.
- [74] T. Wakamura, F. Reale, P. Palczynski, S. Guéron, C. Mattevi, and H. Bouchiat. Strong Anisotropic spin-orbit Interaction Induced in Graphene by Monolayer WS₂. *Physical Review Letters*, **120**(10), 106802, 2018.
- [75] S. Zihlmann, A.W. Cummings, J.H. Garcia, M. Kedves, K. Watanabe, T. Taniguchi, C. Schönenberger, and P. Makk. Large spin relaxation anisotropy and valley-Zeeman spin-orbit coupling in WSe₂/graphene/hBN heterostructures. *Physical Review B*, **97**(7), 075434, 2018.
- [76] A.W. Cummings, J.H. Garcia, J. Fabian, and S. Roche. Giant Spin Lifetime Anisotropy in Graphene Induced by Proximity Effects. *Physical Review Letters*, **119**(20), 206601, 2017.
- [77] S. Kunschuh, M. Gmitra, D. Kochan, and J. Fabian. Theory of spin-orbit coupling in bilayer graphene. *Physical Review B*, **85**(11), 115423, 2012.
- [78] C.R. Dean, A.F. Young, I. Meric, C. Lee, L. Wang, S. Sorgenfrei, K. Watanabe, T. Taniguchi, P. Kim, K.L. Shepard, and J. Hone. Boron nitride substrates for high-quality graphene electronics. *Nature Nanotechnology*, **5**(10), 722, 2010.
- [79] M.H.D. Guimarães, A. Veligura, P.J. Zomer, T. Maassen, I.J. Vera-Marun, N. Tombros, and B.J. van Wees. Spin transport in high-quality suspended graphene devices. *Nano Letters*, **12**(7), 3512, 2012.
- [80] G. Cassabois, P. Valvin, and B. Gil. Hexagonal boron nitride is an indirect bandgap semiconductor. *Nature Photonics*, **10**(4), 262, 2016.
- [81] T. Yamaguchi, Y. Inoue, S. Masubuchi, S. Morikawa, M. Onuki, K. Watanabe, T. Taniguchi, R. Moriya, and T. Machida. Electrical Spin Injection into Graphene through Monolayer Hexagonal Boron Nitride. *Applied Physics Express*, **6**(7), 073001, 2013.
- [82] W. Fu, P. Makk, R. Maurand, M. Bräuninger, and C. Schönenberger. Large-scale fabrication of BN tunnel barriers for graphene spintronics. *Journal of Applied Physics*, **116**(7), 074306, 2014.
- [83] M.V. Kamalakar, A. Dankert, J. Bergsten, T. Ive, and S.P. Dash. Enhanced Tunnel Spin Injection into Graphene using Chemical Vapor Deposited Hexagonal Boron Nitride. *Scientific Reports*, **4**(1), 6146, 2015.
- [84] M.V. Kamalakar, A. Dankert, P.J. Kelly, and S.P. Dash. Inversion of Spin Signal and Spin Filtering in Ferromagnet|Hexagonal Boron Nitride-Graphene van der Waals Heterostructures. *Scientific Reports*, **6**, 21168, 2016.
- [85] B. Radisavljevic, A. Radenovic, J. Brivio, V. Giacometti, and A. Kis. Single-layer MoS₂ transistors. *Nature Nanotechnology*, **6**(3), 147, 2011.
- [86] A.K. Geim and I.V. Grigorieva. Van der Waals heterostructures. *Nature*, **499**(7459), 419, 2013.
- [87] A. Reina, H. Son, L. Jiao, B. Fan, M.S. Dresselhaus, Z. Liu, and J. Kong. Transferring and Identification of Single- and Few-Layer Graphene on Arbitrary Substrates. *The Journal of Physical Chemistry C*, **112**(46), 17741, 2008.
- [88] P.J. Zomer, S.P. Dash, N. Tombros, and B.J. van Wees. A transfer technique for high mobility graphene devices on commercially available hexagonal boron nitride. *Applied Physics Letters*, **99**(23), 232104, 2011.
- [89] P.J. Zomer, M.H.D. Guimarães, J.C. Brant, N. Tombros, and B.J. van Wees. Fast pick up technique for high quality heterostructures of bilayer graphene and hexagonal boron nitride. *Applied Physics Letters*, **105**(1), 013101, 2014.

- [90] A.J.M. Giesbers, K. Uhlířová, M. Konečný, E.C. Peters, M. Burghard, J. Aarts, and C.F.J. Flipse. Interface-Induced Room-Temperature Ferromagnetism in Hydrogenated Epitaxial Graphene. *Physical Review Letters*, **111**(16), 166101, 2013.
- [91] K.M. McCreary, A.G. Swartz, W. Han, J. Fabian, and R.K. Kawakami. Magnetic Moment Formation in Graphene Detected by Scattering of Pure Spin Currents. *Physical Review Letters*, **109**(18), 186604, 2012.
- [92] A.G. Swartz, K.M. McCreary, W. Han, J.J.I. Wong, P.M. Odenthal, H. Wen, J.-R. Chen, R.K. Kawakami, Y. Hao, R.S. Ruoff, and J. Fabian. Integrating MBE materials with graphene to induce novel spin-based phenomena. *Journal of Vacuum Science & Technology B*, **31**(4), 04D105, 2013.
- [93] Z. Wang, C. Tang, R. Sachs, Y. Barlas, and J. Shi. Proximity-Induced Ferromagnetism in Graphene Revealed by the Anomalous Hall Effect. *Physical Review Letters*, **114**(1), 016603, 2015.
- [94] J.B.S. Mendes, O. Alves Santos, L.M. Meireles, R.G. Lacerda, L.H. Vilela-Leão, F.L.A. Machado, R.L. Rodríguez-Suárez, A. Azevedo, and S.M. Rezende. Spin-Current to Charge-Current Conversion and Magnetoresistance in a Hybrid Structure of Graphene and Yttrium Iron Garnet. *Physical Review Letters*, **115**(22), 226601, 2015.
- [95] P. Wei, S. Lee, F. Lemaitre, L. Pinel, D. Cutaia, W. Cha, F. Katmis, Y. Zhu, D. Heiman, J. Hone, J.S. Moodera, and C.-T. Chen. Strong interfacial exchange field in the graphene/EuS heterostructure. *Nature Materials*, **15**(7), 711, 2016.
- [96] M. Evelt, H. Ochoa, O. Dzyapko, V.E. Demidov, A. Yurgens, J. Sun, Y. Tserkovnyak, V. Bessonov, A.B. Rinkevich, and S.O. Demokritov. Chiral charge pumping in graphene deposited on a magnetic insulator. *Physical Review B*, **95**, 024408, 2017.
- [97] P.U. Asshoff, J.L. Sambricio, A.P. Rooney, S. Slizovskiy, A. Mishchenko, A.M. Rakowski, E.W. Hill, A.K. Geim, S.J. Haigh, V.I. Fal'Ko, I.J. Vera-Marun, and I.V. Grigorieva. Magnetoresistance of vertical Co-graphene-NiFe junctions controlled by charge transfer and proximity-induced spin splitting in graphene. *2D Materials*, **4**(3), 031004, 2017.
- [98] Y. Yamasaki, R. Moriya, M. Arai, S. Masubuchi, S. Pyon, T. Tamegai, K. Ueno, and T. Machida. Exfoliation and van der Waals heterostructure assembly of intercalated ferromagnet $\text{Cr}_{1/3}\text{TaS}_2$. *2D Materials*, **4**(4), 041007, 2017.
- [99] P.M. Shand, C. Cooling, C. Mellinger, J.J. Danker, T.E. Kidd, K.R. Boyle, and L.H. Strauss. Magnetic states in nanostructured manganese-intercalated TaS_2 . *Journal of Magnetism and Magnetic Materials*, **382**, 49, 2015.
- [100] C. Gong, L. Li, Z. Li, H. Ji, A. Stern, Y. Xia, T. Cao, W. Bao, C. Wang, Y. Wang, Z.Q. Qiu, R.J. Cava, S.G. Louie, J. Xia, and X. Zhang. Discovery of intrinsic ferromagnetism in 2D van der Waals crystals. *Nature*, **546**(7657), 265, 2017.
- [101] B. Huang, G. Clark, E. Navarro-Moratalla, D.R. Klein, R. Cheng, K.L. Seyler, D. Zhong, E. Schmidgall, M.A. McGuire, D.H. Cobden, W. Yao, D. Xiao, P. Jarillo-Herrero, and X. Xu. Layer-dependent ferromagnetism in a van der Waals crystal down to the monolayer limit. *Nature*, **546**(7657), 270, 2017.
- [102] Z. Wang, D. Sapkota, T. Taniguchi, K. Watanabe, D. Mandrus, and A.F. Morpurgo. Tunneling Spin Valves Based on $\text{Fe}_3\text{GeTe}_2/\text{hBN}/\text{Fe}_3\text{GeTe}_2$ van der Waals Heterostructures. *Nano Letters*, **18**(7), 4303, 2018.
- [103] P. Esquinazi, D. Spemann, R. Höhne, A. Setzer, K.-H. Han, and T. Butz. Induced Magnetic Ordering by Proton Irradiation in Graphite. *Physical Review Letters*, **91**(22), 227201, 2003.
- [104] O.V. Yazyev and L. Helm. Defect-induced magnetism in graphene. *Physical Review B*, **75**(12), 125408, 2007.
- [105] L. Xie, X. Wang, J. Lu, Z. Ni, Z. Luo, H. Mao, R. Wang, Y. Wang, H. Huang, D. Qi, R. Liu, T. Yu, Z. Shen, T. Wu, H. Peng, B. Özyilmaz, K. Loh, A.T.S. Wee, and W. Chen. Room temperature ferromagnetism in partially hydrogenated epitaxial graphene. *Applied Physics Letters*, **98**(19), 193113, 2011.

- [106] P.M. Tedrow, J.E. Tkaczyk, and A. Kumar. Spin-polarized electron tunneling study of an artificially layered superconductor with internal magnetic field: EuO-Al. *Physical Review Letters*, **56**(16), 1746, 1986.
- [107] H. Yang, A. Hallal, D. Terrade, X. Waintal, S. Roche, and M. Chshiev. Proximity Effects Induced in Graphene by Magnetic Insulators: First-Principles Calculations on Spin Filtering and Exchange-Splitting Gaps. *Physical Review Letters*, **110**(4), 046603, 2013.
- [108] A. Hallal, F. Ibrahim, H.X. Yang, S. Roche, and M. Chshiev. Tailoring magnetic insulator proximity effects in graphene: first-principles calculations. *2D Materials*, **4**(2), 025074, 2017.
- [109] J.C. Leutenantsmeyer, T. Liu, M. Gurram, A.A. Kaverzin, and B.J. van Wees. Bias dependent spin injection into graphene on YIG through bilayer hBN tunnel barriers. *Physical Review B*, **98**(12), 125422, 2018.

Abstract

This chapter describes briefly the fabrication and measurement techniques used for the preparation of the graphene devices. The sample fabrication was carried out in the clean room facilities of the Physics of Nanodevices group and the NanoLabNL facility in Groningen.

3.1 Exfoliation and Characterization of Graphene and hBN

Graphene is exfoliated from highly oriented graphite crystals (HOPG, ZYB grade, HQ graphene). The procedure consists of three steps. First a slice of HOPG is transferred from the HOPG crystal with scotch tape and fixed to the table with the graphite side facing upwards. To reduce contamination arising from the glue of the scotch tape, we use adhesive silicon wafer tape (1005R, Ultron Systems Inc.) to pick up thin graphite from the fixed tape. Afterward, the wafer tape with graphite is pressed against a second wafer tape to reduce the density of thicker graphite flakes. This process is repeated four times, which usually yields a good balance between large quantities of thin graphene and the glue residues. The silicon wafers with 300 nm oxide thickness are stored in a 500°C furnace prior to the graphene exfoliation to reduce water and organic residues. The tape is pressed on the substrate and both are annealed in a 100°C furnace for 10 minutes to promote the adhesion between graphene and the silicon oxide surface. This process improves the size of the graphene flakes. After removing the wafer tape, the chip is scanned for graphene.

The contrast analysis of graphene is shown in Figure 3.1. The upper panels show a reference flake with different layers of graphite. We find single layer, bilayer and trilayer flakes, and can calculate from their individual contrast the contrast of one layer. In this microscope, an Olympus BH-2 with a NeoSPlan 100x/0.9 NA objective, single layer graphene has a contrast of $\sim 5\%$. The optical system of the Zeiss Axio Imager.A2m with an EC Epiplan-Neofluar 100x/0.9 NA objective has a higher optical contrast difference of $\sim 10\%$.

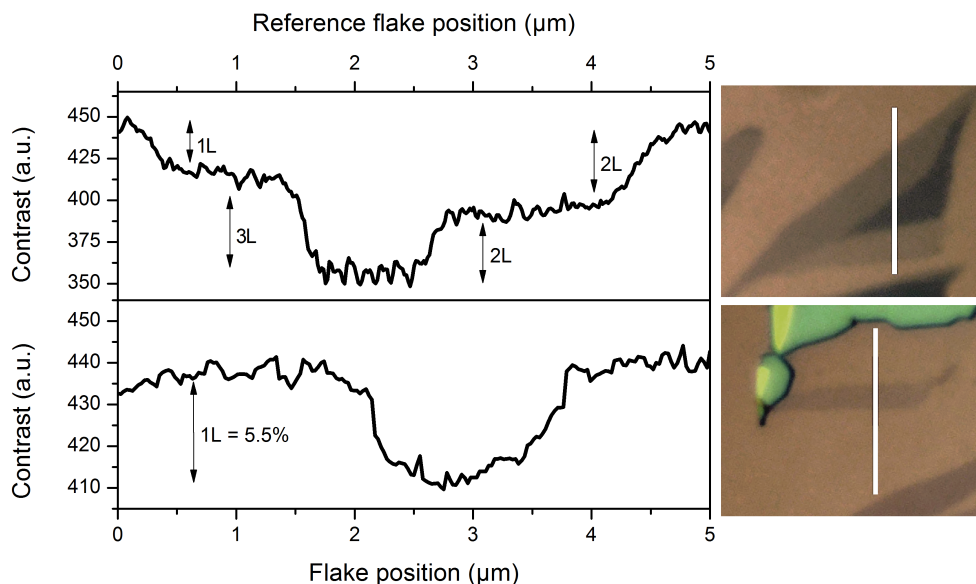


Figure 3.1: Determination of the thickness of a graphene flake through optical contrast. The upper panel contains the contrast and optical image of a reference flake. The white line shows the position of the contrast scan. The bottom panel contains the optical image and the contrast analysis of the graphene flake discussed in Chapter 4.

The exfoliation of thin hBN is analogous to graphene. A small amount of hBN powder is applied to the surface of the wafer tape and spread over the same tape. Once hBN is evenly distributed, new wafer tapes are pressed on the first tape and removed. This process is repeated six times and the first tape is pressed on a silicon substrate with 90 nm oxide to improve the optical contrast of hBN [1]. The identification of thin hBN flakes is more difficult than graphene flakes as the optical contrast of a monolayer hBN flake ranges in the Zeiss system between 2% and 2.5%. The electrical characterization of the tunnel barrier gives a definitive proof of the thickness of the tunnel barrier. Single layer hBN tunnel barriers yield a resistance-area product between $1 \text{ k}\Omega\mu\text{m}^2$ and $5 \text{ k}\Omega\mu\text{m}^2$, bilayer tunnel barriers between $10 \text{ k}\Omega\mu\text{m}^2$ and $30 \text{ k}\Omega\mu\text{m}^2$, and trilayer tunnel barriers between $200 \text{ k}\Omega\mu\text{m}^2$ and $2 \text{ M}\Omega\mu\text{m}^2$.

3.2 Fabrication of van der Waals Heterostructures

Various different techniques are reported to be suitable for pick up and stacking of two dimensional materials. We use the fast pick pickup technique, developed by Zomer et al. [2]. Polycarbonate (PC, Poly(Bisphenol A carbonate), 181641, Sigma

Aldrich Co.) is dissolved 6wt% in chloroform. The solution is drop cast and dried between two glass slide to form a thin and uniform PC film. A scotch tape mask is used to pick up the PC film and transfer it on top of a polydimethylsiloxane (PDMS) stamp. The PDMS/PC stamp is loaded into the transfer stage. To pick up 2D materials, the PC/PDMS mask is slowly brought into contact with the substrate. The substrate is heated to 70°C to melt the PC and increase its stickiness. The PC/PDMS stamp is slowly retracted while cooling the substrate and the flake sticks to the PC/PDMS mask. This process is repeated until all materials are stacked. To deposit the heterostructure, the mask is brought into contact with the target substrate and heated to 180°C. The PC/PDMS stamp is slowly retracted while the PC mask breaks and remains with the flakes on the new substrate. The PC film is removed by immersing the sample for 10 minutes in chloroform. A van der Waals heterostructure with the individual flakes is shown in Figure 2.9.

To further improve the cleanliness of the stack, the sample is annealed in a tube furnace with an argon/5%-hydrogen atmosphere [3]. Good results were obtained by annealing the stack at 350°C for one hour with an Ar/H₂ gas flow of 200 sccm.

3.3 Electron Beam Lithography

The device contacts are defined using electron beam lithography (EBL). An electron beam exposes a resist layer of poly(methyl methacrylate) (PMMA). The molecule chains are broken and the solubility is increased. The exposed regions are selectively removed by the developer (methyl isobutyl ketone, MIBK) and the desired structure is obtained. Positive resists, such as PMMA, are preferred for this lithography step since only the area of the contacts has to be exposed. Negative resists (such as hydrogen silsesquioxane, HSQ) reduce their solubility after electron exposure and remain after the development process. This type of resist is useful for the deposition of etch masks or gate oxides.

The advantage of EBL over optical lithography is the flexibility of the structures. Exfoliated graphene devices require this flexibility since additional flakes need to be avoided to prevent shorted electric circuits. The mainly used resist is a 4% PMMA solution (AR-P 679.04, Allresist GmbH) which is spun between 4 000 rpm and 6 000 rpm, resulting in 300 nm to 200 nm film thickness.

A disadvantage of EBL arises with insulating substrates. Local charging effects can reduce the resolution drastically. This is not an issue for doped silicon substrates with an oxide layer, since charge accumulations can flow into the doped silicon layer. However, EBL on YIG is only possible after the deposition of a conductive layer on top of the PMMA film. This material can be either an evaporated gold layer or a conductive polymer. The advantage of polymers is that the material can be spun directly after PMMA and can be removed before the development step by water. Two

conductive polymers were used: aquaSAVE (Mitsubishi Chemical Co.) and Elektra 92 (Allresist GmbH). The fabricated samples using aquaSAVE gave inconsistent results, the polymer layer often cross-linked and could not be removed with water. This problem did not occur with Elektra 92. The detailed fabrication recipes are described in the Appendix A.5.

The exposure of the contacts consists of two steps. First, markers are written into the PMMA. The markers allow the precise alignment of the contacts, which are written in the second step. If silicon substrates are used, the developed markers provide enough contrast for an accurate alignment. However, the contrast of the developed PMMA film on YIG is too low. Therefore, 5 nm titanium and 35 nm gold are evaporated on the chip with developed markers. Subsequently, the PMMA film needs to be removed and the contacts are written into a new PMMA layer with a conductive polymer.

3.4 Deposition of Metallic Contacts

The electrodes are deposited in a high vacuum chamber with a base pressure below 10^{-7} mbar and an electron beam evaporation source with different metals. Generally two types of contacts are used. Non-magnetic titanium/gold contacts, provide low contact resistances and are used to contact Hall bar samples. A 5 nm titanium layer is evaporated to enhance the adhesion between the graphene and the gold layer, which is usually between 35 nm and 70 nm thick. To improve the homogeneity of the film thickness, the sample holder rotates with 40 rpm during the evaporation.

Ferromagnetic cobalt contacts are used for spin injection. As tunnel barrier aluminum or titanium are evaporated at a rate of $0.7 \text{ \AA}/\text{s}$ with 0.4 nm thickness. The films are subsequently oxidized by introducing pure oxygen into the vacuum chamber (50 sccm flow, 15 minutes). This step is repeated twice, the resulting oxidized tunnel barrier has a thickness between 0.8 nm and 1.0 nm. The measured contact resistances are mostly between $5 \text{ k}\Omega$ and $50 \text{ k}\Omega$. After the evaporation of the tunnel barrier, a 65 nm cobalt film is deposited. Lastly, an aluminum capping layer of 5 nm is evaporated. Since the oxidation of aluminum is self-limited to a few nanometers, the film protects the underlying cobalt from oxidation. For devices with a crystalline hBN tunnel barrier, only 65 nm cobalt and 5 nm aluminum are deposited.

Lastly, the PMMA layer is removed in warm acetone (10 minutes at 40°C) and the sample is ready for characterization.

3.5 Measurement Techniques

The sample is first characterized in an Everbeing C2 probe station. Gold plated tungsten needles are brought in contact with the contact pads and the resistance of the

device is measured with a Keithley 2450 SourceMeter. This setup gives a good impression of the sample quality, the contact resistance and the square resistance.

To measure the devices in low temperatures or high magnetic fields, the samples have to be bonded onto a chip carrier. The substrate is glued on the chip carrier using either silver paint or insulating varnish. For silicon oxide substrates, silver paint connects to the doped silicon layer and provides the connection to the back gate. $\text{Al}_{99}\text{Si}_1$ wires are bonded with an ultrasonic pulse to the contact pads of the device contact and on the pads of the chip carrier. The chip carrier is loaded into the cryostat of the measurement setup and the sample space is evacuated to provide an inert atmosphere and avoid oxidation of the contacts. The cryostat is positioned between the poles of a GMW 5403 electromagnet which can generate magnetic fields up to 1.8 T at 70 A. The connection between the sample and the measurement electronics is controlled via an in-house built switch box.

The electrical characterization setup consists of a custom built IV measurement box (meetkast) and Stanford Research Systems SR830 lock-in amplifiers. The oscillator of the master lock-in sources a voltage to the IV meetkast which converts the voltage to an AC current between 10 nA and 100 mA. Typical AC frequencies vary between 1 Hz and 17 Hz. Additional lock-ins are triggered through the TTL signal from the master lock-in. The response from the sample is amplified between $1\times$ and $10^5\times$ in the meetkast. The AC modulated signal is measured by the lock-ins and the data is recorded via a LabVIEW program. The DC bias-dependence of the hBN/graphene heterostructures is measured by adding a constant voltage to the AC lock-in source signal via a Keithley 2400 SourceMeter. The output of the meetkast is the sum of the AC and DC current, the lock-in measures only the differential part of the signal. A Keithley 2400 SourceMeter is used for DC measurements or to apply gate voltages.

References

- [1] R.V. Gorbachev, I. Riaz, R.R. Nair, R. Jalil, L. Britnell, B.D. Belle, E.W. Hill, K.S. Novoselov, K. Watanabe, T. Taniguchi, A.K. Geim, and P. Blake. Hunting for monolayer boron nitride: Optical and Raman signatures. *Small*, 7(4), 465, 2011.
- [2] P.J. Zomer, M.H.D. Guimarães, J.C. Brant, N. Tombros, and B.J. van Wees. Fast pick up technique for high quality heterostructures of bilayer graphene and hexagonal boron nitride. *Applied Physics Letters*, 105(1), 013101, 2014.
- [3] Y.C. Lin, C.C. Lu, C.H. Yeh, C. Jin, K. Suenaga, and P.W. Chiu. Graphene annealing: How clean can it be? *Nano Letters*, 12(1), 414, 2012.

Proximity-Induced Room-Temperature Ferromagnetism in Graphene Probed with Spin Currents

Published in 2D Materials 4(1), 014001, 2017

Abstract

We present a direct measurement of the exchange interaction in room temperature ferromagnetic graphene. We study the spin transport in exfoliated graphene on an yttrium-iron-garnet substrate where the observed spin precession clearly indicates the presence and strength of an exchange field that is an unambiguous evidence of induced ferromagnetism. We describe the results with a modified Bloch diffusion equation and extract an average exchange field of the order of 0.2 T. Further, we demonstrate that a proximity-induced 2D ferromagnet can efficiently modulate a spin current by controlling the direction of the exchange field. These findings can create a building block for magnetic-gate tunable spin transport in one-atom-thick spintronic devices.

4.1 Introduction

The introduction and control of ferromagnetism in graphene opens up a range of new directions for fundamental and applied studies [1, 2]. Several approaches have been pursued so far, such as introduction of defects, functionalization with adatoms, and shaping of graphene into nanoribbons with well-defined zigzag edges [3–8]. A more robust and less invasive method utilizes the introduction of an exchange interaction by a ferromagnetic insulator (FMI) in proximity with graphene [9–16]. The magnetic proximity effect describes the introduction of ferromagnetic order into an intrinsically nonmagnetic material by an adjacent ferromagnet. Being atomically thin, graphene presents an ideal platform for studying such interaction, in particular when combined with a ferromagnetic insulator. Theory predicts that for the idealized case of (super)lattice matching an exchange splitting of tens of meV can be obtained [16]. Up to date it has been studied experimentally in a number of FMI/graphene systems using materials with low Curie temperature such as EuO ($T_c = 69$ K) and EuS ($T_c = 16.5$ K) [13, 14]. In comparison, Yttrium-Iron-Garnet (YIG) provides the advantage of a Curie temperature of 550 K, along with chemical stability in atmospheric conditions, the preservation of the charge transport proper-

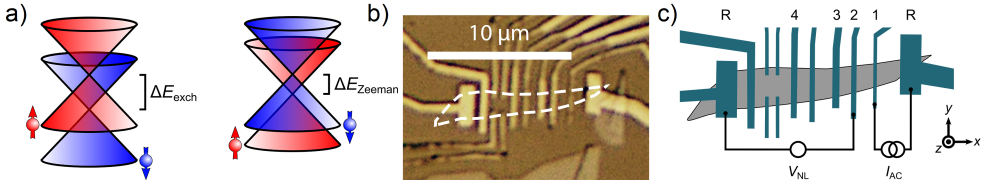


Figure 4.1: Spin transport in graphene in the presence of a proximity-induced exchange field. a) The exchange field ΔE_{exch} creates a splitting of the Dirac cone for each spin species similar to the magnetic field-induced Zeeman splitting ΔE_{Zeeman} . Note that both the sign and magnitude of the exchange and Zeeman splitting can be different. b) Optical micrograph of the graphene/YIG heterostructures indicating the single layer graphene flake and the deposited TiO_2/Co contacts. To control the coercive field of the electrodes for magnetization switching, we define different contact width between 200 nm and 400 nm. c) Schematic sketch of the sample showing the characterized injector/detector contacts 1 – 4) and reference contacts R. The circuit for the measurements shown in Figure 4.2 and Figure 4.3 is indicated.

ties in the graphene and the possibility to directly exfoliate or transfer graphene onto the surface for fabricating graphene-based spintronic devices.

As indication of a ferromagnetic exchange interaction in graphene/YIG heterostructures the observation of an anomalous Hall effect was reported [9]. More recently, the presence of an exchange interaction in YIG/CVD graphene devices was invoked to explain magnetoresistance measurements and ferromagnetic resonance spin pumping [15]. So far, in all the reports the authors employ charge transport, where in addition to exchange interaction also spin-orbit interaction is needed for the understanding, both a priori unknown parameters.

In this work, we probe the induced exchange interaction in graphene in the most direct way using only the spin degree of freedom. The magnetic interaction between the YIG magnetization and the graphene spins is expected to produce an exchange term in the Hamiltonian and to spin split the graphene energy bands (Figure 4.1a). It can be described as an additional effective exchange field that is determined by the direction and magnitude of the YIG magnetization. By studying its effect on spin transport and precession, and fitting the results with the modified Bloch diffusion equation we are able to describe our results qualitatively and quantitatively. We further demonstrate that the precession induced by the exchange field can be used for an efficient modulation of spin currents.

4.2 Sample Fabrication and Characterization

The device is shown in Figures 4.1b and 4.1c. A single layer graphene flake of approximately $12 \mu\text{m}$ by $1.2 \mu\text{m}$ is first exfoliated on SiO_2 and transferred to YIG. Fer-

romagnetic contacts are defined via e-beam lithography followed by Ti deposition, in-situ oxidation to form TiO_2 , Co deposition and liftoff. A non-local spin valve characterization [17] is shown in Figure 4.2. A charge current is sent from the injector to the reference electrode. As a result a pure spin current diffuses through the channel and is detected as a voltage difference between the detecting and another reference electrode. The spin transport measurements are obtained using Contact 1 and Contact 2 as injector and detector with contact spacing $d = 1.2 \mu\text{m}$. The magnetization direction of the injector (detector) can be controlled by sweeping the applied magnetic field along the easy axis of the electrodes. Figure 4.2b shows the change of the non-local resistance (R_{NL}) when the electrode configuration is switched between parallel and antiparallel alignment. The change in R_{NL} is a pure spin signal that increases from $90 \text{ m}\Omega$ at room temperature to $650 \text{ m}\Omega$ at 75 K . To determine the spin relaxation length λ , we fit the dependence of the spin signal on d and extract $\lambda = (490 \pm 40) \text{ nm}$. These values are comparable to our other graphene devices on YIG or SiO_2 [18], which confirms that the basic spin transport properties of graphene are conserved after transfer to YIG.

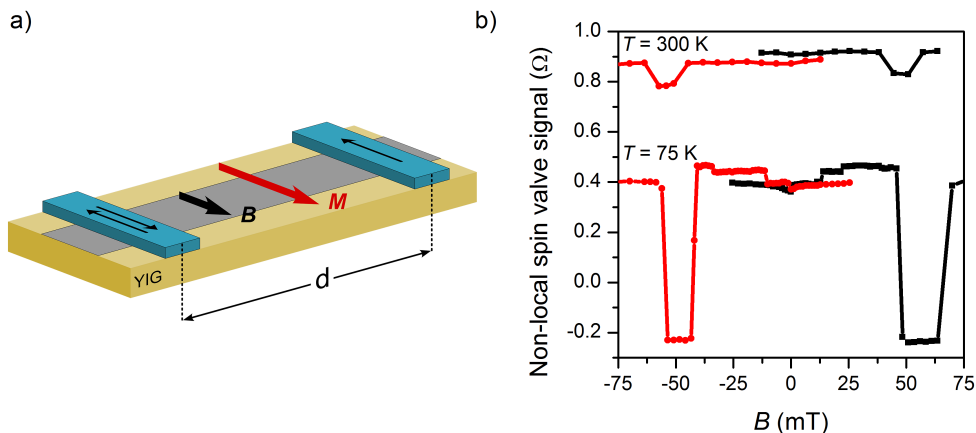


Figure 4.2: Non-local spin transport in graphene spin valves on YIG. a) Schematic measurement to characterize the non-local spin transport by switching the electrode magnetization with an external magnetic field (B). M denotes the magnetization of the YIG film and is parallel to B for these measurements. The exchange field is parallel or antiparallel to the spin accumulation and hence does not affect the spin transport for this type of experiment. b) The experimental data of the spin valve switching at 300 K and 75 K is measured with $d = 1.2 \mu\text{m}$. The black squares (negative to positive) and the red circles (positive to negative) correspond to different sweep directions of B . The other switches can be attributed to smaller contributions of the outer electrodes to the spin signal.

4.3 Analysis and Discussion

To investigate the presence of the exchange field, we study the Hanle spin precession (Figure 4.3a). A perpendicular magnetic field causes injected spins to precess while diffusing along the channel, changing the average polarization and direction of the spins at the detector. The total effective field (B_{tot}) that is sensed by the spins consists of the applied field (B) and exchange field (B_{exch}), $B_{\text{tot}} = B + B_{\text{exch}}$. B is swept perpendicular to the sample plane and causes the Zeeman splitting of the graphene spins, $\Delta E_{\text{Zeeman}} = g\mu_B|B|$. The exchange field is determined by the YIG magnetization direction M and the interface properties and is defined as $\Delta E_{\text{exch}} = g\mu_B|B_{\text{exch}}|$. Here g is the gyromagnetic factor (~ 2 for graphene) and μ_B the Bohr magneton.

Typical Hanle curves for graphene devices on SiO_2 [19] or hBN [20] substrates are smooth over the full measured range, whereas Figures 4.4b and 4.4c show clearly a sharp transition at $B \sim 180$ mT. The kink is seen for both parallel and antiparallel injector/detector magnetization at all measured temperatures although it becomes more pronounced at 75 K. The appearance of such transition requires an additional spin precession caused by the exchange field B_{exch} that is constant in magnitude and collinear with M . When no external field is applied, M together with B_{exch} lies within the sample plane and is gradually pulled out of the plane with increasing

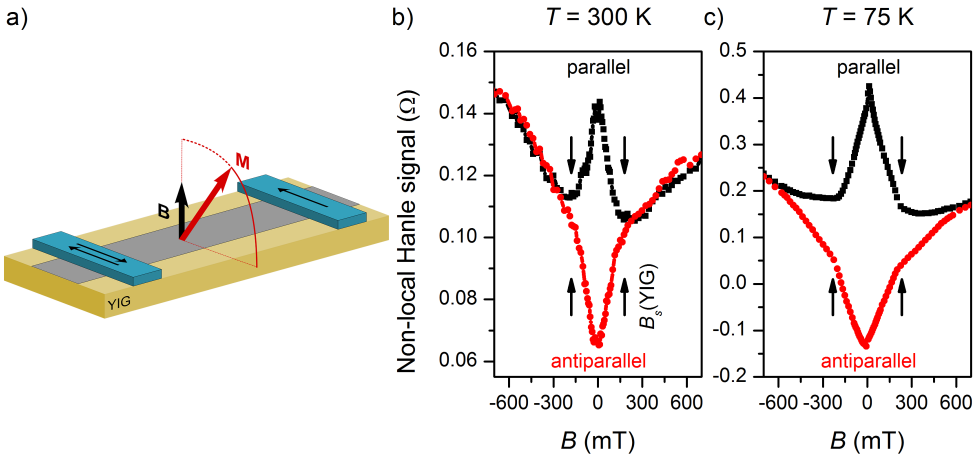


Figure 4.3: Hanle spin precession modified by the proximity-induced exchange field. a) The schematic measurement setup. B is applied perpendicular to plane. The total effective field $B_{\text{tot}} = B + B_{\text{exch}}$ causes Hanle spin precession. b) Non-local resistance at room temperature and c) 75 K. The top curve (black squares) is measured with parallel injecting and detecting electrodes, the bottom curve (red circles) represents their antiparallel alignment. The black arrows indicate the perpendicular saturation field of the underlying YIG film.

B. The transition point coincides with the saturation field of the YIG magnetization ($B_s \sim 180$ mT) above which M and B_{exch} are aligned fully perpendicular to the sample plane. The change of the transition field with temperature is consistent with the change of the magnetization saturation field of the YIG films. Thus, we conclude the existence of an exchange field with a magnitude comparable to the applied field at the transition point (~ 180 mT).

To further confirm the presence and magnitude of the exchange field, we utilize the low in-plane coercivity of YIG. By applying and rotating a small magnetic field of 20 mT in the sample plane we can control the magnetization direction of the YIG without applying a significant spin precession with the applied field. Furthermore, we maintain the parallel/antiparallel alignment of the injector/detector electrodes, leaving the injected/detected spins unaffected. When B_{exch} is collinear with the injected spin polarization ($\beta = \pm 90^\circ$) it has no influence on the spin transport, whereas at $\beta = \pm 0^\circ$ diffusing spins experience the maximum precession and dephasing. In Figure 4.4b the dependence of the spin signal on β is shown for both parallel and antiparallel magnetization alignment. For $d = 0.9 \mu\text{m}$ (Contact 2 and Contact 3) the observed modulation is around 50%, which is substantial and cannot be explained by the effect of B ($= 20$ mT) alone. With increasing distance between both electrodes the modulation reaches $\sim 100\%$ at $d = 4.2 \mu\text{m}$ (Figure 4.4d). In this case all spin

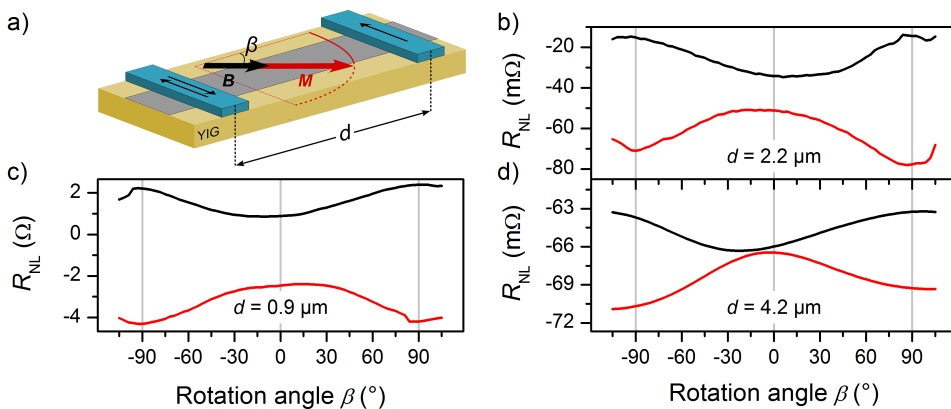


Figure 4.4: Spin transport modulated with an in-plane exchange field. a) Schematic of the experiment. The YIG magnetization is rotated with $|B| = 20$ mT by an angle β in parallel (black) and antiparallel (red) electrode alignment. In this experiment only the exchange field causes significant spin precession, leading to a modulation of the spin signal. b) – d) We show the modulation caused by the additional spin precession originating from the exchange field for three different distances, the full data set is shown in Section 4.6.7. For the farthest distance a smoothed curve is plotted. The relative modulation increases from 50% at $d = 0.9 \mu\text{m}$ up to $\sim 100\%$ at $d = 4.2 \mu\text{m}$ injector to detector spacing.

components perpendicular to B_{exch} are dephased and averaged to zero and the spin signal has a dependence close to $\Delta R_{\text{NL}}(\beta) = \pm R_{\text{NL}}^0 \cos^2 \beta$. These measurements confirm that the magnitude of the exchange field corresponds to approximately 0.2 T.

To model the spin transport in graphene in the presence of an exchange field, we add the exchange field to the one dimensional Bloch equation:

$$0 = D_s \nabla \mu_s - \mu_s / \tau_s + (g \mu_B) / \hbar (B + B_{\text{exch}}) \times \mu_s, \quad (4.1)$$

where D_s denotes the spin diffusion coefficient, μ_s the three-component spin chemical potential, τ_s the spin relaxation time and \hbar the reduced Planck constant. We obtain an analytical expression for the spin accumulation at the detector depending on B . Below the YIG saturation field B_s both M and B_{exch} are determined by the standard easy-plane magnetic anisotropy model, whereas above the saturation field B_{exch} is fixed and aligned with B . We use our model to qualitatively reproduce the observed behavior and also make a quantitative estimation of the exchange field. The fitting of the Hanle curve is shown in Figure 4.5a, where we find the best agreement for $\lambda = 1.8 \mu\text{m}$ ($\lambda = \sqrt{D_s \tau_s}$) and $|B_{\text{exch}}| = 0.2$ T. A possible explanation for the difference between λ extracted from the distance-dependent spin signal ($\lambda = 490$ nm) and from the modeling ($\lambda = 1.8 \mu\text{m}$) is a spatial inhomogeneity of the exchange field. $|B_{\text{exch}}|$ is expected to depend crucially on the overlap between the graphene π -orbitals with the iron d-orbitals of the FMI. One can readily assume that the regions where the electrodes are on top of the graphene experience a different strength of the exchange field than regions where the graphene lies freely on the surface.

Our analysis can be further extended to the spin transport modulation dependencies shown in Figure 4.4. Figure 4.5b shows the modulation of the spin signal depending on d . These results can also be fit with $\lambda = 1.8 \mu\text{m}$ and $|B_{\text{exch}}| = 0.2$ T. When extrapolating the data to $d = 0$, we find $\sim 35\%$ modulation which can be obtained analytically from our model:

$$\frac{R_{\text{NL}}^{\text{max}} - R_{\text{NL}}^{\text{min}}}{R_{\text{NL}}^{\text{max}}} \Big|_{d=0} = 1 - \frac{1}{\sqrt{2}} \frac{\sqrt{1 + \sqrt{1 + (\omega \tau_s)^2}}}{\sqrt{1 + (\omega \tau_s)^2}}, \quad (4.2)$$

where $\omega = g/\hbar \mu_B |B_{\text{exch}}|$. Using $|B_{\text{exch}}| = 0.2$ T, we obtain $\tau_s \sim 40$ ps. Assuming that the spin and charge diffusion (D_c) coefficients coincide, we deduce $\lambda = \sqrt{D_c \tau_s} \sim 500$ nm, which resembles the λ extracted from distance-dependent spin signal, again suggesting an inhomogeneous exchange field.

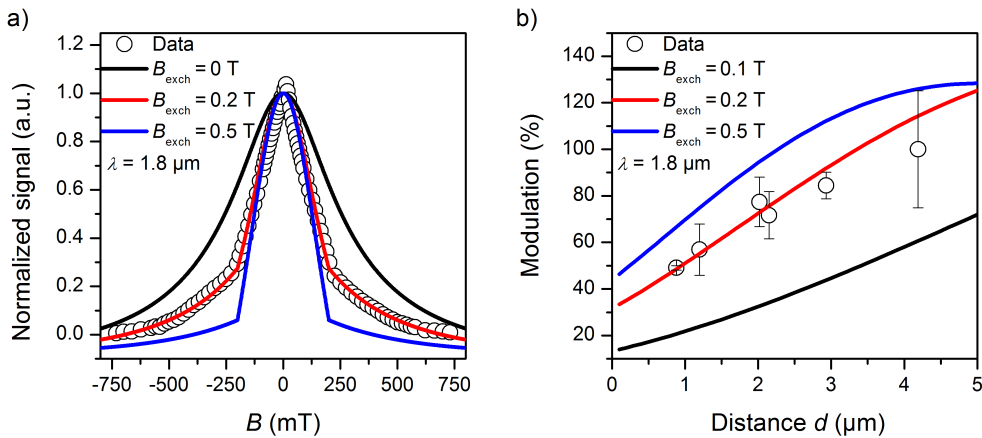


Figure 4.5: Modeling of the spin transport in the presence of an exchange field in the two different experimental configurations. a) The standard Bloch spin diffusion model is modified to take the proximity-induced exchange field into consideration. The pure spin signal is extracted from the Hanle precession curves and shown with the model for three different exchange field contributions. b) The modulation of the spin signal originating from the proximity-induced exchange field is shown for three different exchange field strengths. In both independent measurements we extract $|B_{\text{exch}}| \sim 0.2$ T by fitting the data.

4.4 Conclusion

In summary, we have demonstrated the detection of a ferromagnetic exchange field in graphene by spin transport at room temperature, 75 K and 4.7 K. The exchange field strength is quantified in two different experimental configurations to be 0.2 T. Given the theoretical results on idealized systems, substantial enhancement should be possible by appropriate interface optimization [16]. We proposed spin transport measurements as the most direct way to study the exchange field in graphene. Furthermore, we showed that a spin current can be efficiently modulated by controlling the exchange field, which opens up new directions to control spins in graphene-based spintronic devices.

Acknowledgements We acknowledge A. Aqeel, P.J. Zomer, H.M. de Roos and J.G. Holstein for technical assistance, J. Ingla-Aynés and A.M. Kamerbeek for fruitful discussions. This research has received funding from the European Unions 7th Framework Program within the Marie Curie initial training network ‘Spinograph’ (grant 607904), the ‘Graphene Flagship’ (grant 604391) and the Dutch ‘Foundation for Fundamental Research on Matter’ (FOM).

Author contributions BjvW, JCL, AAK and MW conceived the experiments. JCL and AAK designed and carried out the experiments. JCL, AAK and BjvW analyzed and discussed the data and wrote the manuscript.

4.5 Methods

Our graphene flakes are exfoliated from HOPG graphite crystals (HQ Graphene) on silicon oxide substrates. Single layer graphene flakes are selected by optical contrast and transferred to target substrates with a custom-built transfer stage using a polycarbonate-based pickup technique. The commercially available (111) single crystal YIG films (Matesy GmbH) are grown by liquid phase epitaxy with 210 nm YIG thickness on GGG substrates. The films are cleaned with acetone, isopropanol and 180 s in 200 W oxygen plasma to remove organic residues. To minimize water contamination at the interface between graphene and YIG, the substrates are kept for 15 min in a furnace at 500°C until the graphene transfer at 140°C.

After transfer, the polycarbonate is dissolved in chloroform and the graphene is cleaned for one hour in a furnace at 350°C in an Ar/H₂ atmosphere. The flake is connected with electrodes made of titanium oxide tunnel barriers (0.8 nm), ferromagnetic cobalt electrodes (45 nm) and an aluminum capping layer (5 nm) using e-beam lithography. The samples are characterized in a cryostat with standard AC lock-in measurement techniques at room as well as low temperatures. We apply typical AC currents between 1 and 20 μA with frequencies between 1 Hz and 13 Hz. At 75 K the electrodes show a contact resistance of the order of 1 kΩ – 3 kΩ and a spin signal between 7 Ω at 500 nm contact spacing and 10 mΩ at 3.9 μm spacing. Measurements of Shubnikov-de Haas oscillations at $T = 2$ K, reveal a carrier density of the order of $3 \times 10^{12} \text{ cm}^{-2}$ and a mobility of 720 cm²/Vs. In different graphene/YIG samples we observe holes as charge carriers resulting from doping during the transfer process.

4.6 Supplementary Information

4.6.1 Characterization of the YIG Films

In accordance with an easy-plane magnetization anisotropy model, the magnetization of the YIG substrate (Figure 4.6) can be described as $M_z = |M| \cdot B/B_s$ below B_s . The behavior of M_z saturates at around $B_s \sim 180$ mT at room temperature and at 250 mT at 75 K. The topography of the substrate, measured by atomic force microscopy (AFM), has an RMS surface roughness of the order of 0.1 nm over a 1.75 μm by 1.75 μm square. Smaller scale corrugations (~ 20 nm in lateral dimension) are due to the line scanning of the image. The lateral resolution of the AFM scan is ~ 10 nm.

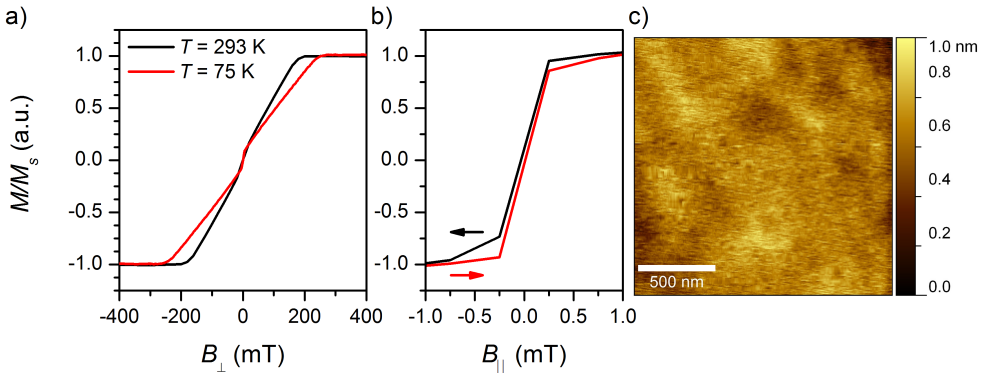


Figure 4.6: a) Magnetization response of the 210 nm (111) YIG film is measured in an applied perpendicular magnetic field at 293 K (black) and 70 K (red). b) Trace and retrace in an in-plane magnetic field is measured at 293 K. The coercive field is less than 0.1 mT. c) The AFM image of a cleaned YIG substrate, the scale bar is 500 nm. The RMS roughness of a $1.75 \mu\text{m}$ by $1.75 \mu\text{m}$ square is approximately 0.1 nm.

4.6.2 Charge and Spin Transport Properties of the Graphene Flake

The thickness of the graphene flake is determined after exfoliation on 300 nm SiO_2 on a Si substrate by optical contrast (on average around 6% per single layer in our system). The discussed flake has a contrast of 5.5% from which we conclude single layer thickness. To estimate the carrier concentration we use the Shubnikov-de Haas oscillations of the longitudinal resistance at $T = 2.2$ K, shown in Figure 4.7.

The reciprocal magnetic field values of the minima are plotted as a function of the peak index and shown in the inset of Figure 4.7. We use only the three highest field minima to assure an accurate estimation of the carrier density. The $1/B$ slope of $(0.0314 \pm 0.0004) \text{ T}^{-1}$ corresponds to a carrier density of $n = (3 \pm 0.05) \times 10^{12} \text{ cm}^{-2}$. This value is in good agreement with our other similarly fabricated samples that show holes as carriers with densities of $n \sim 10^{12}$ to 10^{13} cm^{-2} . Using the resistance of Region 1, we deduced a carrier mobility of $(720 \pm 6.5) \text{ cm}^2/\text{Vs}$, also a typical value for our other graphene/YIG devices. With the obtained carrier density, we calculate a charge diffusion coefficient of $D_c = (66 \pm 3) \text{ cm}^2/\text{s}$.

From the distance-dependent spin signal (Figure 4.8a) we obtain a spin relaxation length $\lambda = (490 \pm 40) \text{ nm}$, which is in agreement with our previous samples of graphene/YIG heterostructures ($\lambda \sim 700 \text{ nm}$).

To analyze the influence of the contact resistance on the spin relaxation length λ , we calculate the conductivity mismatch parameter r for the different regions [18, 21]. The results are shown in Table 4.1. In the case where the contacts have the biggest effect on spin relaxation, $r/\lambda = 0.25$, the intrinsic spin relaxation length can be higher than the calculated value by $\sim 20\%$.

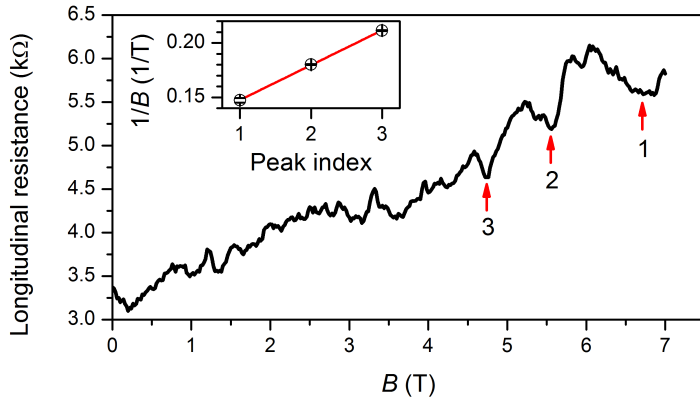


Figure 4.7: The longitudinal resistance of Region 1 in high fields at $T = 2.2$ K. We observe three minima of the Shubnikov-de Haas oscillations. The inset contains the reciprocal field position of the three highest minima as a function of the peak index.

4

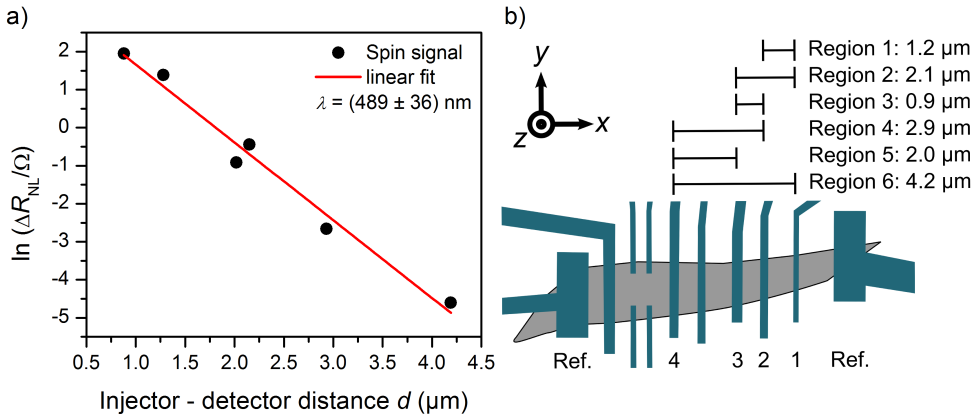


Figure 4.8: a) The distance-dependent spin signal is shown and used to calculate the spin relaxation length λ . b) Schematic image of the graphene flake and patterned contacts. The contacts and pairs of injector-detector with different d used for measurements are labeled and axes defined.

4.6.3 Discussion of the full spin precession data sets: Effect of the cobalt stray field on the YIG magnetization

We measured the spin precession at $T = 4.7$ K, 75 K and 300 K and extracted the spin signal by subtraction of the antiparallel from the parallel Hanle curve. The amplitude of the spin signal is observed to increase with decreasing temperature, which is also consistently seen in the spin valve measurements. The characteristic

Region	R_I k Ω	R_D k Ω	R_c^{eff} k Ω	$d \times w$ μm^2	R k Ω	R_{sq} k Ω	r μm	r/λ
1	1.9	0.89	1.212	1.2×1.1	6.1	5.6	0.238	0.49
2	1.9	0.92	1.240	2.1×1.3	12.8	7.9	0.203	0.42
3	0.98	0.92	0.905	0.9×1.4	6.6	10.3	0.123	0.25
4	0.98	0.65	0.751	2.9×1.4	15.2	7.4	0.143	0.29
5	0.92	0.65	0.762	2.0×1.6	8.5	6.5	0.188	0.38
6	1.90	0.65	0.969	4.2×1.4	21	7.0	0.194	0.40

Table 4.1: Measured and derived parameters of the graphene flake and contacts. The table gives an overview of injector and detector resistances R_I and R_D measured in a three terminal geometry, effective contact resistance $R_c^{\text{eff}} = 2/(1/R_I + 1/R_D)$, length and width of the regions, resistance R of the regions measured in four probe, calculated square resistance $R_{\text{sq}} = R \times w/d$ and conductivity mismatch parameter $r = R_c^{\text{eff}}/R_{\text{sq}} \times w$ with ratio r/λ .

kink at the saturation field of the YIG magnetization as well as the relatively linear shape of the Hanle below saturation field and the remaining spin signal up to about 600 mT are present at all temperatures. We find the kink to shift from 180 mT at room temperature to higher fields with decreasing temperature, which is in agreement with the SQUID measurements of the YIG films (Figure 4.6c).

To extract the spin-dependent signal, we subtract the Hanle curves measured in parallel and antiparallel configurations as plotted in Figure 4.9. The “+” designates the difference between parallel “up-up” and antiparallel “up-down” alignment of the injector/detector electrodes. The “-” denotes the difference between parallel “down-down” and antiparallel “down-up” alignment. Alignment “up” indicates that the contact magnetization is aligned along the y -axis (Figure 4.8), in the positive magnetic field direction. Alignment “down” indicates the opposite, negative field, direction along the y -axis. All four curves (including trace and retrace curves for alignments “+” and “-”) show the transition point where the magnetization of the YIG film saturates.

The switches of the spin signal close to zero applied field are due to the fact that the YIG magnetization around $B = 0$ cannot be well controlled, leading to an abrupt change of the in-plane magnetization direction and resulting in a change of the exchange field acting on the spins. This can be explained with the stray field arising from the contact magnetization. The coercive field of the YIG magnetization in the film plane (easy-plane) is smaller than 0.1 mT (Figure 4.6b). Thus, even a rather small stray field can locally influence M . From the given geometry of the contacts we conclude that the strongest stray field is expected at the ends of the electrodes, which is typically more than $1 \mu\text{m}$ away from the graphene channel. Therefore, the direct contribution from the stray field of the contacts to the field acting on graphene

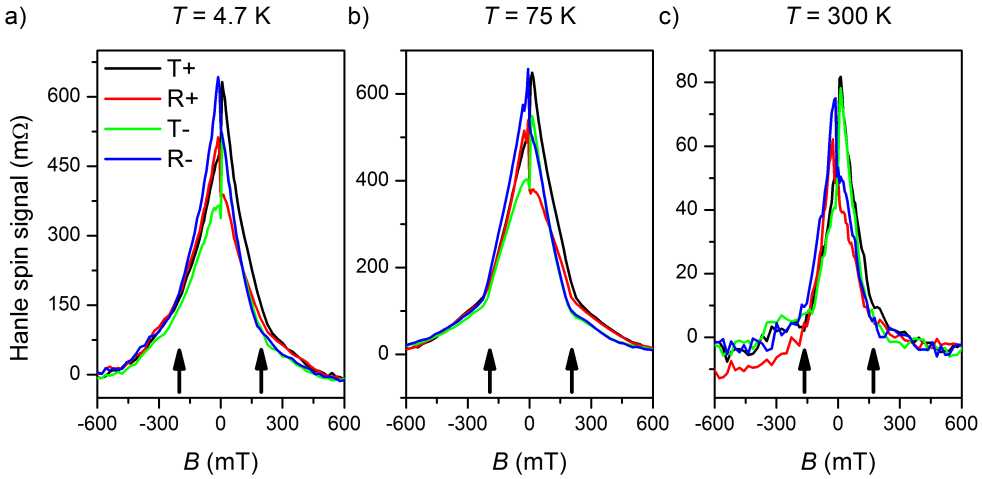


Figure 4.9: Magnetic field-dependence of the spin signal obtained from Hanle precession data sets at different temperatures. The arrows indicate the YIG saturation fields.

is negligible, which we confirmed with finite element modeling in COMSOL multiphysics. However, at small applied fields the YIG magnetization can be influenced by the contact alignment which, thus, determines the exact switching behavior of M . Moreover, it is seen that the switching of "T+" and "R-" or "T-" and "R+" is symmetric with respect to the zero field, which can be understood by taking the magnetization direction of the contacts into account.

4.6.4 Absence of Potential YIG Stray Fields

As discussed in the previous section, the stray fields arising from the contact magnetization are expected to be negligible close to the graphene flake and cannot directly affect the spin transport in the channel. Another possible source of stray fields is the YIG film in direct vicinity to the graphene. Assuming a perfect flatness of the 210 nm YIG film and a typical size of $5 \times 5 \text{ mm}^2$, no stray fields are expected. However, it was shown in by Dash et al. [22] that the finite roughness of the surface of the magnetic material can lead to non homogeneous in-plane and out-of-plane stray fields. Under the assumption of a perfectly flat graphene flake, the out-of-plane stray fields average out spatially, as the total magnetic flux through the graphene surface has to be zero. With finite roughness of the graphene both in-plane and out-of-plane fields can have a non-zero average value.

In our case the roughness of the YIG film is $\sim 0.1 \text{ nm}$ (Figure 4.6c), therefore, we expect a negligible magnitude of any YIG stray field. Moreover, based on our analysis we can exclude the effect of stray fields because of the following reasons. First,

to explain our results with stray fields only, a magnitude of the order of 0.2 T, comparable to the YIG saturation field, would be required. Such a large average stray field cannot originate from the measured YIG roughness. Second, the fitting of both out-of-plane Hanle measurements (Figure 4.3) and in-plane rotation measurement (Figure 4.4) leads to a similar magnitude of the exchange field. Thus, the effect cannot be explained by stray fields as they are expected to be different for in-plane or out-of-plane magnetization configurations.

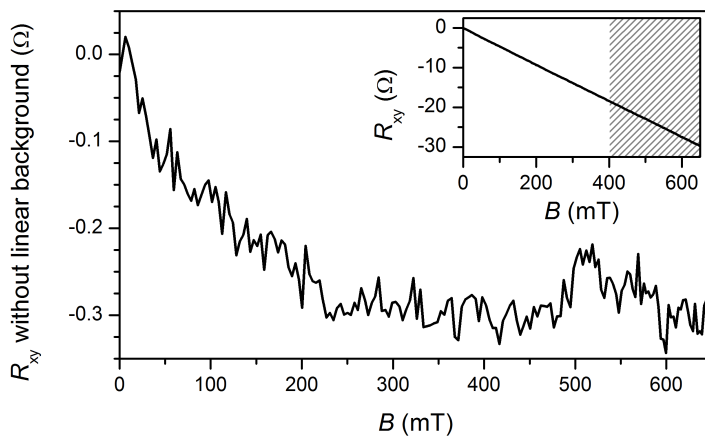


Figure 4.10: Characterization of the Hall effect in graphene on YIG. The transverse resistance (R_{xy}) of a graphene flake is measured and antisymmetrized (inset). After subtraction of the linear Hall effect ($45.3 \text{ } \Omega/\text{T}$, measured in the hatched area of the inset) a non-linear component remains, which has a magnitude of roughly $0.3 \text{ } \Omega$ at $T = 75 \text{ K}$.

Furthermore, we exclude the effect of stray fields using measurements of the Hall effect in similarly fabricated samples of graphene on YIG with non-magnetic titanium/gold contacts. Similarly to Reference [9], we measure the transverse resistance of the graphene flake in a perpendicular applied magnetic field. After antisymmetrization of the data the linear component is determined by a linear fit at high fields (between 400 mT and 650 mT, hatched area in Figure 4.10) and subtracted. The remaining non-linear component is shown in Figure 4.10. If present, the stray field is expected to saturate along with the perpendicular saturation of YIG magnetization and, therefore, should be seen in the non-linear contribution to the Hall voltage. The observed non-linear contribution is ~ 100 times smaller than the linear component. This implies that the maximal strength of the stray field has to be 100 times smaller than the applied magnetic field ($\sim 0.2 \text{ T}$), i.e. $\sim 0.002 \text{ T}$. This is also 100 times lower than the extracted strength of the exchange field and provides an experimental evidence to exclude stray fields as a possible explanation of our results.

4.6.5 Comparison to a Reference Sample

The spin precession data of the additional reference sample (Figure 4.11, red squares, 1 μm contact spacing, 70 K) is plotted together with the same measurement for main text sample (black line, 1.2 μm contact spacing, 75 K). Despite similar fabrication steps, we find a higher contact impedance and an increased noise level in the reference sample. However, we are able to observe a comparable magnitude of the spin signal as well as the characteristic features like the relatively linear shape at lower fields and the kink at the perpendicular saturation field of the substrate. The inset contains a non-local spin valve measurement of the reference sample.

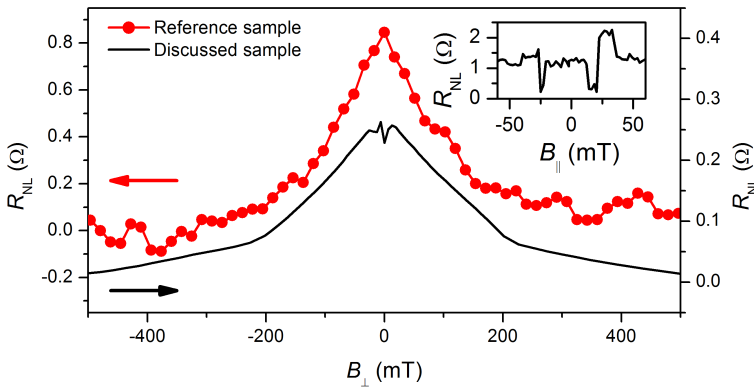


Figure 4.11: Measurement of the spin valve and Hanle spin precession on a second device.

4.6.6 Comparison to Spin Modulation in Metal/YIG Systems

Recent reports from Villamor et al. [23] and our group [24] demonstrated the modulation of spin currents in Cu and Al films on YIG substrates by an in-plane rotation of the YIG magnetization. Although the interaction in this case is also induced by an exchange interaction, in metals the effect causes predominantly an absorption of spins perpendicular to the YIG magnetization. This description arises from circuit theory which is applicable to diffusive metal systems, that support many disordered conduction channels. In case of graphene, this concept does not apply since graphene is a strictly two-dimensional electronic system. The effect of the YIG on the spins in the graphene channel is not caused by absorption but by induced precession, which arises from the exchange interaction, and causes a spin-splitting in the band structure. Our measurements clearly indicate the presence of this exchange interaction since we can extract the strength from our data. It implies that the electronic states of the graphene are modified and we can call the graphene ferromagnetic. Note that in a metal system the density of states close to the interface could in principle also

become spin polarized. However, it would be restricted to the first atomic layer(s), whereas the experiments in metals are done in much thicker layers, where circuit theory is applicable.

4.6.7 Full Set of Spin Transport Modulation Data

Figure 4.12 shows the spin modulation data for all measured device distances. The relative modulation extracted from these measurements is shown in Figure 4.5b.

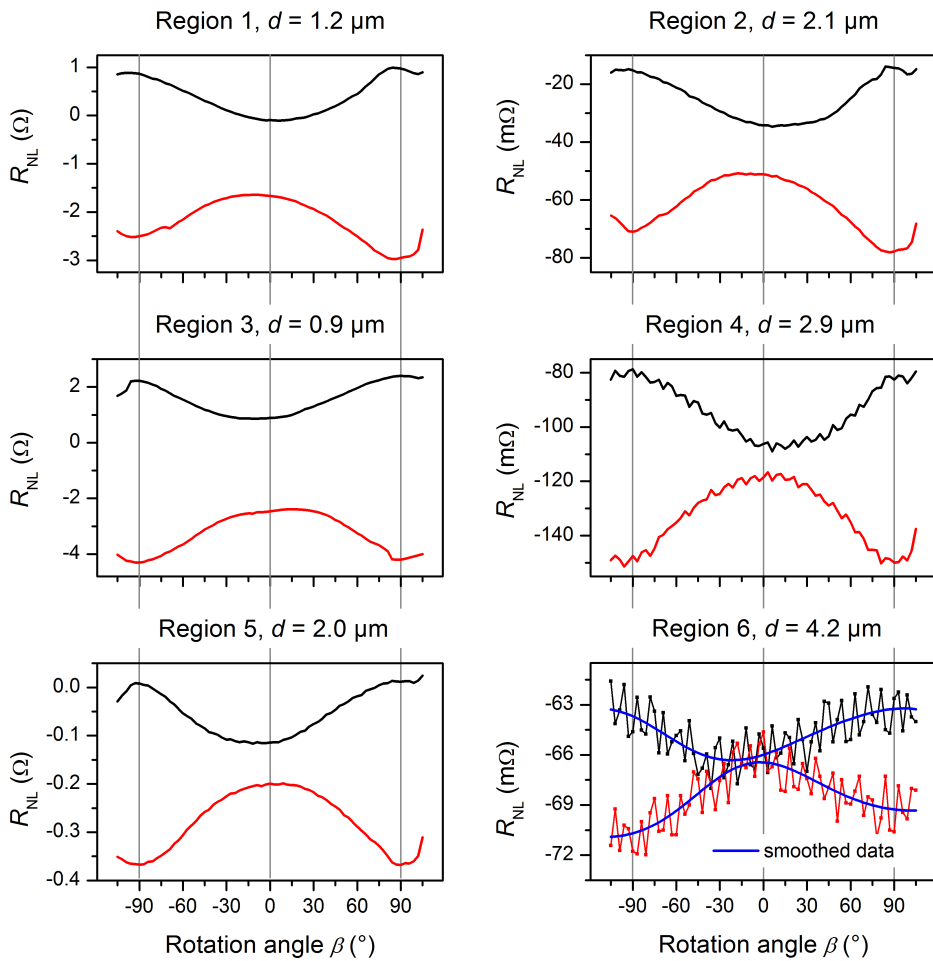


Figure 4.12: Full data set of the spin transport modulation by in-plane rotation of the magnetization direction at $T = 75 \text{ K}$. The extracted relative modulation is discussed in the main text. For the farthest distance the raw data and the smoothed curves are shown.

4.6.8 Spin Transport Modulation at Room Temperature

A comparison of the modulation measured in Region 1 between $T = 75$ K and $T = 300$ K is shown in Figure 4.13. We observe an increase from 57% at $T = 75$ K to 77% at room temperature.

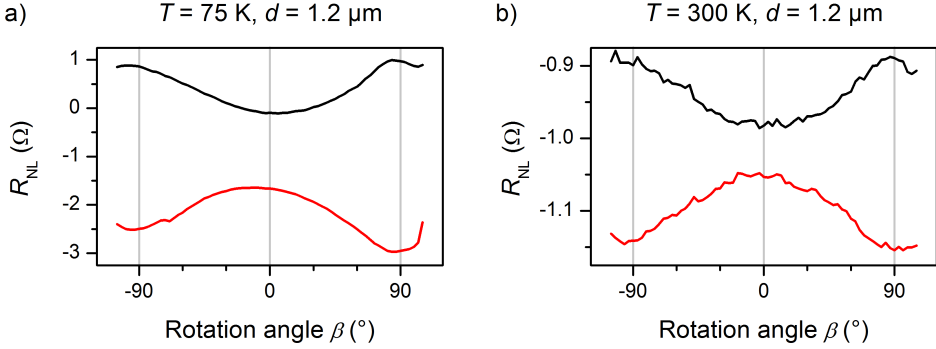


Figure 4.13: a) The spin signal in Region 1 ($d = 1.2 \mu\text{m}$) is modulated at 75 K by 57%. b) The modulation increases to 77% at 300 K.

4.6.9 Modeling

To model the observed data we solve the one dimensional Bloch diffusion equation for a total effective field acting on the spins:

$$0 = D_s \nabla \mu_s - \frac{\mu_s}{\tau_s} + \frac{g\mu_B}{\hbar} \underbrace{(B + B_{\text{exch}})}_{B_{\text{tot}}} \times \mu_s, \quad (4.3)$$

where $\mu_s(x) = (\mu_x(x), \mu_y(x), \mu_z(x))$ and the magnetic field B_{tot} is the vector sum of the external applied magnetic field and exchange field ($B_{\text{tot}} = B + B_{\text{exch}}$). The equation can be solved with the boundary condition for the spin accumulation $\mu_s(x) = (0, 0, 0)$ at $x = \pm\infty$ and the assumption that the spins are injected only in y -direction, $\frac{\partial}{\partial x} \mu_s(x) \sim (0, \mu_y^0, 0)$ at $x = 0$.

The analytical solution for the y -component of the spin accumulation reads:

$$\mu_y(x) = A \frac{B_y^2}{B^2} e^{-\frac{x}{\lambda}} + A \frac{B^2 (B_x - B_z)^2 + (B_x^2 - B_x B_y - B_z B_y + B_z^2)^2}{2B^2 (\alpha_1^2 + \alpha_2^2) (B^2 - B_x B_y - B_y B_z - B_z B_x)} \times \left[\alpha_1 \cos\left(\alpha_2 \frac{x}{\lambda}\right) - \alpha_2 \sin\left(\alpha_2 \frac{x}{\lambda}\right) \right] e^{-\alpha_1 \frac{x}{\lambda}}, \quad (4.4)$$

where A is a scaling parameter, $\alpha_{1(2)} = \frac{1}{\sqrt{2}} \sqrt{\pm 1 + \sqrt{1 + (\omega\tau_s)^2}}$, $\omega = \frac{g}{\hbar} \mu_B |B_{\text{tot}}|$ and $\tau_s = \lambda^2/D_s$. For relevant cases when either $B_x = 0$ or $B_y = 0$ the expression for $\mu_y(x)$ can be simplified:

$$\frac{B^2(B_x - B_z)^2 + (B_x^2 - B_x B_y - B_z B_y + B_z^2)^2}{2B^2(B^2 - B_x B_y - B_y B_z - B_z B_x)} = \begin{cases} \left(\frac{B_z}{B}\right)^2, & \text{when } B_x = 0, \\ 1, & \text{when } B_y = 0. \end{cases} \quad (4.5)$$

Equation 4.4 is used to fit three types measurements. First, we fit the Hanle precession data when the external field is applied perpendicular to the sample plane (Figures 4.3c and 4.5a). A , λ , τ_s and $|B_{\text{exch}}|$ are used as parameters. The best fit is obtained with $|B_{\text{exch}}| \sim 0.2$ T, $\tau_s \sim 27$ ps and $\lambda \sim 1.8$ μm , Figure 4.14. From the modeling we conclude that when M is aligned with B , B and B_{exch} have the same sign. Secondly, we fit the relative modulation of the spin signal as a function of the distance between electrodes when the magnetization of the YIG is rotated in the sample plane (Figure 4.4) with A , λ and $\tau_s \cdot |B_{\text{exch}}|$. The best fit is obtained with $\lambda \sim 1.8$ μm and $\tau_s \cdot |B_{\text{exch}}| = 7.8$ ps·T, $|B_{\text{exch}}| \sim 0.2$ T and $\tau_s \sim 39$ ps, Figure 4.14.

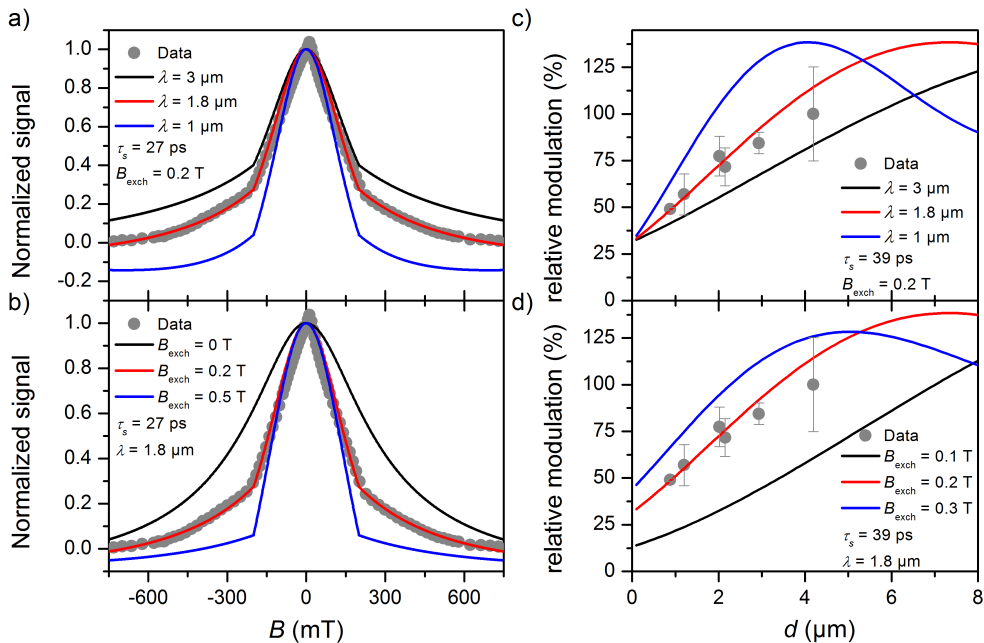


Figure 4.14: Influence of the spin relaxation length and exchange field on the Hanle spin precession and spin signal modulation. The derived model is used to fit experimental results. The circles represent the experimental results and solid lines the model curves for different parameters. a) – b) Fitting of the Hanle curves from Figures 4.3c – 4.3d. c) – d) Fitting of the relative modulation derived from Figure 4.12.

Lastly, we fit the Hanle spin precession data when the direction of applied field is fixed along the x -axis, within the sample plane but perpendicular to the easy-axis of the contact magnetization (Figure 4.15a). Due to smaller in-plane shape anisotropy compared to out-of-plane, we take the rotation of the contact magnetization in-plane into account. While the out-of-plane saturation field is around 1.2 T, the in-plane saturation field along the x -axis is between 100 mT – 200 mT, leading to a deviation of the direction of the injected spins relative to the y -axis. The contact magnetization and, therefore, the spin accumulation is calculated with an easy axis magnetic anisotropy model using the saturation field of the contact magnetization as an additional parameter. With the previously obtained values $\lambda \sim 1.8 \mu\text{m}$ and $|B_{\text{exch}}| \sim 0.2 \text{ T}$ we can qualitatively fit the measured dependencies with $\tau_s \sim 15 \text{ ps}$ and a contact saturation field of 140 mT. It implies that above 140 mT both contact magnetizations and the YIG magnetization are aligned with the external magnetic field, leading to a maximum spin signal. However, we find a further increase of the spin signal of unknown origin when applying magnetic fields up to 7 T (Figure 4.15b).

4

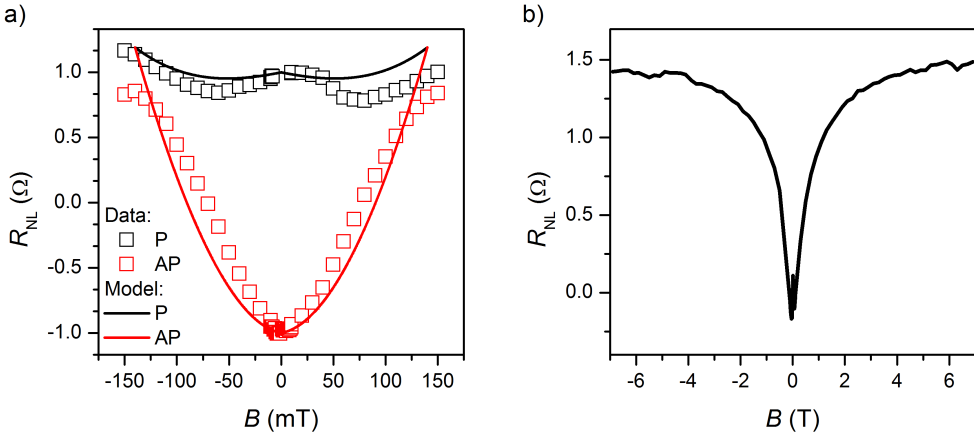


Figure 4.15: a) Hanle spin precession curves with the magnetic field applied in-plane along the x -axis for parallel (black squares) and antiparallel (red squares) alignments fitted with the model (solid lines). b) Measurement of the spin signal up to 7 T.

4.6.10 Absence of a Parallel Magnon Transport Channel

As shown by Cornelissen et al. [25] and Goennenwein et al. [26], a spin accumulation induced in a material in proximity with YIG can excite a magnon current in the FMI, leading to a parallel spin transport channel from the injector to the detector. We can exclude the existence of an additional spin transport channel in our graphene/YIG system, since the magnon transport process is suppressed at low temperatures [26],

while we find an increase of the spin signal, confirming that the signal is not carried by magnons.

References

- [1] W. Han, R.K. Kawakami, M. Gmitra, and J. Fabian. Graphene spintronics. *Nature Nanotechnology*, **9**(10), 794, 2014.
- [2] S. Roche, J. Åkerman, B. Beschoten, J.-C. Charlier, M. Chshiev, S.P. Dash, B. Dlubak, J. Fabian, A. Fert, M.H.D. Guimarães, F. Guinea, I. Grigorieva, C. Schönenberger, P. Seneor, C. Stampfer, S.O. Valenzuela, X. Waintal, and B.J. van Wees. Graphene spintronics: the European Flagship perspective. *2D Materials*, **2**(3), 030202, 2015.
- [3] R.R. Nair, M. Sepioni, I-L. Tsai, O. Lehtinen, J. Keinonen, A.V. Krasheninnikov, T. Thomson, A.K. Geim, and I.V. Grigorieva. Spin-half paramagnetism in graphene induced by point defects. *Nature Physics*, **8**(3), 199, 2012.
- [4] K.M. McCreary, A.G. Swartz, W. Han, J. Fabian, and R.K. Kawakami. Magnetic Moment Formation in Graphene Detected by Scattering of Pure Spin Currents. *Physical Review Letters*, **109**(18), 186604, 2012.
- [5] A.J.M. Giesbers, K. Uhlířová, M. Konečný, E.C. Peters, M. Burghard, J. Aarts, and C.F.J. Flipse. Interface-Induced Room-Temperature Ferromagnetism in Hydrogenated Epitaxial Graphene. *Physical Review Letters*, **111**(16), 166101, 2013.
- [6] O.V. Yazyev and L. Helm. Defect-induced magnetism in graphene. *Physical Review B*, **75**(12), 125408, 2007.
- [7] J. Baringhaus, M. Ruan, F. Edler, A. Tejada, M. Sicot, A. Taleb-Ibrahimi, A.-P. Li, Z. Jiang, E.H. Conrad, C. Berger, C. Tegenkamp, and W.A. de Heer. Exceptional ballistic transport in epitaxial graphene nanoribbons. *Nature*, **506**(7488), 349, 2014.
- [8] G.Z. Magda, X. Jin, I. Hagymási, P. Vancsó, Z. Osváth, P. Nemes-Incze, C. Hwang, L.P. Biró, and L. Tapasztó. Room-temperature magnetic order on zigzag edges of narrow graphene nanoribbons. *Nature*, **514**(7524), 608, 2014.
- [9] Z. Wang, C. Tang, R. Sachs, Y. Barlas, and J. Shi. Proximity-Induced Ferromagnetism in Graphene Revealed by the Anomalous Hall Effect. *Physical Review Letters*, **114**(1), 016603, 2015.
- [10] Y.G. Semenov, K.W. Kim, and J.M. Zavada. Spin field effect transistor with a graphene channel. *Applied Physics Letters*, **91**(15), 153105, 2007.
- [11] H. Haugen, D. Huertas-Hernando, and A. Brataas. Spin transport in proximity-induced ferromagnetic graphene. *Physical Review B*, **77**(11), 115406, 2008.
- [12] H. Yang, A. Hallal, D. Terrade, X. Waintal, S. Roche, and M. Chshiev. Proximity Effects Induced in Graphene by Magnetic Insulators: First-Principles Calculations on Spin Filtering and Exchange-Splitting Gaps. *Physical Review Letters*, **110**(4), 046603, 2013.
- [13] A.G. Swartz, P.M. Odenthal, Y. Hao, R.S. Ruoff, and R.K. Kawakami. Integration of the ferromagnetic insulator EuO onto graphene. *ACS Nano*, **6**(11), 10063, 2012.
- [14] P. Wei, S. Lee, F. Lemaitre, L. Pinel, D. Cutaia, W. Cha, F. Katmis, Y. Zhu, D. Heiman, J. Hone, J.S. Moodera, and C.-T. Chen. Strong interfacial exchange field in the graphene/EuS heterostructure. *Nature Materials*, **15**(7), 711, 2016.
- [15] J.B.S. Mendes, O. Alves Santos, L.M. Meireles, R.G. Lacerda, L.H. Vilela-Leão, F.L.A. Machado, R.L. Rodríguez-Suárez, A. Azevedo, and S.M. Rezende. Spin-Current to Charge-Current Conversion and Magnetoresistance in a Hybrid Structure of Graphene and Yttrium Iron Garnet. *Physical Review Letters*, **115**(22), 226601, 2015.
- [16] A. Hallal, F. Ibrahim, H.X. Yang, S. Roche, and M. Chshiev. Tailoring magnetic insulator proximity effects in graphene: first-principles calculations. *2D Materials*, **4**(2), 025074, 2017.

- [17] F.J. Jedema, H.B. Heersche, A.T. Filip, J.J.A. Baselmans, and B.J. van Wees. Electrical detection of spin precession in a metallic mesoscopic spin valve. *Nature*, **416**(6882), 713, 2002.
- [18] M. Popinciuc, C. Józsa, P.J. Zomer, N. Tombros, A. Veligura, H.T. Jonkman, and B.J. van Wees. Electronic spin transport in graphene field-effect transistors. *Physical Review B*, **80**(21), 214427, 2009.
- [19] N. Tombros, C. Jozsa, M. Popinciuc, H.T. Jonkman, and B.J. van Wees. Electronic spin transport and spin precession in single graphene layers at room temperature. *Nature*, **448**(7153), 571, 2007.
- [20] M.H.D. Guimarães, P.J. Zomer, J. Ingla-Aynés, J.C. Brant, N. Tombros, and B.J. van Wees. Controlling Spin Relaxation in Hexagonal BN-Encapsulated Graphene with a Transverse Electric Field. *Physical Review Letters*, **113**(8), 086602, 2014.
- [21] T. Maassen, I.J. Vera-Marun, M.H.D. Guimarães, and B.J. van Wees. Contact-induced spin relaxation in Hanle spin precession measurements. *Physical Review B*, **86**(23), 235408, 2012.
- [22] S.P. Dash, S. Sharma, J.C. Le Breton, J. Peiro, H. Jaffrès, J.-M. George, A. Lemaître, and R. Jansen. Spin precession and inverted Hanle effect in a semiconductor near a finite-roughness ferromagnetic interface. *Physical Review B*, **84**(5), 054410, 2011.
- [23] E. Villamor, M. Isasa, S. Vélez, A. Bedoya-Pinto, P. Vavassori, L.E. Hueso, F. Sebastián Bergeret, and F. Casanova. Modulation of pure spin currents with a ferromagnetic insulator. *Physical Review B*, **91**(2), 020403, 2015.
- [24] F.K. Dejene, N. Vlietstra, D. Luc, X. Waintal, J. Ben Youssef, and B.J. van Wees. Control of spin current by a magnetic YIG substrate in NiFe/Al nonlocal spin valves. *Physical Review B*, **91**(10), 100404, 2015.
- [25] L.J. Cornelissen, J. Liu, R.A. Duine, J. Ben Youssef, and B.J. van Wees. Long-distance transport of magnon spin information in a magnetic insulator at room temperature. *Nature Physics*, **11**(12), 1022, 2015.
- [26] S.T.B. Goennenwein, R. Schlitz, M. Pernpeintner, K. Ganzhorn, M. Althammer, R. Gross, and H. Huebl. Non-local magnetoresistance in YIG/Pt nanostructures. *Applied Physics Letters*, **107**(17), 172405, 2015.

Chapter 5

Efficient Bias-Dependent Spin Injection into Graphene on YIG through Bilayer hBN Tunnel Barriers

Published in Physical Review B 98(12), 125422, 2018

Abstract

We study the spin injection efficiency into single and bilayer graphene on the ferrimagnetic insulator Yttrium-Iron-Garnet (YIG) through an exfoliated tunnel barrier of bilayer hexagonal boron nitride (hBN). The contacts of two samples yield a resistance-area product between 5 and 30 $k\Omega\mu\text{m}^2$. Depending on an applied DC bias current, the magnitude of the non-local spin signal can be increased or suppressed below the noise level. The differential spin injection efficiency reaches values from -60% to $+25\%$. The results are confirmed with both spin valve and spin precession measurements. The proximity induced exchange field is found in single layer graphene on YIG to be (85 ± 30) mT and in bilayer graphene on YIG close to the detection limit. Our results show that the exceptional spin injection properties of bilayer hBN tunnel barriers reported by Gurram et al. [Nature Communications 8, 248 (2017)] are not limited to fully encapsulated graphene systems but are also valid in graphene/YIG devices. This further emphasizes the versatility of bilayer hBN as an efficient and reliable tunnel barrier for graphene spintronics.

5.1 Introduction

The combination of graphene with other two-dimensional layered materials is an elegant way to create atomically thin devices with adjustable properties [1–3]. The crystalline insulator hexagonal boron nitride is an appealing material for the field of graphene spintronics [4]. Its atomic flatness and sufficiently strong van der Waals interaction with graphene allows the fabrication of heterostructures of 2D materials with minimized contamination, implying good spin transport properties. A long spin diffusion length of 30 μm has been experimentally achieved in graphene where a bulk flake of hBN was used as protective layer to avoid contamination during the fabrication process [5]. Therefore, the use of hBN as a pinhole free tunnel barrier is straightforward since these fully encapsulated graphene devices suggest minimized contamination and highly efficient spin transport. Several experimental studies have investigated the spin injection through tunnel barriers of exfoliated

hBN [6, 7] and large scale hBN grown via chemical vapor deposition [8–11]. However, the experimentally demonstrated spin transport lengths are still far below the values suggested by the low intrinsic spin orbit coupling of graphene [12].

Having graphene in proximity to magnetic materials is a novel approach to tune the intrinsic properties of graphene. Magnetic graphene is characterized by the induced exchange field [13–18]. First principle calculations of idealized systems predict an exchange splitting of the graphene spin states to exceed several tens of meV [19, 20]. However, the experimentally demonstrated exchange fields [13, 14, 21] are still several orders of magnitude below, which can indicate either an imperfect [22] or a non-epitaxial interface between graphene and YIG or both.

The realization of graphene devices with a large exchange field requires the tackling of several challenges. The cleanliness of the interface between graphene and YIG is crucial to obtain a strong exchange effect as indicated by the discrepancy between experimentally achieved values and theoretical predictions. Furthermore, the interface and tunnel barrier between the graphene flake and contacts are crucial for the injection of a large spin accumulation and the observation of large spin signals. In our previous works we employed tunnel barriers of oxidized titanium or aluminum to overcome the conductivity mismatch problem [23, 24]. For these types of tunnel barrier the magnitude of the spin signal is limited by pinholes and resulted in a relatively small spin signal of mostly less than 1Ω , which often did not exceed the electrical noise of the measured signals in the sample. In addition, the contamination arising from the PMMA-based fabrication procedure affects the graphene cleanliness negatively. For this study we replace the Al_2O_3 or TiO_2 tunnel barrier with a bilayer-hBN (2L-hBN) flake, which significantly improves the sample quality and spin signal. Furthermore, we confirm the tunable spin injection reported by Gurram et al. [25] for the graphene/YIG system. While the origin of the DC bias dependence is still unclear, recent reports exclude local gating underneath the contact and carrier drift [26, 27].

5.2 Sample Preparation and Contact Characterization

Thin hBN flakes are exfoliated from hBN crystals (HQ Graphene) onto 90 nm SiO_2 wafers. The thickness of the flakes is estimated through their optical contrast, which is calibrated by atomic force microscopy. In our microscope (Zeiss Axio Imager.A2m with an EC Epiplan-Neofluar 100x/0.9 objective) 2L-hBN corresponds to 2.5% contrast in the green channel. Suitable 2L-hBN flakes are picked up by using a dry polycarbonate-based transfer method [28] and combined with single layer graphene (Sample A) or bilayer graphene (Sample B) exfoliated from HOPG crystals (ZYB grade, HQ Graphene). The stack is placed on a cleaned $12 \mu\text{m}$ YIG grown by liquid phase epitaxy (LPE) on a $600 \mu\text{m}$ gadolinium-gallium-garnet substrate (Matesy

GmbH). Before the transfer, the YIG substrate for Sample A is treated with oxygen plasma to remove organic contaminants and annealed in a 500°C furnace in an oxygen atmosphere prior to the transfer of the graphene/2L-hBN stack. The substrate of Sample B underwent an additional argon plasma treatment before the annealing step.

The polycarbonate is dissolved in chloroform and the 2L-hBN/graphene/YIG stack is cleaned in acetone, isopropanol and sequent annealing for one hour at 350°C in an argon-hydrogen atmosphere. Contacts are defined using a standard PMMA-based electron beam lithography process. To obtain different coercive fields and switch the electrodes independently, the width of the contacts ranges between 250 nm and 500 nm. 45 nm cobalt and a 5 nm aluminum capping layer are evaporated at pressures below 10^{-7} mbar. After the liftoff in warm acetone, the samples are loaded into a cryostat and kept in vacuum during the characterization. Unless specified, all measurements are carried out at 75 K.

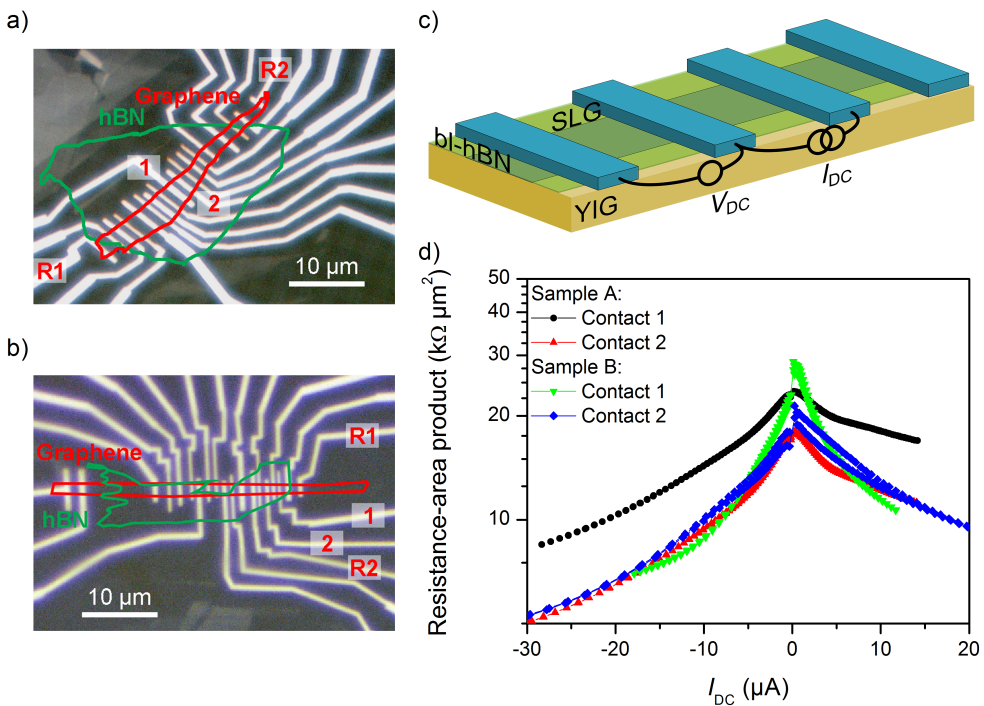


Figure 5.1: a) Optical micrograph of the Sample A. The outer electrodes (R) are not covered by 2L-hBN and used as reference electrodes in both local and non-local measurements. b) Optical micrograph of Sample B. c) Schematic measurement of the three-terminal contact resistance. d) All working contacts have a calculated resistance-area product between 5 and 30 $k\Omega\mu m^2$. The full set of IV characteristics is shown in Section 5.7.1.

After loading into the cryostat of the measurement setup, the samples are cooled down to liquid nitrogen temperature and the contacts are characterized in a three-terminal geometry (Figure 5.1c) using the outermost contacts as reference electrodes. The resistance-area product is calculated from the current-voltage characteristics and shown for Sample A in Figure 5.1d. The contacts on Sample A and Sample B, which employ a 2L-hBN tunnel barrier, yield a typical resistance-area product between 5 and 30 $\text{k}\Omega\mu\text{m}^2$, a range comparable to the one reported in Reference [25]. An hBN covered graphene Hall bar sample fabricated in parallel with Sample B for comparison yields a carrier density of $n = 5 \times 10^{12} \text{ cm}^{-2}$ and a mobility of $\mu = 5\,400 \text{ cm}^2/\text{Vs}$. We found $\mu = 720 \text{ cm}^2/\text{Vs}$ (estimated via the Shubnikov-de Haas oscillations) in our previous work [13] and conclude that the protective hBN layer significantly improves the graphene charge transport properties on YIG.

5.3 Bias-Dependent Spin Injection through Bilayer hBN Tunnel Barriers into Single and Bilayer Graphene on YIG

5

We discuss now the spin transport in graphene on YIG with a 2L-hBN tunnel barrier in a non-local geometry (Figure 5.2a). A current of $I_{AC} = 1 \mu\text{A}$ is sourced and modulated with 3.7 Hz between Contact 2 and R2. The ferromagnetic electrode injects a spin current into the graphene underneath Contact 2. These spins are diffusing along the graphene channel and are probed by a lock-in as a voltage difference V_{NL} between the detector Contact 1 and the reference electrode R1. Using this technique, we can decouple charge and spin transport. The signal can be defined as non-local resistance and calculated via $R_{NL} = V_{NL}/I_{AC}$.

To characterize the basic spin transport properties of the samples an in-plane magnetic field parallel to the electrodes (B) is applied to switch the magnetization of the injector and detector (Figure 5.2a). Depending on the relative magnetization alignment of the injector and detector electrodes, the non-local resistance changes between the parallel and the antiparallel resistance states when the contact magnetization switches. This measurement represents a characteristic spin valve behavior (Figures 5.2b and 5.2c) and gives an estimation of the spin relaxation length in the graphene flake (Figure 5.2d).

To study the effect of the bias on the spin injection, we apply a DC current additionally to the AC current sourced between injector and reference electrode (Figure 5.2a). The dielectric strength of hBN is approximately 1.2 V/nm [29]. Therefore, we limit the DC bias current for Sample A to 20 μA , which corresponds to 0.4 V – 0.6 V, depending on the IV characteristics of the injector contact. To compare differ-

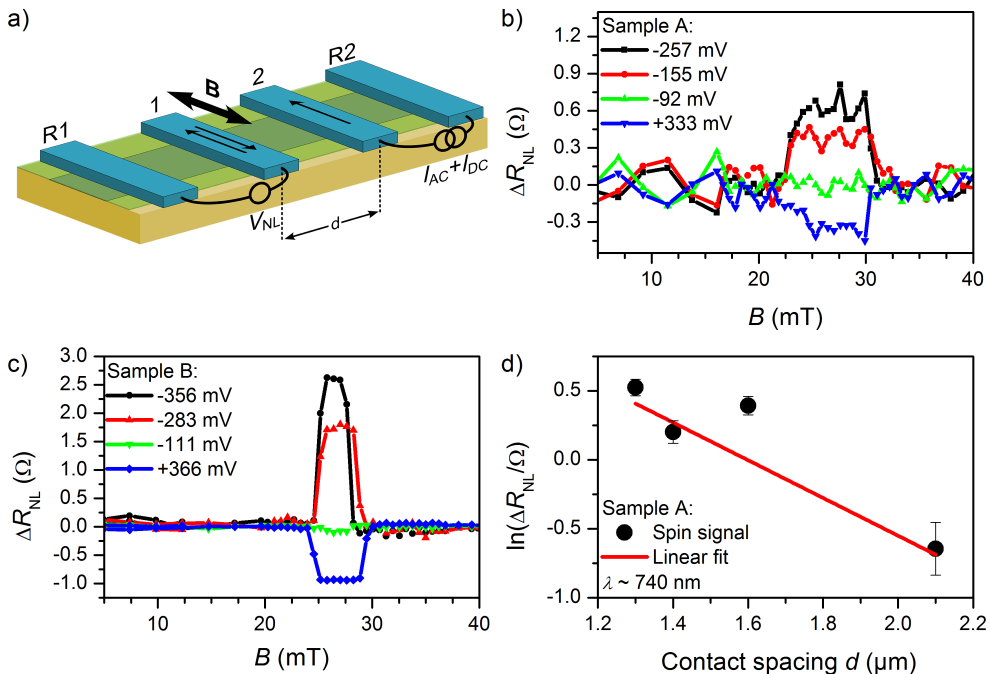


Figure 5.2: a) Schematic setup for a non-local spin valve measurement. b) Non-local spin valve measurements of Sample A (2L-hBN/graphene, $\lambda \sim 740$ nm). The size of the switch between parallel and antiparallel states of Contact 1 and Contact 2 can be tuned with the applied DC bias and is shown for four different values. c) Sample B (2L-hBN/2L-graphene, $\lambda \sim 2.3$ μm) shows a comparable dependence on the applied DC bias. Note that the spin signal changes sign around -92 mV. d) The distance-dependent spin valve measurements of Sample A allow the estimation of the spin relaxation length from the slope of the linear fit. The same analysis for Sample B is discussed in Section 5.7.2.

ent contacts, we calculate the equivalent voltage V_{hBN} across the hBN tunnel barrier from the applied DC bias current and discuss all results plotted as function of V_{hBN} .

Figure 5.2b contains the spin valve measurements of Sample A for four different DC bias currents over distance $d = 1.6$ μm . While no spin signal above noise level is visible at -92 mV, a DC bias current of $+333$ mV results in a clear switching between parallel and antiparallel states with a spin signal of approximately 0.4 Ω . Beyond -92 mV, we find an inverted sign of the non-local resistance switching and a spin signal of -0.4 Ω at -155 mV and -0.7 Ω at -257 mV. Four spin valve measurements of Sample B are shown in Figure 5.2c. where we find compared to Sample A a larger spin signal of up to -2.5 Ω at -356 mV DC bias. The change of the sign of the spin signal occurs in Sample B also between -100 mV and 0 mV, a similar range

as in the measurements on Sample A. The distance-dependence of the spin signal is shown for Sample A in Figure 5.2d, from which we extract the spin relaxation length $\lambda \sim (740 \pm 570)$ nm. In our previous work we found a comparable value of $\lambda = (490 \pm 40)$ nm for a not hBN protected sample. We conclude that even though the charge transport properties have improved significantly, the spin transport parameters remain similar. The same analysis was applied to Sample B, where we found $\lambda \sim (2.3 \pm 1)$ μm (Section 5.7.2). The 2L-hBN tunnel barriers in Figure 5.2d show a less clear trend in the distance-dependence, resulting in a larger error in λ . We can attribute this to two origins: an inhomogeneity of the 2L-hBN tunnel barriers and an inhomogeneity in the graphene flake. Microscopic cracks in the hBN tunnel barrier could arise during the fabrication and could lead to a different spin polarization of each contact. This interpretation is also supported by the considerable spread of the resistance-area product of between $5 \text{ k}\Omega\mu\text{m}^2$ to $30 \text{ k}\Omega\mu\text{m}^2$. As a consequence, the values for the spin relaxation length extracted from the distance-dependent measurements can only be seen as approximation. However, the consistency with the spin precession measurements as discussed in the following sections confirms the validity of the estimation.

5

To extract the DC bias-dependence of the spin injection polarization in the cobalt/2L-hBN/graphene/YIG system, we align the magnetization of injector and detector parallel or antiparallel and sweep the DC bias current. $\Delta R_{\text{NL}} = R_{\text{NL}}(\text{P}) - R_{\text{NL}}(\text{AP})$ is calculated and yields the pure spin signal of Sample A and Sample B shown in Figures 5.3a and 5.3b. For comparison, both curves are plotted as a function of V_{hBN} . While both positive and negative DC biases lead to an enhanced spin injection, a sign change at approximately -80 mV is observed. To extract the bias-dependence of the spin injection polarization, we use the unbiased non-local spin signals to calculate the average differential spin polarization ($\sqrt{p_{\text{in}} \cdot p_{\text{det}}}$) of injector (p_{in}) and detector (p_{det}). This assumption is justified by the similar shape of the non-local resistances in Figures 5.3a and 5.3b, when injector and detector contacts are swapped. This suggests a similar behavior of both contacts. We can extract the differential spin polarization via:

$$p_{\text{in}} \cdot p_{\text{det}} = \frac{\Delta R_{\text{NL}} \cdot w}{R_{\text{sq}} \cdot \lambda} e^{-d/\lambda}, \quad (5.1)$$

where ΔR_{NL} the spin signal, w the width of the flake, R_{sq} the square resistance, λ the spin relaxation length and d the injector to detector distance measured from the centers. Under the assumption that $p_{\text{in}} = p_{\text{det}}$ we obtain an unbiased spin polarization of 14.65% for Sample A and 10.86% for Sample B. Because we apply the DC bias only to the injector contact, the spin polarization of the detector remains constant and can be used to extract the dependence of the differential spin injection polarization on the DC bias. We note that the feature of Sample A around zero DC bias does not

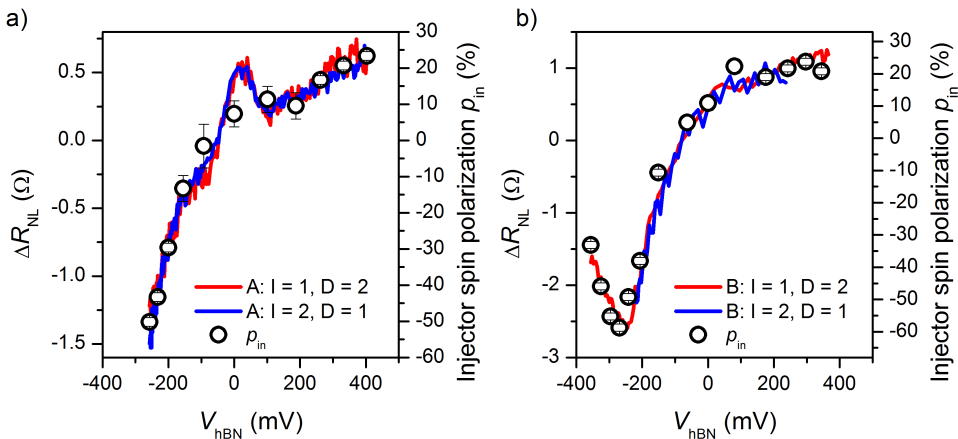


Figure 5.3: Non-local spin transport in a) Sample A and b) Sample B for different DC bias voltages. For comparison, the dependence is shown as a function of the bias voltage applied across the hBN barrier. The blue and red curves correspond to the configuration where detector and biased injector contacts are swapped. The differential spin polarization p_{in} on the right side of both panels is extracted from the independently measured spin valves.

appear on all contacts on Sample A (3 out of 5) and does not appear on Sample B (see Figure 5.8).

5.4 Bias-Dependent Spin Precession Measurements and Estimation of the Proximity-Induced Exchange Field in Bilayer hBN/Graphene on YIG

To estimate the strength of the induced exchange field, we apply and rotate a small magnetic field ($B = 15$ mT) in the sample plane (Figure 5.4a). The low in-plane coercive field of the YIG films allows us to rotate the YIG magnetization and simultaneously the proximity-induced exchange field while leaving the magnetization of the cobalt injector and detector remain unaffected. The resulting modulation of the non-local resistance is a direct consequence of $B + B_{exch}$ and can be only explained by the presence of such [13, 14].

The analysis of this effect gives us an estimate for the strength of the exchange field and allows us the fitting of the Hanle curves to extract further spin transport parameters. The higher order oscillations that remain in the symmetrized data in Figure 5.4b could indicate the presence of local stray fields of the cobalt contacts influencing the local YIG magnetization or an anisotropy arising from the shape of

the YIG substrate which might not be fully aligned with the applied magnetic field of 15 mT. Therefore, we apply a smoothing on the data. The resulting curve is shown in red. We estimate the modulation to be $(11 \pm 5)\%$ over $d = 1.6 \mu\text{m}$, which, given the uncertainty arising from the smoothing process, should be seen as a rather rough approximation. Despite the uncertainty of the exact value of the modulation, the angular-dependence indicates the presence of an exchange field in the sample.

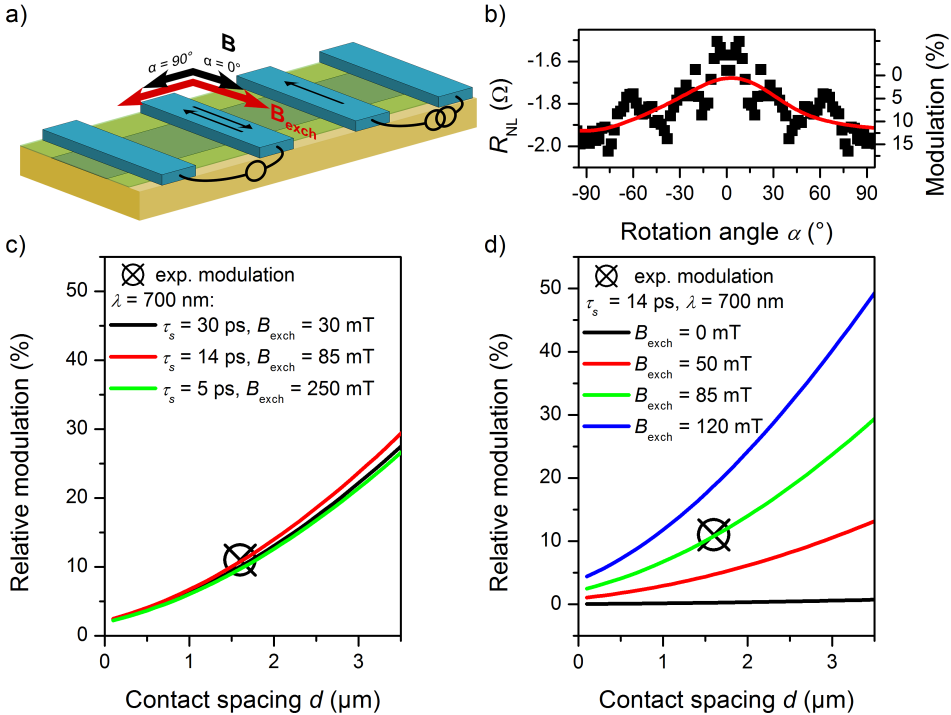


Figure 5.4: Modulation of spin transport with the exchange field in Sample A. a) Schematics of the experiment. B is rotating the YIG magnetization and the exchange field B_{exch} in the sample plane while leaving the electrodes and injected spins unaffected. b) The angle-dependence of the non-local resistance is measured at $T = 10$ K and $-20 \mu\text{A}$ DC bias in parallel and antiparallel alignment. The extracted spin signal is symmetrized. As a guide to the eye the smoothed data is shown in red, from which we estimate a relative modulation of 11%. c) Fitting of the experimental relative modulation of 11% with our model using τ_s and B_{exch} as fitting parameters. $\lambda = 700$ nm and $B = 15$ mT are fixed parameters. d) Relative modulation of the spin signal calculated from the model using best fit parameters $\tau_s = 14$ ps and $\lambda = 700$ nm, obtained as shown in Figure 5.5. B_{exch} is varied as indicated, and $B = 15$ mT.

Using the model reported in Leutenantsmeyer et al. [13] we can simulate the modulation of a spin current by exchange field-induced precession. To estimate the magnitude of the exchange field leading to 11% modulation, we use $\lambda = 700$ nm

(Figure 5.2d) and assume τ_s to be between 5 ps and 30 ps, a common range for our single layer graphene devices on YIG. To match the experimental modulation, an exchange field between 30 mT and 250 mT is required (Figure 5.4c). To determine the exact value of τ_s , we use the parameter pairs of τ_s and B_{exch} to fit, as discussed later, the spin precession measurements in Figure 5.5a. By comparing both, we find that the both measurement sets can only be fit consistently with $\tau_s = 14$ ps and $B_{\text{exch}} = 85$ mT.

Figure 5.4d contains the modulation caused by the combination of the applied magnetic field of 15 mT and different values for the exchange field. The expected relative modulation caused by an applied magnetic field of 15 mT with $\lambda = 700$ nm and $\tau_s = 14$ ps does not exceed 0.5%, whereas the observed modulation is clearly larger. To fit the experimentally found modulation of 11%, we have to assume $B_{\text{exch}} = 85$ mT. This is a strong indication for the presence of an exchange field in this device. We can conclude that within the uncertainty range of the relative modulation of $(11 \pm 5)\%$, the exchange field in Sample A is (85 ± 35) mT.

The Hanle measurements are carried out in parallel and antiparallel alignment of the injector (Contact 1) and detector (Contact 2), see Figure 5.2a for the contact labeling. We extract the spin signal by calculating $[R_{\text{NL}}(\text{P}) - R_{\text{NL}}(\text{AP})]/2$, shown in Figure 5.5a. From the Hanle fit using an exchange field of 85 mT, we extract the differential spin polarization of the injector p_{in} (Figure 5.5b), the spin diffusion coefficient D_s (Figure 5.5c) and the spin diffusion time τ_s (Figure 5.5d). While $D_s = (350 \pm 65)$ cm²/s and $\tau_s = (16 \pm 5)$ ps remain approximately constant over the applied DC bias range we find a dependence of the differential injector spin polarization that resembles the DC bias-dependence of the injector (Figure 5.3a), which implies a consistency in the analysis. Using the spin diffusion coefficient D_s and time τ_s extracted from the Hanle measurements, we can calculate the spin relaxation length $\lambda = \sqrt{D_s \tau_s} = (730 \pm 230)$ nm. When compared to the estimation from the distance-dependent spin valve measurements (Figure 5.2a) both approaches yield similar values which indicates again the consistency of the analysis.

Note that the rather smooth Hanle curves shown in Figure 5.5a could be also fit with a conventional spin precession model that does not include any exchange field. These fittings yield $\tau_s \sim 25$ ps, $D_s \sim 800$ cm²/s and $\lambda \sim 1.4$ μm . Apart from D_s being unrealistically large, the extracted λ is two times larger than the result from the independently measured distance-dependent spin valves (Figure 5.2d) which suggests that the fit of our results with the conventional model is unreliable. Furthermore, if we want to fit the modulation in Figure 5.4b with $\lambda = 1.4$ μm and $\tau_s = 25$ ps, an exchange field of ~ 60 mT would be required to match the data, even though the Hanle fitting did not include any B_{exch} . In return, the parameter sets that match 11% modulation do not fit the spin precession measurements unless the values are close to $\lambda = 700$ nm, $\tau_s = 14$ ps and $B_{\text{exch}} = 85$ mT. In conclusion, this analysis underlines

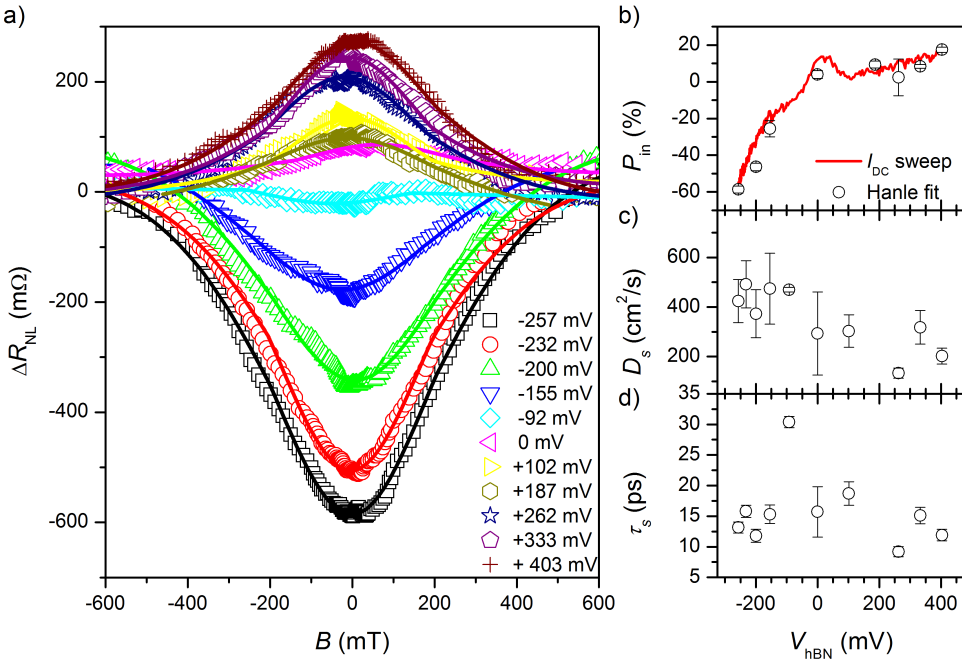


Figure 5.5: Spin precession measurements in Sample A: a) The Hanle spin precession curves from Sample A are fit using our exchange model with $B_{\text{exch}} = 85$ mT (solid lines) for different DC bias currents. Contact 1 is used as injector, Contact 2 as detector (Figure 5.2a). We extract b) the calculated differential spin polarization the injector (p_{in}), c) the spin diffusion coefficient D_s and d) the spin diffusion time τ_s . The DC bias-dependence of p_{in} shows a similar dependence as (red line in panel b, Figure 5.3d).

the relevance to carry out both, angular modulation of R_{NL} and Hanle precession experiments, to characterize the exchange field strength.

5.5 Bias-Dependent Spin Precession in Bilayer hBN/Bi-layer Graphene on YIG

In comparison to Sample A, Sample B is fabricated with a bilayer graphene flake. The extraction of the spin relaxation length via distance-dependent spin valve measurements is done in a similar way as for Sample A and is shown in Figure 5.9. We extract $\lambda = (2.3 \pm 1)$ μm . The modulation of the non-local resistance by rotating the exchange field in the sample plane is shown in Figure 5.6a. The parallel (red) and antiparallel (black) data is measured at 10 K and -366 mV DC bias. The solid line is the smoothed data and used to estimate the relative modulation of the spin signal

after subtraction of the parallel and antiparallel data which results in a modulation of 8%.

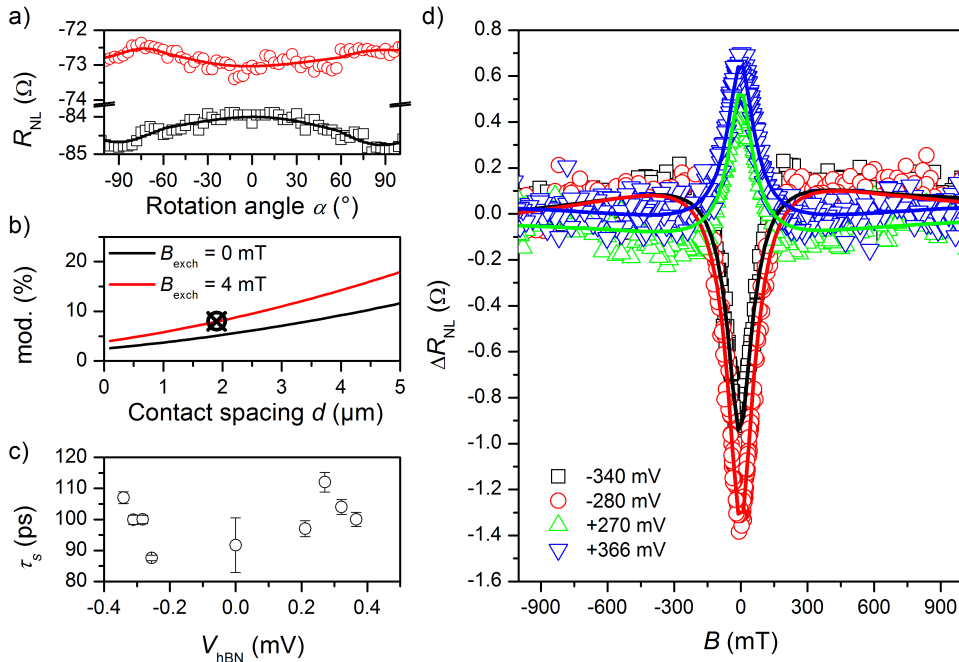


Figure 5.6: a) The non-local resistance can be modulated by 8% by rotating an in-plane magnetic field of 15 mT. The solid lines are smoothed and a guide to the eye. The red line is measured in parallel alignment, the black line in antiparallel configuration. b) Modeling of the 8% modulation with the spin transport parameters of $\lambda = 2.3$ μm and $\tau_s = 100$ ps. The black curve represents the modulation by the applied magnetic field of 15 mT in the absence of an exchange field, the red curve adds an exchange field of 4 mT. c) The spin relaxation time τ_s extracted from the Hanle data in panel d. d) The Hanle spin precession curves of Sample B with the fitting curves (lines) for different DC bias currents. The spin relaxation length of $\lambda = 2.3$ μm is used as parameters for the fitting.

To estimate the exchange field causing this precession, we use $\lambda = 2.3$ μm extracted for Sample B from the distance-dependent measurements and assume $\tau_s = 100$ ps, which is later confirmed by the Hanle spin precession measurements. In this particular case, the modulation of the applied magnetic field of 15 mT (black line, Figure 5.6d) already induces a modulation close to the experimentally found one. To match the data, a small exchange field of only 4 mT would be required, leading us to the conclusion that in this device most likely no exchange interaction is present.

Using the Hanle spin precession data, we also extract $\lambda = 2.3$ μm with a negligible exchange field. We find consistently over all biases a spin diffusion time of

$\tau_s = (100 \pm 8)$ ps and a spin diffusion coefficient of $D_s = \lambda^2/\tau_s = (530 \pm 40)$ cm²/s, which resembles the values used for the modulation fit and indicates consistency throughout our analysis of the spin transport. The possible absence of the exchange field in Sample B stresses the importance of the graphene/YIG interface of these devices. This observation could be also explained with a different proximity effect on each of the two bilayer graphene layers. Nevertheless, Sample B shows a similar dependence on the applied DC bias as Sample A and shows that the tunable spin injection is also present in the 2L-hBN/2L-graphene/YIG system.

5.6 Conclusion

We have studied the spin injection through 2L-hBN tunnel barriers into single and bilayer graphene on YIG, showing a more reliable and efficient spin injection compared to TiO₂ tunnel barriers. The 2L-hBN tunnel barriers yield a resistance-area product between 5 kΩμm² and 30 kΩμm² and the differential spin injection polarization is found to be tunable through a DC bias current applied to the injector. We observe a sign inversion at approximately −80 mV DC bias applied across the 2L-hBN flake. We estimate the proximity-induced exchange field through in-plane and out-of-plane spin precession measurements to be around 85 mT in Sample A and likely to be absent in Sample B. The low magnitude of the exchange field compared to theoretical predictions emphasizes the importance of the graphene/YIG interface on the proximity-induced exchange field and confirms our previously reported low exchange strength for graphene/YIG devices. Nevertheless, our results confirm the unique properties of 2L-hBN for the reliable spin injection into single and bilayer graphene on YIG and stress the importance of this type of tunnel barrier for future application in graphene spintronics.

Acknowledgements We acknowledge the fruitful discussions with J. Ingla-Aynés, and funding from the European Unions Horizon 2020 research and innovation program under Grant No. 696656 and 785219 ('Graphene Flagship' Core 1 and Core 2), the Marie Curie initial training network 'Spinograph' (Grant No. 607904) and the Spinoza Prize awarded to B.J. van Wees by the 'Netherlands Organization for Scientific Research' (NWO).

5.7 Supplementary Information

5.7.1 Full Set of the hBN Tunnel Barrier Characterization

Figure 5.7 shows the microscope images of Sample A and Sample B with all characterized contacts labeled. The contacts with a bilayer hBN tunnel barrier have a

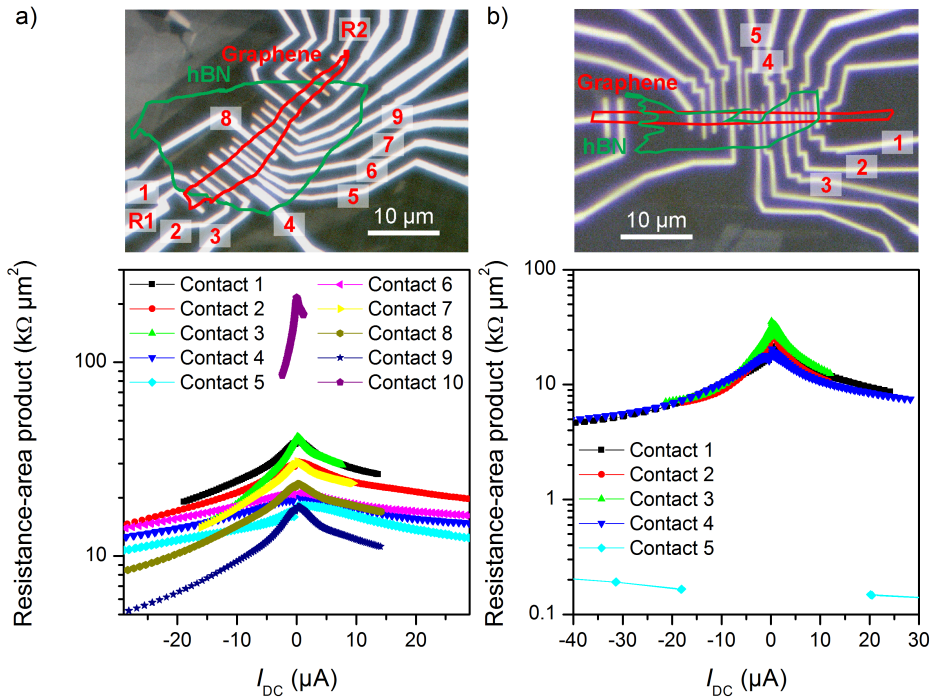


Figure 5.7: a) Optical image and full set of the contact characterization of Sample A and b) Sample B

resistance-area product between 5 and 30 $\text{k}\Omega\mu\text{m}^2$. Given the significantly higher resistance of Contact 10 of Sample A, we conclude that the thickness of the hBN flake is likely to be three layers. The extended measurements of the contacts on Sample B show a similar behavior. Contact 5 shows a linear behavior, as it can be seen in the optical image, the cobalt is in direct contact with the graphene flake.

Figure 5.8 contains the DC bias sweeps for different injector/detector combinations on Sample A. The data is obtained by aligning the injector I and the detector D parallel and antiparallel and subtracting both curves, $\Delta R_{\text{NL}}(\text{P}) - \Delta R_{\text{NL}}(\text{AP})$. Since the detection efficiency remains constant over the applied bias range, the increase of the non-local resistance corresponds to the increase of the spin injection efficiency, which is relatively homogeneous over the contacts. The first two curves are discussed in the main text.

5.7.2 Estimation of the Spin Relaxation Length in Sample B

The non-local spin signals measured at different injector to detector distances on Sample B are shown in Figure 5.9. Note that the large difference in the magnitude

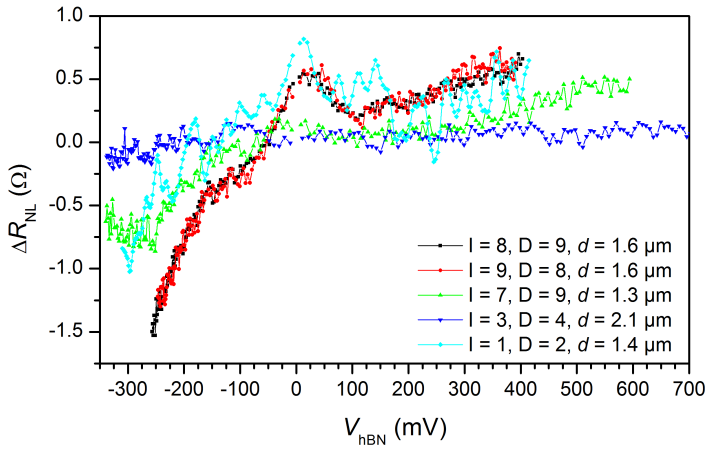


Figure 5.8: Extended measurements of DC bias sweeps on Sample A. See Figure 5.7a for the contact numbering.

5

of the spin signal indicates an either an inhomogeneous spin polarization of the contacts, possibly caused by cracks in the 2L-hBN flake, or inhomogeneous spin transport throughout the graphene channel.

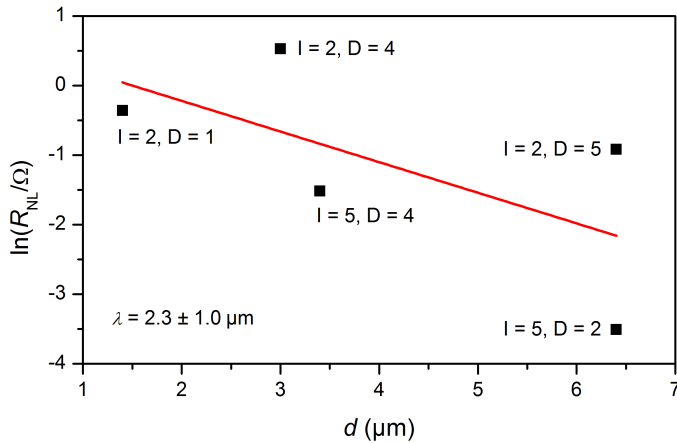


Figure 5.9: Distance-dependent measurements of the spin valves on Sample B. See Figure 5.7b for the contact numbering.

5.7.3 Origin of the Background in the Hanle Curves in Sample B

The data shown in Figure 5.6 contains only the pure spin signal between injecting and detecting electrode. The spin signal is obtained by aligning the injector and detector parallel and antiparallel and subtracting both curves. The remaining signal is in theory the purely spin-dependent signal. Spurious effects that are present in the measured signal are hereby extracted. These effects can be obtained by calculating the background signal by adding the parallel and antiparallel Hanle curves.

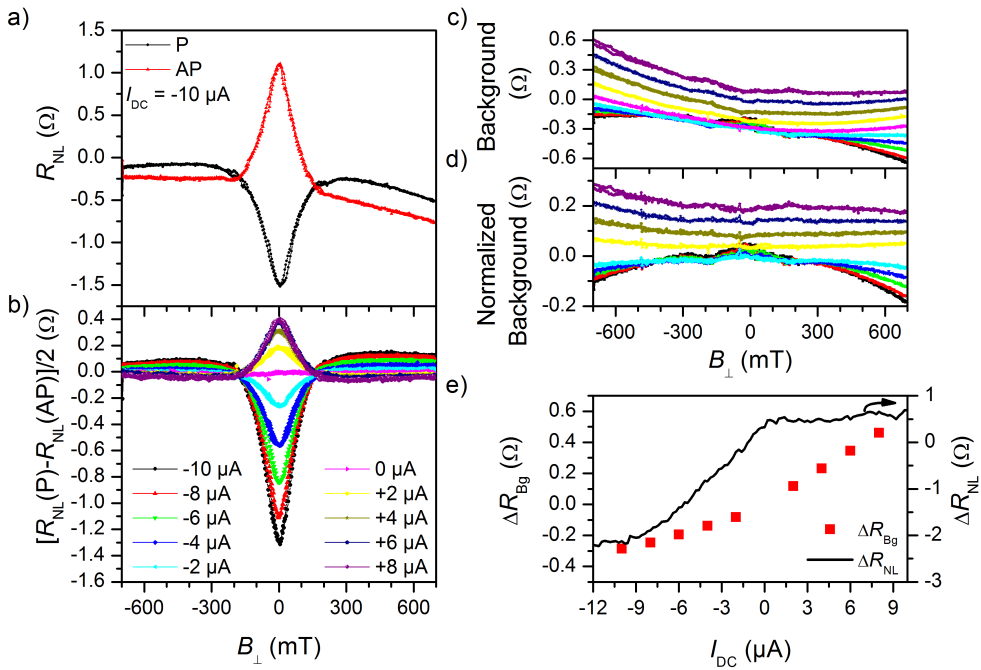


Figure 5.10: a) The raw data of the Hanle measurements on Sample B has a significant background signal that is excluded from b) the spin signal. The dependence of the background signal on the applied DC bias shown in panel c). The background signal is extracted by adding the antiparallel to the parallel Hanle curve. d) To separate the spin and charge-dependent contributions to the background signal, we subtract the data measured with the minimized spin signal (0 μA DC bias) from the individual Hanle background curves and extract the shown background signal. e) The amplitude of the Hanle background signal shows a dependence on the DC bias that roughly resembles the inverted dependence of the injector and detector electrode, which could indicate that the background signal has still a spin related contribution coming from one of the reference contacts.

In Figure 5.10a we show the measured Hanle curves, the extracted spin signal in Figure 5.10b and the extracted background signal in Figure 5.10c. Both spin and background signal show a dependence on the applied DC bias. The presence of a

spin related signal in the background signal is not expected, however, the dependence on the DC bias suggests the opposite case.

To determine the nature of the signal, we normalize the data set to the signal where the spin signal and the differential spin injection polarization is minimized, which is here the case for a DC bias of 0 μA (Figure 5.10b). This way we can separate the charge and spin-dependent signals in the background data that do not depend on the magnetization of the inner detector and injector electrodes. The resulting signal is shown in Figure 5.10c. We find a clear dependence on the applied DC bias. We suspect this signal to arise either as contribution from the current reference electrode or as the rotation of the cobalt electrodes at high magnetic fields out of the sample plane.

If we compare the signal amplitude averaged at ± 700 mT ($[R_{\text{NL}}(+700 \text{ mT}) + R_{\text{NL}}(-700 \text{ mT})]/2$), we find a dependence on the DC bias as shown by the red squares in Figure 5.10e. This slope approximately resembles that of the DC bias measurements but of opposite sign, which suggests that this signal might be actually spin related. Since the inner injector and detector signals are excluded from this data, we can identify the injector reference contact to be likely the origin. This contact is also biased with the DC current but does not have an hBN tunnel barrier. Therefore, the observation of such large signal is still surprising, especially for of the greater distance of the reference electrode to the detector of 4 μm instead of 1.9 μm . At this moment, we are unable to determine the origin of the DC bias-dependence of the background signal. Further work is needed for clarification.

References

- [1] A.K. Geim and I.V. Grigorieva. Van der Waals heterostructures. *Nature*, **499**(7459), 419, 2013.
- [2] W. Han, R.K. Kawakami, M. Gmitra, and J. Fabian. Graphene spintronics. *Nature Nanotechnology*, **9**(10), 794, 2014.
- [3] S. Roche, J. Åkerman, B. Beschoten, J.-C. Charlier, M. Chshiev, S.P. Dash, B. Dlubak, J. Fabian, A. Fert, M.H.D. Guimarães, F. Guinea, I. Grigorieva, C. Schönberger, P. Seneor, C. Stampfer, S.O. Valenzuela, X. Waintal, and B.J. van Wees. Graphene spintronics: the European Flagship perspective. *2D Materials*, **2**(3), 030202, 2015.
- [4] M. Gurram, S. Omar, and B.J. van Wees. Electrical spin injection, transport, and detection in graphene-hexagonal boron nitride van der Waals heterostructures: progress and perspectives. *2D Materials*, **5**(3), 032004, 2018.
- [5] M. Drögeler, C. Franzen, F. Volmer, T. Pohlmann, L. Banszerus, M. Wolter, K. Watanabe, T. Taniguchi, C. Stampfer, and B. Beschoten. Spin Lifetimes Exceeding 12 ns in Graphene Nonlocal Spin Valve Devices. *Nano Letters*, **16**(6), 3533, 2016.
- [6] T. Yamaguchi, R. Moriya, Y. Oki, S. Yamada, S. Masubuchi, K. Hamada, and T. Machida. Spin injection into multilayer graphene from highly spin-polarized Co_2FeSi Heusler alloy. *Applied Physics Express*, **9**(6), 063006, 2016.
- [7] M. Gurram, S. Omar, S. Zihlmann, P. Makk, C. Schönberger, and B.J. van Wees. Spin transport in fully hexagonal boron nitride encapsulated graphene. *Physical Review B*, **93**(11), 115441, 2016.

- [8] W. Fu, P. Makk, R. Maurand, M. Bräuninger, and C. Schönenberger. Large-scale fabrication of BN tunnel barriers for graphene spintronics. *Journal of Applied Physics*, **116**(7), 074306, 2014.
- [9] V.M. Kamalakar, C. Groenvelde, A. Dankert, and S.P. Dash. Long distance spin communication in chemical vapour deposited graphene. *Nature Communications*, **6**, 6766, 2015.
- [10] M.V. Kamalakar, A. Dankert, P.J. Kelly, and S.P. Dash. Inversion of Spin Signal and Spin Filtering in Ferromagnet|Hexagonal Boron Nitride-Graphene van der Waals Heterostructures. *Scientific Reports*, **6**, 21168, 2016.
- [11] M. Gurram, S. Omar, S. Zihlmann, P. Makk, Q.C. Li, Y.F. Zhang, C. Schönenberger, and B.J. van Wees. Spin transport in two-layer-CVD-hBN/graphene/hBN heterostructures. *Physical Review B*, **97**(4), 045411, 2018.
- [12] D. Huertas-Hernando, F. Guinea, and A. Brataas. Spin-orbit coupling in curved graphene, fullerenes, nanotubes, and nanotube caps. *Physical Review B*, **74**(15), 155426, 2006.
- [13] J.C. Leutenantsmeyer, A.A. Kaverzin, M. Wojtaszek, and B.J. van Wees. Proximity induced room-temperature ferromagnetism in graphene probed with spin currents. *2D Materials*, **4**(1), 014001, 2017.
- [14] S. Singh, J. Katoch, T. Zhu, K.-Y. Meng, T. Liu, J.T. Brangham, F. Yang, M.E. Flatté, and R.K. Kawakami. Strong Modulation of Spin Currents in Bilayer Graphene by Static and Fluctuating Proximity Exchange Fields. *Physical Review Letters*, **118**(18), 187201, 2017.
- [15] P. Wei, S. Lee, F. Lemaître, L. Pinel, D. Cutaia, W. Cha, F. Katmis, Y. Zhu, D. Heiman, J. Hone, J.S. Moodera, and C.-T. Chen. Strong interfacial exchange field in the graphene/EuS heterostructure. *Nature Materials*, **15**(7), 711, 2016.
- [16] Z. Wang, C. Tang, R. Sachs, Y. Barlas, and J. Shi. Proximity-Induced Ferromagnetism in Graphene Revealed by the Anomalous Hall Effect. *Physical Review Letters*, **114**(1), 016603, 2015.
- [17] P.U. Asshoff, J.L. Sambricio, A.P. Rooney, S. Slizovskiy, A. Mishchenko, A.M. Rakowski, E.W. Hill, A.K. Geim, S.J. Haigh, V.I. Fal'Ko, I.J. Vera-Marun, and I.V. Grigorieva. Magnetoresistance of vertical Co-graphene-NiFe junctions controlled by charge transfer and proximity-induced spin splitting in graphene. *2D Materials*, **4**(3), 031004, 2017.
- [18] Y. Song. Electric-field-induced extremely large change in resistance in graphene ferromagnets. *Journal of Physics D*, **51**(2), 025002, 2018.
- [19] H. Yang, A. Hallal, D. Terrade, X. Waintal, S. Roche, and M. Chshiev. Proximity Effects Induced in Graphene by Magnetic Insulators: First-Principles Calculations on Spin Filtering and Exchange-Splitting Gaps. *Physical Review Letters*, **110**(4), 046603, 2013.
- [20] A. Hallal, F. Ibrahim, H.X. Yang, S. Roche, and M. Chshiev. Tailoring magnetic insulator proximity effects in graphene: first-principles calculations. *2D Materials*, **4**(2), 025074, 2017.
- [21] M. Evelt, H. Ochoa, O. Dzyapko, V.E. Demidov, A. Yurgens, J. Sun, Y. Tserkovnyak, V. Bessonov, A.B. Rinkevich, and S.O. Demokritov. Chiral charge pumping in graphene deposited on a magnetic insulator. *Physical Review B*, **95**, 024408, 2017.
- [22] S. Pütter, S. Geprägs, R. Schlitz, M. Althammer, A. Erb, R. Gross, and S.T.B. Goennenwein. Impact of the interface quality of Pt/YIG(111) hybrids on their spin Hall magnetoresistance. *Applied Physics Letters*, **110**(1), 012403, 2017.
- [23] G. Schmidt, D. Ferrand, L.W. Molenkamp, A.T. Filip, and B.J. van Wees. Fundamental obstacle for electrical spin injection from a ferromagnetic metal into a diffusive semiconductor. *Physical Review B*, **62**(8), R4790, 2000.
- [24] E.I. Rashba. Theory of electrical spin injection: Tunnel contacts as a solution of the conductivity mismatch problem. *Physical Review B*, **62**(24), R16267, 2000.
- [25] M. Gurram, S. Omar, and B.J. van Wees. Bias induced up to 100% spin-injection and detection polarizations in ferromagnet/bilayer-hBN/graphene/hBN heterostructures. *Nature Communications*, **8**(1), 248, 2017.
- [26] J.C. Leutenantsmeyer, J. Ingla-Aynés, M. Gurram, and B.J. van Wees. Efficient spin injection into graphene through trilayer hBN tunnel barriers. *arXiv preprint*, **1808.00904**, 2018.

- [27] T. Zhu, S. Singh, J. Katoch, H. Wen, K. Belashchenko, I. Žutic, and R.K. Kawakami. Probing Tunneling Spin Injection into Graphene via Bias Dependence. *Physical Review B*, **98**(98), 054412, 2018.
- [28] P.J. Zomer, M.H.D. Guimarães, J.C. Brant, N. Tombros, and B.J. van Wees. Fast pick up technique for high quality heterostructures of bilayer graphene and hexagonal boron nitride. *Applied Physics Letters*, **105**(1), 013101, 2014.
- [29] Y. Hattori, T. Taniguchi, K. Watanabe, and K. Nagashio. Layer-by-Layer Dielectric Breakdown of Hexagonal Boron Nitride. *ACS Nano*, **9**(1), 916, 2015.

Chapter 6

Efficient Spin Injection into Graphene through Trilayer hBN Tunnel Barriers

Accepted for publication in Journal of Applied Physics

Abstract

We characterize the spin injection into bilayer graphene fully encapsulated in hBN using trilayer (3L) hexagonal boron nitride (hBN) tunnel barriers. As a function of the DC bias, the differential spin injection polarization is found to rise up to -60% at -250 mV DC bias voltage. We measure a DC spin polarization of $\sim 50\%$, 30% higher compared to 2L-hBN. The large polarization is confirmed by local, two-terminal spin transport measurements up to room temperature. We observe comparable differential spin injection efficiencies from Co/2L-hBN and Co/3L-hBN into graphene and conclude that possible exchange interaction between cobalt and graphene is likely not the origin of the bias-dependence. Furthermore, our results show that local gating, arising from the applied DC bias is not responsible for the DC bias-dependence. Carrier density-dependent measurements of the spin injection efficiency are discussed, where we find no significant modulation of the differential spin injection polarization. We also address the bias-dependence of the injection of in-plane and out-of-plane spins and conclude that the spin injection polarization is isotropic and does not depend on the applied bias.

6.1 Introduction

Graphene is an ideal material for long distance spin transport due to its low intrinsic spin-orbit coupling and outstanding electronic quality [1–5]. Experimental results have shown that long spin relaxation lengths require the protection of the graphene channel from contamination [4–7]. The most effective way to achieve this is the encapsulation of graphene with hexagonal Boron Nitride (hBN), which substantially improved the spin transport properties [5–11]. Besides of the cleanliness of the channel, the efficient injection and detection of spins into graphene is an essential requirement to fabricate high performance devices. To circumvent the conductivity mismatch problem [12], a tunnel barrier is employed to enhance the spin injection polarization [13]. While commonly used Al_2O_3 and TiO_2 tunnel barriers yield typically spin polarizations below 10% [14]. The use of crystalline MgO [15–17], hBN [18–20], amorphous carbon [21] or SrO [22] as tunnel barrier has led to significant enhancements. In particular, the use of a 2L-hBN flake for spin injection gives rise to bias-dependent differential spin injection polarizations to $p_{\text{in}} = 70\%$,

which is defined as the injected AC spin current i_s divided by the AC charge current i_{AC} . Furthermore, 2L-hBN provides contact resistances in the range of 10 k Ω , which can be close to the spin resistance of high quality graphene and affect spin transport [20]. 3L-hBN tunnel barriers promise higher contact resistances, leaving the spin transport in 3L-hBN/graphene unaffected [19, 23].

While the underlying mechanism for the DC bias-dependent spin injection is still unclear, *ab initio* calculations of cobalt separated from graphene by hBN show that in the optimal case Co can induce an exchange interaction of 10 meV even through 2L-hBN into graphene [24]. Therefore, a comparison between hBN tunnel barriers of different thicknesses can give insight on proximity effects between graphene and cobalt.

Here we show that 3L-hBN tunnel barriers increase the differential spin injection polarization into bilayer graphene (BLG) from a zero bias value of $p_{in} = 20\%$ up to values above $p_{in} = -60\%$ at -250 mV DC bias voltage. The DC spin injection polarization P_{in} , which is defined as the DC spin current I_s divided by the DC charge current I_{DC} , increases up to $P_{in} = 50\%$, at a DC bias current of -2 μ A. This is a substantial advantage over 2L-hBN, which shows $P_{in} \sim 35\%$. The large DC spin polarization allows us to measure spin signals in a DC two-terminal spin valve geometry up to room temperature. We show that the differential spin injection polarization is, contrary to Ringer et al. [25], independent of the carrier density. The rotation of the magnetization of the electrodes out-of-plane under a perpendicular magnetic field B_{\perp} allows us to study the bias-dependence of the spin injection polarization of out-of-plane spins (p_z). We compare p_z with the in-plane polarization p_y and conclude that $p_z/p_y \sim 1$, independent of the applied DC bias.

6.2 Sample Preparation and Contact Characterization

The device geometry is shown in Figure 6.1a. BLG is encapsulated between a 5 nm thick bottom hBN and a 1.2 nm thick 3L-hBN flake, which acts as a tunnel barrier. The stack is deposited on a silicon substrate with 90 nm oxide thickness, that is used as a back gate to tune the carrier concentration in the graphene channel. This device has been used to study the spin-lifetime anisotropy in BLG [26]. Unless noted, all measurements are carried out at $T = 75$ K to improve the signal to noise ratio. The atomic force microscopy image of the stack before the contact deposition is shown in Figure 6.1b. The contact resistances are characterized by measuring the bias-dependence in the three-terminal geometry, $R_c = V_{hBN}/I_{DC}$, and shown in Figure 6.2a as a function of the voltage applied across the 3L-hBN tunnel barrier (V_{hBN}). The bias-dependent contact resistances are normalized to the contact area and plotted as a function of the DC current I_{DC} applied to the hBN barrier in Figure 6.2b. To determine the spin transport properties of our device, we use the standard non-

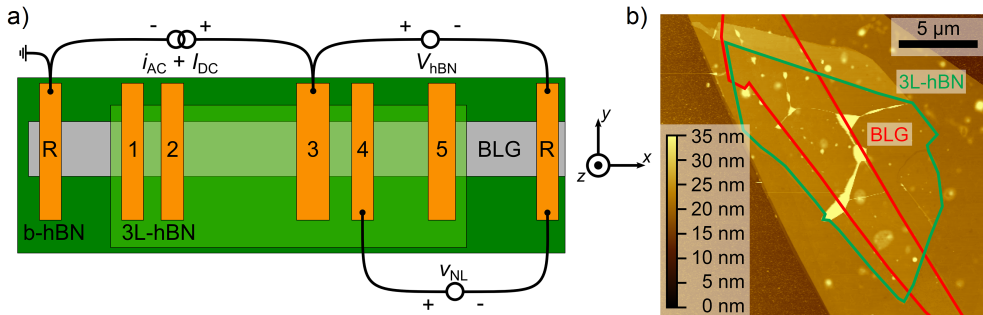


Figure 6.1: a) Schematic device geometry. A BLG flake is encapsulated between a 5 nm thick hBN (b-hBN) and a 1.2 nm 3L-hBN flake, used as a tunnel barrier for spin injection. The different measurement geometries are sketched. V_{hBN} is the DC voltage across the hBN tunnel barrier, from which the contact resistance can be calculated via $R_c = V_{\text{hBN}}/I_{\text{DC}}$. v_{NL} is the AC non-local voltage and used to calculate the non-local resistance $R_{\text{NL}} = v_{\text{NL}}/i_{\text{AC}}$. Additionally to the AC measurement current i_{AC} , a DC current I_{DC} is applied to bias the injector contact. Note that the outer reference contacts (R) do not have an hBN tunnel barrier. b) Atomic force microscopy image of the hBN/BLG/3L-hBN heterostructure before the contact deposition.

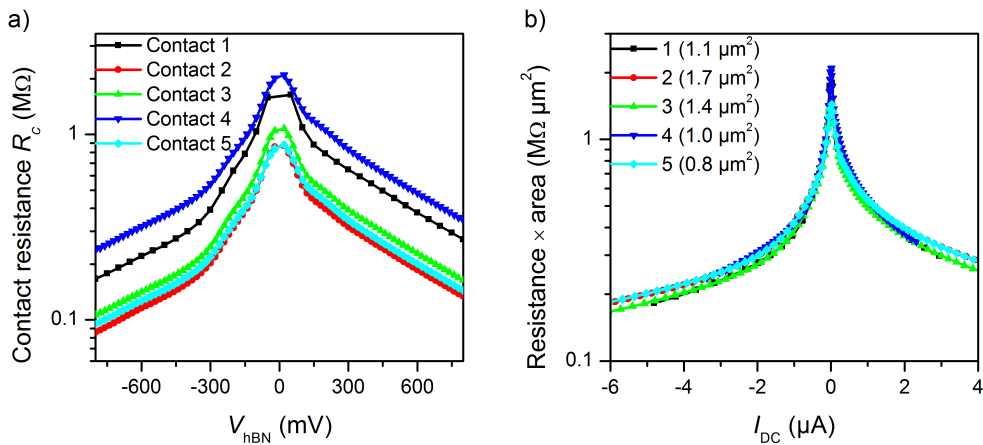


Figure 6.2: a) Contact resistance measurements for different voltages applied across the hBN tunnel barrier (V_{hBN}). b) The calculated resistance-area product ($R_c \times A$) range between 180 $\text{k}\Omega\mu\text{m}^2$ and 2 $\text{M}\Omega\mu\text{m}^2$, depending on the applied DC bias current I_{DC} .

local geometry [27–29], the circuit is indicated in Figure 6.1a. An AC charge current i_{AC} is applied together with I_{DC} between the injector and the left reference contact, which does not have any tunnel barrier and therefore does not inject spins efficiently. Because of the spin polarization of the cobalt/hBN contacts, the injected charge current is spin polarized and induces a spin accumulation into the channel. The spins

diffuse in the BLG channel and are detected by a second cobalt/hBN contact in the non-local geometry.

6.3 Spin Transport and Precession Measurements

The different coercive fields of the cobalt contacts allow the separate switching of individual electrodes with an in-plane magnetic field B_{\parallel} and the measurement of the non-local resistance ($R_{\text{NL}} = v_{\text{NL}}/i_{\text{AC}}$) in different magnetic configurations. The non-local spin valve is shown in Figure 6.3a for different DC bias currents. The abrupt signal changes are caused by the switching of the contact magnetization, the magnetization configurations are indicated with arrows. The spin signal R_{NL} is determined by the difference between parallel [$R_{\text{NL}}(\uparrow\uparrow) = R_{\text{NL}}(\downarrow\downarrow)$] and antiparallel [$R_{\text{NL}}(\uparrow\downarrow) = R_{\text{NL}}(\downarrow\uparrow)$] configurations.

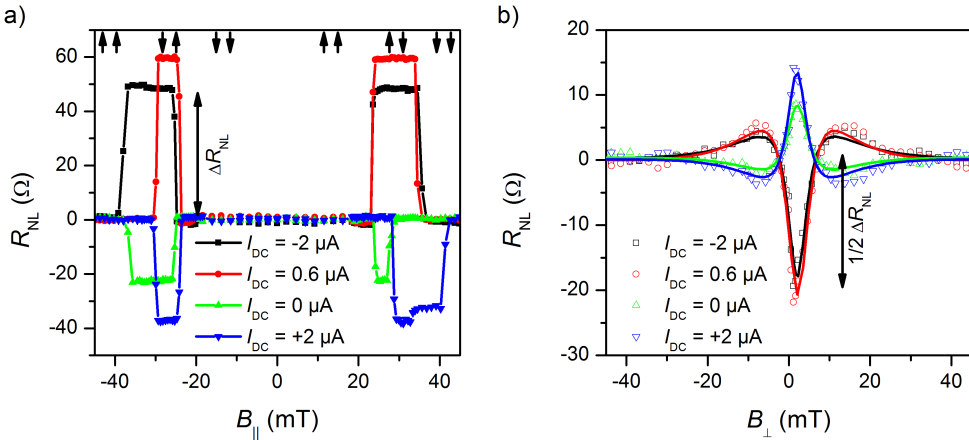


Figure 6.3: Characterization of the spin transport in the fully hBN encapsulated BLG device at different DC bias currents using Contact 1 as injector and Contact 5 as detector. Both electrodes are separated by $d = 10 \mu\text{m}$. a) Non-local resistance R_{NL} measured in an in-plane magnetic field B_{\parallel} where the magnetization of the injector and detector contacts are switched between parallel and antiparallel alignment. b) Spin precession measurement in an out-of-plane magnetic field B_{\perp} . The fitting using the Bloch equations yields the spin transport parameters shown in Table 6.1. Note that non-local background resistances smaller than 35Ω have been subtracted from the data to compare the influence of the different DC bias.

The most accurate way to characterize the spin transport properties of the channel is using spin precession, where the magnetic field is applied perpendicular to the BLG plane (B_{\perp}), causing spins to precess in the x - y plane. By fitting R_{NL} to the Bloch spin diffusion equations, we extract the spin-lifetime (τ_s), spin diffusion coefficient (D_s) and the average polarization of both electrodes (p_y). The data is shown for

different DC bias currents in Figure 6.3b, the fitting curves are shown as solid lines. Note that the spin transport parameters in Table 6.1 are within the experimental uncertainty for all I_{DC} values. Therefore, we average τ_s , D_s , and the spin relaxation length (λ) over all four values and obtain $\tau_s = (1.9 \pm 0.2)$ ns, $D_s = (183 \pm 17)$ cm²/s and $\lambda = \sqrt{D_s \tau_s} = (5.8 \pm 0.6)$ μm . These parameters are comparable to the ones reported in Reference [23]. We conclude that the change in contact resistance with I_{DC} does not affect the spin transport for values above 100 k Ω . This is caused by the fact that the contact resistance remains clearly above the spin resistance of the channel $R_s = R_{\text{sq}} \lambda / w \sim 1.8$ k Ω , where R_{sq} is the graphene square resistance and w the graphene width [30].

I_{DC} μA	$R_c \times A$ $\text{k}\Omega\mu\text{m}^2$	D_s cm^2/s	τ_s ns	λ μm
-2	280	208 ± 25	2.1 ± 0.2	6.4 ± 1.6
-0.6	760	177 ± 21	1.7 ± 0.2	5.5 ± 1.2
0	2 100	171 ± 24	1.7 ± 0.2	5.4 ± 1.5
+2	380	177 ± 24	2.0 ± 0.2	5.8 ± 1.5

Table 6.1: Spin transport parameters extracted from the data shown in Figure 6.3b. The values obtained from averaging over the different I_{DC} are: $D_s = (183 \pm 17)$ cm²/s, $\tau_s = (1.9 \pm 0.2)$ ns and $\lambda = (5.8 \pm 0.6)$ μm .

Note that the spin resistance of graphene can exceed 10 k Ω in high quality devices. This is close to the contact resistance of biased 2L-hBN tunnel barriers, which typically range, depending on I_{DC} , between 5 k Ω and 30 k Ω [31]. Furthermore, the extended data set in Section 6.9.3 and our analysis in Section 7.4.11 confirm that contact-induced spin back flow is not limiting spin transport for contact resistances above 100 k Ω .

6.4 Bias-Dependence of the Spin Injection Efficiency

In Figure 6.4a we show the non-local spin valve signal $\Delta R_{\text{NL}} = R_{\text{NL}}(\uparrow\uparrow) - R_{\text{NL}}(\uparrow\downarrow)$. For a comparison with 2L-hBN tunnel barriers, we calculate V_{hBN} , the voltage applied to the tunnel barrier, by using the current-voltage characteristics of each contact. To resolve small features in the bias-dependence, we source currents as low as $i_{\text{AC}} = 50$ nA. As observed for 2L-hBN barriers [20, 31], ΔR_{NL} changes sign at $V_{\text{hBN}} \sim -100$ mV, which we also observe with a 3L-hBN barrier. Our data also shows additional features: First, $|\Delta R_{\text{NL}}|$ shows a maximum at $V_{\text{hBN}} \sim -250$ mV and decreases again for $V_{\text{hBN}} < -250$ mV. In contrast, we observe a continuous increase for $V_{\text{hBN}} > +300$ mV. Second, we observe a peak at zero V_{hBN} , indicating that the polarization of Co/3L-hBN at zero DC bias is higher than in Co/2L-hBN. Note that

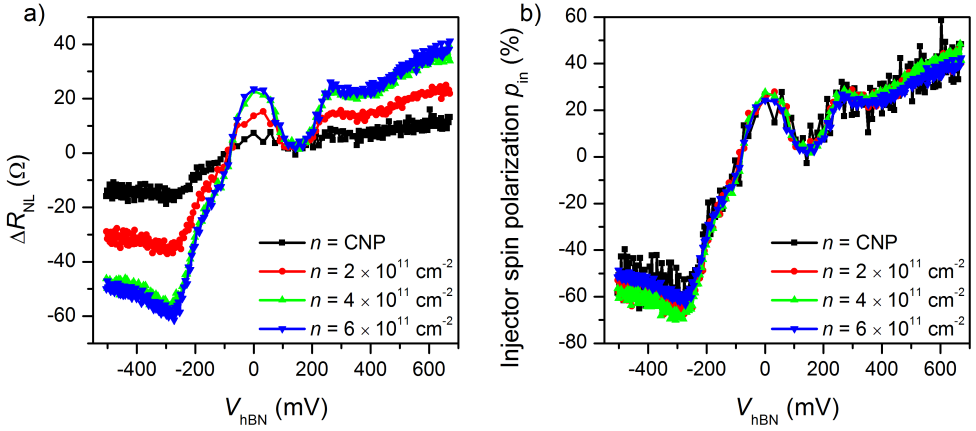


Figure 6.4: a) Measurement of the DC bias-dependence of the R_{NL} at four different carrier concentrations, where Contact 1 is used as injector and Contact 5 as detector. b) The extracted spin polarization of the injector contact using Equation 6.1. The differential spin polarization reaches -60% at negative and $+40\%$ at positive DC bias. Measurements using Contact 2 as injector yield comparable results.

2L-hBN devices in Reference [31] show also these small features around zero DC bias (Figure 6.5b).

To calculate the polarization of the Co/hBN interface from ΔR_{NL} , we use:

$$\Delta R_{NL} = \frac{p_{in} p_{det} R_{sq} \lambda}{w} e^{-d/\lambda}, \quad (6.1)$$

where p_{in} and p_{det} are the differential injector and detector spin polarizations, and d the separation between injector and detector. Following this procedure for $I_{DC} = 0$ at different configurations we obtain the unbiased spin polarizations of all contacts, $p_1 = 24\%$, $p_2 = 23\%$, $p_3 = 30\%$, $p_4 = 36\%$, and $p_5 = 38\%$. Since p_{det} does not depend on the DC bias, which is applied to the injector only, we can calculate the bias-dependence of p_{in} (Figure 6.4b). The absolute sign of p cannot be determined from spin transport measurements [20], and we define p to be positive for $I_{DC} = 0$.

Note that the slope observed in Figure 6.4b is in qualitative agreement with the *ab initio* calculations by Piquemal-Banci et al. [32] for chemisorbed cobalt on hBN, suggesting that the observed DC bias-dependence arises from the Co/hBN interface and not from proximity coupling between cobalt and graphene.

We conclude that $p_{in}(I_{DC})$ can reach values comparable to 2L-hBN tunnel barriers. Moreover, the comparison between different carrier concentrations shows that the differential spin injection polarization does not depend on the carrier density, even at the charge neutrality point. This also indicates that local spin drift in the barrier arising from pinholes is not responsible for the bias-dependence. The drift

velocity is inversely proportional to the carrier density, and therefore, the effect of spin drift is the largest near the neutrality point [4]. Furthermore, if charge carrier drift in the channel would be relevant, the measured Hanle curves would widen [33]. Consequently, the extracted spin-lifetimes would decrease with increasing I_{DC} , which we do not observe here. Furthermore, our I_{DC} is at most 2 μA , whereas a sizable drift effect requires larger charge currents [4]. Local charge carrier drift at the injector, caused by pinholes in the barrier, was used to explain a modulation of the spin injection polarization [14]. From our measurements we can exclude this mechanism as origin due to the negligible modulation of the spin injection polarization with n . Moreover, we use crystalline hBN as tunnel barrier, which has the advantage over evaporated barriers that pinholes are not expected to be present.

6.5 Calculation of the DC Spin Polarization

For practical applications, a large DC spin polarization P_{in} is required. Using the differential spin polarization p_{in} , we can calculate P_{in} via [20]:

$$p_{\text{in}}(I_{\text{DC}}) = \frac{dP_{\text{in}}(I_{\text{DC}})}{dI_{\text{DC}}} I_{\text{DC}} + P_{\text{in}}(I_{\text{DC}}). \quad (6.2)$$

The results obtained for 3L- and 2L-hBN barriers using this procedure are shown in Figure 6.5a and 6.5b. The DC spin polarization of 3L-hBN rises close to 50%, whereas 2L-hBN yield only up to 35%. Measurements on vertical tunnel junctions with 1L- and 2L-hBN tunnel barriers reported a spin polarization of $\sim 1\%$ (1L) and $\sim 12\%$ (2L) [32, 34, 35]. This underlines the potential of cobalt/3L-hBN contacts for highly efficient spin injection into graphene.

The comparison of the differential spin polarization of 1L-, 2L- and 3L-hBN/Co contacts is shown in Figure 6.5c. In the case of 1L-hBN, the polarization remains constant ($\sim 5\%$), mostly independent of the applied V_{hBN} , and clearly below the values of 2L- and 3L-hBN barriers. However, the comparison of 2L- and 3L-hBN yields comparable differential spin polarizations, whereas the electric fields underneath the contacts, which arise from V_{hBN} , change from 1L- to 3L-hBN by a factor of 3. Therefore, local gating underneath the contacts can also be excluded as origin of the bias-dependence. The effect of quantum capacitance is discussed in Section 6.9.5.

Zollner et al. [24] calculated the exchange coupling between cobalt and graphene separated by 1L- to 3L-hBN. Interestingly, graphene exhibits a spin splitting of up to 10 meV when cobalt and graphene are separated by 2L-hBN which decreases with 3L-hBN to 18 μeV . Since we observe comparable results between 2L-hBN and 3L-hBN, we conclude that proximity-induced exchange splitting is most likely not the origin for the DC bias-dependent spin injection efficiency in Co/hBN/graphene.

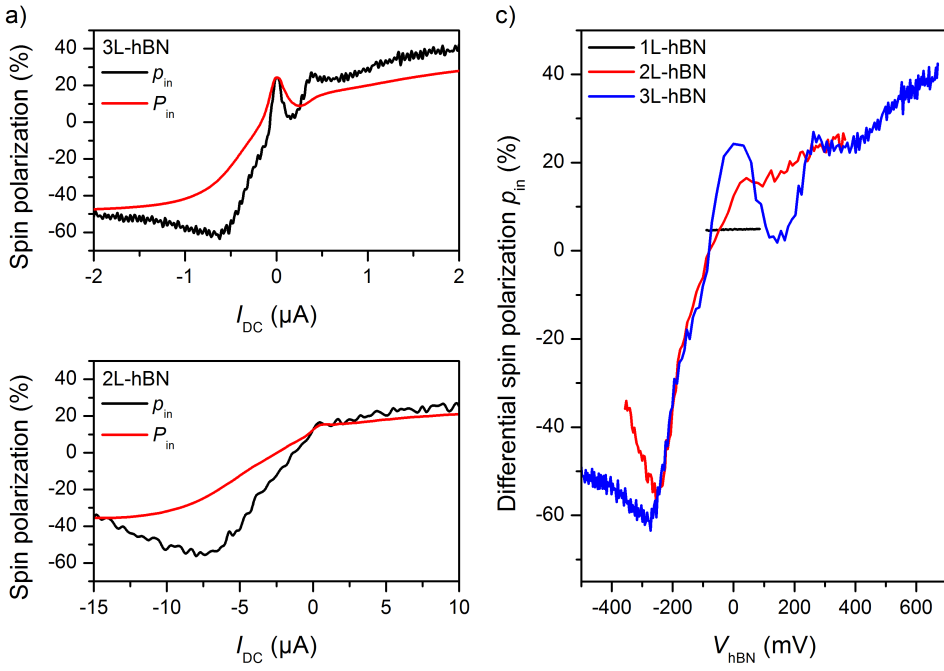


Figure 6.5: Differential (p_{in}) and DC (P_{in}) injector spin polarization of the a) 3L-hBN device using Contact 1 and Contact 5 and b) a 2L-hBN device from Reference [31]. Note that the numerical integration of p_{in} averages the noise out of P_{in} . c) Comparison of the differential spin polarization of 1L-, 2L- and 3L-hBN tunnel barriers. The data of the 1L-hBN device is taken from Reference [20].

6

6.6 Isotropy of the Spin Injection Mechanism

By applying a large $B_{\perp} \sim 1.2$ T, we can rotate the cobalt magnetization close to out-of-plane and characterize the spin injection efficiency of 3L-hBN tunnel barrier for out-of-plane spins. This measurement technique was used to determine the spin-lifetime anisotropy of graphene [36], which can be also measured using oblique spin precession with lower applied magnetic fields [26, 37, 38]. By comparing both results, we can separate the anisotropy of the BLG channel from the anisotropy of the spin injection and detection polarization.

Figure 6.6 shows the Hanle curves measured at a carrier density of $n = 6 \times 10^{11} \text{ cm}^{-2}$, which is the highest density accessible in our device and was chosen to minimize the effect of magnetoresistance and spin-lifetime anisotropy of the BLG channel. The data is normalized to $R_{NL0} = R_{NL}(B_{\perp} = 0 \text{ T})$. The normalized measurements at different I_{DC} overlap each other, which indicates that p_z/p_y is independent of I_{DC} . We model the spin transport using the Bloch equations for anisotropic

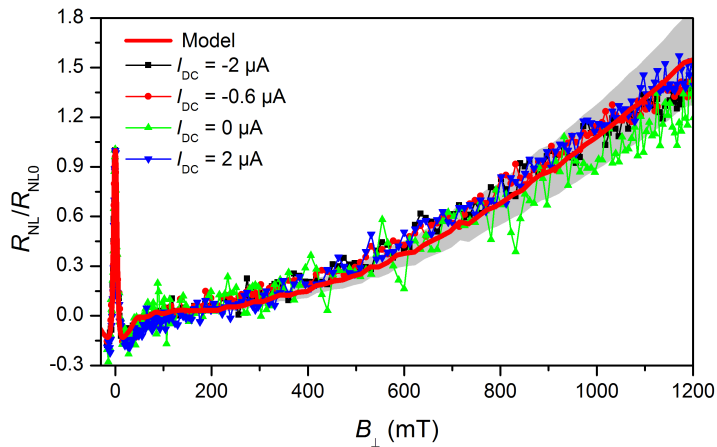


Figure 6.6: Hanle spin precession curves measured up to $B_{\perp} = 1.2$ T. For comparison, R_{NL} is normalized to R_{NL} at $B_{\perp} = 0$ (R_{NL0}). The measurements at different I_{DC} are shown as scattered lines, the red solid line is simulated with isotropic spin injection ($p_z/p_y = 1$). The gray shaded area accounts for the uncertainty of the extracted spin-lifetime anisotropy.

spin transport as discussed in Reference [26]. Additionally, we include the rotation of the contact magnetization, which we extract from anisotropic magnetoresistance measurements, shown in Section 6.9.4. The modeled curve is shown by the solid red line, the gray shaded area is determined by the uncertainty in the spin-lifetime anisotropy. The good agreement between the data and our model suggests that the spin injection polarization is isotropic, and, hence, $p_z/p_y \approx 1$.

6.7 Two-Terminal DC Spin Transport Measurements up to Room Temperature

Lastly, we use the large DC spin polarization of our device to measure spin transport in a local two-terminal geometry, which is especially interesting for applications. For this experiment we source a DC current (I_{DC}) and measure simultaneously the DC voltage V_{DC} between Contact 2 and Contact 1. The data is shown in Figure 6.7. The local, two-terminal signal is defined as $R_{2T} = V_{DC}/I_{DC}$, with the spin signal $\Delta R_{2T} = \Delta R_{2T}(\uparrow\uparrow) - \Delta R_{2T}(\uparrow\downarrow)$. We measure a spin signal of is 162Ω at $I_{DC} = -2 \mu\text{A}$ (Figure 6.7a) 75Ω at $I_{DC} = +1 \mu\text{A}$ (Figure 6.7b).

A spin precession measurement between Contact 3 and Contact 2 is shown in Figure 6.7c. We observe a clear Hanle curve and fit the data with $\tau_s = (740 \pm 60)$ ps, $D_s = (560 \pm 70)$ cm^2/s and calculate $\lambda = 6.5 \mu\text{m}$. Note that the change of these values compared to Table 6.1 was caused by an exposure of the sample to air. Using

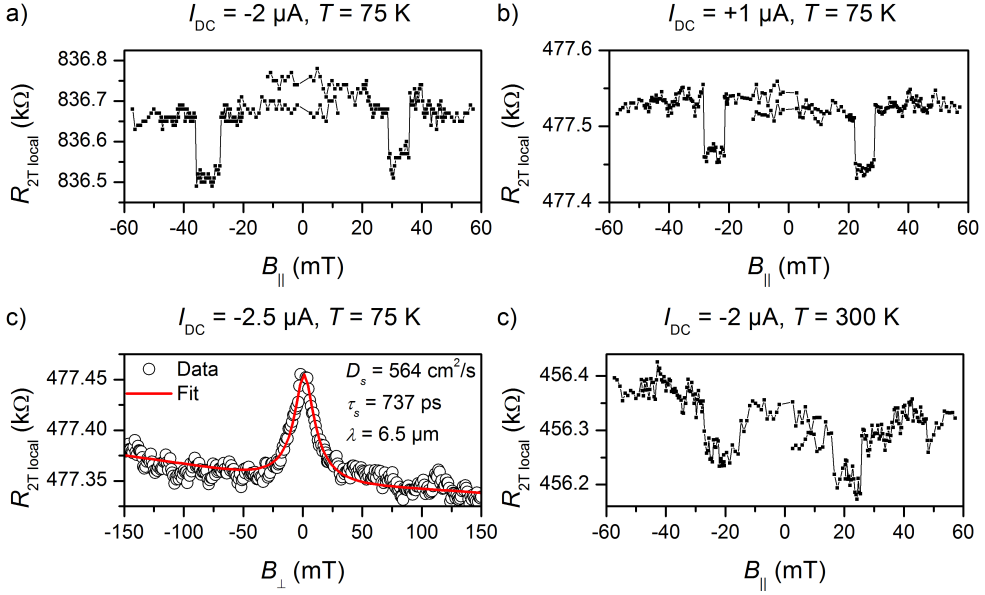


Figure 6.7: a) Local two-terminal spin signal measured with $I_{DC} = -2 \mu\text{A}$, and b) $I_{DC} = +1 \mu\text{A}$. c) Hanle precession data measured at $T = 75 \text{ K}$ between Contact 3 and Contact 2 with $I_{DC} = -2.5 \mu\text{A}$. d) Room temperature spin valve measurement between Contact 2 and Contact 1 with $I_{DC} = -2 \mu\text{A}$.

the spin polarization of the biased contacts and the extracted spin relaxation length, we can calculate the expected local 2T spin valve signal [20]:

$$\Delta R_{2T} = [P_A(+I_{DC})P_B(-I_{DC}) + P_A(-I_{DC})P_B(+I_{DC})] \frac{R_{sq}\lambda}{w} e^{-d/\lambda}, \quad (6.3)$$

where the indexes A and B denote both contacts at the bias I_{DC} . We calculate using the spin polarization values $\Delta R_{2T} = -177 \Omega$ at $I_{DC} = -2 \mu\text{A}$ and $R_{2T} = -108 \Omega$ at $I_{DC} = +1 \mu\text{A}$, which is in agreement with the measured data in Figure 6.7a and 6.7b of 162Ω and 80Ω . The measurement of R_{2T} at $T = 300 \text{ K}$ is shown in Figure 6.7d, where ΔR_{2T} is $\sim 100 \Omega$ and is clearly present. This indicates no dramatic change of the DC spin polarization with increasing temperature. These results underline the relevance of 3L-hBN barriers for graphene spintronics.

6.8 Summary

In conclusion, we have shown that 3L-hBN tunnel barriers provide a large, tunable spin injection efficiency from cobalt into graphene. The zero bias spin injection polarization is between 20% and 30%, and the differential spin injection polarization

can increase to -60% by applying a negative DC bias. The resulting DC spin polarization of up to 50% allows spin transport measurements in a DC two-terminal configuration up to room temperature. We study the carrier concentration-dependence of the spin injection polarization and find that it does not depend on the carrier density. From a comparison between 3L- and 2L-hBN, we observe that the DC bias-dependence scales with the voltage and not the electric field, indicating that local gating is not the dominant mechanism. We also compare the spin injection polarization for in-plane and out-of-plane spins and find that it is isotropic and that p_z/p_y is independent of the applied DC bias.

During the preparation of this manuscript we became aware of a related work [39], where a DC bias-dependent spin signal is reported in Co/SrO/graphene heterostructures. Furthermore, the authors exclude also carrier drift as origin.

Acknowledgements We acknowledge the fruitful discussions with A.A. Kaverzin and technical support from H. Adema, J.G. Holstein, H.M. de Roos, T.J. Schouten, and H. de Vries. This project has received funding from the European Unions Horizon 2020 research and innovation program under the grant Grant No. 696656 and 785219 ('Graphene Flagship' Core 1 and 2), the Marie Curie initial training network 'Spinograph' (Grant No. 607904) and the Spinoza Prize awarded to B.J. van Wees by the 'Netherlands Organization for Scientific Research' (NWO).

6.9 Supplementary Information

6.9.1 Fabrication Details

The 3L-hBN/bilayer graphene (BLG)/bottom-hBN stack is fabricated with the scotch tape technique to exfoliate hBN from hBN powder (HQ Graphene) and graphene from HOPG (ZYB grade, HQ Graphene). The materials are stacked using a polycarbonate-based dry transfer technique [40]. The transfer polymer is removed in chloroform and the sample is annealed for one hour in Ar/H₂. PMMA is spun on the sample and contacts are exposed using e-beam lithography. The sample is developed in MIBK:IPA and a 65 nm Co layer and a 5 nm Al capping layer are deposited. The PMMA mask is removed in warm acetone. The sample is bonded on a chip carrier and loaded into a cryostat where the sample space is evacuated below 10^{-6} mbar.

6.9.2 Determination of the Contact Spin Polarizations

Figure 6.8 shows the non-local spin valve measurement obtained from all different contact combinations. To calculate the unbiased spin polarization of each contact, we apply $i_{AC} = 50$ nA to the injector and obtain the values in Table 6.2. The measure-

ment is done without any DC bias current and back gate voltage applied, $V_{BG} = 0$, the corresponding carrier concentration is $4 \times 10^{11} \text{ cm}^{-2}$.

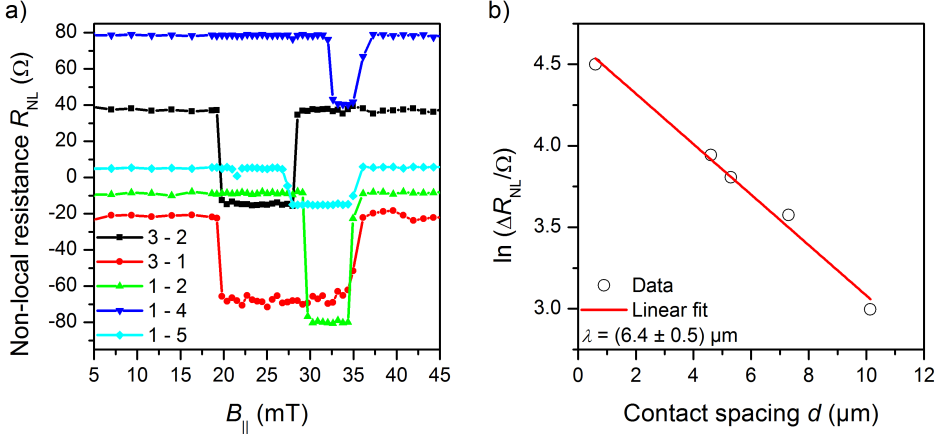


Figure 6.8: Non-local spin valves for all used injector/detector pairs to calculate the unbiased spin polarization for each contact.

6

To calculate the spin polarization of each contact, we use Equation 6.4:

$$p_A = \frac{\Delta R_{NL} w}{p_B R_{sq} \lambda} \exp(d/\lambda), \quad (6.4)$$

where ΔR_{NL} is the spin signal extracted from Figure 6.8a, $w = 3 \mu\text{m}$ the width of the BLG and R_{sq} the square resistance of the BLG. The results are shown in Table 6.2. Note that the larger differential spin polarization values for the larger spacings (Contact 4 and Contact 5) can be explained with the uncertainty in determining the spin relaxation length.

Injector	Detector	ΔR_{NL} Ω	d μm
3	2	52	4.6
3	1	48	5.3
1	2	89	0.6
1	4	40	7.3
1	5	21	11.1

Table 6.2: Measured spin valve signals extracted from the data in Figure 6.8. We calculate the unbiased differential spin polarization p of each contact and obtain $p_1 = 24\%$, $p_2 = 23\%$, $p_3 = 30\%$, $p_4 = 36\%$, and $p_5 = 38\%$ using Equation 6.4.

6.9.3 Full Set of Spin Transport Parameters

Table 6.3 contains the results of the full set of spin transport measurements.

I_{DC} μA	V_{BG} V	R_{sq} Ω	D_s cm^2/s	τ_s ns	λ μm
-2	-2	1600	112 ± 27	1.5 ± 0.3	4.1 ± 1.8
-0.6	-2	1600	114 ± 24	1.4 ± 0.3	4.0 ± 1.6
0	-2	1600	138 ± 43	1.6 ± 0.5	4.8 ± 2.8
2	-2	1600	86 ± 21	1.0 ± 0.3	2.9 ± 1.3
-2	-1	1400	133 ± 22	1.7 ± 0.3	4.8 ± 1.5
-0.6	-1	1400	140 ± 20	1.7 ± 0.3	4.9 ± 1.3
0	-1	1400	160 ± 40	1.8 ± 0.4	5.4 ± 2.5
2	-1	1400	137 ± 22	1.8 ± 0.3	5.0 ± 1.5
-2	0	900	202 ± 26	2.0 ± 0.3	6.4 ± 1.6
-0.6	0	900	176 ± 21	1.7 ± 0.2	5.5 ± 1.2
0	0	900	170 ± 24	1.7 ± 0.3	5.4 ± 1.5
2	0	900	174 ± 24	1.9 ± 0.3	5.8 ± 1.5
-2	1	750	226 ± 24	2.2 ± 0.2	7.1 ± 1.4
-0.6	1	750	230 ± 25	1.8 ± 0.2	6.5 ± 1.3
0	1	750	214 ± 27	1.8 ± 0.2	6.1 ± 1.5
2	1	750	222 ± 25	2.1 ± 0.2	6.8 ± 1.4

Table 6.3: Basic spin and charge transport parameters measured by Hanle spin precession using Contact 1 and Contact 5.

6.9.4 Extraction of the Magnetization Angle

To accurately model the dependence of R_{NL} on B_{\perp} , we measure the anisotropic magnetoresistance (AMR) effect, shown in Figure 6.9a. The angle of the cobalt magnetization α can be calculated at any given B_{\perp} via [41]:

$$\cos(\alpha(B_{\perp})) = \sqrt{\frac{R_{\text{AMR}}(B_{\perp}) - R_{\text{AMR}}(B_{\perp} = 0)}{R_{\text{AMR}}(B_{\perp} = 2\text{T}) - R_{\text{AMR}}(B_{\perp} = 0)}}. \quad (6.5)$$

The calculated magnetization angle $\alpha(B_{\perp})$ is shown in Figure 6.9b and used to model the spin precession curves in the main text.

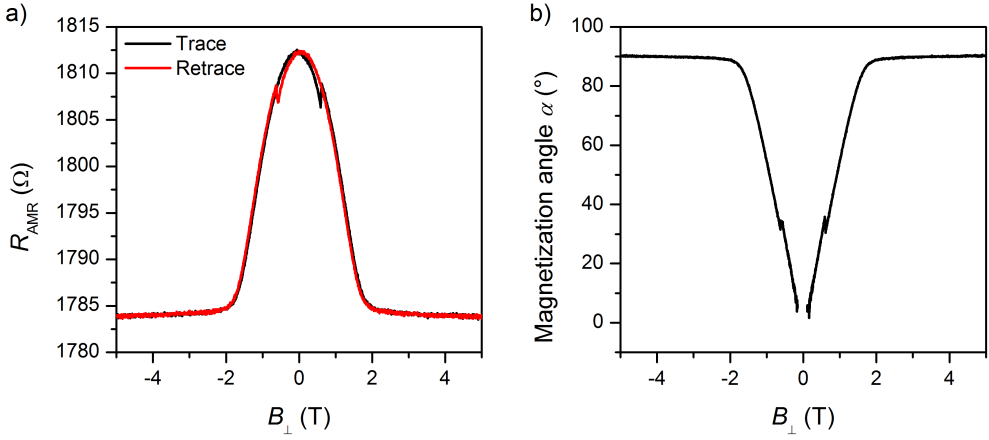


Figure 6.9: a) AMR measurement of a 65 nm cobalt electrode. b) Calculated magnetization angle under B_{\perp} .

6.9.5 Quantum Capacitance Correction to DC Bias-Induced Gating

The quantum capacitance correction becomes relevant when the geometrical capacitance of a gate is large, or the density of states of the channel is small. The quantum capacitance correction is calculated via [42]:

$$e\Delta V_{\text{hBN}} = \Delta E_F + \frac{e^2 \Delta n t_{\text{hBN}}}{\epsilon_0 \epsilon_r}, \quad (6.6)$$

where V_{hBN} denotes the voltage applied to the contact, t_{hBN} the hBN tunnel barrier thickness, e the electron charge, ϵ_0 the vacuum permittivity, and ϵ_r the relative permittivity of hBN. The Fermi energy in the conduction band of BLG is determined by [43]:

$$E_F = -\frac{\gamma_1}{2} + \frac{\sqrt{\gamma_1^2 + 4n\pi\hbar^2 v_F^2}}{2}, \quad (6.7)$$

where γ_1 is the interlayer hopping constant, \hbar the reduced Plank constant, and $v_F = 10^6$ m/s the Fermi velocity in graphene. Using Equation 6.6 and Equation 6.7, we calculate the carrier density for a DC bias of 300 mV in Table 6.4, assuming that the charge neutrality point lies at zero DC bias. We find that the quantum capacitance can have a significant effect on the carrier density n_{corr} compared to classical gating $n_{\text{geo}} = \epsilon_0 \epsilon_r V_{\text{hBN}} / (e t_{\text{hBN}})$.

In conclusion, we find a substantial quantum capacitance correction. However, even with the quantum correction applied, the difference in the carrier concentration of 2L- and 3L-hBN is $\sim 30\%$. Consequently, we can still exclude local gating as origin of the DC bias-dependence.

V_{hBN} mV	t_{hBN} nm	ϵ_r	n_{corr} cm^{-2}	n_{geo} cm^{-2}
300	0.7 (2L)	3.44	4.78×10^{12}	8.15×10^{12}
300	1.2 (3L)	3.52	3.35×10^{12}	4.86×10^{12}

Table 6.4: Calculation of the quantum capacitance corrections. The change in n induced by the bias applied to the contacts n_{corr} is determined using Equation 6.6. The classical gating n_{geo} is shown for comparison. The values for the relative permittivity are taken from Reference [44].

References

- [1] D. Huertas-Hernando, F. Guinea, and A. Brataas. Spin-orbit coupling in curved graphene, fullerenes, nanotubes, and nanotube caps. *Physical Review B*, **74**(15), 155426, 2006.
- [2] W. Han, R.K. Kawakami, M. Gmitra, and J. Fabian. Graphene spintronics. *Nature Nanotechnology*, **9**(10), 794, 2014.
- [3] S. Roche, J. Åkerman, B. Beschoten, J.-C. Charlier, M. Chshiev, S.P. Dash, B. Dlubak, J. Fabian, A. Fert, M.H.D. Guimarães, F. Guinea, I. Grigorieva, C. Schönenberger, P. Seneor, C. Stampfer, S.O. Valenzuela, X. Waintal, and B.J. van Wees. Graphene spintronics: the European Flagship perspective. *2D Materials*, **2**(3), 030202, 2015.
- [4] J. Ingla-Aynés, R.J. Meijerink, and B.J. van Wees. Eighty-Eight Percent Directional Guiding of Spin Currents with 90 μm Relaxation Length in Bilayer Graphene Using Carrier Drift. *Nano Letters*, **16**(8), 4825, 2016.
- [5] M. Drögeler, C. Franzen, F. Volmer, T. Pohlmann, L. Banszerus, M. Wolter, K. Watanabe, T. Taniguchi, C. Stampfer, and B. Beschoten. Spin Lifetimes Exceeding 12 ns in Graphene Nonlocal Spin Valve Devices. *Nano Letters*, **16**(6), 3533, 2016.
- [6] P.J. Zomer, M.H.D. Guimarães, N. Tombros, and B.J. van Wees. Long-distance spin transport in high-mobility graphene on hexagonal boron nitride. *Physical Review B*, **86**(16), 161416, 2012.
- [7] M.H.D. Guimarães, P.J. Zomer, J. Ingla-Aynés, J.C. Brant, N. Tombros, and B.J. van Wees. Controlling Spin Relaxation in Hexagonal BN-Encapsulated Graphene with a Transverse Electric Field. *Physical Review Letters*, **113**(8), 086602, 2014.
- [8] M. Drögeler, F. Volmer, M. Wolter, B. Terrés, K. Watanabe, T. Taniguchi, G. Güntherodt, C. Stampfer, and B. Beschoten. Nanosecond spin lifetimes in single- and few-layer graphene-hBN heterostructures at room temperature. *Nano Letters*, **14**(11), 6050, 2014.
- [9] J. Ingla-Aynés, M.H.D. Guimarães, R.J. Meijerink, P.J. Zomer, and B.J. van Wees. 24- μm Spin Relaxation Length in Boron Nitride Encapsulated Bilayer Graphene. *Physical Review B*, **92**(20), 201410, 2015.
- [10] M. Gurram, S. Omar, S. Zihlmann, P. Makk, C. Schönenberger, and B.J. van Wees. Spin transport in fully hexagonal boron nitride encapsulated graphene. *Physical Review B*, **93**(11), 115441, 2016.
- [11] S. Singh, J. Katoch, J. Xu, C. Tan, T. Zhu, W. Amamou, J. Hone, and R.K. Kawakami. Nanosecond spin relaxation times in single layer graphene spin valves with hexagonal boron nitride tunnel barriers. *Applied Physics Letters*, **109**(12), 122411, 2016.
- [12] G. Schmidt, D. Ferrand, L.W. Molenkamp, A.T. Filip, and B.J. van Wees. Fundamental obstacle for electrical spin injection from a ferromagnetic metal into a diffusive semiconductor. *Physical Review B*, **62**(8), R4790, 2000.
- [13] E.I. Rashba. Theory of electrical spin injection: Tunnel contacts as a solution of the conductivity mismatch problem. *Physical Review B*, **62**(24), R16267, 2000.

- [14] C. Józsa, M. Popinciuc, N. Tombros, H.T. Jonkman, and B.J. van Wees. Controlling the efficiency of spin injection into graphene by carrier drift. *Physical Review B*, **79**(8), 081402, 2009.
- [15] W. Han, K. Pi, K.M. McCreary, Y. Li, J.J.I. Wong, A.G. Swartz, and R.K. Kawakami. Tunneling spin injection into single layer graphene. *Physical Review Letters*, **105**(16), 167202, 2010.
- [16] F. Volmer, M. Drögeler, E. Maynicke, N. Von Den Driesch, M.L. Boschen, G. Güntherodt, and B. Beschoten. Role of MgO barriers for spin and charge transport in Co/MgO/graphene non-local spin-valve devices. *Physical Review B*, **88**(16), 161405, 2013.
- [17] F. Volmer, M. Drögeler, E. Maynicke, N. Von Den Driesch, M.L. Boschen, G. Güntherodt, C. Stampfer, and B. Beschoten. Suppression of contact-induced spin dephasing in graphene/MgO/Co spin-valve devices by successive oxygen treatments. *Physical Review B*, **90**(16), 165403, 2014.
- [18] M.V. Kamalakar, A. Dankert, J. Bergsten, T. Ive, and S.P. Dash. Enhanced Tunnel Spin Injection into Graphene using Chemical Vapor Deposited Hexagonal Boron Nitride. *Scientific Reports*, **4**(1), 6146, 2015.
- [19] M.V. Kamalakar, A. Dankert, P.J. Kelly, and S.P. Dash. Inversion of Spin Signal and Spin Filtering in Ferromagnet|Hexagonal Boron Nitride-Graphene van der Waals Heterostructures. *Scientific Reports*, **6**, 21168, 2016.
- [20] M. Gurram, S. Omar, and B.J. van Wees. Bias induced up to 100% spin-injection and detection polarizations in ferromagnet/bilayer-hBN/graphene/hBN heterostructures. *Nature Communications*, **8**(1), 248, 2017.
- [21] I. Neumann, M.V. Costache, G. Bridoux, J.F. Sierra, and S.O. Valenzuela. Enhanced spin accumulation at room temperature in graphene spin valves with amorphous carbon interfacial layers. *Applied Physics Letters*, **103**(11), 112401, 2013.
- [22] S. Singh, J. Katoch, T. Zhu, R.J. Wu, A.S. Ahmed, W. Amamou, D. Wang, K.A. Mkhoyan, and R.K. Kawakami. Strontium oxide tunnel barriers for high quality spin transport and large spin accumulation in graphene. *Nano Letters*, **17**(12), 7578, 2017.
- [23] M. Gurram, S. Omar, and B.J. van Wees. Electrical spin injection, transport, and detection in graphene-hexagonal boron nitride van der Waals heterostructures: progress and perspectives. *2D Materials*, **5**(3), 032004, 2018.
- [24] K. Zollner, M. Gmitra, T. Frank, and J. Fabian. Theory of proximity-induced exchange coupling in graphene on hBN/(Co, Ni). *Physical Review B*, **94**(15), 155441, 2016.
- [25] S. Ringer, M. Rosenauer, T. Völkl, M. Kadur, F. Hopperdietzel, D. Weiss, and J. Eroms. Spin field-effect transistor action via tunable polarization of the spin injection in a Co/MgO/graphene contact. *Applied Physics Letters*, **113**(13), 132403, 2018.
- [26] J.C. Leutenantsmeyer, J. Ingla-Aynés, J. Fabian, and B.J. van Wees. Observation of Spin-Valley-Coupling-Induced Large Spin-Lifetime Anisotropy in Bilayer Graphene. *Physical Review Letters* **121**(12), 127702, 2018.
- [27] F.J. Jedema, A.T. Filip, and B.J. van Wees. Electrical spin injection and accumulation at room temperature in an all-metal mesoscopic spin valve. *Nature*, **410**(6826), 345, 2001.
- [28] F.J. Jedema, H.B. Heersche, A.T. Filip, J.J.A. Baselmans, and B.J. van Wees. Electrical detection of spin precession in a metallic mesoscopic spin valve. *Nature*, **416**(6882), 713, 2002.
- [29] N. Tombros, C. Józsa, M. Popinciuc, H.T. Jonkman, and B.J. van Wees. Electronic spin transport and spin precession in single layer graphene layers at room temperature. *Nature*, **448**(7153), 571, 2007.
- [30] T. Maassen, I.J. Vera-Marun, M.H.D. Guimarães, and B.J. van Wees. Contact-induced spin relaxation in Hanle spin precession measurements. *Physical Review B*, **86**(23), 235408, 2012.
- [31] J.C. Leutenantsmeyer, T. Liu, M. Gurram, A.A. Kaverzin, and B.J. van Wees. Bias dependent spin injection into graphene on YIG through bilayer hBN tunnel barriers. *Physical Review B*, **98**(12), 125422, 2018.
- [32] M. Piquemal-Banci, R. Galceran, F. Godel, S. Caneva, M.-B. Martin, R.S. Weatherup, P.R. Kidambi, K. Bouzehouane, S. Xavier, A. Anane, F. Petroff, A. Fert, S. Mutien-Marie Dubois, J.-C. Charlier, J. Robertson, S. Hofmann, B. Dlubak, and P. Seneor. Insulator-to-Metallic Spin-Filtering in 2D-

- Magnetic Tunnel Junctions Based on Hexagonal Boron Nitride. *ACS Nano*, **12**(5), 4712, 2018.
- [33] B. Huang and I. Appelbaum. Spin dephasing in drift-dominated semiconductor spintronics devices. *Physical Review B*, **77**(16), 165331, 2008.
- [34] A. Dankert, M. Venkata Kamalakar, A. Wajid, R.S. Patel, and S.P. Dash. Tunnel magnetoresistance with atomically thin two-dimensional hexagonal boron nitride barriers. *Nano Research*, **8**(4), 1357, 2015.
- [35] P.U. Ashhoff, J.L. Sambricio, A.P. Rooney, S. Slizovskiy, A. Mishchenko, A.M. Rakowski, E.W. Hill, A.K. Geim, S.J. Haigh, V.I. Fal'ko, I.J. Vera-Marun, and I.V. Grigorieva. Magnetoresistance of vertical Co-graphene-NiFe junctions controlled by charge transfer and proximity-induced spin splitting in graphene. *2D Materials*, **4**(3), 031004, 2017.
- [36] N. Tombros, S. Tanabe, A. Veligura, C. Jozsa, M. Popinciuc, H.T. Jonkman, and B.J. van Wees. Anisotropic spin relaxation in graphene. *Physical Review Letters*, **101**(4), 046601, 2008.
- [37] B. Raes, J.E. Scheerder, M.V. Costache, F. Bonell, J.F. Sierra, J. Cuppens, J. van de Vondel, and S.O. Valenzuela. Determination of the spin-lifetime anisotropy in graphene using oblique spin precession. *Nature Communications*, **7**, 11444, 2016.
- [38] B. Raes, A.W. Cummings, F. Bonell, M.V. Costache, J.F. Sierra, S. Roche, and S.O. Valenzuela. Spin precession in anisotropic media. *Physical Review B*, **95**(8), 085403, 2017.
- [39] T. Zhu, S. Singh, J. Katoch, H. Wen, K. Belashchenko, I. Žutic, and R.K. Kawakami. Probing Tunneling Spin Injection into Graphene via Bias Dependence. *Physical Review B*, **98**(98), 054412, 2018.
- [40] P.J. Zomer, M.H.D. Guimarães, J.C. Brant, N. Tombros, and B.J. van Wees. Fast pick up technique for high quality heterostructures of bilayer graphene and hexagonal boron nitride. *Applied Physics Letters*, **105**(1), 013101, 2014.
- [41] L.A. Benítez, J.F. Sierra, W. Savero Torres, A. Arrighi, F. Bonell, M.V. Costache, and S.O. Valenzuela. Strongly anisotropic spin relaxation in graphene/transition metal dichalcogenide heterostructures at room temperature. *Nature Physics*, **14**(3), 303, 2018.
- [42] D. Braga, I. Gutiérrez Lezama, H. Berger, and A.F. Morpurgo. Quantitative Determination of the Band Gap of WS₂ with Ambipolar Ionic Liquid-Gated Transistors. *Nano Letters*, **12**(10), 5218, 2012.
- [43] E. McCann and M. Koshino. The electronic properties of bilayer graphene. *Reports on Progress in Physics*, **76**(5), 056503, 2013.
- [44] A. Laturia, M.L. van de Put, and W.G. Vandenberghe. Dielectric properties of hexagonal boron nitride and transition metal dichalcogenides: from monolayer to bulk. *npj 2D Materials and Applications*, **2**(1), 6, 2018.

Observation of Spin-Valley-Coupling-Induced Large Spin-Lifetime Anisotropy in Bilayer Graphene

Published in Physical Review Letters 121(12), 127702, 2018

Abstract

We report the first observation of a large spin-lifetime anisotropy in bilayer graphene (BLG) fully encapsulated between hexagonal boron nitride. We characterize the out-of-plane (τ_{\perp}) and in-plane (τ_{\parallel}) spin-lifetimes by oblique Hanle spin precession. At 75 K and the charge neutrality point (CNP) we observe a strong anisotropy of $\tau_{\perp}/\tau_{\parallel} = 8 \pm 2$. This value is comparable to graphene/TMD heterostructures, whereas our high quality BLG provides with τ_{\perp} up to 9 ns, a more than two orders of magnitude larger spin-lifetime. The anisotropy decreases to 3.5 ± 1 at a carrier density of $n = 6 \times 10^{11} \text{ cm}^{-2}$. Temperature-dependent measurements show above 75 K a decrease of $\tau_{\perp}/\tau_{\parallel}$ with increasing temperature, reaching the isotropic case close to room temperature. We explain our findings with electric field induced spin-valley coupling arising from the small intrinsic spin-orbit fields in BLG of 12 μeV at the CNP.

7.1 Introduction

Coupling between the electronic spin and valley degree of freedom arises in materials without inversion symmetry such as single layer transition-metal dichalcogenides (TMDs) [1, 2] where the electronic bands are spin split by the spin-orbit fields. Because of time reversal symmetry, the induced spin splitting is opposite for the K and K' points of the Brillouin zone. This leads to a coupling between the spin and valley degrees of freedom, and enables new functionalities such as the optical injection of spin currents with circularly polarized light [3, 4]. The spin-valley coupling has been imprinted on the band structure of monolayer graphene by placing it in proximity with a TMD and measured using spin [5–7] and charge transport [8–10]. However, it remains a question if similar behavior can be observed in pristine graphene devices.

BLG has an intrinsic spin-orbit coupling of $\lambda_I \sim 12 \mu\text{eV}$, which points out of the BLG plane. A perpendicular electric field, induced by asymmetric crystal alignment, gating, and/or doping, breaks the inversion symmetry, and, as a consequence, the intrinsic spin-orbit coupling induces an out-of-plane spin splitting of $2\lambda_I \sim 24 \mu\text{eV}$

at the K points [11]. The splitting has opposite sign in K and K' and therefore a valley-dependence. Recent *ab initio* calculations show that the encapsulation of BLG in hexagonal boron nitride (hBN) preserves the presence of the spin splitting with a similar magnitude [12].

Thermal broadening and inhomogeneities due to doping fluctuations [13] prevent the direct measurement of such a small spin splitting in conventional charge transport experiments. However, spin precession experiments can resolve spin splittings much smaller than $k_B T$, if the splitting extends over a sufficiently large region in reciprocal space and energy [14]. In the presence of an out-of-plane spin splitting, the dephasing of spins follows the Dyakonov-Perel mechanism [15]. The in-plane spin-lifetime τ_{\parallel} is inversely proportional to the intervalley scattering time, $\tau_{\parallel} \propto \lambda_I^2 / \tau_{iv}$ [5]. Hence, τ_{\parallel} is sensitive to the spin-orbit coupling strength.

Apart from the intrinsic spin-orbit coupling, breaking of the inversion symmetry leads to Rashba spin-orbit fields in the graphene plane [16, 17] that affect both in-plane and out-of-plane (τ_{\perp}) spin-lifetimes. Therefore, spin relaxation in BLG is a result of an interplay between intrinsic and Rashba spin-orbit coupling. The Rashba spin-orbit coupling depends on the Fermi velocity, which increases with the carrier density n , whereas the intrinsic spin-orbit splitting decreases with n . As a consequence, the spin-lifetime anisotropy ($\tau_{\perp} / \tau_{\parallel}$) is expected to depend strongly on n near the CNP [11, 18] allowing the electrical control of the spin-lifetime anisotropy.

7.2 Results and Discussion

Here we study τ_{\perp} and τ_{\parallel} in fully hBN encapsulated BLG using oblique spin precession. Our results show that, in contrast with monolayer graphene [17, 19–21], at temperatures below 300 K, the ratio $\tau_{\perp} / \tau_{\parallel}$ is significantly above 1 over the full measured range of n . At $T = 75$ K we observe a dependence of $\tau_{\perp} / \tau_{\parallel}$ on the carrier concentration which increases from 3.5 ± 1 at $n = 6 \times 10^{11} \text{ cm}^{-2}$ to 8 ± 2 at the CNP confirming the role of the spin-valley coupling on the spin transport. The anisotropy at the CNP is comparable to graphene/TMD systems [6, 7]. However, the spin-lifetimes in our BLG devices are two orders of magnitude larger [22–27]. These results show that small spin-orbit fields can induce sizable effects on the spin relaxation and indicate that the spin relaxation in our devices is limited by λ_I and Rashba spin-orbit coupling.

The device is shown in Figure 7.1 where the BLG is protected from contamination by a trilayer hBN tunnel barrier on top and a 5 nm thick bottom hBN flake below [28]. The stack is deposited on a 90 nm SiO₂/Si wafer which is used as a back gate. Ferromagnetic cobalt contacts are defined using standard e-beam lithography and e-beam evaporation techniques and are used for spin injection and detection. The contacts are non-invasive with a resistance-area product of $2 \text{ M}\Omega\mu\text{m}^2$. With a back

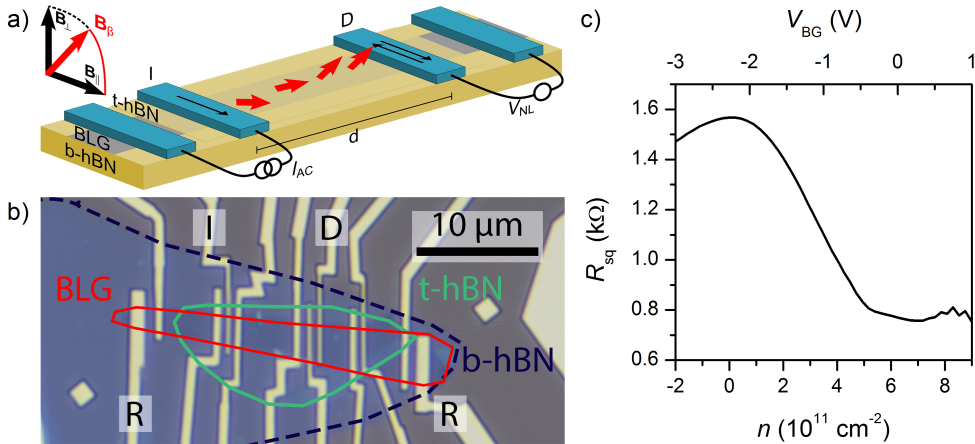


Figure 7.1: a) Schematic and b) optical image of the device geometry. BLG is encapsulated by a 1 nm thick hBN tunnel barrier (t-hBN) and a 5 nm (b-hBN) flake. A low frequency AC current (I_{AC}) injects a spin accumulation into the BLG. The non-local signal (V_{NL}) is measured using standard lock-in technique. The precession of injected in-plane spins around the magnetic field B_β is illustrated in the encapsulated BLG channel. Note that the outer reference contacts (R) are not covered by the hBN tunnel barrier. The injector (I) and detector contact (D) used for the measurements discussed in the main text are labeled and have a spacing of $d = 7 \mu\text{m}$. c) Gate voltage and carrier concentration-dependence of the BLG square resistance.

gate we tune the carrier concentration from the hole regime, slightly beyond the CNP ($2 \times 10^{11} \text{ cm}^{-2}$) up to $6 \times 10^{11} \text{ cm}^{-2}$ in the electron regime. The CNP is at $V_{BG} = -2 \text{ V}$ applied to the back gate, indicating a small background doping. The electric field at the CNP is estimated to be between 40 and 80 mV/nm (see Section 7.4.3). Note that the application of large electric fields (above 2 V/nm) to BLG can result in band gaps up to 200 meV [29–31]. However, the small fields applied to our sample lead to band gap openings significantly smaller than $k_B T$ and are neglected in our analysis.

The mobility μ of the sample is $12000 \text{ cm}^2/\text{Vs}$ at $n = 4 \times 10^{11} \text{ cm}^{-2}$ obtained using $\mu = 1/e d\sigma/dn$ where σ is the conductivity and e the electron charge. The charge diffusion coefficient is $D_c = 260 \text{ cm}^2/\text{s}$, which is in agreement with the spin diffusion coefficient $D_s = (210 \pm 50) \text{ cm}^2/\text{s}$ obtained from Hanle spin precession. This indicates the consistency of the analysis.

To optimize the spin injection efficiency, we apply additionally to the AC measurement current a DC bias current of $-0.6 \mu\text{A}$ to the trilayer hBN barrier [32, 33]. Note that the negative bias applied to the injector causes a sign change in the spin polarization of the injector and, therefore in R_{NL} . For comparison with conventional Hanle curves, we have inverted the sign of R_{NL} .

Figures 7.2a – 7.2c show the experimental results obtained from oblique Hanle spin precession measurements (see Figure 7.1a for the schematics of the experiment)

at three different carrier densities. The data shown in panels 7.2a and 7.2d is measured at $n = 6 \times 10^{11} \text{ cm}^{-2}$, 7.2b and 7.2e at $n = 4 \times 10^{11} \text{ cm}^{-2}$, whereas the data in 7.2c and 7.2f is measured at the CNP. $R_{\text{NL}\beta}$ is defined as the spin signal where the spin accumulation perpendicular to the magnetic field B_β is fully dephased. We extract $R_{\text{NL}\beta}$ from the experiment by averaging R_{NL} between 50 mT and 100 mT, indicated by the gray area at low magnetic fields in Figures 7.2a – 7.2c.

The spins are injected collinear to the in-plane magnetization of the ferromagnetic electrode with efficiency p_{in} . Since only the component parallel to B_β is conserved, the injection and detection efficiencies for the measured spins become $p_{\text{in}} \cdot \cos(\beta)$. Consequently, $R_{\text{NL}\beta}$ is proportional to $\cos^2(\beta)$. Therefore, at $\beta = 45^\circ$, one would expect $R_{\text{NL}\beta}$ to be reduced by 50% compared to $R_{\text{NL}0}$ in an isotropic system. We find at 75 K that at all different carrier concentrations in Figure 7.2a – 7.2c, $R_{\text{NL}\beta}/R_{\text{NL}0}$ is clearly above 0.5 for $\beta = 45^\circ$, which can only be the case if $\tau_\perp/\tau_\parallel > 1$. This can be seen from Equation 7.1, which can be used to quantify the degree of anisotropy [20, 34]:

$$\frac{R_{\text{NL}\beta}}{R_{\text{NL}0}} = \sqrt{\frac{\tau_\beta}{\tau_\parallel}} \exp \left[\frac{-d}{\lambda_\parallel} \left(\sqrt{\frac{\tau_\parallel}{\tau_\beta}} - 1 \right) \right] \cos^2(\beta), \quad (7.1)$$

$$\frac{\tau_\beta}{\tau_\parallel} = \left(\cos^2(\beta) + \frac{\tau_\parallel}{\tau_\perp} \sin^2(\beta) \right)^{-1}. \quad (7.2)$$

However, this model is only applicable for a channel significantly longer than both the in-plane and out-of-plane spin relaxation length. The out-of-plane spin relaxation length ($\sim 12 \mu\text{m}$) is longer than the closest spacing between sample edge and the injector ($8 \mu\text{m}$). Therefore, the exact device geometry has to be taken into account for a quantitative analysis.

To carefully account for the device geometry, we solve the Bloch equations for anisotropic spin transport numerically. Furthermore, we include both the effect of B_β on the contact magnetization direction using a Stoner-Wohlfarth model and the influence of the finite resistances of the reference contacts, Section 7.4.11 [35, 36]. The Hanle precession curves are simulated for different ratios $\tau_\perp/\tau_\parallel$ and different angles β . We obtain $R_{\text{NL}\beta}/R_{\text{NL}0}$ from the simulated curves using the same procedure as used for the experimental data.

The resulting curves are shown in Figures 7.2d to 7.2f where the red solid line represents the best fit to the data. The gray areas correspond to the estimated error margin with the annotated values. The case of an isotropic system is shown by the dotted gray lines. We find $\tau_\perp/\tau_\parallel$ to be 3.5 ± 1 ($n = 6 \times 10^{11} \text{ cm}^{-2}$), 5 ± 2 ($n = 4 \times 10^{11} \text{ cm}^{-2}$), and 8 ± 2 (CNP). We have measured and analyzed different contact spacings and different injector/detector contact pairs which all showed a consistent behavior and are discussed in Section 7.4.5.

When a large B_\perp is applied, the Co magnetization direction rotates out of the sample plane. As a consequence, a perpendicular spin component is injected mak-

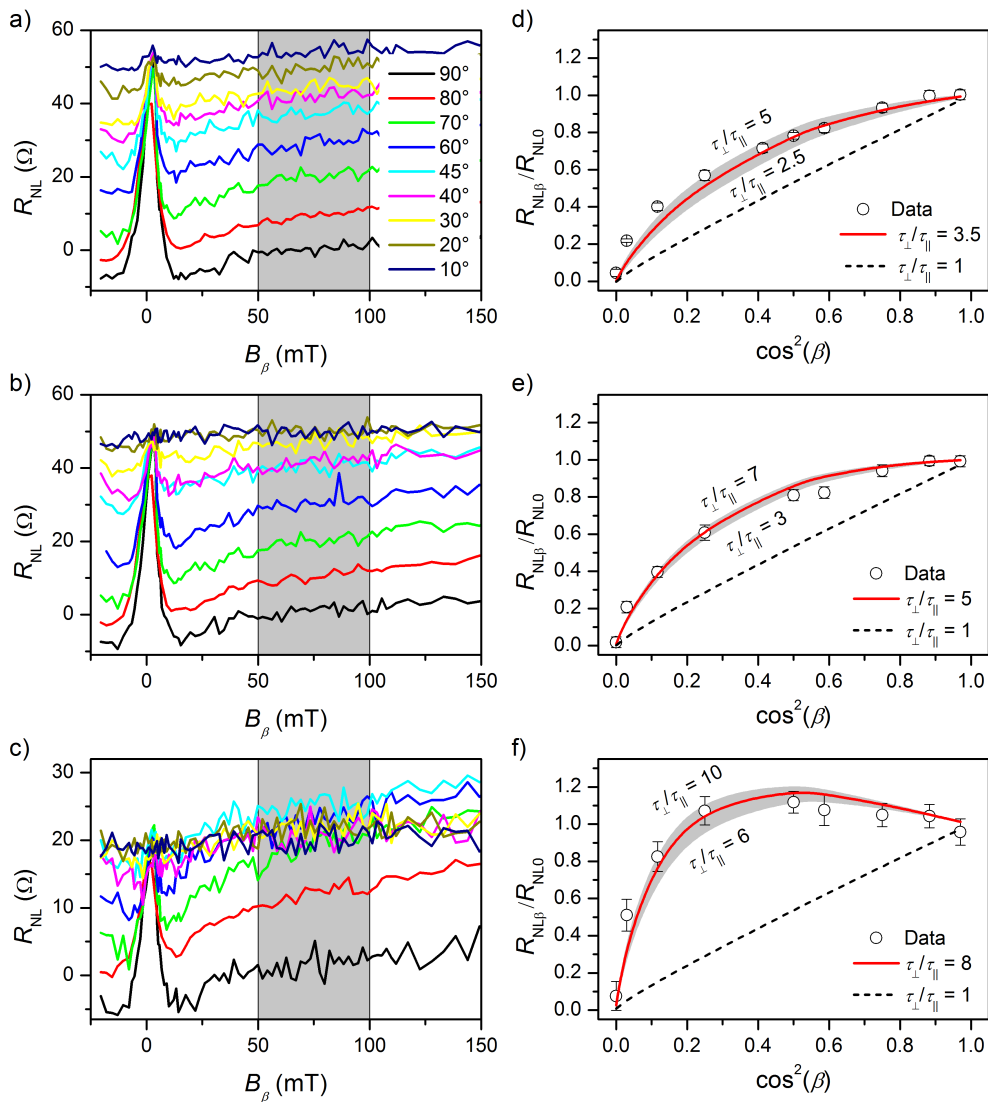


Figure 7.2: Oblique Hanle spin precession data for $n = 6 \times 10^{11} \text{ cm}^{-2}$ (a, d), $n = 4 \times 10^{11} \text{ cm}^{-2}$ (b, e), and the CNP (c, f). R_{NL0} denotes the non-local resistance at zero field and $R_{NL\beta}$ the non-local resistance where the perpendicular spin component has fully dephased. $R_{NL\beta}$ is obtained by averaging R_{NL} over the shaded area (50 mT – 100 mT). Panels d – e show the comparison between the ratios $R_{NL\beta}/R_{NL0}$ and our model for different anisotropy values. The shaded area corresponds to the estimated error margin with the denoted anisotropy values. Note that panels a – c have a small background of 9.3 Ω , 18 Ω and 17.8 Ω subtracted.

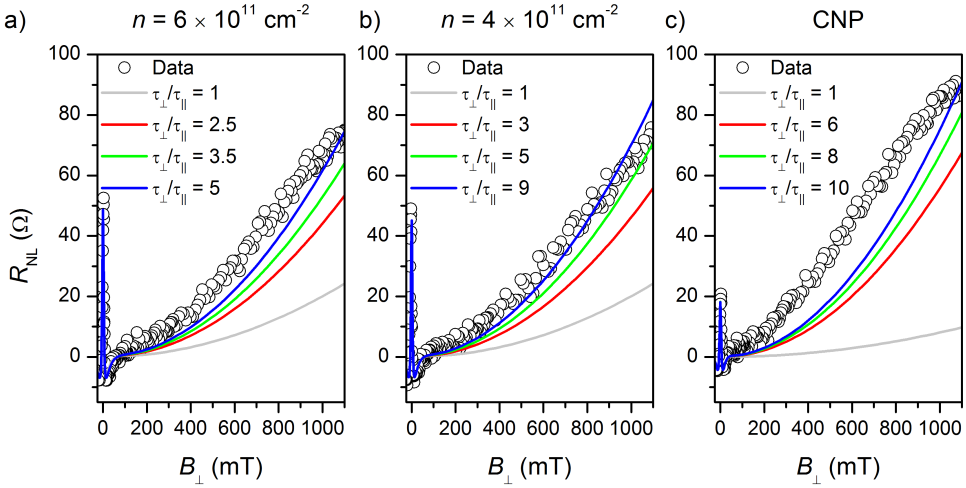


Figure 7.3: High-field Hanle spin precession curves at $\beta = 90^\circ$ and $T = 75$ K for the three discussed carrier concentrations. We simulate the spin precession using the parameters from Figure 7.2. The gray line corresponds to the isotropic case. The perpendicular saturation field of the cobalt contacts is 1.5 T. Note that the same background as in Figure 7.2 has been subtracted.

ing R_{NL} sensitive to the spin-lifetime anisotropy. The data measured up to a large B_{\perp} is shown in Figure 7.3 together with the simulated Hanle curves. It should be noted that for all carrier concentrations $R_{\text{NL}}(B_{\perp} = 1.1 \text{ T})$ clearly exceeds $R_{\text{NL}}(B_{\perp} = 0 \text{ T})$, which is a direct consequence of $\tau_{\perp} > \tau_{\parallel}$. The Hanle curves are simulated for different $\tau_{\perp}/\tau_{\parallel}$ ratios, where the gray lines represent the isotropic case. We attribute the difference between the low- (Figure 7.2) and high-field analysis (Figure 7.3) to two origins. First, our simulations use a simple out-of-plane shape anisotropy model to describe the rotation of the electrode magnetization under B_{\perp} whereas the magnetization behavior can deviate from the idealized system. Second, we observe magnetoresistance of the BLG channel, which can reach up to 50% at high fields and at the CNP. Its possible influence on the measured data is discussed in Section 7.4.9 However, for magnetic fields below 0.1 T at the CNP the magnetoresistance is below 1%. Hence, magnetoresistance does not affect our low-field analysis.

We can estimate the intervalley scattering time τ_{iv} from the extracted τ_{\parallel} and τ_{\perp} by assuming a Dyakonov-Perel type of spin relaxation as predicted theoretically [5, 15]:

$$\frac{1}{2\tau_{\perp}} + \left(\frac{2\lambda_I}{\hbar}\right)^2 \tau_{\text{iv}} = \frac{1}{\tau_{\parallel}}, \quad (7.3)$$

where $1/\tau_{\perp} = 2\lambda_R/\hbar$ with the Rashba spin-orbit coupling λ_R . The relevant spin and charge transport parameters are shown in Table 7.1. We observe the shortest τ_{iv} at

the CNP, which we attribute to two origins: First, λ_I is 12 μeV at the CNP but decays quickly with increasing momentum from the CNP [11]. As a consequence, the effective λ_I is smaller than 12 μeV , and our extracted τ_{iv} should be seen as lower bound. Second, the spin splittings have opposite sign in the conduction and valence bands. Hence, non energy conserving scattering between both bands plays the same role as intervalley scattering when both electrons and holes contribute to the transport. τ_{iv} becomes an effective parameter (τ_{iv}^*) determined by both intervalley and interband scattering (τ_{ib}), $\tau_{iv}^{*-1} = \tau_{ib}^{-1} + \tau_{iv}^{-1}$.

T K	n cm^{-2}	R_{sq} Ω	D_s cm^2/s	τ_{\parallel} ns	τ_{\perp} ns	$\tau_{\perp}/\tau_{\parallel}$	λ_I μeV	λ_R μeV	τ_{iv} ps	τ_p fs
75	CNP	1550	100	1.1	8.8	8	12	-	0.6	-
75	4×10^{11}	900	180	1.9	9.4	5	2	6.5	12	280
75	6×10^{11}	750	210	1.7	6.1	3.5	1	9	45	220
300	4×10^{11}	510	300	1.2	1.4	1.2	2	13	4	400

Table 7.1: Spin and charge transport parameters of the discussed device. τ_{iv} is calculated using Equation 7.3. The density-dependence of λ_I is extracted from Reference [11] at a constant electric field of 25 mV/nm. The momentum scattering time τ_p is obtained assuming $D_s = D_c = v_F^2 \tau_p / 2$, where v_F is the Fermi velocity.

Note that the values of λ_I from Table 7.1 are calculated in pristine BLG with an applied electric field of 25 mV/nm [11]. The accurate determination of λ_I from first principles requires the knowledge of the alignment between the crystal planes of hBN and BLG. However, preliminary *ab initio* calculations support the presence of a spin splitting in the range of 24 μeV at the K and K' points in hBN encapsulated BLG under small electric fields [12].

It should be mentioned that our out-of-plane spin-lifetimes in BLG (up to 9 ns) are close to the largest measured lifetimes of 12 ns in monolayer graphene [37]. Therefore, the spin relaxation length becomes comparable to the device size, and uncertainties such as the spin-lifetime in the adjacent uncovered BLG regions can affect the analysis. Moreover, it is not clear whether the spin relaxation follows purely the Dyakonov-Perel mechanism and if other sources of spin-orbit coupling become relevant for limiting τ_{\parallel} and τ_{\perp} in BLG [38–40].

Lastly, we discuss the temperature-dependence of the spin-lifetime anisotropy. The carrier density-dependence of $\tau_{\perp}/\tau_{\parallel}$ at $T = 5$ K is discussed in Section 7.4.6 and gives comparable results to $T = 75$ K ($\tau_{\perp}/\tau_{\parallel} = 2$ at $6 \times 10^{12} \text{ cm}^{-2}$ and $\tau_{\perp}/\tau_{\parallel} = 8$ at the CNP). Figure 7.4a shows the ratio $R_{NL\beta}/R_{NL0}$ measured at an angle of $\beta = 45^\circ$ and zero back gate voltage ($n = 4 \times 10^{11} \text{ cm}^{-2}$, measured at 5 K and 75 K). We observe a continuous decrease of $R_{NL\beta}/R_{NL0}$ as the temperature increases. At room

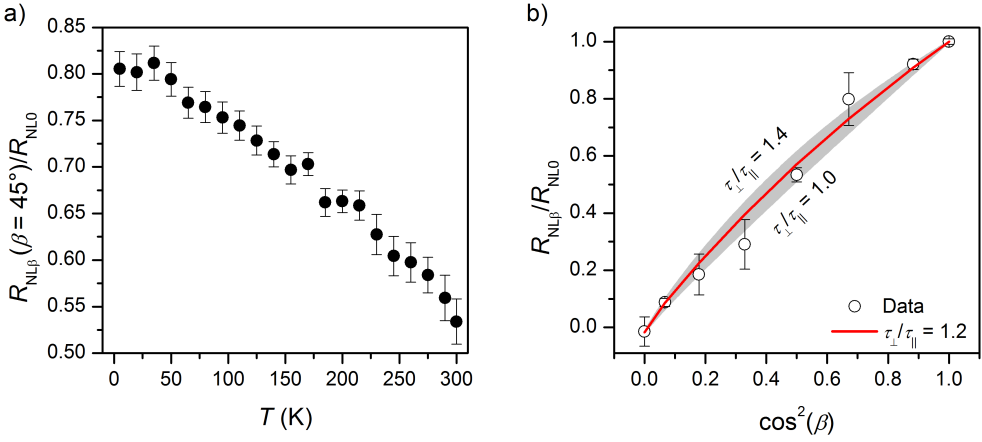


Figure 7.4: a) Temperature-dependence of the ratio $R_{NL\beta}/R_{NL0}$ measured at $\beta = 45^\circ$. The trend towards $R_{NL\beta}/R_{NL0} = 0.5$ with increasing temperature implies that the anisotropy decreases. b) Extraction of the $\tau_\perp/\tau_\parallel$ for $T = 300$ K analogous to Figure 7.2. We conclude that $\tau_\perp \sim \tau_\parallel$ at room temperature.

temperature $R_{NL\beta}/R_{NL0}$ is close to 0.5, which corresponds to an isotropic system where $\tau_\perp/\tau_\parallel \approx 1$.

The full angular-dependence of $R_{NL\beta}/R_{NL0}$ at $T = 300$ K is shown in Figure 7.4b. We extract here $\tau_\perp/\tau_\parallel = 1.2$, where we estimate the error margin to be between 1 and 1.4. Due to an increased gate leakage current, we are unable to reach the CNP at 300 K. Therefore, we assume that the doping of the BLG flake remains constant over the measured temperature range, and, consequently the carrier concentration at room temperature is $4 \times 10^{11} \text{ cm}^{-2}$. We calculate $\tau_p \approx 0.4 \text{ ps} \sim \tau_{iv}/10$ indicating that the decrease of anisotropy at 300 K is caused by the decrease of τ_{iv} . Note that the thermal broadening at 300 K causes a sizable spread in momenta that can lead to lower lifetime anisotropies because λ_I diminishes fast with increasing n .

Theoretical calculations predict in contrast to our results a maximum of the anisotropy around 175 K [18]. Additionally, the anisotropy is predicted to be below 1 at low temperatures due to the suppression of intervalley scattering induced by electron-phonon interaction. Both predictions are not consistent with our observations, which we attribute to two main differences between theory and experiment. Firstly, the calculations are performed at $n = 3 \times 10^{12} \text{ cm}^{-2}$, which is significantly above n for our device. As we have demonstrated in this letter, the anisotropy is strongly affected by n . Secondly, our device is fully encapsulated in hBN, which can affect the phonon modes in BLG. At room temperature, these calculations predict $\tau_\perp/\tau_\parallel$ above 50 with τ_\parallel greater than 10 ns, whereas we find an almost isotropic system and $\tau_\parallel = 1.2 \text{ ns}$.

7.3 Conclusion

In summary, we have studied the spin-lifetime anisotropy in BLG by oblique spin precession. τ_{\perp} is found to be up to 8 times larger than τ_{\parallel} at the CNP. The anisotropy is found to decrease with increasing carrier concentration. An increase in temperature above 75 K causes a decrease of $\tau_{\perp}/\tau_{\parallel}$, and around room temperature τ_{\perp} approaches a similar value as τ_{\parallel} , implying that BLG becomes isotropic. We attribute this to the intrinsic out-of-plane spin-orbit fields in BLG, which, despite of their small magnitude, induce a significant spin-valley coupling that can be used to control spins in BLG [11, 18].

Acknowledgements The authors acknowledge fruitful discussions with M. Gmitra, A.A. Kaverzin, and K. Zollner. This project has received funding from the European Unions Horizon 2020 research and innovation program under Grant No. 696656 and 785219 ('Graphene Flagship' Core 1 and Core 2), the Marie Curie initial training network 'Spinograph' (Grant No. 607904), the DFG SFB 1277 (Projects No. A09 and No. B07) and the Spinoza Prize awarded to B.J. van Wees by the 'Netherlands Organization for Scientific Research' (NWO).

7.4 Supplementary Information

7.4.1 Fabrication Details

Thin hBN flakes are exfoliated from hBN powder (HQ Graphene) onto 90 nm SiO₂ wafers. Suitable hBN flakes are selected by their optical contrast and the thin-hBN/BLG/bottom-hBN stack is fabricated using a polycarbonate-based dry transfer technique [28]. The bottom hBN flake has a thickness of 5 nm. The use of a thin-hBN flake (~ 1 nm, trilayer) as tunnel barrier for spin injection allows us to measure spin transport in a fully encapsulated high quality bilayer graphene device. Figure 7.5 shows the optical image and optical contrast analysis of the used BLG flake exfoliated from HOPG (HQ Graphene) on a 300 nm SiO₂ wafer. Its optical contrast, shown in Figure 7.5c, is twice the single layer contrast, which is determined from the reference flake image in Figure 7.5b. The BLG thickness is confirmed by atomic force microscopy and is ~ 0.8 nm.

After the removal of the transfer polymer in chloroform the sample is annealed (1 h in Ar/H₂ atmosphere) to clean the hBN surface and promote the adhesion of the metal film. Contacts are defined using standard two step PMMA-based e-beam lithography. Markers are exposed and developed in a first step and used for the contact exposure as reference.

The sample is loaded after development of the exposed resist to an e-beam deposition system, and 65 nm of cobalt are evaporated at a base pressure below 10^{-7} mbar.

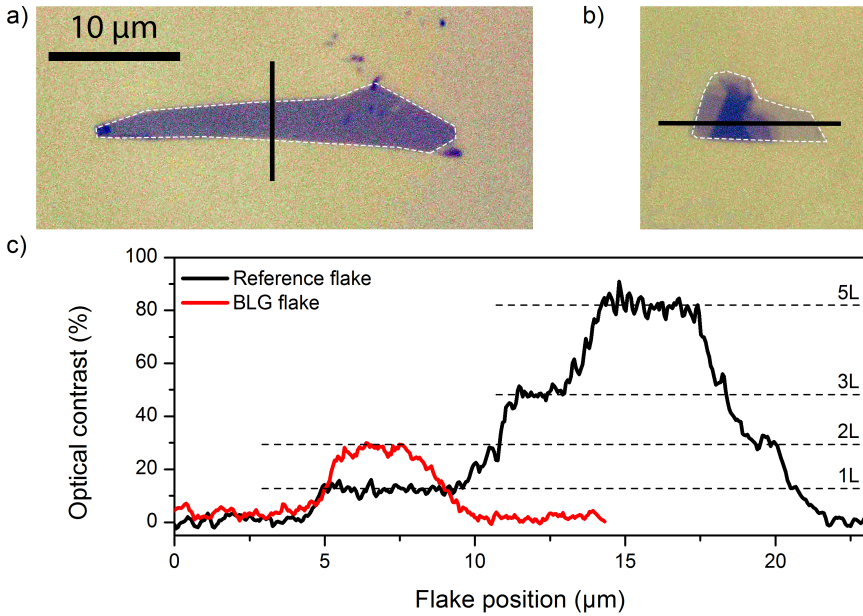


Figure 7.5: a) Optical image of the used BLG flake and b) the contrast reference flake. The dashed white lines mark the edges of the flakes. The black line indicates the position where the optical contrast is measured. c) The contrast analysis confirms the graphene thickness to be two layers.

7

Additionally, a 5 nm aluminum capping layer is deposited to prevent the oxidation of the cobalt. After liftoff in warm acetone, the finished device (Figure 7.6) is loaded into a cryostat where the sample space is evacuated below 10^{-6} mbar.

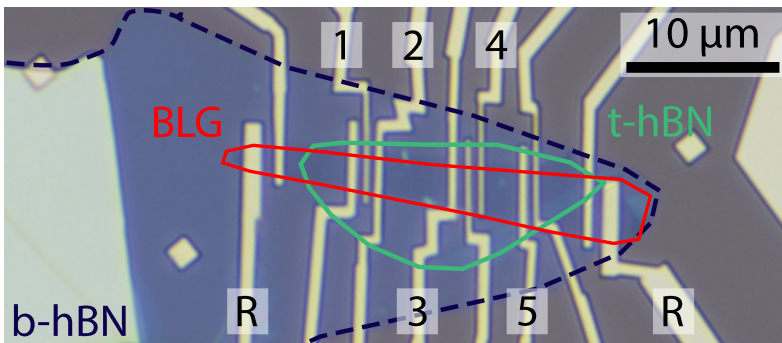


Figure 7.6: Optical image of the finished sample with labeled contacts. The outermost contacts are used as reference electrodes (R) and do not have an hBN tunnel barrier.

7.4.2 Charge and Spin Transport Characterization

The carrier density-dependence of the square resistance R_{sq} of the BLG flake between Contact 1 and Contact 3 is shown in Figure 7.7a. We can tune the carrier concentration n through the 90 nm SiO_2 and the 5 nm thick b-hBN from $6 \times 10^{11} \text{ cm}^{-2}$ in the electron regime to slightly beyond the charge neutrality point (CNP) at $2 \times 10^{11} \text{ cm}^{-2}$ in the hole regime. In this range we observe a gate leakage current below 10 nA. The carrier concentration in BLG is calculated via:

$$n = \epsilon_0 \epsilon (V_{\text{BG}} - V_{\text{CNP}}) / (t_{\text{BG}} \cdot e), \quad (7.4)$$

where $\epsilon_0 = 8.854 \times 10^{-12} \text{ F/m}$ denotes the vacuum permittivity, $\epsilon = 3.9$ the relative dielectric permittivity of SiO_2 , V_{BG} the voltage applied to the back gate, $V_{\text{CNP}} = -2 \text{ V}$ the gate voltage at the CNP and t_{BG} the thickness of the gate oxide. Here we assume that the dielectric permittivity of hBN has approximately the same value as SiO_2 and use the dielectric thickness of $t_{\text{BG}} = t_{\text{SiO}_2} + t_{\text{hBN}} = 95 \text{ nm}$. Note that the gate leakage current increased during the measurements and prohibited in the end to reach the CNP at room temperature.

The basic characterization of the spin transport in the non-local geometry is shown in Figures 7.7b and 7.7c. Here we use, as in the main text, Contact 1 as injector and Contact 4 as detector electrodes. The contacts are separated by $d = 7 \mu\text{m}$. We use the outermost contacts as reference electrodes which do not have a tunnel barrier. We source an AC current of 50 nA between the ferromagnetic injector and the left reference electrode (R). A spin accumulation is injected through the hBN tunnel barrier and diffuses along the BLG flake. The detector probes the spin accumulation underneath its contact relative to the right reference electrode as V_{NL} . In this particular measurement we do not apply any DC bias or gate voltage, n is here $4 \times 10^{11} \text{ cm}^{-2}$ in the electron regime.

We observe a signal of $\Delta R_{\text{NL}} = \Delta V_{\text{NL}} / I_{\text{AC}} = 25 \Omega$ in the spin valve, Figure 7.7b. The spin precession in a perpendicular magnetic field B_{\perp} in (anti)parallel alignment is shown in Figure 7.7c. By fitting the Hanle spin precession data we extract the spin relaxation time $\tau_{s\parallel} = (1.9 \pm 0.2) \text{ ns}$ and a spin diffusion constant $D_{s\parallel} = (201 \pm 32) \text{ cm}^2/\text{s}$ of our device and calculate the in-plane spin relaxation length $\lambda_{\parallel} = \sqrt{D_{s\parallel} \tau_{s\parallel}} \sim 6.2 \mu\text{m}$.

From the measurements of the spin valve signals without any DC bias current in three different configurations with alternating injector and detector combinations we extract an unbiased spin polarization of 21%, which is consistent throughout all measured contacts. A characteristic feature of spin injection from cobalt electrodes into graphene through hBN tunnel barriers is the dependence of the spin injection efficiency on the voltage applied across the hBN tunnel barrier. We found that a positive bias increases the spin injection efficiency and a negative bias also results in a sign change in the spin injection, and consequently, in R_{NL} [32, 33]. For the data

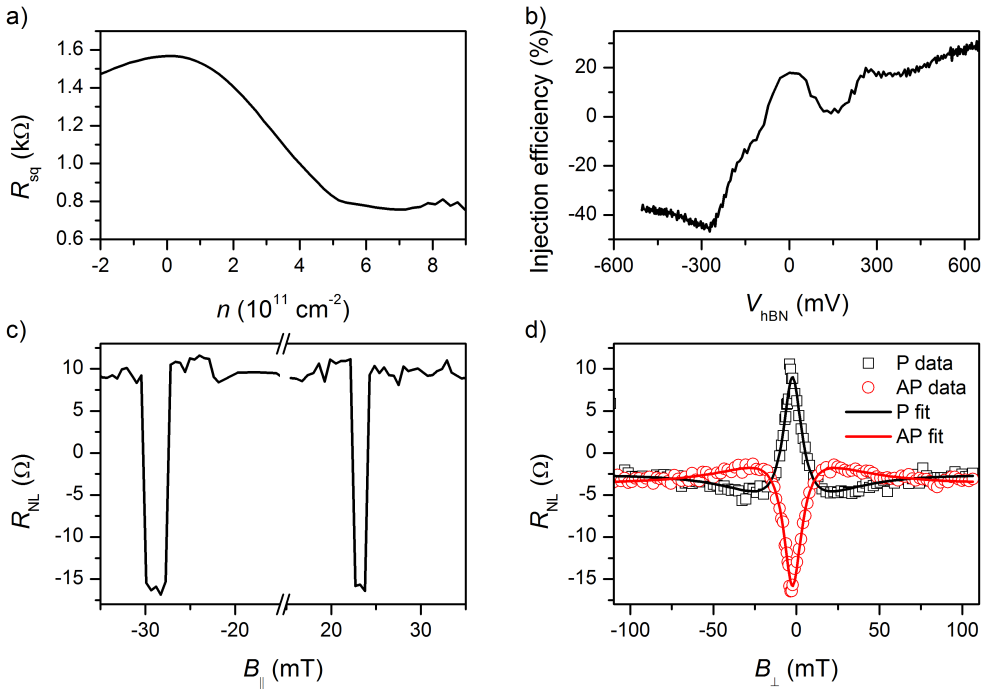


Figure 7.7: a) Dependence of the BLG square resistance on the carrier density n . b) DC bias-dependence of the spin injection efficiency of Contact 2 (injector used in the main text). c) Spin valve measurement of the device. d) Spin precession in (anti)parallel alignment of the injector and detector electrode.

shown in the main text we apply, additionally to the AC current, a DC bias current of $-0.6 \mu\text{A}$, which corresponds to a voltage of -300 mV and increases the unbiased spin injection efficiency from 21% to above -40% . The spin injection efficiency of the injector as a function of the applied DC bias is shown in Figure 7.7b. The DC bias improves the signal to noise ratio which significantly enhances the data quality for measurements at the CNP. Note that the negative DC bias changes also the sign of R_{NL} . To avoid confusion with the conventional sign of R_{NL} , we have inverted the sign for all biased Hanle curves. Our analysis and the resulting claims are not affected by this.

7.4.3 Estimation of the Electric Field

To determine the electric field applied to the BLG flake we try to estimate the doping at the top and bottom side of the BLG. Since we have only one gate, we cannot control the electric field and carrier density independently. Hence, we estimate the

lower bound of the electric field under the assumption that the doping is equal at both sides of the BLG flake. The carrier density is determined by:

$$n = \epsilon_0 \epsilon V_{\text{BG}} / (t_{\text{BG}} \cdot e) + n_{\text{bottom}} + n_{\text{top}}, \quad (7.5)$$

where n_{top} and n_{bottom} are the carrier densities induced by the doping at the top and bottom sides of the BLG flake. The external electric field is defined as:

$$E = \epsilon V_{\text{BG}} / 2t_{\text{BG}} - en_{\text{bottom}} / 2\epsilon_0 + en_{\text{top}} / 2\epsilon_0. \quad (7.6)$$

When assuming that $n_{\text{bottom}} = n_{\text{top}}$, we obtain as lower bound:

$$E_{\text{CNP}} = \epsilon V_{\text{BG}} / 2t_{\text{BG}} \sim 40 \text{ mV/nm}. \quad (7.7)$$

Assuming that all doping arises from the BLG top, $n_{\text{bottom}} = 0$, we obtain as upper bound $E_{\text{CNP}} = 80 \text{ mV/nm}$.

7.4.4 Spin-Lifetime Anisotropy at Zero DC Bias

Figure 7.8a shows the measurement of the oblique spin precession for $I_{\text{DC}} = 0 \mu\text{A}$ and $n = 6 \times 10^{-11} \text{ cm}^{-2}$. The measurement is equivalent to the data presented in Figures 7.2a and 7.2d. The extraction of $\tau_{\perp} / \tau_{\parallel}$ is shown in Figure 7.8b, where the gray area corresponds to the anisotropy boundaries of $\tau_{\perp} / \tau_{\parallel} = 2.5$ and $\tau_{\perp} / \tau_{\parallel} = 5$. The red curve shows $\tau_{\perp} / \tau_{\parallel} \sim 3.5$, the value we also extracted in the main text (Figure 7.2d). Therefore, we can conclude that the applied DC bias does not affect our analysis.

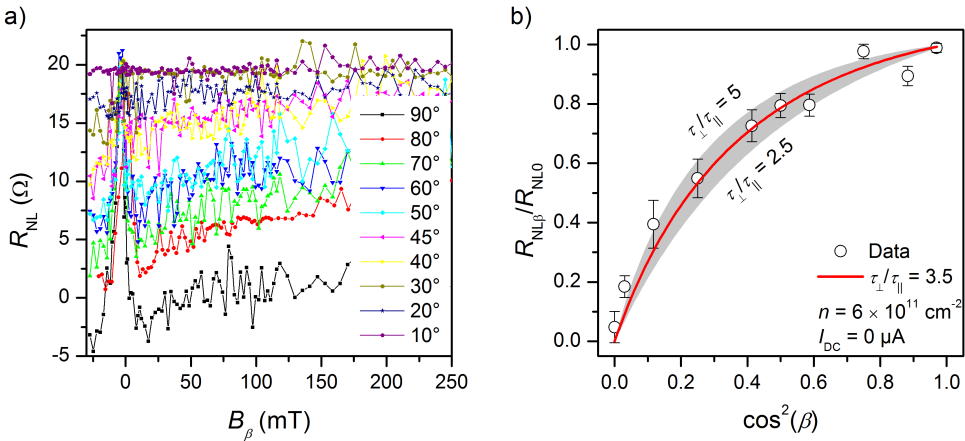


Figure 7.8: a) Measurement of the oblique Hanle with an unbiased injector contact. b) Extraction of the spin-lifetime anisotropy.

7.4.5 Measurements over Different Injector-Detector Spacings

Figure 7.9 contains the $R_{\text{NL}\beta}/R_{\text{NL}0}$ ratio for two different injector-detector spacings measured at $T = 75$ K and $n = 6 \times 10^{11} \text{ cm}^{-2}$. The measurements in Figures 7.3a and 7.3d yield $\tau_{\perp}/\tau_{\parallel} = 3.5$ for the same carrier concentration.

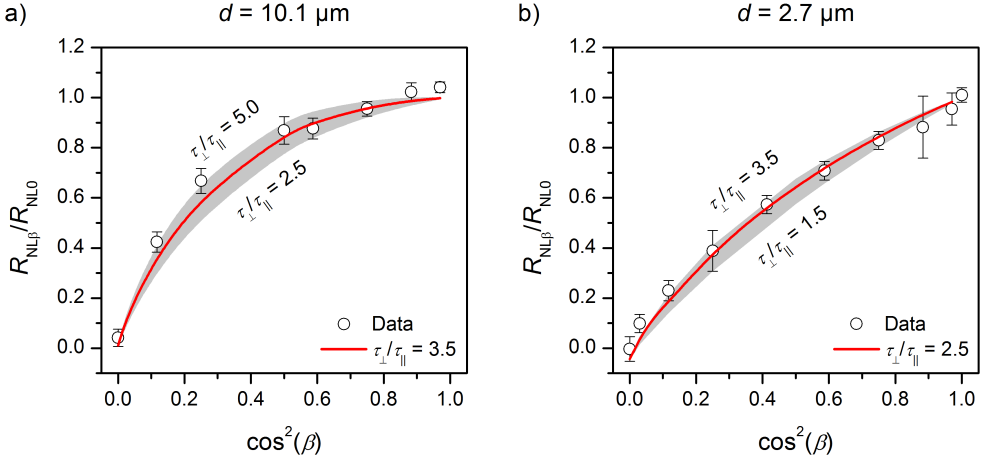


Figure 7.9: Extraction of the spin-lifetime anisotropy for a) $d = 10.1 \mu\text{m}$ (Contact 1 and Contact 5) and b) $d = 2.7 \mu\text{m}$ (Contact 4 and Contact 5) at $n = 6 \times 10^{11} \text{ cm}^{-2}$ and $T = 75$ K. The shaded area corresponds to the estimated error margin.

7

Figure 7.9a is measured at a longer spacing of $d = 10.1 \mu\text{m}$ where Contact 1 is used as injector and Contact 5 as detector. Figure 7.9b uses Contact 4 as injector and Contact 5 as detector, where $d = 2.7 \mu\text{m}$. For $d = 10.1 \mu\text{m}$, we find a similar value as discussed in the main text of $\tau_{\perp}/\tau_{\parallel} = 3.5 \pm 1$.

With a different injector contact and a shorter spacing of $d = 2.7 \mu\text{m}$, we extract a slightly smaller value. Within the experimental uncertainty, all different spacings and injector and detector configurations yield similar anisotropies. As a consequence we conclude that our device is homogeneous and the results from our analysis do not depend on the specific contact pair used.

7.4.6 Low Temperature Anisotropy Measurements

Figure 7.10 contains the $R_{\text{NL}\beta}/R_{\text{NL}0}$ ratio extracted from oblique Hanle measurements at $T = 5$ K using Contact 1 and Contact 3 as injector and detector ($d = 5.2 \mu\text{m}$). In comparison to the measurements at 75 K and $d = 7 \mu\text{m}$, we find comparable values of the spin-lifetime anisotropy and dependence on the carrier density.

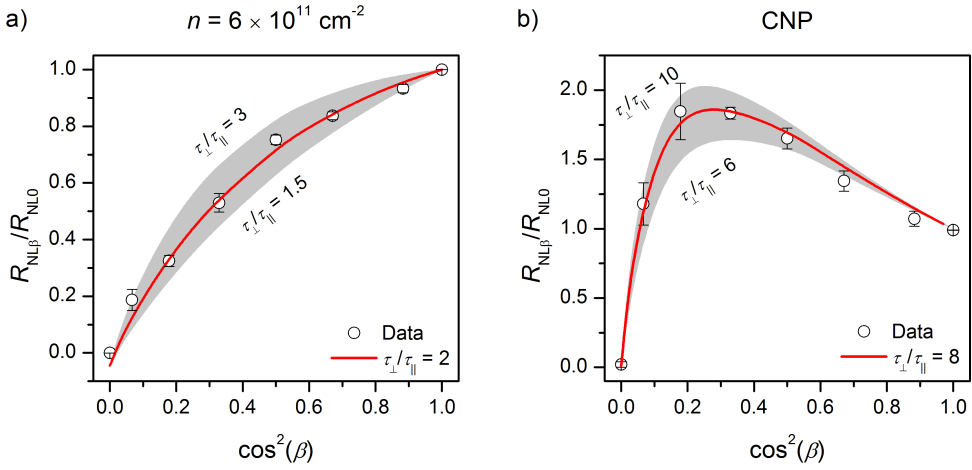


Figure 7.10: $R_{NL\beta}/R_{NL0}$ and the extracted $\tau_{\perp}/\tau_{\parallel}$ ratio at $T = 5$ K gives similar anisotropies as the measurements at $T = 75$ K discussed in the main text.

7.4.7 Carrier Concentration-Dependence of the In-Plane Spin-Lifetime

We have measured the carrier density-dependence of the in-plane spin-lifetime at 5 K and 75 K (Figure 7.11). As a result we obtained that, at both temperatures, τ_{\parallel} increases with increasing density in the conduction band. This result is in contrast with other reports of bilayer graphene on SiO_2 [22–24], where the opposite trend was observed at 5 K.

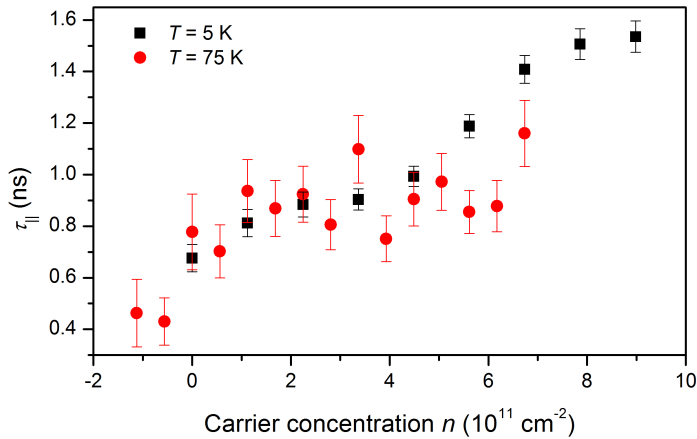


Figure 7.11: Carrier density-dependence of the in-plane spin-lifetime at 5 K (black squares) and 75 K (red circles) measured with B_{\perp} .

7.4.8 Spin Precession Measurements with In-Plane Magnetic Fields

Figure 7.12 contains the measurements of the spin precession with an in-plane magnetic field perpendicular to the injected spin direction, along the device length. In this experiment the magnetic field rotates the injected spins in the B_{\parallel} and B_{\perp} plane. Therefore, both in-plane and out-of-plane spin-lifetimes will be probed. The data shown in Figure 7.12 is measured with Contact 1 as injector and Contact 5 as detector, $d = 10.1 \mu\text{m}$. R_{NL} is extracted from the spin precession measurement in (anti)parallel electrode configuration. Using the model described below that accounts for the actual device geometry, we model anisotropic spin transport by using τ_{\parallel} , p_{in} , and D_s obtained from spin precession measurements in B_{\perp} . We estimate $\tau_{\perp}/\tau_{\parallel} \sim 1.5$ at $6 \times 10^{11} \text{ cm}^{-2}$ and $\tau_{\perp}/\tau_{\parallel} \sim 3$ near the CNP. In comparison to the oblique Hanle measurements we find slightly smaller anisotropies, which is consistent with Reference [21]. We attribute this observation to a change in the sample parameters that occurred prior to this measurement due to unloading of the sample from the cryostat. Nevertheless, the anisotropy remains tunable with the applied gate voltage.

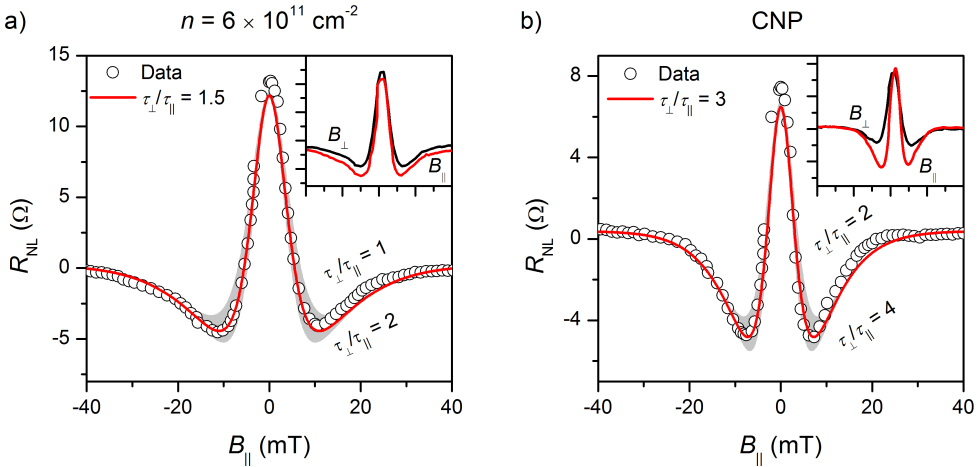


Figure 7.12: Spin precession around B_{\parallel} over $d = 10.1 \mu\text{m}$ at $T = 75 \text{ K}$ and two different carrier concentrations. The gray area corresponds to the estimated error margin, the red line to the fit of $\tau_{\perp}/\tau_{\parallel}$. The insets compare the spin precession curves measured with B_{\perp} (black) and B_{\parallel} (red), the scale is identical to the large panel.

A comparison between the spin precession data measured in an in-plane and out-of-plane magnetic field is shown in the insets of Figure 7.12. As it is expected from the weak spin-lifetime anisotropy at $n = 6 \times 10^{11}$ of $\tau_{\perp}/\tau_{\parallel} = 1.5$, both curves are almost identical and the shoulders of the red B_{\parallel} curve are only slightly deeper. However, at the CNP in Figure 7.12b it can be clearly seen that the spin-lifetime

anisotropy strongly modifies the Hanle line shape by pronouncing the shoulders significantly.

Note that the spin precession curves differ from TMD/graphene devices in [6, 7], where the signal at zero magnetic field is strongly suppressed. The signal in Reference [6] is determined by the in-plane spin relaxation length ($\sim 0.35 \mu\text{m}$), which is six times shorter than the length of the TMD covered region ($\sim 2 \mu\text{m}$). In our BLG device, the in-plane spin relaxation length is $\sim 4 \mu\text{m}$ at the CNP, which is only by a factor 2 shorter than the injector-detector distance. As a consequence, the spin signal at zero magnetic field remains sizable in comparison to the shoulders.

7.4.9 Carrier Density-Dependence of the Magnetoresistance

Figure 7.13 shows the four-terminal magnetoresistance of the graphene channel. The magnetoresistance is negligible and less than 1% at low magnetic fields between 50 mT and 100 mT. Therefore, it does not affect our low-field analysis. At higher magnetic fields of 1.2 T, the magnetoresistance reaches up to 50% at the CNP. At higher carrier densities this value decreases to 25%. Since the possible contribution from magnetoresistance to R_{NL} depends on the background resistances, which are smaller than 20Ω , and the agreement between the low- and high-field analysis, we conclude that the effect is not dominant for the high-field analysis.

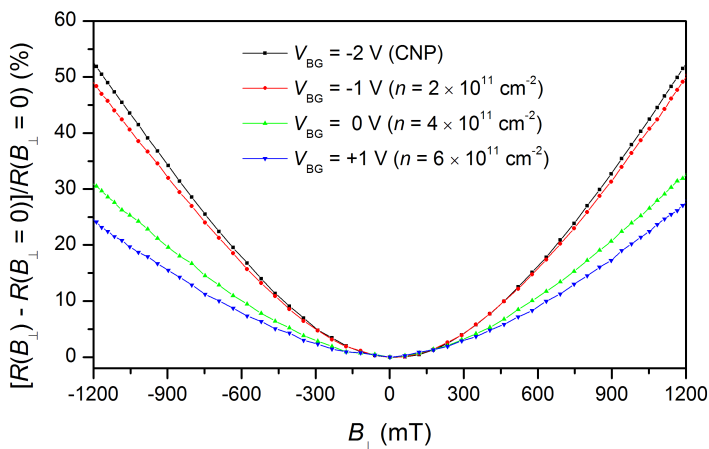


Figure 7.13: Magnetoresistance of the graphene channel at different gate voltages at $T = 75 \text{ K}$.

7.4.10 Modeling of the Spin-Lifetime Anisotropy

As described in the main text, our device length is comparable to the in- and out-of-plane spin relaxation lengths. As a consequence, we have to take the effect of the

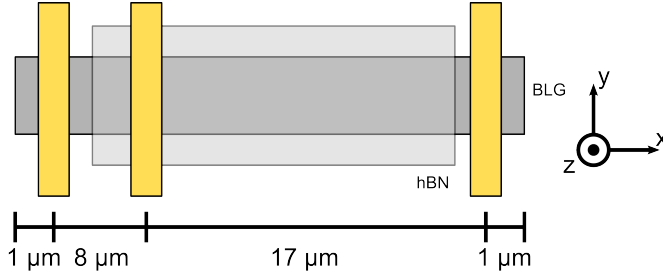


Figure 7.14: Sketch of the simulated device geometry. The reference contact resistances are simulated with 500Ω .

finite length on the extracted parameters into account. Therefore, we use a numerical model that accounts for the following:

1. The spin-lifetime anisotropy in the channel.
2. The finite length of the channel.
3. The effect of spin absorption by the reference contacts that do not have any tunnel barrier.
4. The effect of the magnetic field in the contact magnetization direction, which we estimate to have a maximum angle of 4° for $\beta = 90^\circ$ at $B = 0.1 \text{ T}$.

The model is based on the Bloch equations with anisotropic spin relaxation [20, 41] using the device geometry sketched in Figure 7.14.

$$0 = D_s \frac{d^2 \mu_{sx}}{dx^2} - \frac{\mu_{sx}}{\tau_{\parallel}} + \gamma B_y \mu_{sz} - \gamma B_z \mu_{sy} \quad (7.8)$$

$$0 = D_s \frac{d^2 \mu_{sy}}{dx^2} - \frac{\mu_{sy}}{\tau_{\parallel}} + \gamma B_z \mu_{sx} - \gamma B_x \mu_{sz} \quad (7.9)$$

$$0 = D_s \frac{d^2 \mu_{sz}}{dx^2} - \frac{\mu_{sz}}{\tau_{\perp}} + \gamma B_x \mu_{sy} - \gamma B_y \mu_{sx}, \quad (7.10)$$

where $\mu_s = [\mu_{sx}, \mu_{sy}, \mu_{sz}]$ is the three dimensional spin accumulation, D_s is the spin diffusion coefficient, τ_{\parallel} , and τ_{\perp} are the in- and out-of-plane spin relaxation times, and $\gamma B = g\mu_B B/\hbar$ is the Larmor frequency with the Landé factor $g = 2$, μ_B the Bohr magneton, and \hbar the reduced Planck constant. In our devices, the ferromagnetic contacts go all across the channel. This makes the spin accumulation constant over the sample width w and allows us to simplify our analysis to one dimension. Here we use the average width ($3 \mu\text{m}$) of the relevant region of the BLG flake.

The magnetization direction is determined using the Stoner-Wohlfarth model [42]. Because the magnetic field is applied in the y - z -plane, we solve the Stoner-Wohlfarth equation numerically:

$$\sin(2(\phi - \beta))/2 + h \sin(\phi) = 0, \quad (7.11)$$

where $h = B/B_s$ is the effective external field. B_s is the field at which the electrode magnetization saturates in the direction perpendicular to the easy axis. In our case, we assume that $B_s = 1.5$ T based on earlier measurements of comparable cobalt electrodes with similar thickness. As defined in the main text, β is the angle between the magnetic field and the easy axis of the ferromagnet, ϕ is the angle between the contact magnetization and the applied magnetic field. The angle between the magnetization M and the easy axis is $\gamma = \beta - \phi$. To determine the spin signal in the channel we use the following boundary conditions:

- The spin accumulation μ_s is continuous everywhere.
- The spin current is $I_s = w/(2eR_{sq})(d\mu_{sx}/dx, d\mu_{sy}/dx, d\mu_{sz}/dx)$, where w is the width of the graphene channel, R_{sq} the graphene square resistance, and e the electron charge.
- The spin current has a discontinuity of $\Delta I_s = I \times p_{in}/2[0, \cos(\gamma), \sin(\gamma)]$ at the injection point.
- The spin current is discontinuous at the transparent outer contacts due to the spin back flow effect. This discontinuity is $\Delta I_s = -I_{back} = -\mu_s/(2eR_c)[1, 1, 1]$ where R_c is the resistance of the reference contacts.
- The spin current at the sample edge is zero.

Using these equations, we have performed a finite difference calculation that implements an implicit Runge-Kutta method in Matlab to determine the spin signal.

7.4.11 Effect of the Contact Resistance on the Anisotropy

The interface resistances of the outer contacts are comparable to the resistances of the cobalt leads. Therefore, it is not possible to determine their exact interface resistance from three-terminal measurements. To estimate the resulting uncertainty, we have performed simulations of angle-dependent spin precession with different contact resistances using the model described in the previous section. Here we use the spin transport parameters measured at $n = 6 \times 10^{11} \text{ cm}^{-2}$ and an anisotropy of $\tau_{\perp}/\tau_{\parallel} = 2.5$. The simulated Hanle curves are analyzed by evaluating the average signal between $B_{\beta} = 50$ mT and $B_{\beta} = 100$ mT. The output of this operation is defined as $R_{NL\beta}$ and is normalized to the value of R_{NL0} at $B_{\beta} = 0$ mT to obtain the ratio $R_{NL\beta}/R_{NL0}$. The angle-dependence of $R_{NL\beta}/R_{NL0}$ is shown in Figure 7.15a for

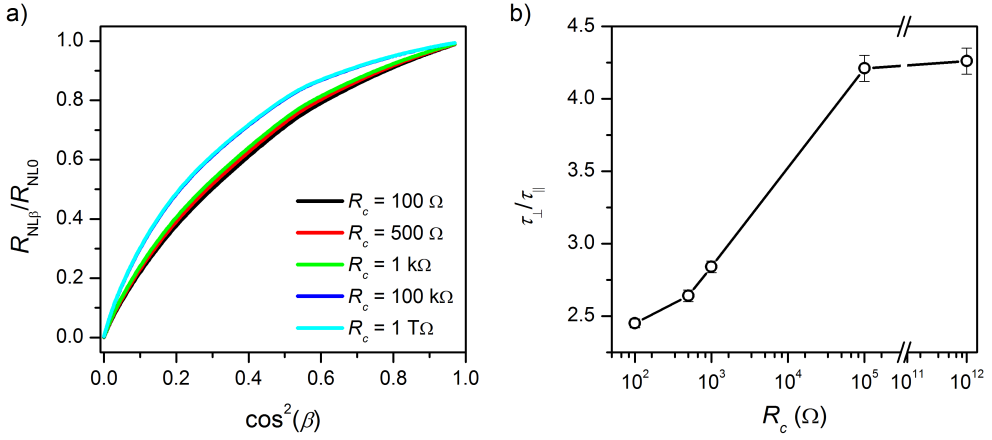


Figure 7.15: a) Effect of the contact resistance of the reference contacts on the ratio $R_{NL\beta}/R_{NL0}$ as a function of the angle β between the magnetic field and the y -axis. b) The values of $\tau_{\perp}/\tau_{\parallel}$ are obtained from fits to Equation 7.12 for different contact resistances R_c . The simulated anisotropy is $\tau_{\perp}/\tau_{\parallel} = 2.5$ and is substantially overestimated by Equation 7.12.

different contact resistances. To determine the effect of these changes in the spin-lifetime anisotropy, we fit the results from a to the infinitely long channel model [20]:

$$\frac{R_{NL\beta}}{R_{NL0}} = \sqrt{\frac{\tau_{\beta}}{\tau_{\parallel}}} \exp\left(-\frac{d}{\lambda_{\parallel}} \left(\sqrt{\frac{\tau_{\parallel}}{\tau_{\beta}}} - 1\right)\right) \cos^2(\beta) \quad (7.12)$$

$$\frac{\tau_{\beta}}{\tau_{\parallel}} = \left(\cos^2(\beta) + \frac{\tau_{\parallel}}{\tau_{\perp}} \sin^2(\beta)\right)^{-1}. \quad (7.13)$$

The results from this calculation are shown in Figure 7.15b and we conclude that:

1. The finite device size, without the presence of invasive contacts, leads to a substantial overestimation of the lifetime anisotropy when using Equation 7.12.
2. The anisotropy extracted from $R_c = 100$ k Ω is almost exactly the same as the high resistance reference ($R_c = 1$ T Ω). As a consequence, the effect of spin back flow into the contact is negligible when $R_c \geq 100$ k Ω . This is the case for all contacts with an hBN tunnel barrier. Furthermore, this justifies that we do not have to take additional contacts between injector and detector electrodes into account.
3. The invasive reference contacts reduce the effect of the lifetime anisotropy on the measured signal, compensating for the confinement effect. Since for those contacts R_c is lower than 500 Ω , the absolute uncertainty in the anisotropy is about 0.25 and lower than the uncertainty in fitting the experimental data.

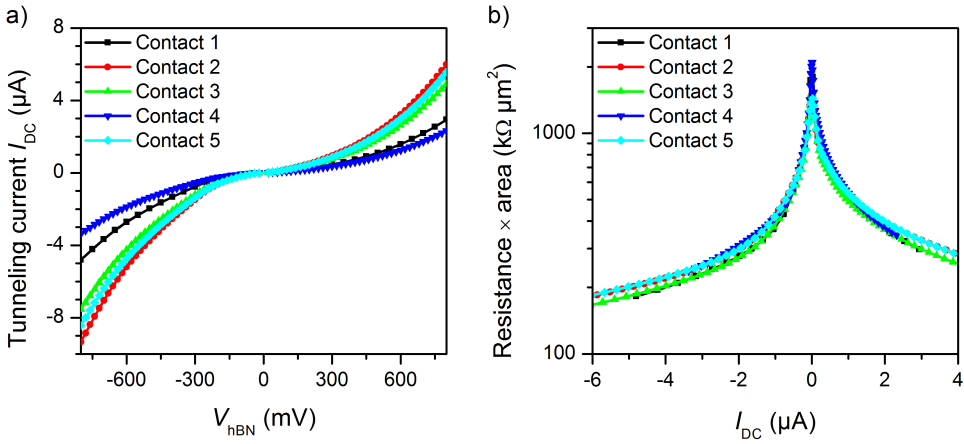


Figure 7.16: a) Current-voltage characteristic of the tunnel barrier. b) Calculated resistance-area product.

7.4.12 Measurement of the Contact Resistances

The tunneling characteristics are measured in a standard three-terminal geometry. The current-voltage characteristics for all contacts are shown in Figure 7.16a and are clearly non-linear.

The calculated resistance-area product is shown in Figure 7.16b, where all five contacts yield comparable results, underlining the homogeneity of hBN flakes as tunnel barriers. The resistance-area product is for all measured DC bias currents well above $100 \text{ k}\Omega \mu\text{m}^2$. Therefore, we conclude that the spin transport is not affected by invasive contacts.

7.4.13 Measurements on a Second BLG Device

Lastly, we discuss the spin precession measurements of a BLG flake deposited on an Yttrium-Iron-Garnet (YIG) substrate. In contrast to our previous study of SLG on YIG, where we found an exchange field of the order of 0.2 T [14], the exchange field of this BLG sample was determined to be below 4 mT and can therefore be neglected in the following analysis. This sample is not fully hBN encapsulated, only a bilayer hBN tunnel barrier is used for spin injection. Compared to the fully encapsulated sample, we observe significantly reduced spin-lifetime, $\tau_{\parallel} = (99.1 \pm 7.5) \text{ ps}$, and $D_s = (532 \pm 41) \text{ cm}^2/\text{s}$. The in-plane spin relaxation length is $2.3 \mu\text{m}$. The carrier concentration cannot be directly measured in this type of samples. Similarly fabricated Hall bars show $n \sim 4 \times 10^{12} \text{ cm}^{-2}$ and we expect the carrier concentration to be in a comparable range.

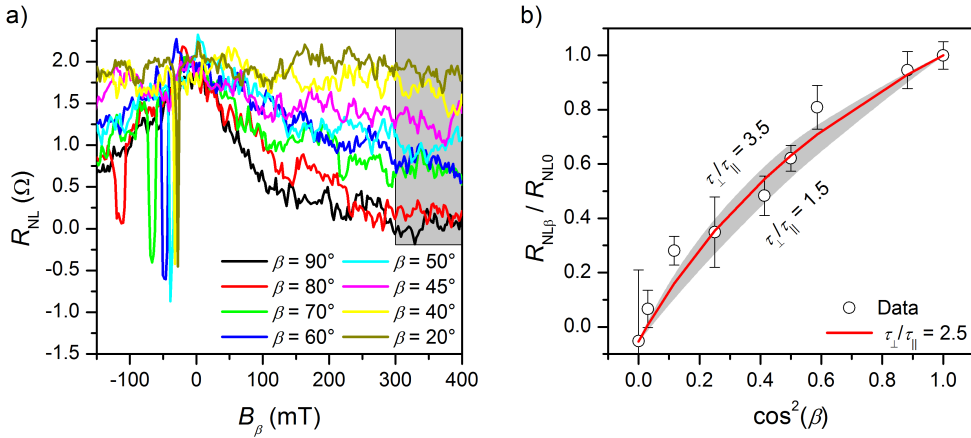


Figure 7.17: a) Measurements of the oblique Hanle spin precession in BLG without a bottom hBN flake. The reduced spin transport parameters require a larger field scan at which the in-plane field component starts to switch the injector and detector electrodes. b) The extracted $R_{NL\beta}/R_{NL0}$ ratio indicates $\tau_\perp/\tau_\parallel = 3.5$. The data is measured at 75 K and an additionally applied DC bias current of $-10 \mu\text{A}$.

Figure 7.17 contains the $R_{NL\beta}/R_{NL0}$ ratio measured at different angles β . Note that the short values of τ cause a broadening of the Hanle curves. Therefore, we have to average the R_{NL} at higher fields to obtain $R_{NL\beta}(300 \text{ mT} - 400 \text{ mT})$. Nevertheless, we observe clearly anisotropic spin transport in the BLG flake, and $R_{NL\beta}$ at $\beta = 45^\circ$ is clearly above 0.5. Figure 7.17b shows the full analysis of the angle sweep. We extract $\tau_\perp/\tau_\parallel = 2.5$ using our model. In comparison to the fully encapsulated BLG sample, we observe in this hBN-covered sample a smaller anisotropy, which we attribute to the difference in the carrier concentration of both samples. At $6 \times 10^{11} \text{ cm}^{-2}$, we measured in the fully encapsulated device $\tau_\perp/\tau_\parallel = 3.5$. An anisotropy value of $\tau_\perp/\tau_\parallel = 2.5$ at around $4 \times 10^{12} \text{ cm}^{-2}$ is therefore in good agreement with the carrier concentration-dependence of the sample discussed in the main text.

References

- [1] D. Xiao, G.-B. Liu, W. Feng, X. Xu, and W. Yao. Coupled spin and valley physics in monolayers of MoS_2 and other group-VI dichalcogenides. *Physical Review Letters*, **108**(19), 196802, 2012.
- [2] J.R. Schaibley, H. Yu, G. Clark, P. Rivera, J.S. Ross, K.L. Seyler, W. Yao, and X. Xu. Valleytronics in 2D materials. *Nature Reviews Materials*, **1**, 16055, 2016.
- [3] Y.K. Luo, J. Xu, T. Zhu, G. Wu, E. Joan, W. Zhan, M.R. Neupane, and R.K. Kawakami. Opto-Valleytronic Spin Injection in Monolayer MoS_2 /Few-Layer Graphene Hybrid Spin Valves. *Nano Letters*, **17**(6), 3877, 2017.
- [4] A. Avsar, D. Unuchek, J. Liu, O. Lopez Sanchez, K. Watanabe, T. Taniguchi, B. Özyilmaz, and A. Kis. Optospintronics in Graphene via Proximity Coupling. *ACS Nano*, **11**(11), 11678, 2017.

- [5] A.W. Cummings, J.H. García, J. Fabian, and S. Roche. Giant Spin Lifetime Anisotropy in Graphene Induced by Proximity Effects. *Physical Review Letters*, **119**(20), 206601, 2017.
- [6] T.S. Ghiasi, J. Ingla-Aynés, A.A. Kaverzin, and B.J. van Wees. Large Proximity-Induced Spin Lifetime Anisotropy in Transition-Metal Dichalcogenide/Graphene Heterostructures. *Nano Letters*, **17**(12), 7528, 2017.
- [7] L.A. Benítez, J.F. Sierra, W. Savero Torres, A. Arrighi, F. Bonell, M.V. Costache, and S.O. Valenzuela. Strongly anisotropic spin relaxation in graphene/transition metal dichalcogenide heterostructures at room temperature. *Nature Physics*, **14**(3), 303, 2018.
- [8] Z. Wang, D.-K. Ki, H. Chen, H. Berger, A.H. MacDonald, and A.F. Morpurgo. Strong interface-induced spin-orbit interaction in graphene on WS₂. *Nature Communications*, **6**, 8339, 2015.
- [9] Z. Wang, D.K. Ki, J.Y. Khoo, D. Mauro, H. Berger, L.S. Levitov, and A.F. Morpurgo. Origin and magnitude of ‘designer’ spin-orbit interaction in graphene on semiconducting transition metal dichalcogenides. *Physical Review X*, **6**(4), 041020, 2016.
- [10] S. Zihlmann, A.W. Cummings, J.H. Garcia, M. Kedves, K. Watanabe, T. Taniguchi, C. Schönenberger, and P. Makk. Large spin relaxation anisotropy and valley-Zeeman spin-orbit coupling in WSe₂/graphene/hBN heterostructures. *Physical Review B*, **97**(7), 075434, 2018.
- [11] S. Konschuh, M. Gmitra, D. Kochan, and J. Fabian. Theory of spin-orbit coupling in bilayer graphene. *Physical Review B*, **85**(11), 115423, 2012.
- [12] M. Gmitra, K. Zollner, and J. Fabian. in preparation, 2018.
- [13] J. Martin, N. Akerman, G. Ulbricht, T. Lohmann, J.H. Smet, K. Von Klitzing, and A. Yacoby. Observation of electron-hole puddles in graphene using a scanning single-electron transistor. *Nature Physics*, **4**(2), 144, 2008.
- [14] J.C. Leutenantsmeyer, A.A. Kaverzin, M. Wojtaszek, and B.J. van Wees. Proximity induced room-temperature ferromagnetism in graphene probed with spin currents. *2D Materials*, **4**(1), 014001, 2017.
- [15] D. Van Tuan, S. Adam, and S. Roche. Spin dynamics in bilayer graphene: Role of electron-hole puddles and Dyakonov-Perel mechanism. *Physical Review B*, **94**(4), 041405, 2016.
- [16] E.I. Rashba. Graphene with structure-induced spin-orbit coupling: Spin-polarized states, spin zero modes, and quantum Hall effect. *Physical Review B*, **79**(16), 161409, 2009.
- [17] M.H.D. Guimarães, P.J. Zomer, J. Ingla-Aynés, J.C. Brant, N. Tombros, and B.J. van Wees. Controlling Spin Relaxation in Hexagonal BN-Encapsulated Graphene with a Transverse Electric Field. *Physical Review Letters*, **113**(8), 086602, 2014.
- [18] L. Wang and M.W. Wu. Electron spin relaxation in bilayer graphene. *Physical Review B*, **87**(20), 205416, 2013.
- [19] N. Tombros, S. Tanabe, A. Veligura, C. Jozsa, M. Popinciuc, H.T. Jonkman, and B.J. van Wees. Anisotropic spin relaxation in graphene. *Physical Review Letters*, **101**(4), 046601, 2008.
- [20] B. Raes, J.E. Scheerder, M.V. Costache, F. Bonell, J.F. Sierra, J. Cuppens, J. van de Vondel, and S.O. Valenzuela. Determination of the spin-lifetime anisotropy in graphene using oblique spin precession. *Nature Communications*, **7**, 11444, 2016.
- [21] S. Ringer, S. Hartl, M. Rosenauer, T. Völkl, M. Kadur, F. Hopperdietzel, D. Weiss, and J. Eroms. Measuring anisotropic spin relaxation in graphene. *Physical Review B*, **97**(20), 205439, 2018.
- [22] W. Han and R.K. Kawakami. Spin relaxation in single-layer and bilayer graphene. *Physical Review Letters*, **107**(4), 047207, 2011.
- [23] T.Y. Yang, J. Balakrishnan, F. Volmer, A. Avsar, M. Jaiswal, J. Samm, S.R. Ali, A. Pachoud, M. Zeng, M. Popinciuc, G. Güntherodt, B. Beschoten, and B. Özyilmaz. Observation of long spin-relaxation times in bilayer graphene at room temperature. *Physical Review Letters*, **107**(4), 047206, 2011.
- [24] A. Avsar, T.Y. Yang, S. Bae, J. Balakrishnan, F. Volmer, M. Jaiswal, Z. Yi, S.R. Ali, G. Güntherodt, B.H. Hong, B. Beschoten, and B. Özyilmaz. Toward wafer scale fabrication of graphene based spin valve devices. *Nano Letters*, **11**(6), 2363, 2011.

- [25] I. Neumann, J. van de Vondel, G. Bridoux, M.V. Costache, F. Alzina, C.M. Sotomayor Torres, and S.O. Valenzuela. Electrical detection of spin precession in freely suspended graphene spin valves on cross-linked poly(methyl methacrylate). *Small*, **9**(1), 156, 2013.
- [26] J. Ingla-Aynés, M.H.D. Guimarães, R.J. Meijerink, P.J. Zomer, and B.J. van Wees. 24- μm Spin Relaxation Length in Boron Nitride Encapsulated Bilayer Graphene. *Physical Review B*, **92**(20), 201410, 2015.
- [27] A. Avsar, I.J. Vera-Marun, J.Y. Tan, G.K.W. Koon, K. Watanabe, T. Taniguchi, S. Adam, and B. Özyilmaz. Electronic spin transport in dual-gated bilayer graphene. *NPG Asia Materials*, **8**(6), e274, 2016.
- [28] P.J. Zomer, M.H.D. Guimarães, J.C. Brant, N. Tombros, and B.J. van Wees. Fast pick up technique for high quality heterostructures of bilayer graphene and hexagonal boron nitride. *Applied Physics Letters*, **105**(1), 013101, 2014.
- [29] E.V. Castro, K.S. Novoselov, S.V. Morozov, N.M.R. Peres, J.M.B. Lopes dos Santos, J. Nilsson, F. Guinea, A.K. Geim, and A.H. Castro Neto. Biased bilayer graphene: Semiconductor with a gap tunable by the electric field effect. *Physical Review Letters*, **99**(21), 216802, 2007.
- [30] J.B. Oostinga, H.B. Heersche, X. Liu, A.F. Morpurgo, and L.M.K. Vandersypen. Gate-induced insulating state in bilayer graphene devices. *Nature Materials*, **7**(2), 151, 2008.
- [31] Y. Zhang, T.-T. Tang, C. Girit, Z. Hao, M.C. Martin, A. Zettl, M.F. Crommie, Y. Ron Shen, and F. Wang. Direct observation of a widely tunable bandgap in bilayer graphene. *Nature*, **459**(7248), 820, 2009.
- [32] M. Gurram, S. Omar, and B.J. van Wees. Bias induced up to 100% spin-injection and detection polarizations in ferromagnet/bilayer-hBN/graphene/hBN heterostructures. *Nature Communications*, **8**(1), 248, 2017.
- [33] M. Gurram, S. Omar, and B.J. van Wees. Electrical spin injection, transport, and detection in graphene-hexagonal boron nitride van der Waals heterostructures: progress and perspectives. *2D Materials*, **5**(3), 032004, 2018.
- [34] B. Raes, A.W. Cummings, F. Bonell, M.V. Costache, J.F. Sierra, S. Roche, and S.O. Valenzuela. Spin precession in anisotropic media. *Physical Review B*, **95**(8), 085403, 2017.
- [35] T. Maassen, I.J. Vera-Marun, M.H.D. Guimarães, and B.J. van Wees. Contact-induced spin relaxation in Hanle spin precession measurements. *Physical Review B*, **86**(23), 235408, 2012.
- [36] T. Zhu and R.K. Kawakami. Modeling the oblique spin precession in lateral spin valves for accurate determination of the spin lifetime anisotropy: Effect of finite contact resistance and channel length. *Physical Review B*, **97**(14), 144413, 2018.
- [37] M. Drögeler, C. Franzen, F. Volmer, T. Pohlmann, L. Banszerus, M. Wolter, K. Watanabe, T. Taniguchi, C. Stampfer, and B. Beschoten. Spin Lifetimes Exceeding 12 ns in Graphene Nonlocal Spin Valve Devices. *Nano Letters*, **16**(6), 3533, 2016.
- [38] D. Kochan, S. Irmer, M. Gmitra, and J. Fabian. Resonant Scattering by Magnetic Impurities as a Model for Spin Relaxation in Bilayer Graphene. *Physical Review Letters*, **115**(19), 196601, 2015.
- [39] D. Van Tuan, F. Ortman, D. Soriano, S.O. Valenzuela, and S. Roche. Pseudospin-driven spin relaxation mechanism in graphene. *Nature Physics*, **10**(11), 857, 2014.
- [40] W. Han, R.K. Kawakami, M. Gmitra, and J. Fabian. Graphene spintronics. *Nature Nanotechnology*, **9**(10), 794, 2014.
- [41] J. Fabian, A. Matos-Abiague, C. Ertler, P. Stano, and I. Zutic. Semiconductor Spintronics. *Acta Physica Slovaca*, **57**(4), 342, 2007.
- [42] E.C. Stoner and E.P. Wohlfarth. A Mechanism of Magnetic Hysteresis in Heterogeneous Alloys. *Philosophical Transactions of the Royal Society A*, **240**(826), 599, 1948.

Abstract

In this chapter preliminary results of projects are discussed, that are related to the previous experimental chapters and address open questions in the field of graphene spintronics.

8.1 Spin Transport Measurements on Graphene on YIG

Chapter 4 and Chapter 5 discussed the effect of the proximity of graphene to YIG. The data was measured in the first harmonic signal in a conventional non-local geometry like the spin valve in Figure 8.1a. However, the simultaneously measured second harmonic signal in Figure 8.1b shows also two characteristic switches, one close to zero magnetic field and one at 45 mT, which is the switching field of the detecting electrode. Cornelissen et al. [1] demonstrated that a temperature gradient in YIG can be used for the thermal generation of magnons. Since the magnitude of the temperature gradient is determined by the square of the current generating the temperature gradient, the signal arising from thermal excitation can be found in a lock-in measurement in the second harmonic signal.

In this context, the data shown in Figure 8.1b can be explained as signal arising from thermal excitation of magnons. The injector circuit in the non-local measurement geometry generates a temperature gradient in the YIG film underneath the graphene. The thermally excited magnons are then detected in the non-local voltage circuit. This interpretation is supported by the fact that the switches in the second harmonic signal coincide with the in-plane coercive field of the underlying YIG film (close to 0.1 mT) and with the coercive field of the detector electrode (45 mT). Furthermore, no switch is present at the coercive field of the injector electrode (~ 40 mT) which supports that spin injection from the injector does not influence the signal substantially. However, no further conclusions can be drawn from this data set. A systematic study is needed to clarify the exact origin of this signal and could give insights into coupling between YIG magnons and graphene spins.

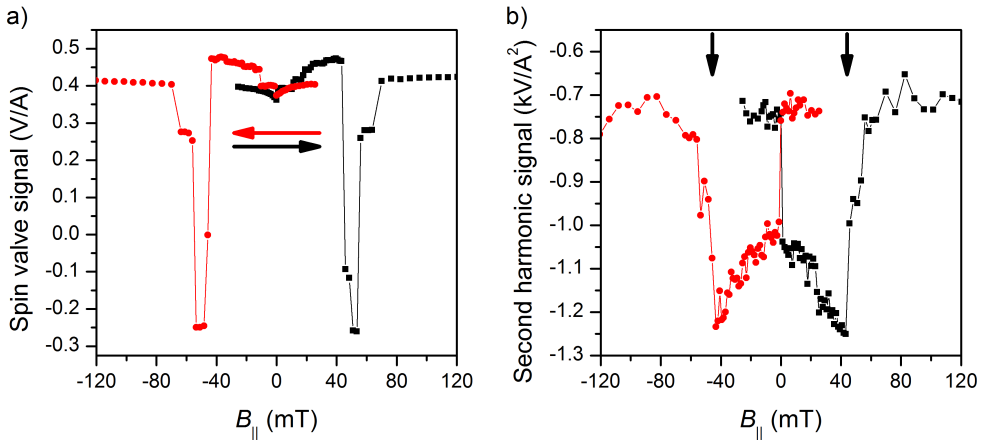


Figure 8.1: a) Measurement of the spin valve signal in a graphene device on YIG at $T = 75$ K and $I_{AC} = 10$ μ A. The exchange field in this device is 0.2 T, the sweep direction of the magnetic field is indicated by the horizontal arrows. b) The simultaneously measured second harmonic signal shows switches close to zero magnetic field and at the same field as the detector electrode in the spin valve measurement (indicated with black arrows). This observation could be explained with a coupling between YIG magnons and graphene spins.

8.2 Anomalous Hall Effect in Graphene on YIG

The first experimental paper on the introduction of magnetism into graphene on YIG presented measurements of a non-linear component in the Hall resistance. This was explained with the occurrence of the anomalous Hall effect, a characteristic feature of magnetic materials. Several graphene Hall bars on YIG were fabricated in the beginning of this research project, which showed also non-linear contributions to the Hall resistance. However, this contribution could not be clearly identified as anomalous Hall effect. Another issue of the early experiments was that the carrier concentration could not be controlled, since no electric field could be applied through the YIG/GGG substrate. Samples that employed a top gate suffered from extended fabrication steps and eventually did not work.

In more recent samples, we have employed liquid ion gating as a straightforward technique to tune the carrier concentration in graphene on YIG. To protect the graphene layer, we added a protective hBN flake on top and employed one dimensional edge contacts through the hBN to graphene. The device is shown in Figure 8.2a, the fabrication steps are discussed in Appendix A.1. As a consequence of the protected graphene, the measured mobility increased by a factor 10 (6 500 cm^2/Vs) compared to unprotected Hall bars (700 cm^2/Vs).

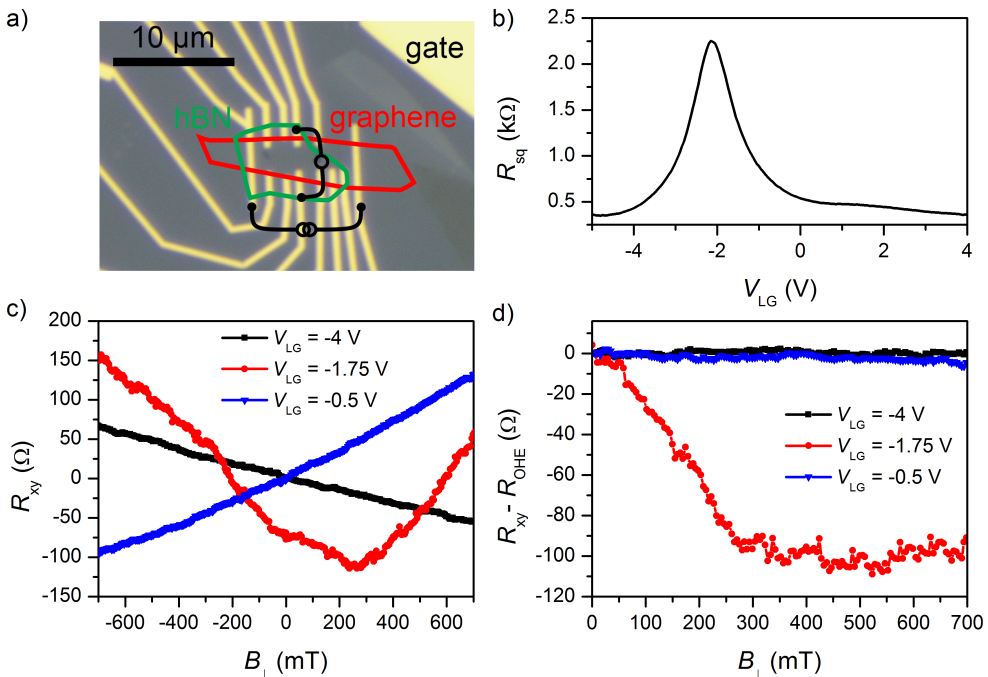


Figure 8.2: a) Optical image of a single layer graphene Hall bar on YIG with a protective hBN flake. The measurement circuit is sketched. b) Gate voltage-dependence of the graphene square resistance using the ionic liquid as top gate. The neutrality point is at $V_{LG} = -2$ V. c) The Hall resistance R_{xy} at $T = 75$ K is measured at different gate voltages, which are applied before cooling down. Near the neutrality point ($V_{LG} = -1.75$ V) magnetoresistive effects play a major role. d) R_{xy} is antisymmetrized, $[R_{xy}(+B) - R_{xy}(-B)]/2$, and the ordinary Hall effect (R_{OHE}) subtracted. A non linear component remains that shows a transition point around 250 mT.

The measurement of the gate voltage-dependence is shown in Figure 8.2b, where a clear modulation of the graphene square resistance can be seen. The charge neutrality point is at $V_{LG} = -2$ V. Since the ionic liquid freezes at around $T = 260$ K, the procedure to measure at low temperature requires the application of V_{LG} at or near room temperature and a slow cooling of the cryostat to avoid breaking of the ionic liquid. The result using this procedure is shown in Figure 8.2c, where the sign of the slope of the transverse resistance R_{xx} clearly changes between $V_{LG} = -4$ V and $V_{LG} = -0.5$ V. The measurement near the neutrality point shows a strong contribution of quadratic magnetoresistance (Section 7.4.9)

After the antisymmetrization of R_{xy} and the subtraction of the linear Hall effect (R_{OHE}), a non linear component remains in Figure 8.2d. The slope has a transition point at $B_{\perp} \sim 250$ mT, which corresponds approximately to the perpendicular

saturation field of the underlying YIG substrate and could therefore be interpreted as anomalous Hall effect. When moving away from the neutrality point, the effect decreases quite rapidly, at $V_{LG} = -4$ V and $V_{LG} = -0.5$ V the signal is close to the background noise of this device. Further experiments suggest a detailed study of the gate voltage-dependence of this non-linear contribution.

Additionally, a follow-up study could investigate of the quantum anomalous Hall effect (QAHE), which has been demonstrated in magnetic topological insulators [2]. Qiao et al. [3] proposed the QAHE in graphene in proximity to the antiferromagnetic insulator BiFeO₃. The QAHE requires an exchange interaction and spin-orbit coupling, both present in graphene on YIG. As a consequence, a topological band gap opens at the neutrality point, where the anomalous Hall resistance is quantized with $2e^2/h$. An approach to further enhance the spin-orbit coupling in these devices replaces the protective hBN flake with a TMD layer.

8.3 Spin Injection and Detection into Graphene Using Two-Dimensional Ferromagnets

One of the most active research field in 2D materials is currently the investigation of magnetic 2D materials. A magnetic tunnel junction of layered materials recently demonstrated spin-dependent tunneling [4] and motivates to investigate the spin injection and detection into graphene through a layered ferromagnet.

As discussed in Chapter 4 and 5, the proximity of graphene to YIG induces magnetism into graphene. A device to study the spin injection from magnetic graphene into non-magnetic graphene could be realized by transferring a graphene flake to YIG and incorporating a small hBN flake to partially separate graphene from YIG. The contacts on the magnetic graphene are non-magnetic, whereas the contacts in the hBN separated region are magnetic to sense an injected spin accumulation. However, the exchange splitting found in Chapter 4 and 5 is rather small ($\sim 10^{-5}$ eV), which could be too small to inject a sizable spin accumulation and could be even further limited by a conductivity mismatch.

The recent discoveries of intrinsic layered ferromagnets triggered an intense research focus on this class of materials. The large exchange splitting observed in magnetic TMDs makes these materials more appealing for spin injection experiments in integrated van der Waals heterostructures. We have studied several compounds that are reported to show magnetism, however, the fabrication of graphene/magnetic TMD devices using our conventional techniques turned out to give inconsistent results. The device yield suffered from the oxidation of the magnetic 2D materials, which implies the need to move fabrication into an oxygen free atmosphere.

Our first characterized device is shown in Figure 8.3a. The device consists of a Fe_{0.25}TaS₂ flake, in contact with a few-layer graphene flake (FLG). Reference elec-

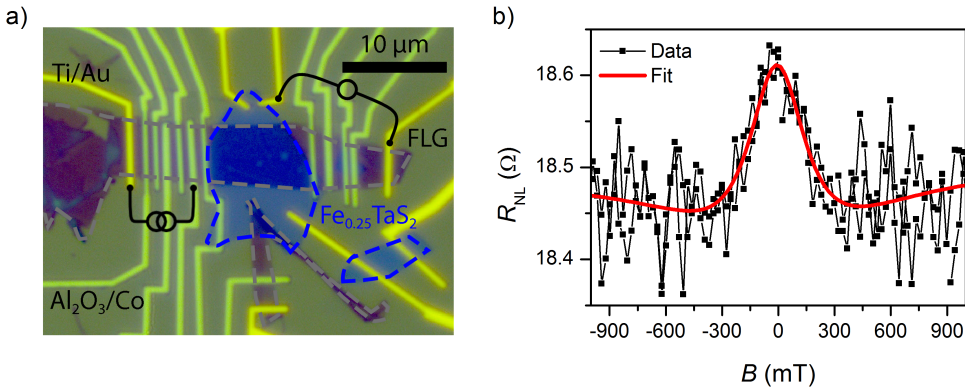


Figure 8.3: a) Optical image of the device. A few-layer graphene flake (FLG) is in contact with $\text{Fe}_{0.25}\text{TaS}_2$. The non-local measurement geometry is indicated. b) Non-local measurement of the device, the data could be explained with spin precession.

trodes and the contacts to the $\text{Fe}_{0.25}\text{TaS}_2$ flake are made of Ti/Au, the ferromagnetic electrodes have a 0.8 nm Al_2O_3 tunnel barrier and a 65 nm cobalt layer with a 5 nm protective aluminum capping layer. The measurement at $T = 75$ K, which is below the Curie temperature of $\text{Fe}_{0.25}\text{TaS}_2$ [5], is shown in Figure 8.3b. The shape of R_{NL} can be either explained by magnetoresistance of the $\text{Fe}_{0.25}\text{TaS}_2$ flake or non-local spin transport between the $\text{Al}_2\text{O}_3/\text{Co}$ electrode and the $\text{Fe}_{0.25}\text{TaS}_2$ flake. While magnetoresistance measurements of $\text{Fe}_{0.25}\text{TaS}_2$ showed no saturation below a magnetic field of several Tesla [6], the signal saturates here around 200 mT. The shape of R_{NL} resembles what would be expected from Hanle spin precession curves and can be fit with the Bloch equations. The parameters of the shown fit are in a realistic range for graphene, $\tau_s = (31 \pm 8)$ ps, $D_s = (350 \pm 11)$ cm²/s. The corresponding spin relaxation length is $\lambda = 1$ μm. Furthermore, the signal vanishes at about 120 K, which is also in agreement with the reported values of the $\text{Fe}_{0.25}\text{TaS}_2$ Curie temperature of ~ 110 K [5, 6]. In conclusion, these preliminary strongly suggest further experiments on graphene/magnetic TMD heterostructures.

8.4 Spin to Charge Conversion in Graphene and TMDs

Spin pumping is an effective technique to inject spins from a magnetic material into an adjacent, non-magnetic layer. A high frequency electromagnetic field h_{RF} is applied through a strip line to a YIG film, driving it into precession when the resonance condition is met. As a consequence, spins are emitted from YIG into adjacent layers which is schematically shown in Figure 8.4a. This effect is often studied in

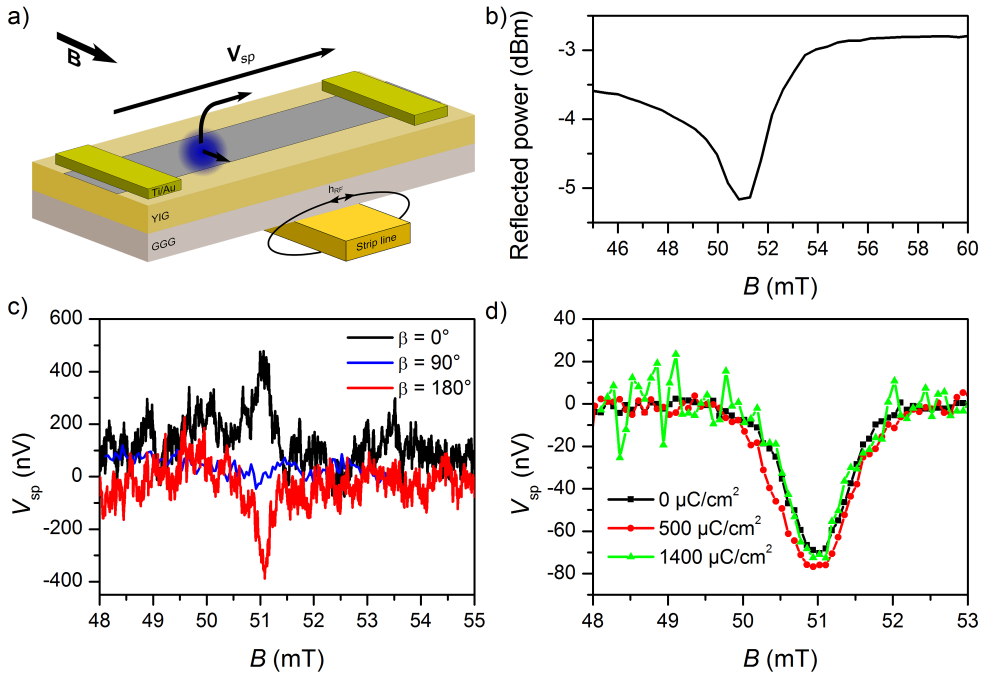


Figure 8.4: a) Schematic of the spin pumping experiment. h_{RF} drives the YIG magnetization into resonance, the YIG magnetization precesses and injects spins into graphene. The inverse spin-Hall effect converts the spin current into a charge current, which is measured as V_{sp} by non-magnetic electrodes. b) A measurement of the RF power, reflected from the YIG film, reveals the resonance condition at $B \sim 51$ mT for an RF frequency of 3 GHz. c) The measurement between two Ti/Au contacts on graphene shows a peak at $B \sim 51$ mT, the resonance field of the YIG film. When the field direction is reversed ($\beta = 180^\circ$), the direction of the injected spins reverses and consequently the sign of V_{sp} . For $\beta = 90^\circ$, the voltage is generated along the contacts and cannot be probed in this geometry. d) The graphene layer is coated with HSQ and gradually exposed to functionalize graphene with hydrogen, which is reported to enhance the spin-orbit coupling. However, in this experiment no signs of an enhanced V_{sp} could be measured.

platinum/YIG films. Platinum has a strong spin-orbit coupling which results in an efficient conversion from spin into charge current via the inverse spin-Hall effect. A similar observation was reported in graphene/YIG by Mendes et al. [7]. The observation of a spin to charge conversion was explained with the Rashba-Edelstein effect. However, a study by Dushenko et al. [8] claimed the spin-Hall effect as origin of the spin to charge conversion.

Figure 8.4b contains a magnetic field scan of the RF power reflected from a 200 nm YIG film. The RF frequency f_{RF} is 3 GHz. At $B = 51$ mT, the reflected power drops

down, due to an absorption of RF power into the YIG film at resonance. Figure 8.4c shows the signal measured with two non-magnetic Ti/Au contacts on graphene on YIG. A voltage of approximately 400 nV is measured that reverses its sign, when the direction of the applied magnetic field and injected spins is reversed. When the magnetic field is rotated perpendicular to the contacts, V_{sp} is generated along the contacts and therefore cannot be measured in this geometry. These three measurements confirm that the origin of the signal is the spin pumping and spin to charge conversion in graphene.

The spin-orbit coupling in graphene is reported to be enhanced by the partial hydrogenation using hydrogen silsesquioxane (HSQ) [9]. When exposed with an electron beam, HSQ emits hydrogen atoms that bond to an underlying graphene layer and can enhance the spin-orbit coupling. To study the influence of an enhanced spin-orbit coupling on the spin to charge conversion, we deposit and expose a 200 nm HSQ layer on graphene on YIG. The exposure doses in Figure 8.4d correspond to an estimated hydrogen density of 0.006% and 0.02%, determined by Raman spectroscopy in Reference [10]. In the HSQ covered sample we measure $V_{sp} \sim 70$ nV without exposure, which does not change significantly with increasing exposure dose and remains nearly constant. This implies that either the graphene does not get functionalized, or that the hydrogenation adatoms do not enhance the spin-orbit coupling in graphene. Since the graphene resistance increased from 20 k Ω before exposure to 35 k Ω after exposure with 1 400 $\mu\text{C}/\text{cm}^2$, and the fact that this increase returned to ~ 23 k Ω within one week after exposure, we have a strong indication that the graphene surface was reversibly hydrogenated. Therefore, it is likely that hydrogenation using HSQ did not affect the spin to charge conversion in graphene on YIG.

Several experimental studies of graphene/TMD heterostructures have consistently shown that the spin-orbit coupling can be enhanced by proximity to a TMD. Therefore, spin pumping and spin to charge conversion experiments employing TMD/graphene structures are interesting for follow-up studies. Moreover, the electrical spin injection and detection using the spin-Hall and Rashba-Edelstein effect in TMD/graphene heterostructures as proposed by Garcia et al. [11] suggest further experiments into this direction.

8.5 Related Spin Lifetime Anisotropy Experiments

Chapter 7 has shown that a strong spin lifetime anisotropy is present in pristine bilayer graphene. This effect is, with similar magnitude, also present in graphene/TMD heterostructures. However, the lifetime of the graphene/TMD devices is in the 10 ps range, $100\times$ smaller than in pristine bilayer graphene, which yield $\tau_{\perp} \sim 9$ ns and $\tau_{\parallel} \sim 2$ ns. This striking difference makes bilayer graphene an appeal-

ing platform to realize novel devices like a spin polarizer, where in-plane spins are blocked and out-of-plane spins transmitted [11].

Recent *ab initio* calculations predict in heterostructures of graphene and the topological insulator Bi_2Se_3 $\tau_{\perp}/\tau_{\parallel}$ above 100 at the graphene Dirac point [12]. In comparison to graphene/TMD heterostructures, the proximity coupling to Bi_2Se_3 is expected to have a stronger dependence on electrostatic gating, which could open a new route to the electrical control of spin currents in graphene.

References

- [1] L.J. Cornelissen, J. Liu, R.A. Duine, J. Ben Youssef, and B.J. van Wees. Long-distance transport of magnon spin information in a magnetic insulator at room temperature. *Nature Physics*, **11**(12), 1022, 2015.
- [2] C.-Z. Chang, J. Zhang, X. Feng, J. Shen, Z. Zhang, M. Guo, K. Li, Y. Ou, P. Wei, L.-L. Wang, Z.-Q. Ji, Y. Feng, S. Ji, X. Chen, J. Jia, X. Dai, Z. Fang, S.-C. Zhang, K. He, Y. Wang, L. Lu, X.-C. Ma, and Q.-K. Xue. Experimental observation of the quantum anomalous Hall effect in a magnetic topological insulator. *Science*, **340**, 167, 2013.
- [3] Z. Qiao, W. Ren, H. Chen, L. Bellaïche, Z. Zhang, A.H. MacDonald, and Q. Niu. Quantum Anomalous Hall Effect in Graphene Proximity Coupled to an Antiferromagnetic Insulator. *Physical Review Letters*, **112**(11), 116404, 2014.
- [4] Z. Wang, D. Sapkota, T. Taniguchi, K. Watanabe, D. Mandrus, and A.F. Morpurgo. Tunneling Spin Valves Based on $\text{Fe}_3\text{GeTe}_2/\text{hBN}/\text{Fe}_3\text{GeTe}_2$ van der Waals Heterostructures. *Nano Letters*, **18**(7), 4303, 2018.
- [5] T. Danz, Q. Liu, X.D. Zhu, L.H. Wang, S.W. Cheong, I. Radu, C. Ropers, and R.I. Tobey. Structural and magnetic characterization of large area, free-standing thin films of magnetic ion intercalated dichalcogenides $\text{Mn}_{0.25}\text{TaS}_2$ and $\text{Fe}_{0.25}\text{TaS}_2$. *Journal of Physics: Condensed Matter*, **28**(35), 356002, 2016.
- [6] L. Liang. Field Effect Controlled Magnetism and Magnetotransport in Low Dimensions. PhD thesis, University of Groningen, 2017.
- [7] J.B.S. Mendes, O. Alves Santos, L.M. Meireles, R.G. Lacerda, L.H. Vilela-Leão, F.L.A. Machado, R.L. Rodríguez-Suárez, A. Azevedo, and S.M. Rezende. Spin-Current to Charge-Current Conversion and Magnetoresistance in a Hybrid Structure of Graphene and Yttrium Iron Garnet. *Physical Review Letters*, **115**(22), 226601, 2015.
- [8] S. Dushenko, H. Ago, K. Kawahara, T. Tsuda, S. Kuwabata, T. Takenobu, T. Shinjo, Y. Ando, and M. Shiraishi. Gate-Tunable Spin-Charge Conversion and the Role of Spin-Orbit Interaction in Graphene. *Physical Review Letters*, **116**(16), 166102, 2016.
- [9] J. Balakrishnan, G. Kok Wai Koon, M. Jaiswal, A.H. Castro Neto, and B. Özyilmaz. Colossal enhancement of spin-orbit coupling in weakly hydrogenated graphene. *Nature Physics*, **9**(5), 284, 2013.
- [10] A.A. Kaverzin and B.J. van Wees. Electron transport nonlocality in monolayer graphene modified with hydrogen silsesquioxane polymerization. *Physical Review B*, **91**(16), 165412, 2015.
- [11] J.H. Garcia, M. Vila, A.W. Cummings, and S. Roche. Spin transport in graphene/transition metal dichalcogenide heterostructures. *Chemical Society Reviews*, **47**(9), 3359, 2018.
- [12] K. Song, D. Soriano, A.W. Cummings, R. Robles, P. Ordejón, and S. Roche. Spin Proximity Effects in Graphene/Topological Insulator Heterostructures. *Nano Letters*, **18**(3), 2033, 2018.

Summary

During the last decades, the developments in the semiconductor industry have spread information technology into all aspects of daily life. Together with the increasing range of applications, the performance requirements have also increased. So far, all achieved improvement was mainly realized by the reduction of the element size on a single chip. This trend followed for decades “Moore’s law”, which predicts the doubling of the amount of chip elements every two years. Nowadays, microchip elements have reached scales below 10 nm and it is clear that the miniaturization potential approaches a fundamental limit. Therefore, novel concepts are required to ensure that the increasing performance requirements of the information age are fulfilled.

In this context, spintronics is a promising field to meet the future requirements to information technology. The term describes the use of the spin degree of freedom, a quantum mechanical property, as information carrier. While spin related effects in metallic systems are already used in hard disks for several years, spin-based logic devices are still in an early research stage. The realization of such devices requires the tackling of several experimental challenges such as an efficient manipulation of spins while simultaneously maintaining a long spin-lifetime. In metallic and semiconductor films, the spin-lifetime is often limited to a few picoseconds at room temperature. On the contrary, graphene is a promising platform for spin-based logic devices due to a relatively weak spin scattering rate and a predicted spin-lifetime up to microseconds.

Graphene consists of carbon atoms, arranged in a hexagonal lattice and only one atom thick. Given the low intrinsic spin-orbit coupling in carbon, graphene is predicted to provide spin-lifetimes several orders of magnitude above typical values for conventional metallic and semiconductor systems. However, the small spin-orbit coupling strength and the lack of a band gap makes the electrical control of spins in graphene rather inefficient.

This thesis addresses two current topics of graphene spintronics: the efficient control of spin by inducing magnetism into graphene (Chapter 4 and Chapter 5) and the spin transport in fully hBN encapsulated high quality graphene (Chapter 6). The high sample quality of encapsulated graphene allows the first measurement of the coupling between the spin and valley degree of freedom in pristine bilayer graphene (Chapter 7).

Spin Transport in Magnetic Graphene

The tuning of the intrinsic properties of graphene is an appealing approach to add new functionalities to graphene. This is of great interest for fundamental and applied studies. In particular, the introduction of magnetism into graphene brings novel, highly desired properties into the field of graphene spintronics.

Chapter 4 and Chapter 5 demonstrate that the proximity of graphene to the ferromagnetic insulator YIG induces a magnetic exchange field into graphene. The presence of an exchange field is proven by an additional spin precession term, which is controlled through the magnetization of the underlying YIG substrate. The strength of the proximity-induced exchange field is in Chapter 4 determined in two independent experiments. It is consistently found to be of the order of 0.2 T. While our measured strength of the exchange interaction is weak compared to the theoretical predictions of several tens of Tesla, it should be noted that the *ab initio* calculations require a super lattice matching which might not be the case in a real device. However, the results also show that a relatively weak exchange field strongly affects spin transport in the graphene channel and can be used for the highly efficient manipulation of spin currents in graphene. In the experiment, the angle between the spin accumulation and the exchange field is controlled. A modulation up to 100% could be found.

The spin injection in Chapter 4 was realized using TiO_2/Co contacts. These contacts have a typical spin polarization below 10% and are therefore limiting the magnitude of the spin signal. Chapter 5 demonstrates that the spin signal in graphene/YIG devices can be enhanced by replacing TiO_2 with an exfoliated bilayer hBN tunnel barrier. When a DC bias is applied to the injector electrode, the differential spin polarization of the tunneling interface increases substantially up to -60% at negative DC bias. This effect was previously demonstrated in fully encapsulated graphene devices (hBN/graphene/bilayer hBN/Co) and is also present in graphene on YIG (YIG/graphene/bilayer hBN/Co), where a reliable and efficient spin injection is vital for measurements of the proximity-induced exchange field. Another advantage of this system is that the spin signal can be controlled electrically through the applied DC bias. The bias-dependence of the spin injection shows a sign change close to an applied DC bias of -80 mV. At this point, the spin signal is suppressed below the noise level and the spin signal can be switched off.

A positive effect of the hBN flake is the protection of the graphene channel from contamination during the sample fabrication. Our polymer-based processes often leave a substantial amount of residues behind that can worsen the transport properties of the graphene flake. For example, the carrier mobility of the device presented in Chapter 4 was $720 \text{ cm}^2/\text{Vs}$, whereas the incorporation of a protective hBN flake enhanced the mobility of graphene on YIG above $5000 \text{ cm}^2/\text{Vs}$. However, the effect on the spin transport properties seems not to be significant. The spin relaxation length of Sample A in Chapter 5 ($0.7 \text{ }\mu\text{m}$) is comparable to the $0.5 \text{ }\mu\text{m}$ measured in Chapter 4.

Spin Transport in Fully hBN Encapsulated Graphene

The improved device yield of the Co/hBN/graphene/YIG devices compared to Co/TiO₂/graphene/YIG has motivated spin transport studies in fully hBN encapsulated devices. The encapsulation of graphene in hBN is a promising approach to fabricate clean and homogeneous devices with large spin-lifetimes, demonstrating spin transport over distances as long as $30 \text{ }\mu\text{m}$.

Chapter 6 studies the spin transport in a fully hBN encapsulated bilayer graphene flake. The bilayer hBN tunnel barrier was here replaced with a trilayer hBN barrier which shows a comparable dependence on the injector DC bias as the bilayer hBN tunnel barrier in Chapter 5. Even though the underlying mechanism is still under debate, the experimental observations provide more information towards the understanding of the origin of the DC bias-dependence of the cobalt/hBN interface. The comparison between the spin polarization in devices using a single layer, bilayer and trilayer hBN tunnel barrier shows, that trilayer hBN provides the best performance, with a differential spin polarization of up to -60% and a DC spin polarization reaching up to 50% . The large polarization allows us to directly measure spin transport in a local two-terminal geometry using only a DC current. This measurement geometry is of particular interest for practical applications, in which a non-local geometry or an AC lock-in measurement cannot be used. Our presented spin transport measurements up to room temperature, are therefore a step towards the realization of graphene-based spintronic devices. Furthermore, we find homogeneous spin transport parameters with spin-lifetimes up to 9 ns . This is amongst the largest reported values, and therefore emphasizes the potential of hBN encapsulated graphene for spintronics.

The high quality of the fully encapsulated device allows to measure in Chapter 7 accurately the in-plane and out-of-plane spin-lifetimes in a fully hBN encapsulated bilayer graphene device. Interestingly, a strong spin-lifetime anisotropy was observed, in which out-of-plane spins have an up to eight times larger spin-lifetime than in-plane spins. This observation is explained with the intrinsic coupling between the spin and valley degree of freedom in bilayer graphene which arises when

the inversion symmetry is broken by a perpendicular electric field. This coupling is present in materials without inversion symmetry, such as monolayer TMDs, and can be imprinted into graphene by proximity coupling in a graphene/TMD heterostructures. A spin-lifetime anisotropy up to 10 was reported in these devices. However, a crucial difference between graphene/TMD and bilayer graphene systems lies in the spin-lifetime: it is up to 100 times larger in pristine bilayer graphene. Therefore, bilayer graphene is an appealing platform for the realization of graphene-based spintronic devices, in which the spin direction (in-plane or out-of-plane) determines the output of the device.

Samenvatting

Gedurende de afgelopen decennia hebben ontwikkelingen in de halfgeleiderindustrie gezorgd voor een verspreiding van de informatietechnologie naar alle facetten van het dagelijks leven. Samen met het toenemend aantal toepassingen zijn ook de eisen aan de prestaties van de microchips steeds zwaarder geworden. Tot dusverre werden alle verbeteringen gerealiseerd door de elementen van een chip te verkleinen. Deze trend wordt sinds tientallen jaren beschreven in de “wet van Moore”: hierin wordt de verdubbeling van de hoeveelheid chipelementen elke twee jaar voorspeld. Tegenwoordig zijn microchipelementen kleiner dan 10 nm en het wordt duidelijk dat de miniaturisatie een fundamentele limiet nadert. Daarom zijn er nieuwe benaderingen nodig die ervoor zorgen dat de ontwikkelingen van de microchip gelijke tred houden met de steeds toenemende prestatie-eisen van dit informatietijdperk.

In deze context is spintronica een veelbelovend onderzoeksveld waarmee wellicht aan de toekomstige eisen van de informatietechnologie kan worden voldaan. De term spintronica beschrijft het gebruik van een spin, een kwantummechanische eigenschap, als informatiedrager. Terwijl spingerelateerde effecten in metallische systemen al enkele jaren worden gebruikt in harde schijven, bevindt de ontwikkeling van spingebaseerde logische circuits zich nog in een pril stadium. De ontwikkeling van dergelijke circuits vereist het aanpakken van enkele experimentele uitdagingen, zoals het efficiënt manipuleren van de spin met tegelijkertijd het behouden van een lange spinlevensduur. In metaal en dunne halfgeleiderfilms is de levensduur van spins meestal niet meer dan enkele picoseconden. Daartegenover is grafeen door zijn relatief zwakke spinverstrooiing een veelbelovend materiaal voor spintronica.

Grafeen bestaat uit één enkele atoomlaag van koolstofatomen, die in een zeshoekig rooster gerangschikt zijn. Koolstof heeft een lage intrinsieke spin-orbit-koppeling waardoor een spinlevensduur van enkele ordes hoger dan de typische waarden van metallische en halfgeleider films verwacht mag worden. Echter, de lage spin-

orbit-koppeling en de afwezigheid van een bandgap zorgen ervoor dat het elektrisch controleren van spins in grafeen tamelijk inefficiënt is.

Dit proefschrift behandelt twee actuele onderwerpen van grafeenspintronica: het effectief controleren van spins door het induceren van magnetisme in grafeen (hoofdstuk 4 en 5) en het transport van spins in volledig ingekapselde hBN (hoofdstuk 6 en 7). De hoge kwaliteit van ingekapseld grafeen stelt ons in staat om in hoofdstuk 7 de eerste meting van de koppeling tussen de spin- en valley-vrijheidsgraden in puur dubbellaags grafeen te beschrijven.

Spintransport in magnetisch grafeen

Het beïnvloeden van de intrinsieke eigenschappen van grafeen is een voor de hand liggende methode om grafeen extra eigenschappen te geven, hetgeen van groot belang is voor fundamenteel en toegepast onderzoek. Vooral het introduceren van magnetisme voegt nieuwe en bovendien zeer gewenste eigenschappen toe aan het onderzoeksveld van spintronica.

Ons onderzoek in het grafeen/YIG systeem in hoofdstuk 4 en 5 laat zien dat grafeen in de nabijheid van de ferrimagnetische isolator YIG een magnetische exchange veld in het grafeen tot gevolg heeft. De aanwezigheid van het geïnduceerde magnetisch exchange veld wordt vastgesteld middels een extra bron voor een spinprecession: deze wordt gecontroleerd door de magnetisatie van een onderliggende YIG laag. De sterkte van het in de nabijheid veroorzaakte magnetische exchange veld is met twee onafhankelijke experimenten vastgesteld en bepaald op een consistente waarde van ongeveer 0.2 T. Hoewel onze gemeten waarde zwak is in vergelijking met theoretische *ab initio* berekeningen van enkele tientallen Tesla, moet worden opgemerkt dat deze berekeningen uitgaan van een superlattice matching, hetgeen in de praktijk wellicht niet het geval is. Desalniettemin laten onze resultaten zien dat een relatief zwak wisselveld het spintransport in het grafeen al sterk beïnvloedt en gebruikt kan worden voor een zeer efficiënte controle van spinstromen in grafeen. In onze experimenten controleren we de hoek tussen spin en exchange veld en constateren we een 100% modulatie van het spinsignaal.

De injectie van de spinstroom in hoofdstuk 4 is gerealiseerd door gebruik te maken van TiO_2/Co contacten. Deze contacten hebben een typische spinpolarisatie van minder dan 10% en beperken daardoor de grootte van het spinsignaal. Hoofdstuk 5 laat zien dat het spinsignaal in grafeen/YIG verbeterd kan worden door de TiO_2 barrière te vervangen door een dubbellaagse barrière van hBN. Als er bovendien een DC bias wordt toegepast op de injector electrode dan neemt de differentiële spinpolarisatie substantieel toe, van 10% tot -60% bij een negatieve DC bias. Dit effect is eerder aangetoond in volledig door hBN ingekapseld grafeen (hBN/grafeen/dubbellaags hBN/kobalt) en is ook aanwezig in een YIG/grafeen/dubbellaags hBN/kobalt systeem, waar een betrouwbare en efficiënte spininjectie van vitaal belang is

voor metingen aan het wisselveld. Een ander voordeel van dit systeem is dat het spinsignaal elektrisch gecontroleerd kan worden door de toegepaste DC bias. De bias-afhankelijkheid van de spininjectie veroorzaakt een tekenomslag bij een DC bias van ongeveer -80 mV. Op dit punt komt het spinsignaal onder het ruisniveau en kan zo worden uitgeschakeld.

Een ander positief effect van een hBN laag is de bescherming van het grafeen tegen verontreiniging tijdens de fabricatie. Onze op polymeren gebaseerde processen laten vaak een aanzienlijke hoeveelheid residu achter, die de transporteigenschappen van grafeen niet ten goede komen. Bijvoorbeeld: de mobiliteit van het grafeen in hoofdstuk 4 was ruim $720 \text{ cm}^2/\text{Vs}$, terwijl de door hBN beschermde grafeen/YIG uit hoofdstuk 5 een 6 keer grotere mobiliteit vertoonde. Het effect op de spintransport eigenschappen lijkt echter niet significant. De spintransportlengte van Sample A in hoofdstuk 5 ($0.7 \text{ }\mu\text{m}$) is vergelijkbaar met de $0.5 \text{ }\mu\text{m}$ die we gemeten hebben in hoofdstuk 4.

Spintransport in volledig hBN ingekapseld grafeen

De verbeterde eigenschappen van Co/hBN/grafeen/YIG in vergelijking tot kobalt/TiO₂/grafeen/YIG hebben ons gemotiveerd om het spintransport in volledig door hBN ingekapseld grafeen nader te onderzoeken. De inkapseling van grafeen met hBN is een veelbelovende methode om homogeen spintransport door grafeen te realiseren, met een lange spinlevensduur die een spintransport mogelijk maakt over afstanden tot wel $30 \text{ }\mu\text{m}$.

Hoofdstuk 6 behandelt het spintransport in volledig hBN ingekapseld dubbellaags grafeen. De dubbellaagse hBN tunnelbarrière werd hier vervangen door een drielaagse barrière, die een vergelijkbare afhankelijkheid van een DC bias als in de dubbellaagse hBN tunnelbarrière uit hoofdstuk 5 laat zien. Alhoewel het onderliggende mechanisme nog steeds ter discussie staat, bieden onze experimentele observaties meer informatie waardoor we de oorsprong van de DC biasafhankelijkheid van de Co/hBN overgang beter begrijpen. Een vergelijking tussen de differentiële spinpolarisatie van enkellaagse, dubbellaagse en drielaagse hBN barrière laat duidelijk zien dat een drielaagse hBN barrière met een differentiële spinpolarisatie tot wel -60% en een DC spinpolarisatie tot wel 50% de beste prestaties levert. De hogere DC spinpolarisatie stelt ons in staat om direct spintransport te meten in een two-terminal geometrie door slechts gebruik te maken van een DC bias. Deze meetwijze is vooral van belang voor praktische toepassingen, waar een non-local geometrie of AC metingen niet kunnen worden gebruikt. De door ons gepresenteerde spintransportmetingen tot kamertemperatuur zijn dan ook een stap dichterbij de realisatie van op grafeen gebaseerde spintronische apparaten. Verder zien we zeer homogene spintransportparameters met een spinlevensduur tot wel 9 ns ,

welke behoren tot de hoogste gerapporteerde waarden en de potentie van door hBN ingekapseld grafeen voor spintronica benadrukken.

Dankzij de hoge kwaliteit van het volledig ingekapseld grafeen zijn we in hoofdstuk 7 in staat om heel precies de spinlevensduren in tweelaags grafeen van in-plane en out-of-plane spins te meten. Interessant is dat we een sterke anisotropie van de verticale spinlevensduur meten, waarbij out-of-plane spins een tot achtmaal langere levensduur hebben dan in-plane spins. Wij verklaren deze waarneming met de intrinsieke koppeling tussen de spin- en valley-vrijheidsgraden in dubbellaags grafeen, die ontstaat wanneer die inversiesymmetrie wordt verbroken door een haaks elektrisch veld. Deze koppeling is ook aanwezig in materialen zonder inversiesymmetrie, zoals eenlaagse TMDs, die ook in grafeen kunnen worden geïnduceerd. In dat systeem werd een verticale spinlevensduur anisotropie tot 10 gerapporteerd. Een belangrijk verschil tussen grafeen/TMD en dubbellaagse grafeensystemen is de spinlevensduur, die in puur dubbellaags grafeen tot 100 keer groter is. Daarmee is dubbellaags grafeen een aantrekkelijk platform voor het realiseren van op grafeen gebaseerde spintronische apparaten waar de spinrichting (in-plane of out-of-plane) het uitgangssignaal bepaalt.

Appendix A

Detailed Fabrication Techniques and Recipes

A.1 Fabrication of One-Dimensional Contacts

One dimensional contacts describe a configuration where the overlap between metallic electrode and the 2D material is minimized and the contact is realized laterally in the plane. This technique can avoid doping of the material by the contact and results in a homogeneous system. We have used the approach of one dimensional contacts to study high quality graphene devices on YIG where a thin hBN flake of a few nanometers protects the graphene from contamination during the fabrication process. A direct comparison between protected and unprotected devices yields an enhancement of the mobility of approximately one order of magnitude, from $700 \text{ cm}^2/\text{Vs}$ to over $5000 \text{ cm}^2/\text{Vs}$.

The fabrication involves the stacking of a few-layer hBN flake (5 – 6 layers) with a graphene flake on a YIG substrate. After EBL of the contacts and the development, the sample is loaded into a RIE system and etched in a 5 W oxygen plasma for 30 s. The hBN flake and underlying graphene is etched at the exposed contacts. The sample is directly loaded into the e-beam deposition system. The standard PMMA resist can withstand up to 120 s of oxygen plasma while maintaining a good liftoff after the deposition of 5 nm titanium and 35 nm gold.

A.2 Liquid Gating of Graphene on YIG

We have tried different approaches of applying an electric field to a graphene flake on a YIG substrate. To gain the ability to tune the carrier concentration in our graphene/YIG devices, we have followed several different routes, which were mostly unsuccessful. Our tests involved the transfer of a thick hBN flake on a fully fabricated Hall bar sample and evaporating the gate electrode on top of the hBN flake and also using HSQ resist as gate dielectric, which after the exposure with an electron beam becomes SiO_2 . In both cases the initially already low quality of the Hall bar contacts was further degrading by the additional fabrication steps. All devices that have been fabricated had either no working Hall bar pairs or a short between the gate electrode and the graphene channel.

Liquid gating describes a technique where the gate voltage is applied through a side gate which aligns the ions in an ionic liquid and applies an electric field to the graphene channel. One further advantage of liquid gating is that large electric field can be realized since the voltage drop responsible for the electric field occurs at the interface between the ionic liquid and the graphene. Compared to gating through 300 nm silicon oxide the distance of the voltage drop to the material is on the nanometer scale, which enhances the gating efficiency.

The material of choice is lithium perchlorate (LiClO_4 , 431567, Sigma Aldrich Co.) dissolved in polyethylene oxide with a molecular weight average of 100 000 (PEO, 181986, Sigma Aldrich Co.). The solution is deposited on the sample after the fabrication and requires only the presence of an electrode near the graphene flake. A typical gating efficiency of this liquid gate with an additional 2 nm hBN spacer is of the order $3 \times 10^{12} \text{ cm}^{-2}/\text{V}$, whereas a 300 nm thick SiO_2 gate yields $6 \times 10^{10} \text{ cm}^{-2}/\text{V}$, almost two orders of magnitude less. The ionic liquid is transparent in for visible light and freezes between 260 K and 270 K. The measurement at low temperatures requires therefore the application of the gate voltage at room temperature and the subsequent cooling to the desired temperature. During the cooling the device resistance and the gate leakage current should be monitored to notice a breaking of the ionic liquid. The gate leakage current is usually of the order of 10 nA, when the liquid freezes the current jumps to zero and the applied gate voltage can then be ramped down. When the liquid breaks, jumps are visible in the device resistance.

- PEO: LiClO_4 :de-ionized water is mixed with the ratio 9 mg:1 mg:300 ml. Instead of water, methanol can also be used as the solvent.
- To avoid the dewetting of ionic polymer gel from the surface, the sample is cleaned with acetone and isopropanol. The sample is dried with nitrogen and annealed on a hot plate (30 s at 100°C).
- The ionic polymer gel is spun on sample for 120 s at 6 000 rpm. The thickness is around 350 nm.
- The ionic liquid can be removed by rinsing the chip in acetone and isopropanol. The liquid gate is then applied again to the sample.
- If the liquid gate broke due to high voltage or de-wetting, annealing at 100°C inside the cryostat melts the polymer gel and can revive the broken gate.

A

A.3 YIG Cleaning Recipe

- Cutting of the YIG/GGG substrates with a protective PMMA layer on top.
- Cleaning in acetone and isopropanol in an ultrasonic bath (5 min, power 9).
- Oxygen plasma cleaning (3 min, 40 W).

- Annealing for 15 min in a 500°C furnace.
- Storing in a 180°C furnace until transfer.

A.4 Transfer of CVD Graphene from Copper Foil

- Spinning and baking of a protective PMMA layer (4 000 rpm, 30 min at 180°C).
- Cleaning of the backside of the copper foil in oxygen plasma (40 W, 180 s).
- Etching of the copper in 1M ammonium-persulfate for at least 3 hours.
- Transfer of the floating graphene/PMMA lamella using a silicon substrate to fresh deionized water. This step is repeated three times with at least three hours between the transfers.
- Transfer the graphene/PMMA lamella to the target substrate.
- Annealing of the chip on a hotplate for 5 min at 60°C, 90°C and 120°C, and for 30 min at 180°C.
- Removing of the PMMA layer either in warm acetone (45°C, 1 h) or by annealing in the tube furnace (2 h at 400°C, 500 sccm Ar/H₂ flow).

A.5 Electron Beam Lithography on YIG

- This recipe was used in Chapter 4 and Chapter 5.
- Spin coating of 4% PMMA (AR-P 679.04, Allresist GmbH) onto the substrate (6 000 rpm, 60 s).
- Baking of the chip for 4 min at 180°C.
- Spin coating of Elektra 92 (Allresist GmbH) onto the substrate (4 000 rpm, 60 s).
- Baking of the chip for 90 s at 180°C.
- Exposure at 30 kV with an area dose of 400 $\mu\text{C}/\text{cm}^2$.
- Rinsing for 30 s in de-ionized water to remove the Elektra 92 film.
- Developing for 60 s in 3:1 mixed isopropanol:methyl isobutyl ketone.
- Stopping the development process by rinsing the chip for 30 s in pure isopropanol.

A.6 Standard Electron Beam Lithography Recipe

- This recipe was used in Chapter 6 and Chapter 7.

- Spin coating of 4% PMMA (AR-P 679.04, Allresist GmbH) onto the substrate (6 000 rpm, 60 s).
- Baking of the chip for 4 min at 180°C.
- Exposure at 30 kV with an area dose of 500 $\mu\text{C}/\text{cm}^2$.
- Developing for 60 s in 3:1 mixed isopropanol:methyl isobutyl ketone.
- Stopping of the development process by rinsing the chip for 30 s in pure isopropanol.

A.7 High Resolution Electron Beam Lithography

- Spin coating of 4% PMMA (AR-P 679.04, Allresist GmbH) onto the substrate (6 000 rpm, 60 s).
- Baking of the chip for 4 min at 180°C.
- Spin coating of Elektra 92 (Allresist GmbH) onto the substrate (4 000 rpm, 60 s).
- Baking of the chip for 90 s at 180°C.
- Exposure at 30 kV with an area dose of 1 500 $\mu\text{C}/\text{cm}^2$.
- Developing for 90 s in 10°C cold 3:1 mixed isopropanol:methyl isobutyl ketone.
- Stopping the development process by rinsing the chip for 30 s in pure isopropanol.
- The exposed lines with a nominal width of 50 nm lines had a real width of 60 nm, measured by electron microscopy.

A.8 Negative Electron Beam Lithography with HSQ

- Mixing of 16% hydrogen silsesquioxane (FOX-16, Dow Corning Co.) with methyl isobutyl ketone depending on the desired film thickness in a ratio between 1:1 (200 nm) to 1:10 (50 nm).
- Spin coating of the mixed solution onto the substrate (6 000 rpm, 60 s).
- Exposure at 30 kV with an area dose of 25 $\mu\text{C}/\text{cm}^2$.
- Developing for 2 min in tetramethylammonium hydroxide (Microdeposit MF-CD-26, MicroChem Corp.).
- Stopping of the development process by rinsing the chip for 30 s in deionized water.

Acknowledgements

Four and a half years have passed since my first visit to Groningen that influenced my life for the next years. In the end, time has passed incredibly fast, and I am truly grateful for all the lucky coincidences that have led me to pursue a PhD at the RUG. My way has been guided by several people whom I wish to thank with the following lines.

Bart, you have been an outstanding supervisor. Even though it was sometimes challenging for me to follow your thoughts, I enjoyed our discussions. Your physical understanding is remarkable and your critical feedback gave my manuscripts and talks the finishing touch. Ivan, I wish we could have worked together in Groningen, but I am glad to see you making your career in Manchester. Thank you for coming back to Groningen for my defense and remaining as my Copromoter.

I thank the reading committee Prof. J. Fernández-Rossier, Prof. B. Noheda Pinuaga, and Prof. S.O. Valenzuela for reviewing my thesis and giving feedback. For their support with organizing the defense of my thesis, I thank my paranymphs Carmem and Pep.

Over the last four years, I have received an enormous amount of input for my projects, for which I want to acknowledge Pep and Alexey. Especially the last half year of my PhD, has been a great pleasure and incredibly productive, leading to most of the publications described in this thesis. Pep, I really enjoyed the countless conferences and workshops we attended together and I wish you all the best pursuing your academic career. Alexey, your critical feedback was always appreciated. Good luck also for your future!

I want to thank the “Physics of Nanodevices” group for the discussions and suggestions I have received, but also the nice time we spent together outside of the labs. I truly enjoyed the weekly FND circuit training sessions with Jantje, Jing, Ludo, Martijn, Nynke, Rick, Roald, and Xu, which were a great help to balance mental exercises with physical training. But also the frequent cooking sessions with Antonio, Carmem, Jantje, Jorge, Xu and Zahra were great to discover genuine Italian dishes and Chinese delivery services. For their efforts to fix my attempts of using the Dutch language I thank Tom Bosma, Els van Rooij and Tom Schouten. I am grateful for the

administrative and technical support that I have received from Herman Adema, Andrea Dijkema, Johan Holstein, Anna McEwan-Bos, Martijn de Roos, Tom Schouten, and Hans de Vries. I thank Niko, Paul and Rudolf from HQ Graphene for supplying the crystals for this thesis and their input for fabrication techniques. Furthermore, the valuable feedback on my thesis manuscript from Alexey, Carmem, Fabian, Imke, Pep, and Rike is greatly acknowledged.

I thank the AMO GmbH in Aachen for their hospitality during my secondment in Aachen and especially the support from Daniel Neumaier, Muhammad Mohsin, Mehrdad Shaygan, and Zhenxing Wang.

For the last two years I have served as a board member of the Graduate School of Science and Engineering and the PhD council, which gave me a lot of insights into the faculty. I truly enjoyed contributing to the optimization of the PhD education and want to acknowledge here especially Petra Rudolf, Marco Koopman, Ika Neven, and Peter Timmerman from the GSSE and Carmem, Daniel, Frita, Monique, Olivier, Renate, Sabrina, Saurabh, Vincent, Yvonne, and Zsofia from the PhD council.

I would like to thank the funding agencies that supported me over the last eight years: For the time in Göttingen and Greifswald, I acknowledge funding from the DFG SFB 602, the WE-Heraeus foundation, the DFG SPP 1538 "Spin Caloric Transport" and the DFG SPP 1666 "Topological Insulators". My research projects at the University of Groningen were funded by the EU Commission's Marie Curie initial training network "Spinograph" (Grant No. 607904), with additional funding from the European Unions Horizon 2020 research and innovation program under Grant No. 696656 and Grant No. 785219 ("Graphene Flagship" Core 1 and Core 2), and the "Netherlands Organization for Scientific Research" (NWO). I would like to thank especially the coordinator of the "Spinograph" program, Joaquín Fernández-Rossier, for organizing the various training events and the "Spinograph" fellows for the great time we had together at conferences, in- and outside of the lecture rooms.

On a personal level, I would like to thank my friends in Groningen for the great time they kept me outside of the lab. *Meinen Freunden und meiner Familie danke ich für die forwährende Unterstützung, die ich in den letzten zehn Jahren im Studium erfahren habe.*

Johannes Christian Leutenantsmeyer
Groningen, The Netherlands
August 6, 2018

List of publications

1. "Efficient Spin Injection into Graphene through Trilayer hBN Tunnel Barriers",
J.C. Leutenantsmeyer, J. Ingla-Aynés, M. Gurram, and B.J. van Wees,
Accepted for publication in Journal of Applied Physics, highlighted as *Editor's Pick*.
2. "Bias-Dependent Spin Injection into Graphene on YIG through Bilayer hBN Tunnel Barriers",
J.C. Leutenantsmeyer, T. Liu, M. Gurram, A.A Kaverzin, and B.J. van Wees,
Physical Review B **98**(12), 125422, 2018.
3. "Observation of Spin-Valley-Coupling-Induced Large Spin-Lifetime Anisotropy in Bilayer Graphene",
J.C. Leutenantsmeyer, J. Ingla-Aynés, J. Fabian, and B.J. van Wees,
Physical Review Letters **121**(12), 127702, 2018, highlighted as *Editors' Suggestion* and featured in *Physics*.
4. "Proximity-Induced Room-Temperature Ferromagnetism in Graphene Probed with Spin Currents",
J.C. Leutenantsmeyer, A.A. Kaverzin, M. Wojtaszek, and B.J. van Wees,
2D Materials **4**(1), 014001, 2017.
5. "Comparison of the Magneto-Peltier and Magneto-Seebeck Effects in Magnetic Tunnel Junctions",
J. Shan, F.K. Dejene, **J.C. Leutenantsmeyer**, J. Flipse, M. Münzenberg, and B.J. van Wees,
Physical Review B **92**, 020414(R), 2015, highlighted as *Editors' Suggestion*.
6. "Spin-Transfer Torque Switching at Ultra Low Current Densities",
J.C. Leutenantsmeyer, V. Zbarsky, M. Walter, S. Wittrock, P. Peretzki, H. Schuhmann, A. Thomas, K. Rott, T.H. Kim, M. Seibt, and M. Münzenberg,
Materials Transactions **56** (9), 1323, 2015.

7. "Parameter Space for Thermal Spin-Transfer Torque",
J.C. Leutenantsmeyer, M. Walter, V. Zbarsky, M. Münzenberg, R. Gareev, K. Rott,
A. Thomas, G. Reiss, P. Peretzki, H. Schuhmann, M. Seibt, M. Czerner, and C.
Heiliger,
SPIN **3**, 1350002, 2013.

Curriculum Vitae

Johannes Christian Leutenantsmeyer

06/1989 Born in Nordhorn, Germany.

Education

- 08/2014–09/2018 PhD program at the “Groningen Graduate School of Science and Engineering” as Marie Curie ESR-fellow within the “Initial Training Network” “Spinograph.”
Supervisor: Prof. Dr. B.J. van Wees
Research performed at: “Physics of Nanodevices”, University of Groningen, The Netherlands
- 10/2013–07/2014 Research assistant at “I. Physikalisches Institut”, Georg-August-Universität Göttingen, Germany.
- 10/2011–09/2013 Master of Science course in Solid-State Physics.
Thesis: “Parameter Space for Thermal Spin-Transfer Torque”.
Supervisor: Prof. Dr. M. Münzenberg
Research performed at: “I. Physikalisches Institut”, Georg-August-Universität Göttingen, Germany
- 08/2008–09/2011 Bachelor of Science course in Solid-State Physics.
Thesis: “Nanopatterning of CoFeB/MgO/CoFeB-based Tunneljunctions”.
Supervisor: Prof. Dr. M. Münzenberg
Research performed at: “I. Physikalisches Institut”, Georg-August-Universität Göttingen, Germany